

# Integrated Continuous Flow Photoreactor: Photooxidation of sulfides with singlet oxygen

Noémie Emmanuel

PhD advisor: Prof. Jean-Christophe Monbaliu

---

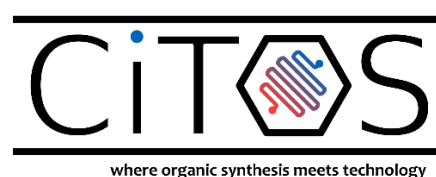
*Thesis submitted in fulfillment of the requirements for the degree of PhD of  
Sciences*

PhD dissertation



Université de Liège, Faculté des Sciences

Academic Year 2020-2021





## Acknowledgments

First, I would like to express my sincere gratitude to my thesis supervisor, Prof. Jean-Christophe Monbaliu. Not every PhD candidate has the luck to be guided by a supervisor who always considers his students as his priority. Thank you, Patron, for all the time you did not have but still spent on inspirational scientific discussions and even more inspirational non-scientific conversations. I will hold your advice for the future ahead.

I am deeply grateful to the president of the jury, Prof. Christian Damblon, and jury members, Prof. Benoît Heinrichs, Prof. Laurent Dreesen, Prof. Annemieke Madder and Dr. Guillaume Gauron for their careful reading of this PhD manuscript and for their wise suggestions that helped me improve this work.

I would like to thank Prof. Benoît Heinrichs's engineering team, Dr. Carlos Mendoza (Dr. Carlitos) and the late Dr. Carlos Alberto Pàez-Martinez (Dr. Beto) for the fruitful exchanges during meetings and for their significant contribution to this work.

My gratitude also goes to the whole Corning team for the successful collaborations with the CITOS group and for integrating me to the team for a few weeks.

I also thank Prof. Julien Legros for his precious support and insightful comments on the neutralization of chemical warfare agent simulants.

These 4 years were scientifically and emotionally challenging. I was lucky enough to share this journey with an unusually amazing team. Romaric (Rogé), Romain (Romodo), Guillaume (Guiguuiiii), Mich-Mich (Mich-Mich <3), Thomas (Toupy), Victor (VEK), Pauline (Paw), Claire, Martin, Julius, Yuesu and Diana, the shrimps and the friends we made along the way, be sure that I will keep in mind all the good memories, the Huggy's, the apéros and e-péros, the barbecues (Thank you Geoffroy), the parties, the choo-choo trains, the conferences and even the painting sessions. Take care of each other like we always did, I love you all. Long live the CITOS!

I must thank my fellow chemists from the 2016 batch production. You were there from the beginning and it is awesome to know that we still can rely on each other. Special thanks to Thomas Jungers (Thoju) for his undying support during all those years, you are the best.

Most importantly, none of this could have been possible without the encouragement of my friends and family who were there to congratulate me in the good times and to comfort me with warm words and warm food during the hard times. Mouche, Ju, Ro, Les Gras Compagnons, I will always be thankful for your unconditional love through all those years of hearing me complain. Talking about complains, I also especially thank Séverine Faorlin for her moral support.

I kept the best for the end. Tew, no words will ever describe how grateful I am to have you by my side during these past 12 years, but especially during my thesis. You can understand more than anyone else what the achievement of my thesis means to me. I want to be there for you like you've been there for me. I know that we can go through anything together and that the best is yet to come.



## Abstract

The current necessity to limit environmental and economic impacts of chemical processes combined to the need of meeting an exponentially increasing demand led scientists to rethink traditional processes. Recent advances in continuous flow chemistry motivate the transition in that direction. The inherent assets of flow chemistry such as an enhanced heat and mass transfer, better controlled reaction parameters and the handling of harsh conditions allow chemists to access to new reaction pathways that are more respectful of current demands. Photochemistry represents an economically and environmentally advantageous way to perform chemical transformations such as oxidation. Usual oxidizing agents such as  $\text{H}_2\text{O}_2$ ,  $\text{NaIO}_4$  or other inorganic salts are often toxic or expensive compounds that are not suitable with production scale syntheses. Peroxides, for example, are unstable species that represent a significant risk of explosion when stocked in large quantities. In opposition, gaseous oxygen is the most abundant, widely available, cheap and environmentally benign oxidant. Furthermore, the intrinsic reactivity of ground state oxygen can be enhanced to singlet oxygen, a more reactive species with a high oxidative power, using a photochemical process. The potential for spatial and temporal control of singlet oxygen combined to its oxidative power furnishes a robust tool for the selective oxidation of organic substrates without the need for explosive or environmentally problematic oxidizers. Sulfoxides, a common structural group found in many bioactive compounds can be obtained by selective oxidation of sulfides with singlet oxygen. However, photooxidation performances at larger scale are challenging to achieve due to problems inherent to the reactor size. Continuous flow technology opens up new horizon for photochemistry as it offers the possibility of seamless scale-up to industrial production while preserving the performance and safety of lab scale experiments. In this PhD dissertation, the optimization of the selective photooxidation of sulfides into higher value-added sulfoxides is described, covering diverse application fields. The continuous flow photoreactor involved is a low footprint, robust and versatile technology which can be adapted for safe and scalable productions.

## Table of contents

Acknowledgments .....	3
Abstract .....	5
List of abbreviations .....	8
Chapter 1. Introduction.....	9
1.1. Photochemistry .....	9
1.2. Singlet oxygen .....	11
1.2.1. General intro .....	11
1.2.2. Generation of <sup>1</sup> O <sub>2</sub> for photooxidation.....	13
1.3. Sulfide oxidation.....	15
1.3.1. H <sub>2</sub> O <sub>2</sub> and radical species oxidation pathway.....	17
1.3.2. <sup>1</sup> O <sub>2</sub> oxidation pathway.....	23
1.4. Continuous flow .....	28
1.4.1. General principles.....	28
1.4.2. Gas-liquid reactions in flow.....	35
1.4.3. Photochemistry in continuous flow .....	40
1.5. Aim of the thesis.....	48
1.6. References.....	49
Chapter 2. Scalable and selective photooxidation of methionine with singlet oxygen in a continuous flow reactor .....	55
2.1. Introduction.....	55
2.1.1. References.....	57
2.2. Transitioning from conventional batch to microfluidic processes for the efficient singlet oxygen photooxygenation of methionine.....	58
2.2.1. General information and authors contributions.....	58
2.2.2. Templated copy of the article .....	58
2.3. Scalable Photocatalytic Oxidation of Methionine under Continuous-Flow Conditions.....	74
2.3.1. General information and authors contributions.....	74
2.3.2. Templated copy of the article .....	74
2.4. Improving Continuous Flow Singlet Oxygen Photooxygenations with Functionalized Mesoporous Silica Nanoparticles.....	90
2.4.1. General information and authors contributions.....	90
2.4.2. Templated copy of the article .....	91

Chapter 3. A safe and compact flow platform for the neutralization of a mustard gas simulant with air and light .....	112
3.1. Introduction: Chemical Warfare Agents.....	112
3.1.1. References.....	114
3.2. General information and authors contributions .....	114
3.3. Templated copy of the article .....	115
Chapter 4. Photooxidation of sulfides into APIs – synthesis of smart drug modafinil.....	167
4.1. Introduction.....	167
4.2. Modafinil synthesis.....	174
4.2.1. Batch synthesis .....	174
4.2.2. Continuous flow synthesis.....	175
4.3. Conclusion .....	179
4.4. References .....	180
4.5. Supporting information .....	181
4.5.1. Flow experiments .....	181
4.5.2. HPLC method:.....	181
4.5.3. NMR spectra .....	182
Chapter 5. Conclusion and perspectives .....	186
5.1. Summary and conclusion of the PhD results.....	186
5.1.1. Conclusion and achievements of Chapter 2 .....	187
5.1.2. Conclusion and achievements of Chapter 3 .....	188
5.1.3. Conclusion and achievements of Chapter 4.....	189

## List of abbreviations

CWA	Chemical Warfare Agent
CEES	Chloroethyl ethyl sulfide
CEESO	Chloroethyl ethyl sulfoxide
CEESO <sub>2</sub>	Chloroethyl ethyl sulfone
DCA	9,10-dicyanoanthracene
DHAA	Dihydroartemisinic acid
EtOH	Ethanol
FDA	U.S Food and Drug Administration
HD	Mustard gas
HDO	Mustard gas sulfoxide
HDO <sub>2</sub>	Mustard gas sulfone
MB	Methylene Blue
Met	Methionine
MetO	Methionine sulfoxide
Msr	Methionine sulfoxide reductases
MFC	Mass flow controller
MOF	Metal-organic framework
OFC	Oscillatory Flow Reactor
OPCW	Organization for the Prohibition of Chemical Weapons
PDMS	poly(dimethylsiloxane)
POP	Porous organic copolymer
PS	Photosensitizer
RB	Rose Bengal
ROS	Reactive Oxygen Species
SCS	Sodium carbamoylmethyl sulfate
TPP	Tetraphenylporphyrin



## Chapter 1. Introduction

### 1.1. Photochemistry

Since the origin of the Universe, the interaction of light with matter has shaped our world, enabled the appearance of life and is still essential to our environment. The very essence of Science is to gain knowledge through the experimentation of an observed phenomenon and from this perspective, scientists have always been inspired by Nature. 4000 years ago, the ancient Egyptians were already aware that light could help revealing the curative potential of some plants. *Ammi Majus*, a plant that grows near the Nile was given to people suffering from vitiligo, a skin disorder responsible of a pigmentation loss. The patient had to be exposed to sunlight after ingesting the plant. The active ingredient of *Ammi Majus* is now identified as psoralen (Figure 1) and is still used to this day as a treatment against psoriasis.<sup>1,2</sup>

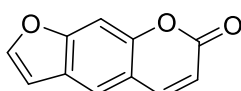


Figure 1 – Psoralen, active ingredient in *Ammi Majus*.

Scientists named “photochemistry” the branch of chemistry studying chemical transformations that are triggered by light and applications resulting from photochemistry can be found everywhere. These chemical transformations result from the interaction between matter and a photon of a suitable energy, typically belonging to the visible or ultraviolet fraction of the light spectrum to correspond to a radiation energy similar to the excitation energy of the majority of organic compounds<sup>3</sup> (Figure 2).

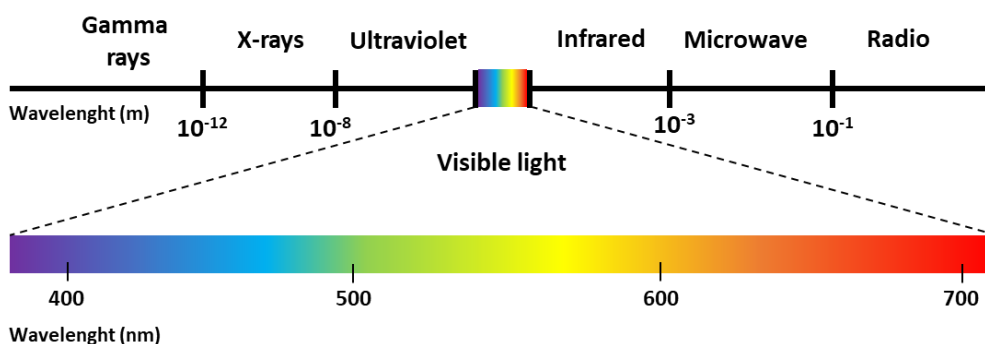
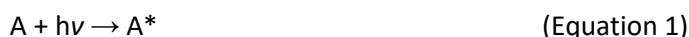


Figure 2 – Light electromagnetic spectrum.

A molecule A initially at ground state, absorbs a photon ( $h\nu$ ) and its electrons gain access to higher energy levels, the molecule A is said to be in the excited state,  $A^*$  (Equation 1).<sup>4</sup>



The notation “ $h\nu$ ” is commonly employed by photochemists to represent a photon but technically speaking,  $h\nu$  is the energy of the photon given by Planck’s Law (Equation 2).<sup>5</sup>

$$E = h\nu \quad (\text{Equation 2})$$

Where  $h = 6.63 \times 10^{-34}$  Js (Planck constant) and  $\nu$  is the frequency of oscillation of the wave (in  $s^{-1}$  or Hz).

Basic rules of photochemistry imply that chemical changes can only be caused by the light that is absorbed (Grotthuss-Draper law) and that one photon absorbed will only activate one molecule of the absorbing substance (Stark-Einstein law).<sup>3</sup>

Following these two laws, the quantum yield  $\Phi$  has been defined as:

$$\Phi = \frac{\text{\# molecules undergoing photochemical process}}{\text{\# photon absorbed}}$$

Quantum yield maximum value should always be equal to 1. However, some intense irradiation sources such as powerful lasers can cause the absorption of multiple photons derogating from Stark-Einstein law.<sup>1,5</sup>

The absorption of light energy by an organic molecule, its transition to an excited state and its relaxation back to ground state are commonly described by a Jablonski diagram (Figure 3)<sup>6</sup>. The energy given by the photon when it interacts with the absorbing molecules changes its electronic configuration so that the compound is no longer in its stable ground state ( $S_0$ ) but in an excited state ( $S_1$  or  $S_2$ ) of higher energy. The absorbed photon disappears and its energy becomes a part of the excited state of the molecule. Once in that excited state, different radiative or nonradiative processes can happen so the unstable excited molecule can lower or redistribute its excessive energy. Two isoenergetic radiationless transitions are possible. First, internal conversion can happen (arrow 2 on Figure 3) where the transition happens between two electronic states of the same multiplicity (here, two singlet states). Second, intersystem crossing (arrow 3 on Figure 3) which is a similar radiationless transition yet it involves a change of multiplicity (here, singlet to triplet) which makes it a spin-forbidden transition in regards to the selection rule. The last possible radiationless process is vibrational relaxation (arrows 4 on Figure 3). Vibrational relaxation results from collisions with surrounding environment such as solvent molecules, hence the energy is released as heat. Two other spontaneous radiative processes which lower the energy of the system can also happen. Fluorescence (arrow 5 on Figure 3) is a radiative transition, implying that a photon is emitted, between states of the same multiplicity. Phosphorescence (arrow 6 on Figure 3) is a radiative transition that is also spin-forbidden as it concerns a change of spin multiplicity.

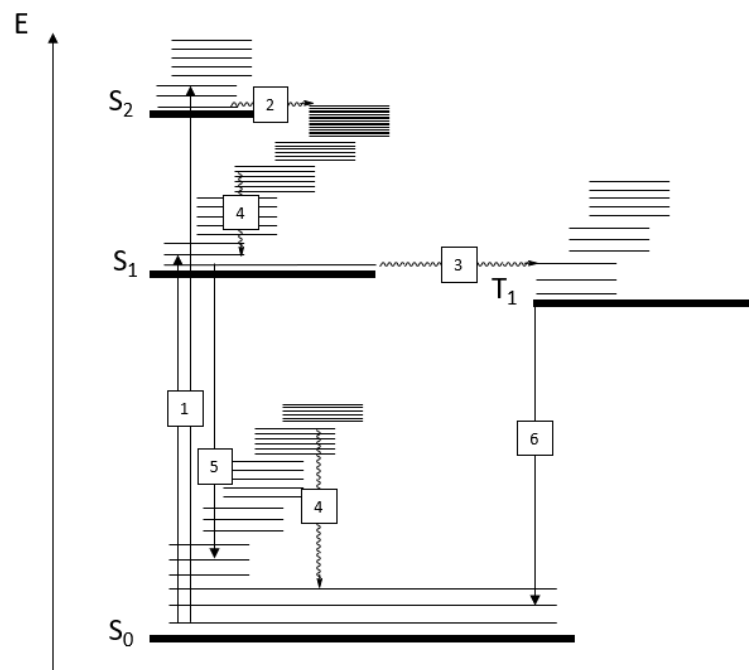


Figure 3 – General Jablonski diagram representing the different molecular states and energy transitions during the photophysical process. 1 – Absorption of a photon, 2 – Internal conversion, 3 – Intersystem crossing, 4 – Vibrational relaxation, 5 – Fluorescence, 6 – Phosphorescence.  $S_0$ ,  $S_1$  and  $S_2$  are all singlet states while  $T_1$  is a triplet state.

Hence, photochemistry can give simple access to particularly reactive molecular states that would not be easily available otherwise. One noticeable example of a photochemical transformation involving a change of spin multiplicity is the case of singlet oxygen.

## 1.2. Singlet oxygen

### 1.2.1. General intro

Oxygen is the most available oxidant on Earth, already present everywhere, hence inoffensive for health and environment and rather cheap to obtain contained in pressurized bottles for lab experiments. Ground state molecular oxygen, triplet oxygen ( $^3\text{O}_2$ ,  $^3\Sigma_g$ ), is the only stable form of molecular oxygen but has a rather moderate reactivity towards organic molecules.  $^3\text{O}_2$  is indeed a paramagnetic molecule with unpaired electrons of parallel spins in two different  $\pi^*$  molecular orbitals (Figure 4). As most of organic compounds are diamagnetic, the reaction with  $^3\text{O}_2$  is not favored because of the spin restriction. To gain in reactivity,  $^3\text{O}_2$  can be excited to create 2 new unstable forms ( $^1\Delta_g$  and  $^1\Sigma_g$  on Figure 4). Following the selection rule, transitions between states are only allowed if the spin multiplicity is conserved. Relaxation from  $^1\Sigma_g$  to  $^1\Delta_g$  is thus faster than relaxation from  $^1\Delta_g$  to  $^3\Sigma_g$ . This explains why the lifetime of the second excited state is much shorter than the first one (7 to 12 s for  $^1\Sigma_g$  versus 45 min for  $^1\Delta_g$  in gas phase) and usually does not let  $^1\Sigma_g$  enough time to react with other compounds.<sup>7</sup> Conventionally when speaking about singlet oxygen in chemical reactions, only  $^1\Delta_g$  is considered.

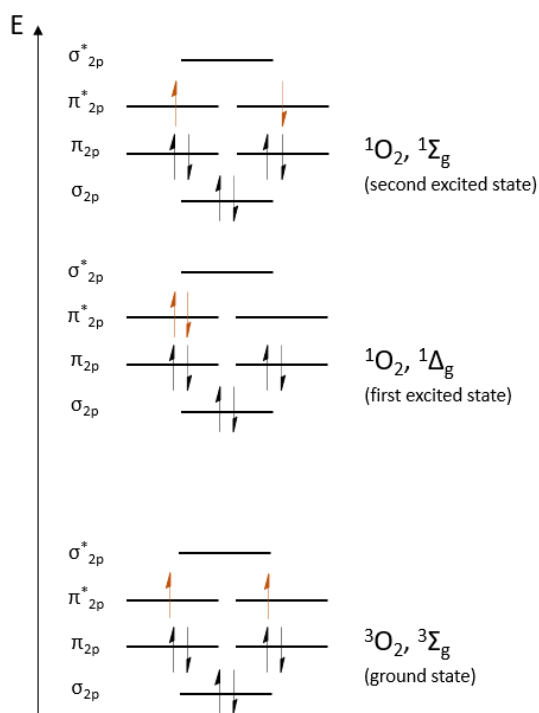


Figure 4 – Molecular orbital diagram for ground state oxygen and its 2 first excited states.

Singlet oxygen can be quenched following 2 different processes: physical quench and chemical quench. The latter typically corresponds to oxidation reactions where the substrate quench the oxygen by binding to it, creating an oxidation product. Physical quenching of singlet oxygen happens through collisions with surrounding molecules. Oxygen is deactivated and returns to ground state without formation of any new chemical product. Solvent plays a major role in this relaxation process as solvents with heavier atoms have a weaker vibrational energy, lower collision occurrences and favors singlet oxygen lifetime.<sup>7,8</sup> Many examples of singlet oxygen oxidations can be found where solvent is employed under its deuterated form because of the positive influence of those heavy solvents on  $^1\text{O}_2$  lifetime.

Ogilby *et al.* made a thorough study on singlet oxygen lifetime and the influence of the solvent and temperature.<sup>9</sup> Although the temperature effect reported was not that significant for the majority of solvents, the switch from solvent- $h_x$  to solvent- $d_x$  was significant (Table 1).

Table 1 – Singlet oxygen lifetime in different solvents at 25 °C.<sup>9</sup>

Solvent	$^1\text{O}_2$ lifetime ( $\mu\text{s}$ )
<i>n</i> -Hexane- $h_{14}$	32.1
<i>n</i> -Hexane- $d_{14}$	588
Methanol- $h_4$	9.5
Methanol-OD	31.3
Methanol- $d_4$	275
Acetonitrile- $h_3$	80.9
Acetonitrile- $d_3$	1613
H <sub>2</sub> O	3.45
D <sub>2</sub> O	67.9

## 1.2.2. Generation of $^1\text{O}_2$ for photooxidation

Singlet oxygen can be generated in various ways. A first technique was described by Turro *et al.*, and consists of the thermal decomposition of a  $^3\text{O}_2$ /acetylene complex.<sup>10</sup> In this study, the authors proposed a mechanism (Figure 5) that starts with the formation of a weak complex (**2**) from  $^3\text{O}_2$  and acetylene (**1**) in which an electron from the  $\pi_y$  of **1** is transferred to an oxygen  $\pi^*$  followed by a spin jump from  $p_x$  to  $p_y$  on the other oxygen. The ionic character of the complex favors the spin inversion rate and the complex evolves in either a zwitterion **3** or a peroxide **4**. These species can finally fragment into **1** and  $^1\text{O}_2$ .

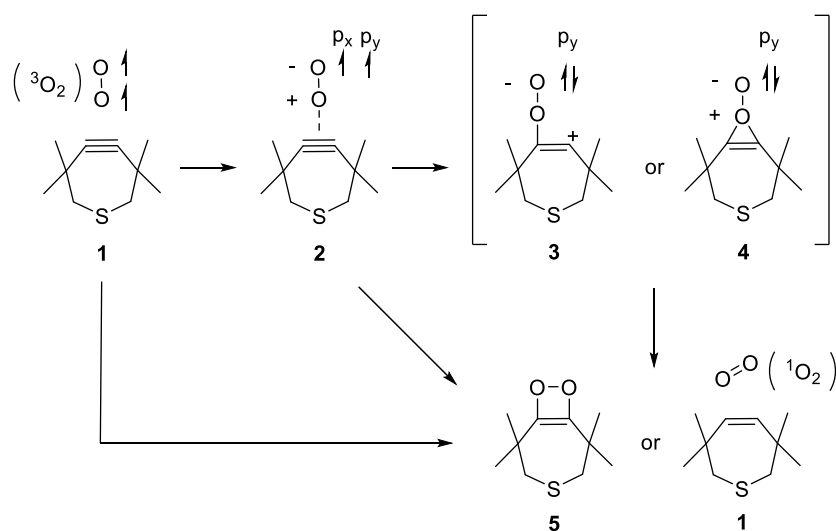


Figure 5 – Singlet oxygen generation by thermal decomposition of a triplet oxygen/acetylene complex.

A second generation method is the decomposition of peroxides. The reaction between  $\text{H}_2\text{O}_2$  and hypochlorite is one of these reactions:  $\text{H}_2\text{O}_2 + \text{ClO}^- \rightarrow \text{H}_2\text{O} + \text{Cl}^- + ^1\text{O}_2$ .<sup>11,12</sup> It has been shown that singlet oxygen can also emerge from  $\text{H}_2\text{O}_2$  decomposition with mineral compounds<sup>13</sup> or from the decomposition of other peroxides such as aromatic endoperoxides<sup>14</sup>.

However, the most common way to produce  $^1\text{O}_2$  is to use a photosensitizer (PS) combined with an appropriate irradiation. A PS is a compound bearing chromophores which can absorb light radiation and transfer it to other molecules. In type-I photooxygenation, the excited PS reacts with the substrate through electron or hydrogen transfer resulting in the formation of free radicals that will react with ground state oxygen to create new active oxygen species such as superoxide anion, hydroxyl radical or hydrogen peroxide. However, the photooxidation mechanism that will be studied in this dissertation is the type-II (Figure 6) as it results in the formation of singlet oxygen which is a milder oxidant species than those resulting from type-I. In type-II photooxygenation, the ground state PS, a singlet state ( $^1\text{PS}$ ), is irradiated by a light source of adequate wavelength which turns it into an excited singlet state PS ( $^1\text{PS}^*$ ). This unstable species quickly transfers its energy to its excited triplet state ( $^3\text{PS}^*$ ) through intersystem crossing. Now that oxygen and PS have the same spin multiplicity, their interaction is allowed and result in the formation of singlet oxygen.<sup>15</sup>

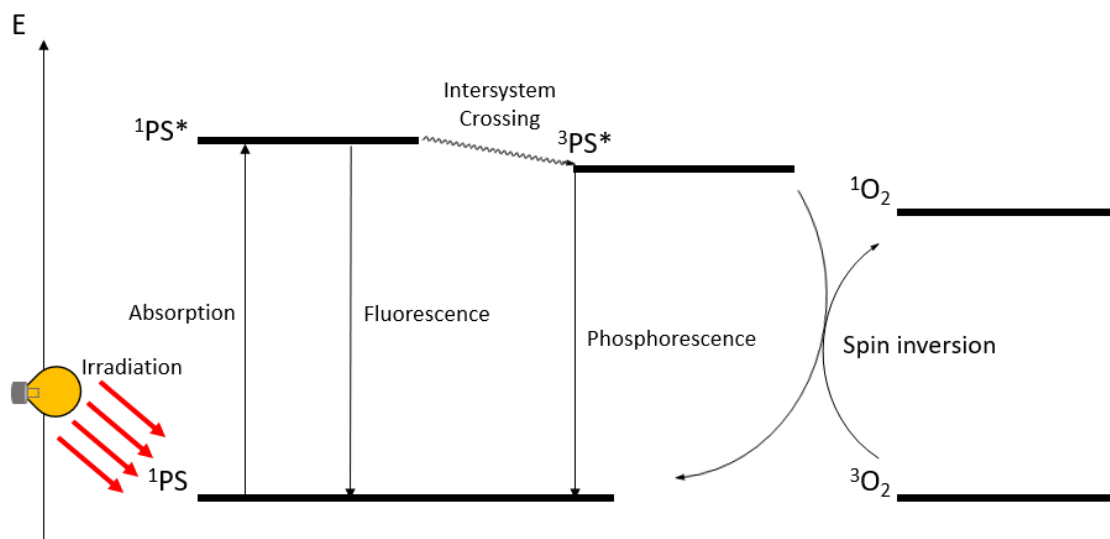


Figure 6 – Simplified Jablonski diagram for the generation of singlet oxygen through Type-II mechanism.

PS are usually classified into two categories: homogeneous PS and heterogeneous PS. Homogeneous PS are dyes or chromophores compounds that can be dissolved in the same solvent as the substrate to oxidize. Common homogeneous PS are Rose Bengal (RB), Methylene Blue (MB) and modified porphyrins such as TCPP (Tetrakis(4-carboxyphenyl)porphyrin) (Figure 7). With quantum yield around 0.7 for RB, 0.5 for MB and between 0.7 and 0.9 for TCPP in organic solvents.<sup>16</sup> Heterogeneous PS are chromophores molecules that are bound to a metal, often in metal-organic frameworks (MOFs) or on nanoparticles and that will remain solid during the whole oxidation process. Both categories present their own advantages and drawbacks and the choice between homogeneous and heterogeneous catalyst affects the reaction in terms of costs, purification, toxicity or irradiation source. The catalyst is thus a key parameter of any photoreaction.

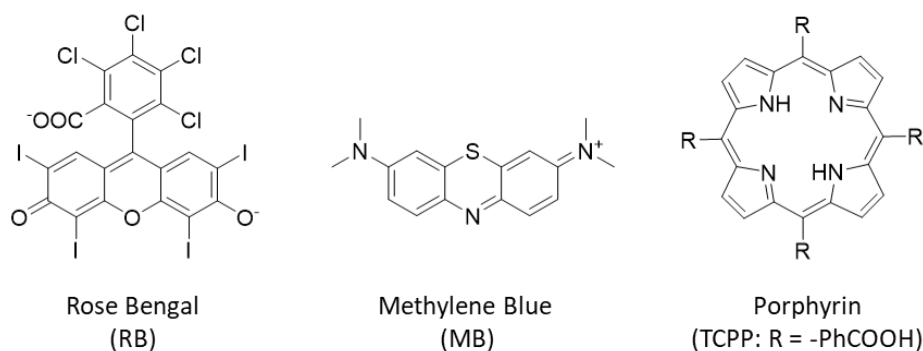


Figure 7 – Chemical structure of common photosensitizers. In porphyrins, R most often stands for a phenyl group or a carboxyphenyl group.

Most photocatalysts do not have an unlimited stability and will degrade after a few cycles of irradiation-relaxation. This photodegradation is called photobleaching<sup>17,18</sup> and results in the irreversible loss of PS capacities. Some PS are more resistant than others to photobleaching and this asset will guide the choice of PS regarding of the application requirements. Chemical modifications on the PS can improve its resistance toward photobleaching.<sup>19</sup>

It is important to note that  $^1\text{O}_2$ , although being the main theme of this PhD thesis, is not the only Reactive Oxygen Species (ROS). Depending on the catalyst, irradiation or oxygen source employed for the reaction, other ROS can be generated such as superoxide radical anion ( $\text{O}_2^{\cdot-}$ ), peroxide ( $-\text{OOH}$ ) and hydroxyl radical ( $\text{HO}^{\cdot}$ ). In synthesis applications, it is common to observe the simultaneous generation of several ROS under the same conditions. The competition between those ROS can then lead to overoxidation or side product formation.

In biological environment, ROS are responsible of cell oxidative stress due to their reactivity. This process results in damaging the cell and is thus employed in photodynamic therapy where a combination of light and PS generates ROS *in vivo* to destroy targeted cells (cancerous cells or cells involved in skin diseases)<sup>20</sup>. This destructive potential of ROS is also employed for the inactivation of microorganisms in antimicrobial photodynamic therapy<sup>21</sup> or for the degradation of organic pollutant in water<sup>22</sup>.

### 1.3. Sulfide oxidation

Sulfur is the 3<sup>rd</sup> most abundant mineral in the human body and represents 0.3% of total body mass in an adult.<sup>23</sup> The recommended daily consumption of sulfur is of 14 mg per kg body weight (for average young man).<sup>24</sup> The uptake of sulfur occurs through nutrition as the mineral atom is included in several biological molecules, mainly amino acids and derivatives: cysteine, methionine and taurine. Methylsulfonylmethane is another major sulfur source from diet (Figure 8).

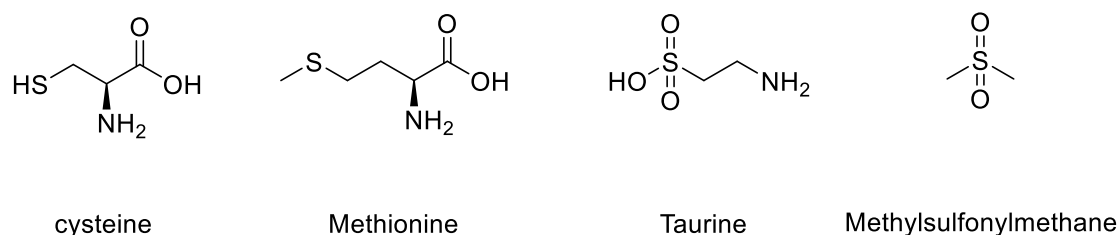


Figure 8 – Major sulfur-containing biological molecules.

Sulfur-containing compounds represent a vast category of molecules involved in organic chemistry and medicinal science. The ability of sulfur to react with oxidizers to give sulfoxides or sulfones (Figure 9) participates in a number of biological processes. Sulfides, sulfoxides and sulfones are hence found in a plethora of pharmaceuticals, amino acids and natural molecules (Figure 10).<sup>25,26</sup>

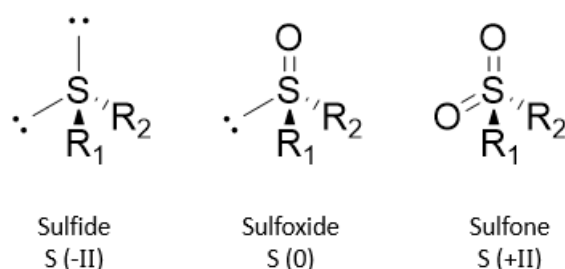


Figure 9 – Sulfide oxidation states.

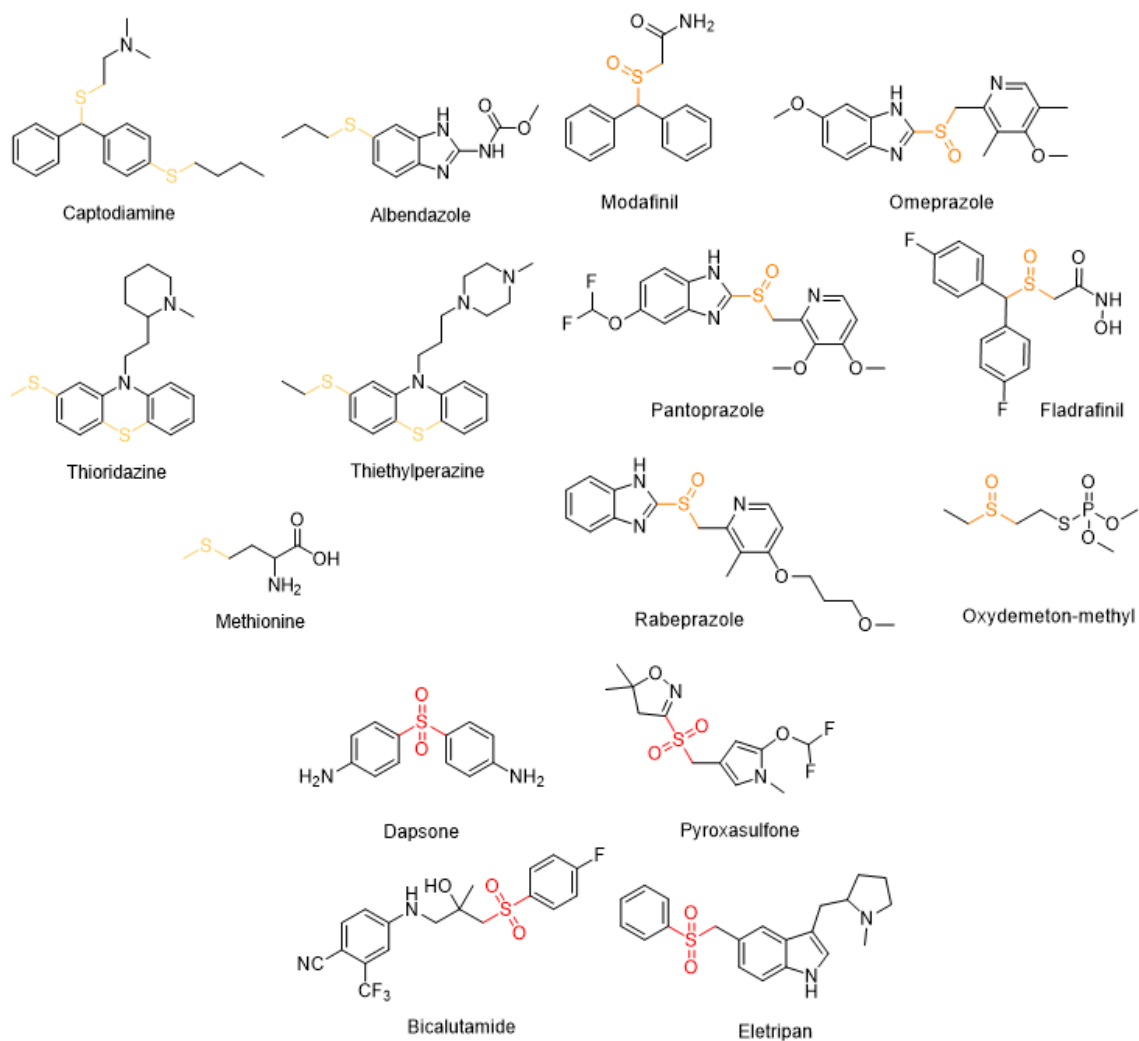


Figure 10 – Pharmaceutically and biologically active compounds bearing sulfides (yellow), sulfoxides (orange) or sulfones (red).

Sulfoxides, the intermediate level of sulfide oxidation, are of tremendous importance as they potentially bear a stereogenic center, the stereochemistry of which influences the biological activity of the molecule.<sup>27</sup> Omeprazole, a commercial anti-acid, is one of these molecules (Figure 11). The omeprazole chirality relies on the sulfoxide group and the *S* enantiomer is the most active. Esomeprazole, the *S* enantiomer, shows an increased acid inhibition compared to racemic mixture.<sup>28-30</sup> However, the most common pharmaceutical formulation is a racemate (Figure 11).<sup>31,32</sup>

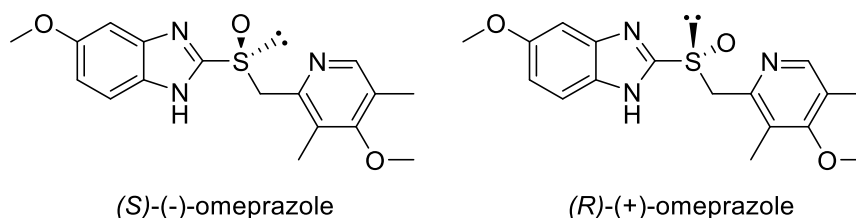


Figure 11 – Omeprazole enantiomers.



Although the stereochemistry of sulfoxides is not the subject of this PhD thesis, this property attracted the attention of chemists for many applications outside of bioactivity such as catalysis<sup>33–35</sup> and analytical applications<sup>36</sup> but symmetrical sulfoxides are also used to mediate organic reactions<sup>37,38</sup>. Sulfoxides are found in important FDA approved pharmaceuticals, including the prazole family gathering proton pump inhibitors with similar structure to omeprazole<sup>25,39,40</sup> and which reduce stomach acidity, or in wake-promoting agents such as Modafinil and derivatives<sup>41,42</sup>. Researches are currently conducted to modify already existing drugs by inserting a sulfoxide moiety to fight against malaria parasite's resistance<sup>43</sup> or to reduce drug's side effects<sup>44</sup>.

### 1.3.1. H<sub>2</sub>O<sub>2</sub> and radical species oxidation pathway

**N.B.:** The state of the art in this section gathers the most recent advances concerning general sulfide oxidation. More specific literature to the applications covered in this PhD manuscript can be found in each introductory sections of each chapter below.

A classical and straightforward oxidation pathway is to use hydrogen peroxide on sulfides. H<sub>2</sub>O<sub>2</sub> is often found as diluted aqueous solution (30 wt%), it is affordable and efficient. However, peroxides can decompose in a violent exothermic reaction and should be kept in a fridge to diminish the risks. Moreover, this strong oxidant often leads to overoxidation, hence leading to a mixture of both sulfoxide and sulfone. To alleviate this poor selectivity issue, H<sub>2</sub>O<sub>2</sub> is regularly coupled with an inorganic/metallic catalyst.

Loh *et al.* used a molybdenum catalyst that is known for having a tendency to bind to sulfur atoms<sup>45</sup> and which would ease the oxidation. Although the method was first developed in order to fully oxidize sulfides into sulfones, the authors attempted the semi-oxidation by reducing the amount of peroxide to 1.1 equivalent versus 2.5 equivalents for the full oxidation. A variety of aromatic sulfoxides were obtained with yields ranging from 67% to 88% (Figure 12). The authors claimed that the process is chemoselective but did not provide any precision concerning the selectivity. The role of hydroxyl radicals in the oxidation was confirmed by electron paramagnetic resonance measurements.

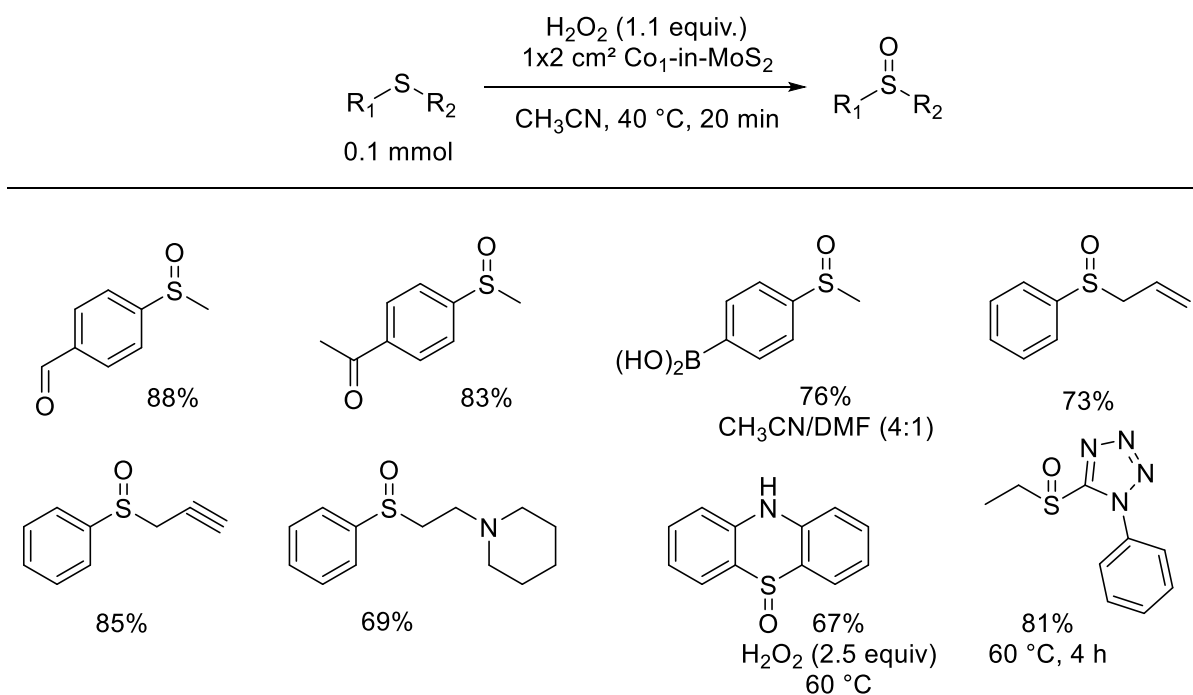


Figure 12 – Selective oxidation of various sulfides into their corresponding sulfoxide with H<sub>2</sub>O<sub>2</sub> and Co<sub>1</sub>-in-MoS<sub>2</sub> as a catalyst. Yields are indicated.

Shokouhimehr *et al.* also studied the selective oxidation of thioanisole and other aromatic sulfides with H<sub>2</sub>O<sub>2</sub> and oxygen-enriched molybdenum supported on bipyridinium bridge mesoporous silica (MoO(O<sub>2</sub>)<sub>2</sub>@Bipy-PMO-IL) as a heterogeneous catalyst.<sup>46</sup> Although the catalyst allowed full conversion of thioanisole within 30 min in water, sulfoxide was produced along with 10% of sulfone under the best conditions. The various other aromatic sulfides covered in this scope also gave a mixture of both oxidation products (Figure 13).

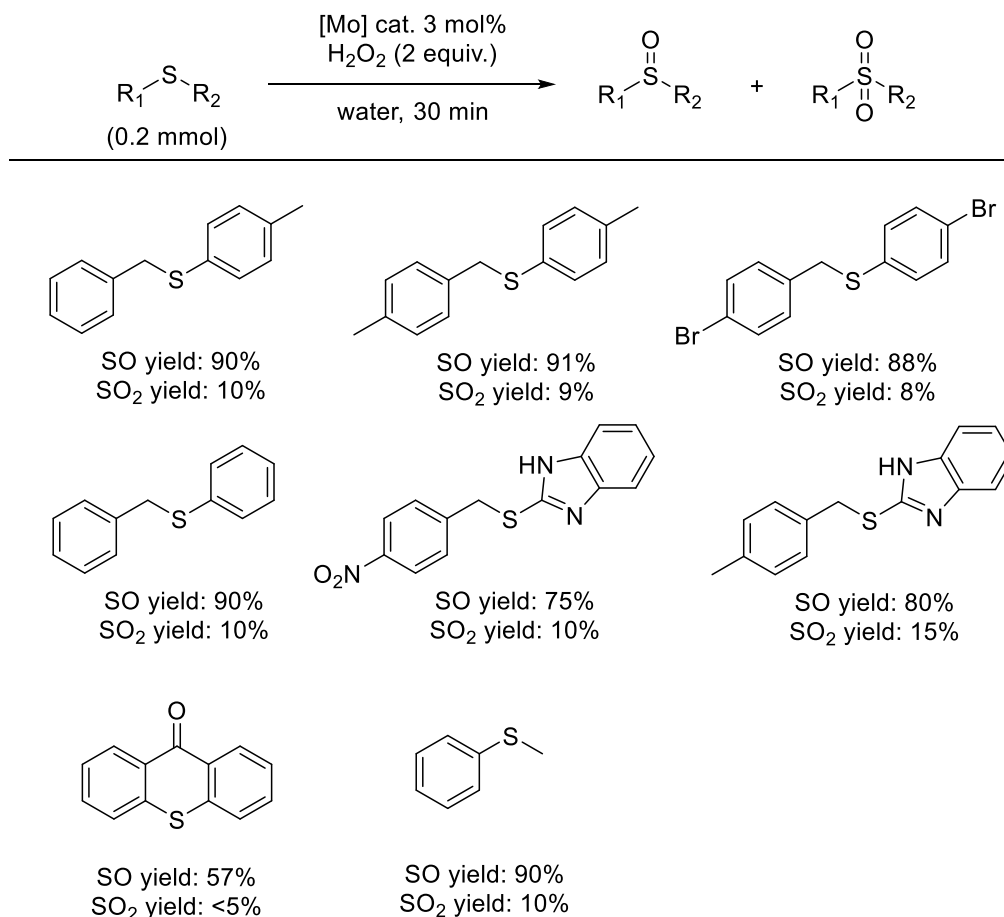


Figure 13 – Oxidation of various sulfides with H<sub>2</sub>O<sub>2</sub> and MoO(O<sub>2</sub>)<sub>2</sub>@Bipy-PMO-IL.

Peroxides can also be photoactivated by a catalyst and the nature of the catalyst determines the ROS. Chmielarz *et al.* studied the selectivity of the oxidation of diphenyl sulfide (Ph<sub>2</sub>S) with H<sub>2</sub>O<sub>2</sub> in the presence of TiO<sub>2</sub> doped with metals: Zn, Sn, V.<sup>47</sup> All reactions were carried in the dark and under UV light as TiO<sub>2</sub> is known to photochemically activate H<sub>2</sub>O<sub>2</sub>. Cut off filters were applied to avoid direct oxidation of the sulfide. The control oxidation with TiO<sub>2</sub> only resulted in a total conversion of Ph<sub>2</sub>S in acetonitrile in 30 min under UV light, yet, giving both Ph<sub>2</sub>SO and Ph<sub>2</sub>SO<sub>2</sub>. The same experiment was first conducted with V-TiO<sub>2</sub> as a catalyst. The selectivity for the sulfoxide reached 98% under irradiation but the conversion did not surpass 90% even after 3h of oxidation. The oxidation in presence of Sn-TiO<sub>2</sub> was complete after 2.5 h with 99% of selectivity. However, pursuing the oxidation for more than 2.5 h resulted in a quick selectivity drop, emphasizing the need to control the reaction time. Best results were obtained with Zn-TiO<sub>2</sub> as a catalyst. The conversion was complete after 2 h, almost exclusively to the sulfoxide and the selectivity was not significantly affected by longer reaction times. TiO<sub>2</sub> under irradiation can activate both H<sub>2</sub>O<sub>2</sub> and O<sub>2</sub> into hydroxyl radicals (HO<sup>•</sup>) and superoxide radical anions (O<sub>2</sub><sup>•-</sup>). As the reaction flask was not sealed, a small amount of oxygen could reach the reaction middle. Although an experiment in the presence of a HO<sup>•</sup> scavenger demonstrated that the oxidation is majorly due to HO<sup>•</sup>, the oxidation was not completely suppressed and is thus partly due to O<sub>2</sub><sup>•-</sup>.

Hydrogen peroxide is produced by a catalytic reduction/oxidation cycle of anthraquinone.<sup>48</sup> Recently, Huang *et al.* mimicked this process to generate peroxide in-situ for more safety.<sup>49</sup> The authors used 1,6-pyrenedione instead of anthraquinone and isopropanol as a hydrogen donor. This catalytic cycle is triggered under blue LEDs irradiation and creates a radical on the 1,6-pyrenedione that will be reduced by two consecutive hydrogen atom transfers. The final oxidation of the resulting 1,6-pyrenediol releases H<sub>2</sub>O<sub>2</sub> with recovered 1,6-pyrenedione (Figure 14). The slow release of H<sub>2</sub>O<sub>2</sub> is favorable to a more controlled oxidation. Thioanisole, 4-bromothioanisole, diphenylsulfide and tetramethylsulfide were successfully oxidized into their corresponding sulfoxide on a 0.2 mmol scale with 90%, 95%, 75% and 95% yield respectively. However, reaction times ranged from 24 to 40 h. Quenching experiments revealed the implication of superoxide radical anion in the oxidation.

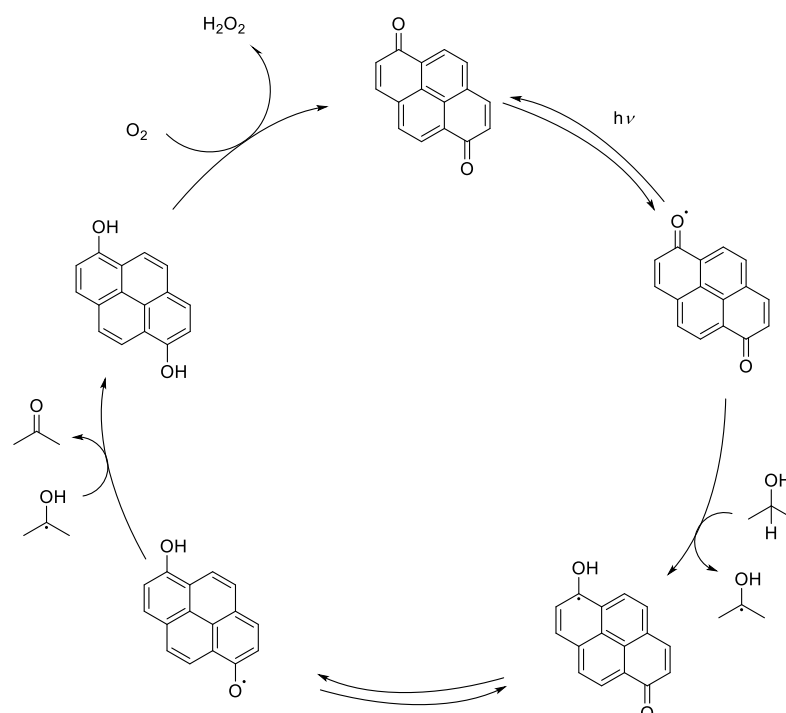


Figure 14 – Catalytic cycle for the in-situ generation of H<sub>2</sub>O<sub>2</sub> with 1,6-pyrenedione and isopropanol.

Radical oxygen species such as O<sub>2</sub><sup>•-</sup> can also be generated by the photoactivation of a catalyst in the presence of oxygen which suppress the need for peroxides. To control the semi- or full oxidation of sulfides, Suzuki *et al.* proposed a protocol employing a decavanadate tetraphenylphosphonium salt (TPPV<sub>10</sub>) as a catalyst in methyl ethyl ketone (MEK).<sup>50</sup> The oxidation pathway involved a sulfide radical cation (R<sub>2</sub>S<sup>•+</sup>) and a superoxide radical anion. The outcome of the reaction was governed by the presence of water in the solvent which allowed to switch from semi- to full oxidation (Figure 15). The authors believed that water prevented the formation of MEK-derived peroxides that were responsible for the second oxidation which stopped the reaction after the sulfoxide formation.

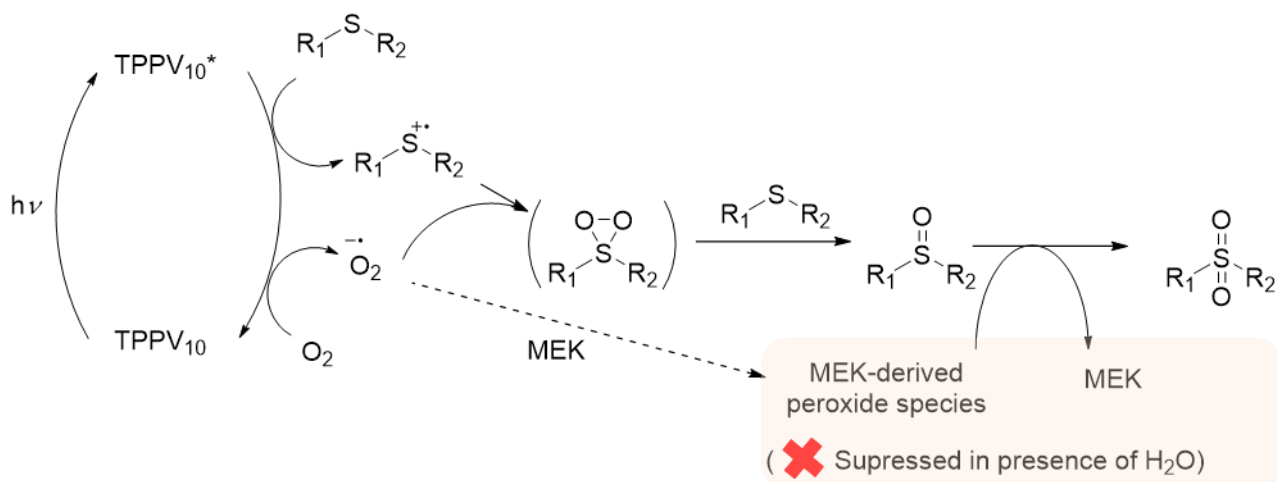


Figure 15 – Oxidation mechanism with  $O_2$  and TPPV<sub>10</sub> as a catalyst in MEK or MEK/water.

Wang *et al.* opted for a reusable heterogeneous catalytic system where a complex of Cu(II) and pyridine coupled with TEMPO could trigger the oxidation of various sulfides.<sup>51</sup> The authors proposed a mechanism involving single electron transfer (Figure 16) leading to the generation of  $O_2^{\cdot-}$ . The Cu(II) complex was reduced in the presence of TEMPO allowing TEMPO+ to create the active sulfide radical cation. The Cu(I) resulting from the previous reduction interacted with molecular oxygen to generate the superoxide anion radical species that could react with the sulfide radical cation to create an intermediate peroxysulfoxide which in turns became a sulfoxide in the presence of a protic solvent. In a more practical way, their oxidation experiments consisted in mixing 0.5 mmol of sulfide with CuSO<sub>4</sub> (5 mol%), pyridine (20 mol%) and TEMPO (4 mol%) under a  $O_2$  atmosphere and at 65 °C with reaction times varying between 8 h and 72 h depending on the sulfide structure. Total conversion of sulfides was reached within those reaction times but the majority of experiments showed overoxidation signs with formation of sulfone, up to 9% for diphenyl sulfide. However, diphenyl sulfide was oxidized with a 85% yield (91% selectivity) and the reaction efficiency was not affected when the scale was increased to 10 mmol. The advantage of heterogeneous catalyst is their ability to be filtered and recycle in successive oxidations. The Cu(II)-pyridine complex could be reused 3 times without altering its efficiency.

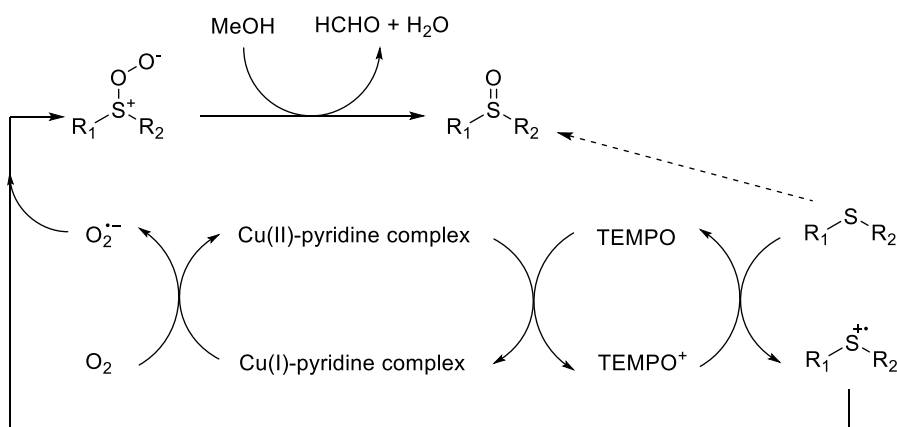


Figure 16 – Catalytic cycle for the formation of sulfoxides with a Cu(II)-pyridine catalyst complex with  $O_2$ .

Ye and Wei performed a  $O_2^{\bullet-}$  generation with three Ir-Zr-MOFs in aqueous solution and selectively oxidized sulfides bearing diverse functional groups.<sup>52</sup> The three MOFs tested,  $Zr_6$ -Irbpy (bpy is 2,2'-bipyridine),  $Zr_6$ -IrbpyOMe (bpyOMe is 4,4'-dimethoxy-2,2'-bipyridine) and  $Zr_6$ -Irrphen (phen is 1,10-phenanthroline), were selected for their high stability and activity towards sulfoxidation in aqueous environment. In these experiments, a model sulfide, thioanisole (0.25 mmol), was dissolved with catalyst (4 mol%) in distilled water (4 mL) in a glass vessel covered with a balloon filled with oxygen. The whole mixture was irradiated under blue light (100 W LEDs) for 6 to 18 h. A quantitative yield was reached with  $Zr_6$ -Irrphen as a photocatalyst in 6 h. The same results were obtained in EtOH and MeOH but the sulfoxidation took 12 and 10 h respectively in these solvents. The formation of hydrogen bonds that stabilize the persulfoxide intermediates favors the sulfoxidation in polar protic solvents. For comparison, the same reaction in MeCN, a polar aprotic solvent, or in DCE, a non-polar solvent, gave much lower yields even after 18 h of irradiation. Thioanisole sulfoxide was obtained with a 79% yield in MeCN while only traces were detected in DCE. Sulfone could not be detected in any of the experiments demonstrating the chemoselectivity of the reaction. The reusability of  $Zr_6$ -Irrphen was then assessed. The reaction was carried for 6 h, then the catalyst was separated by centrifugation, washed with distilled water and used in another 6 h run. No loss in catalytic activity could be observed even after 10 reutilizations. Modifying thioanisole with electron-donating groups in *para* position didn't affect the reaction while electron withdrawing groups required longer reaction times to obtain the same yield (23 h for Cl and 32 h for Br). Those reaction times were even increased to 54 h for Br in *ortho* position of the phenyl ring compared to only 20 h for -OMe in the same position. The chemoselectivity of the oxidation was not affected by the introduction of functional groups such as vinyl, aldehyde and cyan group as they all remained intact after oxidation of the sulfide. The photo oxidation was then performed on a benzimidazole sulfide (Figure 17). This structure is frequently found as sulfoxide in FDA approved drugs such as anti-acids. The oxidation conditions required to be slightly modified as the solvent was replaced by a water/MeOH 1:1 mix and the quantity of catalyst was doubled. Nevertheless, the corresponding sulfoxide was successfully obtained in 96% yield in 42 h. No sulfone could be observed.

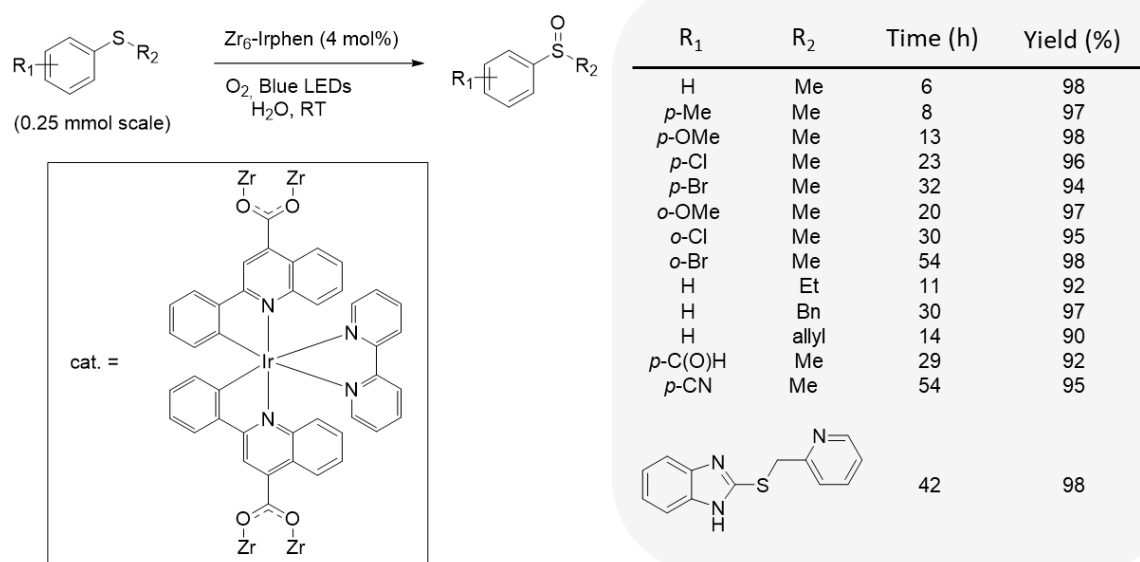


Figure 17 – Sulfide photooxidation with  $Zr_6$ -Irrphen as a PS and oxygen.

A substrate scope investigation enabled to demonstrate the ease in switching from sulfoxide to sulfone just by modifying the solvent (Figure 18). All experiments were conducted on a 0.1 to 0.2 mmol scale and gave moderate to good yields. However, selectivity for the sulfoxide synthesis is almost always lower than for the sulfone production.

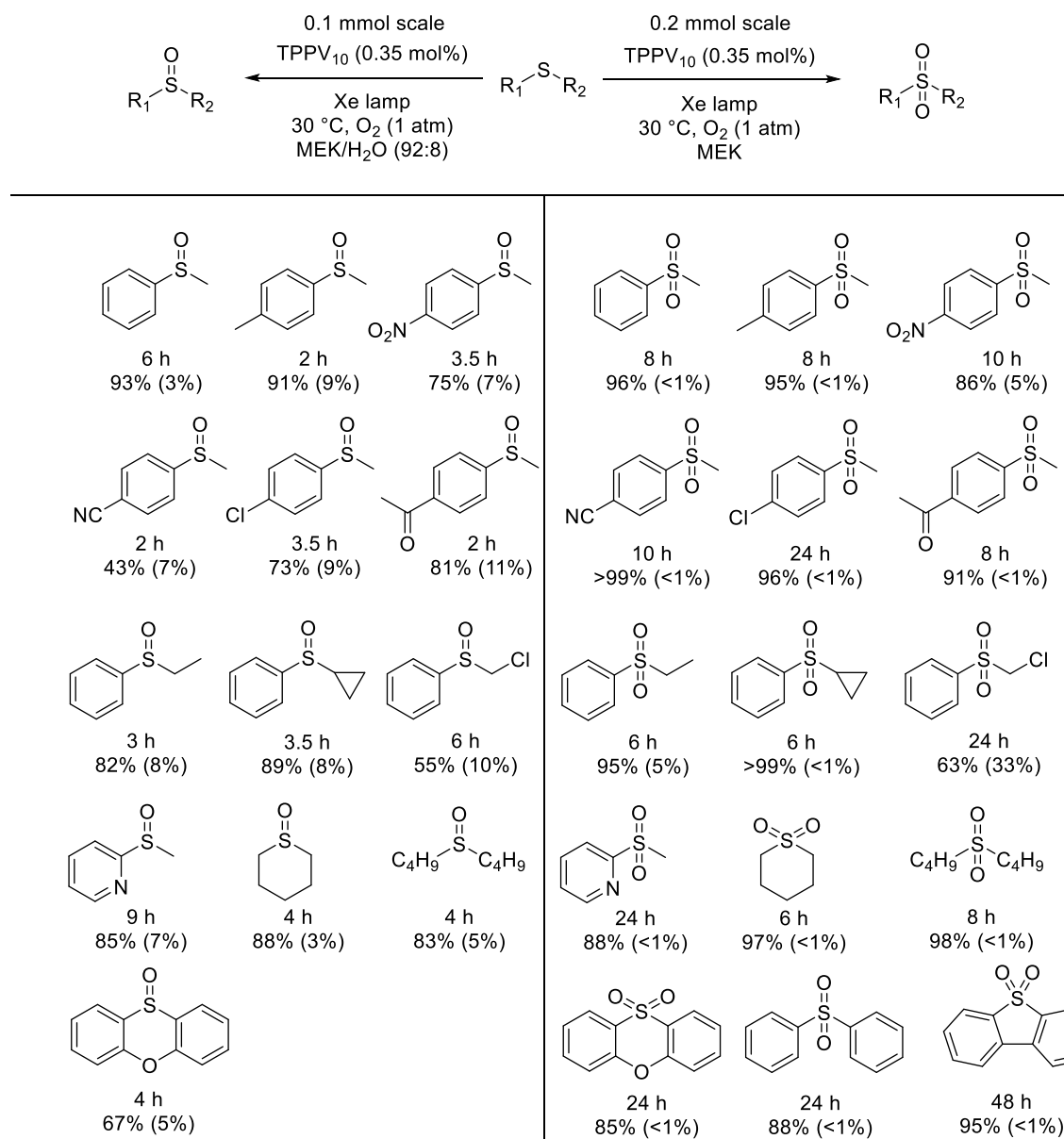


Figure 18 – Substrate scope for the oxidation of sulfides with TPPV<sub>10</sub> in MEK/water or MEK. Isolated yields are provided with amount of sulfone (for MEK/H<sub>2</sub>O protocol)/sulfoxide (for MEK protocol) between parentheses.

Better yields and selectivities were obtained by Ye *et al.* who opted for a bismuth oxyhalide catalyst (Bi<sub>4</sub>O<sub>5</sub>Br<sub>2</sub>).<sup>53</sup> The bismuth catalyst could be dispersed in water with the hydrophobic sulfide. The production of hydrophilic sulfoxide gradually removed the product from the surface where the reaction occurred which was favorable to the reaction. The activation under blue light generated an electron-hole pair on the catalyst that in turn created a superoxide radical anion from oxygen and a sulfur radical cation from the substrate. Those radicals subsequently reacted together to form the sulfoxide. A scope of thioanisole derivatives was successfully oxidized with high selectivities for the sulfoxide on a 0.2 mmol scale (Figure 19).

Vázquez *et al.* worked on the selective oxidation of diphenyl sulfide with H<sub>2</sub>O<sub>2</sub> and a novel catalyst consisting of silica/alumina matrix in which heteropolyacids derived from phosphomolybdic acid containing niobium (PNbMo) were included.<sup>54</sup> The sulfide (1 mmol) was dissolved in EtOH (8 mL) with the different catalysts (12 mg) and mixed with H<sub>2</sub>O<sub>2</sub> 35 wt% (1.5 mmol). Regarding their niobium derived catalysts, their efficiency toward the oxidation of diphenyl sulfide was dependent of the matrix constitution (Si, Al or SiAl-1:1 or SiAl-4:1). Most of them allowed to reach full conversion after 5 h but with poor selectivities between 42% and 68%. The best results were obtained with PNbMo-Si that gave a 92% conversion (94% selectivity) in 4 h and with PNbMo-SiAl-4:1 that gave a 92% conversion (95% selectivity) in 4 h.

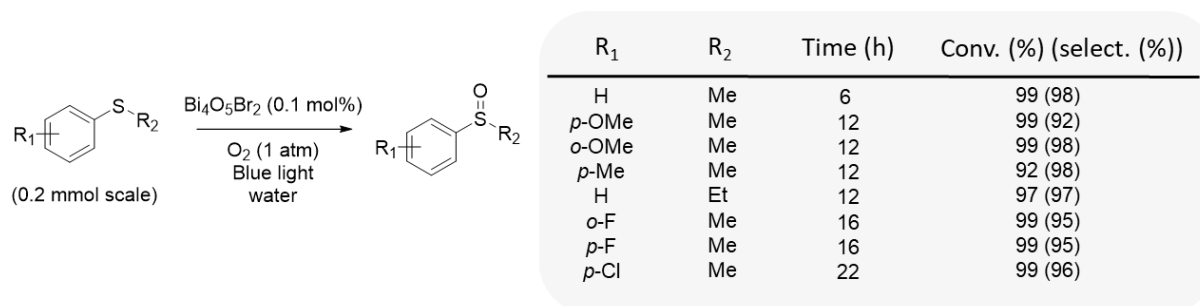


Figure 19 – Photooxidation of thioanisole derivatives with radical oxygen species generated by irradiation of Bi<sub>4</sub>O<sub>5</sub>Br<sub>2</sub> and oxygen in water.

Another catalytic oxidation pathway was developed by Zhang *et al.* who synthesized a salen-chromium-(V)-oxo complex that was able to activate PhI(OAc)<sub>2</sub> for sulfides oxidation.<sup>55</sup> The initial Cr(III) catalyst was first oxidized in a Cr(V) complex under visible light and in ambient air. The authors did not identify the active ROS in this catalytic system but suggested that the salen-Cr(V)-oxo complex, in the presence of water, might activate PhI(OAc)<sub>2</sub> into PhIO which has a greater oxidizing power. Thioanisole derivatives were oxidized with good yields and selectivities on a 0.5 mmol scale (Figure 20).

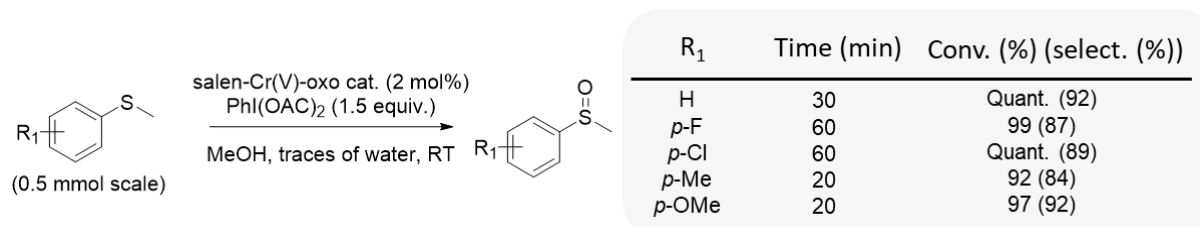


Figure 20 – Sulfides oxidation with PhI(OAc)<sub>2</sub> and Cr(V) catalyst.

### 1.3.2. <sup>1</sup>O<sub>2</sub> oxidation pathway

As a milder oxidant, <sup>1</sup>O<sub>2</sub> has been studied for decades, applied to a plethora of oxidations and remains an excellent alternative to harsh oxidizers such as peroxides or radicals.

In 1998, Clennan *et al.* studied the mechanism of addition of singlet oxygen on a sulfide taking dimethylsulfide as a model substrate.<sup>56</sup> In the very first step of sulfoxide genesis, one of the sulfide lone pairs is given to the electrophile singlet oxygen leading to formation of the peroxyulfoxide (**2**) or the thiadioxirane (**3**). Once the peroxyulfoxide formed, different potential pathways are opened. It can just be quenched with a return to ground state for oxygen and no chemical transformation for the sulfide (Figure 21, pathway A). Peroxyulfoxide **2** can also give its outer oxygen to either a sulfide or a sulfoxide (Figure 21, pathway B). However, the authors calculated the activation barriers for the transfer to a sulfide and it appears to be less likely to happen. Indeed, the transition state for this transfer is 5 kcal mol<sup>-1</sup> above the energy of both separated species, while the transition state for the

transfer to a sulfoxide is 6 kcal mol<sup>-1</sup> below the separated species. The presence of a protic solvent such as water or MeOH can influence the evolution of intermediate **2** depending on its concentration. At low concentration, the protic solvent acts as a proton source for the ylide (pathway F) and gives the sulfone. At high concentration, it can add itself on **2** to form a sulfurane (**5**) that reacts with a sulfide molecule to give 2 sulfoxides (Figure 21, pathway C). An intramolecular hydrogen abstraction (Figure 21, pathway D) that mimics an ene reaction can lead to a S-hydroperoxysulfonium ylide (**4**) that will eventually lead to a sulfone by exchanging a proton with surrounding solvent (pathway F) or to molecules resulting from the breaking of peroxy bond and C-S bond (pathway E). Intermediate **4** can also give its -OH to a sulfide molecule that returns the proton to yield to two sulfoxides molecules (pathway H).

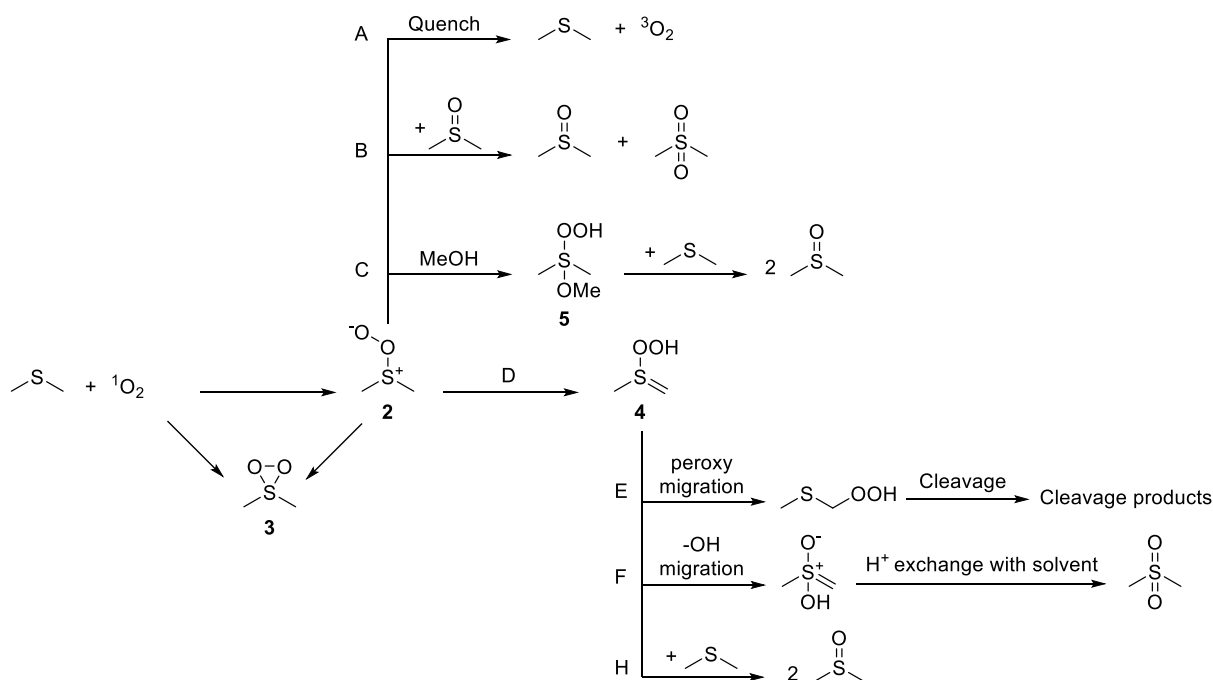


Figure 21 – Mechanism proposed by Clennan *et al.* for the reaction of singlet oxygen with a dimethyl sulfide.

The reaction with dialkyl sulfides is indeed favored as the HOMO of such sulfides is located on a  $n_s$  ( $p_y$ ) orbital.<sup>57</sup> For diaryl and aryl alkyl sulfides, however, the HOMO is located on a  $\pi$  ( $p_z$ ) which lower the nucleophilicity of the sulfide. This phenomenon coupled to steric hindrance explains why the oxidation of aromatic or sterically crowded sulfides with singlet oxygen is slower.

Several organo-PS and metallic PS are known to generate  $^1\text{O}_2$  under irradiation<sup>58–60</sup> such as previously cited RB<sup>61</sup>, MB<sup>62,63</sup> or porphyrins<sup>15,64,65</sup>. However, new catalysts are continuously developed to increase the efficiency and the selectivity of the oxidation. Rao *et al.* exploited the similarities between Emodin and natural cercosporin structure to assess its photophysical properties.<sup>66</sup> Cercosporin is a natural molecule extracted from a fungus with a quinone moiety, which is a common feature with Emodin. A wide scope of thioanisole derivatives was chosen as demonstration substrates for selective oxidations (Figure 22). The position of the aromatic ring substituents was determining in the efficiency of the oxidation. Electron-donating group gave excellent conversions in every position on the ring while sulfides with halides substituents were harder to oxidize in *ortho*- then in *para*- or *meta*-position. Electron withdrawing groups led to moderate oxidations. The authors identified the ROS species superoxide radical anion and singlet oxygen after experiments with inhibitors. No sulfone was detected in those experiments.



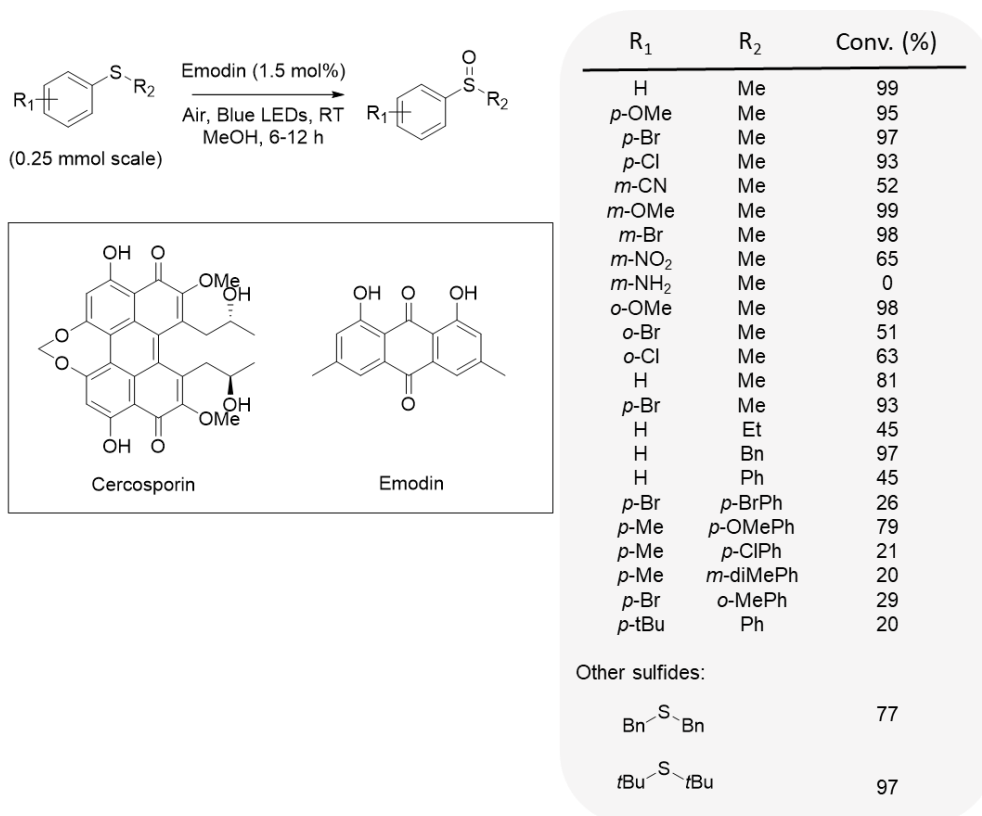


Figure 22 – Substrate scope for the photooxidation of sulfides with Emodin under blue LEDs irradiation.

Another metal-free PS was synthesized by Dick *et al.* who used an aminated alloxazine to mimic the structure of flavin and riboflavin tetraacetate.<sup>67</sup> Again, both <sup>1</sup>O<sub>2</sub> and O<sub>2</sub><sup>•-</sup> were responsible for the sulfide oxidation. All sulfides were completely and selectively oxidized into their corresponding sulfoxides, except for the nitro-aromatic substituted compounds that is thought to quench radicals which prevent efficient oxidation (Figure 23). However, these excellent yields were obtained on a particularly small scale (0.02 mmol).

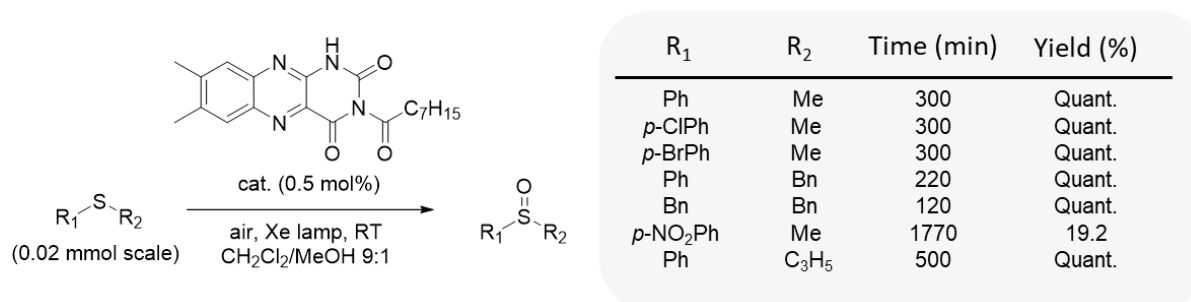


Figure 23 – Substrate scope for the photooxidation of sulfides with an aminated alloxazine.

Fan *et al.*, worked with a perylene diimide photocatalyst (PDI) for the selective photooxidation of methyl phenyl sulfide along with a large panel of other alkyl, aryl alkyl and aryl sulfides.<sup>68</sup> The mix of 0.5 mmol of sulfide and PS (2 mol%) was irradiated in MeOH under blue LED for reaction times between 8 and 16 h. With a pressure of oxygen above the solution, sulfoxides were obtained with yields between 68% for methyl phenyl sulfide with a *o*-OMe and 91% for methyl phenyl sulfide (Figure 24). The same procedure with air instead of oxygen did not give such conversions. The authors decided to perform a scale-up on a 20 mmol scale of methyl phenyl sulfide and obtained a lower but still good yield of 80%. A mechanistic study revealed that not only <sup>1</sup>O<sub>2</sub> but also O<sub>2</sub><sup>•-</sup> were both responsible for the oxidation.

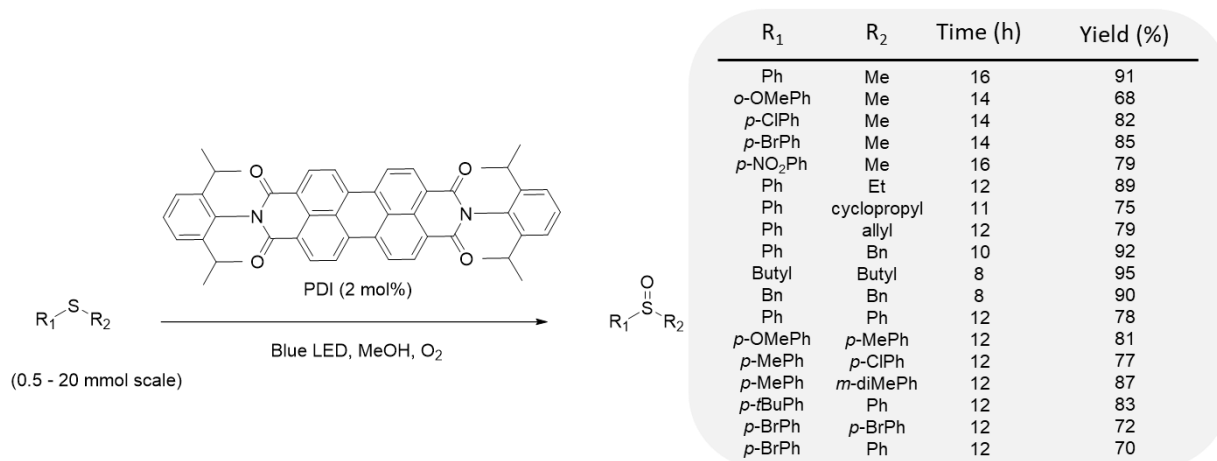


Figure 24 – Sulfide photooxidation with oxygen activated by a perylene diimide photocatalyst.

Guo *et al.*, realized the aerobic photooxidation of diverse sulfides into their corresponding sulfoxides using a metal free catalyst: 4-phenyl thioxanthone.<sup>69</sup> Sulfides (1 mmol) and thioxanthone derivative (0.1 mol%) were mixed in MeOH under air atmosphere and irradiated by purple LEDs (Figure 25). Irradiation of 5 h to 40 h were necessary to reach good conversion into sulfoxide. Under these conditions, the oxidation of their model sulfide, methyl phenyl sulfide, resulted in the sulfoxide with a selectivity of 99% with only 1% of sulfone. The authors did not discuss the selectivities for the library of sulfides but identified the ROS as both <sup>1</sup>O<sub>2</sub> and O<sub>2</sub><sup>•</sup>. A 10 mmol scale was attempted on diphenyl sulfide but the duration of irradiation needed to be increased to 72 h to obtain the 95% yield obtained in 8 h for a 1 mmol scale.

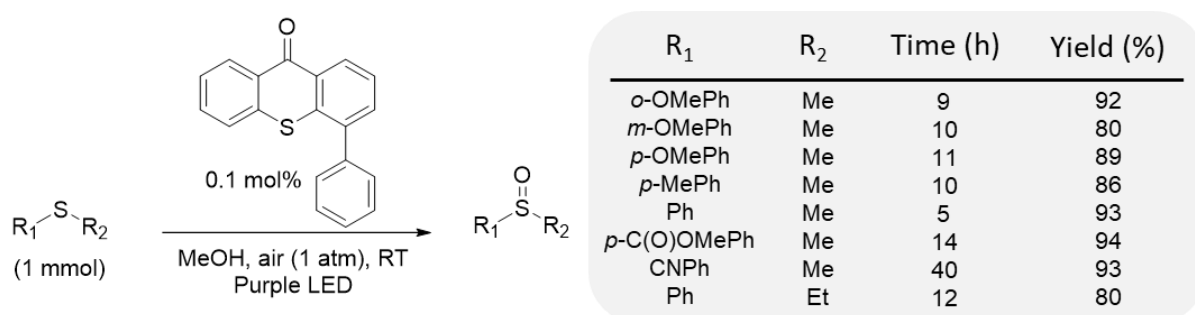


Figure 25 – Sulfide photooxidation with 4-phenyl thioxanthone as a catalyst.

Braunschweig *et al.* synthesized diketopyrrolopyrrol (DPP) bi-functionalized with amino acids to serve as organic chromophore and precursor of hydrogels.<sup>70</sup> The photoactive precursor has to undergo an *in-situ* enzymatic hydrolysis to become a supramolecular hydrogel. To compare the efficiency of this <sup>1</sup>O<sub>2</sub> generator on aromatic and aliphatic substrates, both thioanisole and cyclohexyl methyl sulfide were selected for the oxidation. All experiments were carried in water but on a 4 μmol scale and the irradiation had to last 48 h. A white halogen lamp was used as a light source and was connected to the reactor through an optical fiber. For each sulfide, tyrosine bi-functionalized DPP gave excellent results and the oxidations were selective toward the sulfoxide. Phenylalanine and leucine gave more moderate yields. All catalysts underwent enzymatic hydrolysis by α-chymotrypsin in the reactor prior to the addition of sulfides and before irradiation. However, to obtain such yields with the aromatic substrate, the reaction required to be performed in D<sub>2</sub>O, in which <sup>1</sup>O<sub>2</sub> has a longer life-time, even at such a low sulfide concentration (Figure 26).

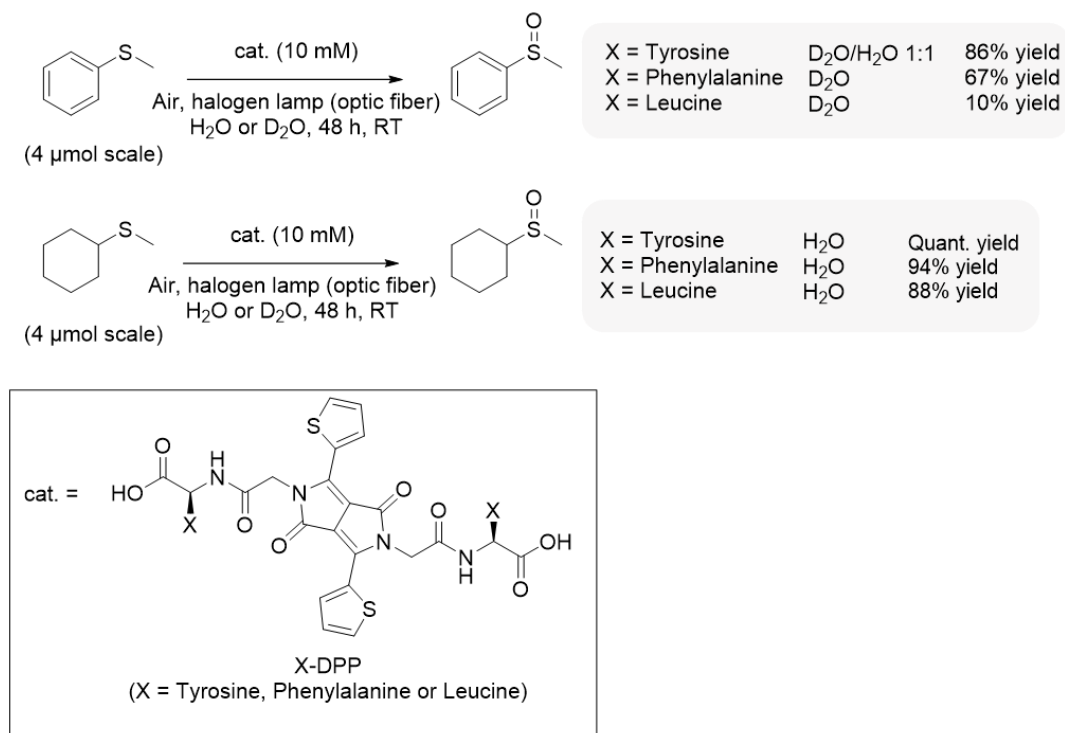


Figure 26 – Photooxidation of thioanisole and cyclohexyl methyl sulfide by a photoactive supramolecular hydrogel.

Jing *et al.* also oxidized thioanisole with  $^1\text{O}_2$  generated by ultrathin carbon nitride nanosheets.<sup>71</sup> The optimized nanosheets were prepared with equivalent amounts of melamine and cyanuric acid had a thickness of only 4 nm. In the optimal experiment 0.5 mmol of thioanisole were suspended with 5 mg of nanosheets in acetonitrile and oxygen was bubbled through the solution for 20 min before being irradiated with a Xe lamp. Total conversion and selectivities were obtained in 3 h.

Interestingly, Huang *et al.* worked on a metallic catalyst that is able to generate  $^1\text{O}_2$  in the dark.<sup>72</sup> Although  $\text{Bi}_2\text{O}_3$  with oxygen vacancies (ov- $\text{Bi}_2\text{O}_3$ ) is a much better  $^1\text{O}_2$  generator under visible light irradiation, it is able to produce enough  $^1\text{O}_2$  in the dark to observe a slight oxidation. This was explained by a study of the interaction of oxygen with  $\text{Bi}_2\text{O}_3$  and ov- $\text{Bi}_2\text{O}_3$  by DFT calculations. While the adsorption energy of oxygen on  $\text{Bi}_2\text{O}_3$  corresponded to a physical adsorption (0.5 meV), the higher energy for its adsorption on ov- $\text{Bi}_2\text{O}_3$  was characteristic of a chemical adsorption (1.66 eV). Furthermore, after adsorption, the distance between both oxygen atoms in  $\text{O}_2$  increased of 30 Å which was also attributed to a chemical adsorption. Calculations also revealed that both  $\frac{1}{2}$  and  $-\frac{1}{2}$  spins occupied the  $\pi^*$  orbital in the ov- $\text{Bi}_2\text{O}_3$  which allowed the identification of oxygen in its excited state. The catalyst was tested on several thioanisole derivatives (2  $\mu\text{mol}$ ) in hexane with constant oxygen bubbling for 10 h under irradiation of a Xe lamp. The experiment in the dark required a longer oxygenation time (16 h) but allowed to observe a conversion in sulfoxide while the same experiment with  $\text{Bi}_2\text{O}_3$  only gave traces of the same sulfoxide (Figure 27).

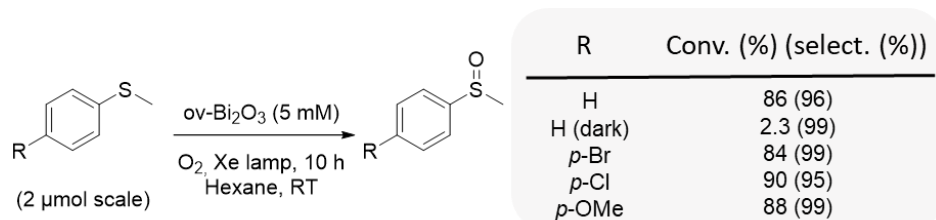


Figure 27 – Photooxidation and oxidation of thioanisole derivatives by ov- $\text{Bi}_2\text{O}_3$ .

Ye and Li worked with a bicyclic iridium(III) complex that allowed the selective oxidation of sulfides on a 0.5 mmol scale with excellent yields (Figure 28).<sup>73</sup> Sulfide (0.5 mmol) and PS (2.4 mg, 0.5 mol %) were dispersed in EtOH in a 20 mL glass reactor equipped with a pressure of O<sub>2</sub> contained in a balloon. Sulfides were fully oxidized in 4 h to 30 h of a blue light irradiation. The same procedure was tested in the presence of 1,4-diazabicyclo[2.2.2]octane (DABCO), a well-known singlet oxygen scavenger. The conversion dropped from 100% to 15% while superoxide radical and sulfide radical cation scavengers, benzoquinone and 1,4-dimethoxybenzene, did not prevent the oxidation to happen proving singlet oxygen to be the main reactive oxygen species (ROS) in the photooxidation process.

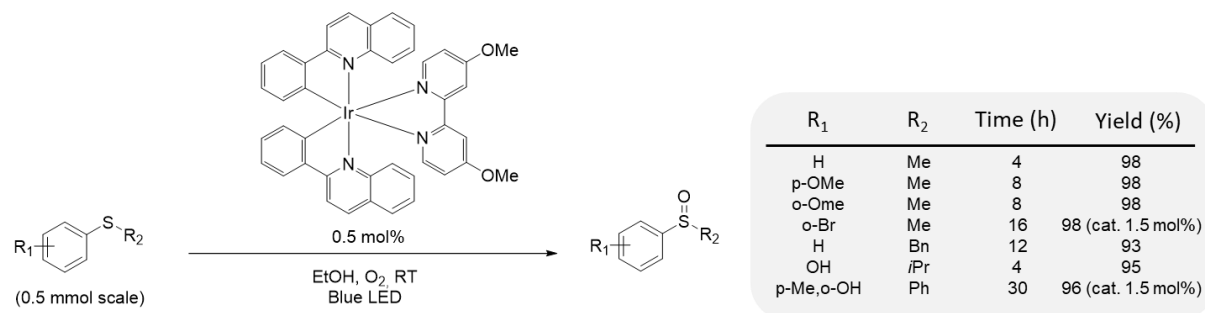


Figure 28 – Sulfide photooxidation catalyzed by a bicyclic iridium(III) complex.

The majority of the previous examples of sulfides batch oxidation/photooxidation are conducted on small scales ( $\mu\text{mol}$  to  $\text{mmol}$ ). High selectivity is indeed challenging to reach when the quantity of initial substrate, hence the volume of the reactor, increases. In the last two decades, a novel type of reactor emerged and offered new possibilities to chemists and researchers: continuous flow reactors.

## 1.4. Continuous flow

### 1.4.1. General principles

Continuous flow processing is a relatively young but game-changing set of technology for chemists in both fields of research and production. For centuries, batch reactors have fulfilled their role as practical and versatile laboratory equipment that can manage the majority of chemical reactions. Even today, these reactors remain and will remain an essential production instrument for researchers. However, in 2007, the European Commission enacted the REACH Regulation which purpose is to have a better control and understanding of the risk that chemical products represent from production step to commercial and disposal steps. This Regulation encourages the progressive transition from old procedures to new alternatives more respectful of security, health and environment. In October 2020, the Commission wrote a new detailed communication about the strategy to adopt. Among several criteria in the program concerning the industrial production<sup>74</sup>:

- “research, development and deployment of low-carbon and low environmental impact chemical and material production processes;”
- “research and development of innovative business models such as performance-based business model to ensure a more efficient use of chemicals and other resources and the minimization of wastes and emissions;”
- “re-skilling and up-skilling the workforce involved in the production and use of chemicals towards the green and digital transition;”

- “increase the current deployment rate of available technologies for manufacturing purposes such as internet of things, big data, artificial intelligence, automation, smart sensors and robotics.”

REACH Regulation also demands to prioritize “safe and sustainable-by-design approach to chemicals”:

*“At this stage, safe and sustainable-by-design can be defined as a pre-market approach to chemicals that focuses on providing a function (or service), while avoiding volumes and chemical properties that may be harmful to human health or the environment, in particular groups of chemicals likely to be (eco) toxic, persistent, bio-accumulative or mobile. Overall sustainability should be ensured by minimising the environmental footprint of chemicals in particular on climate change, resource use, ecosystems and biodiversity from a lifecycle perspective.”<sup>74</sup>*

The demand for high value-added molecules will not decrease but the procedures that are currently employed for their synthesis have to be adapted to correspond to these new health and environmental criteria. Toxic or hazardous chemicals, even if efficient in synthesis, have to be avoided. This encourages chemists and engineers to favor procedures that get the best reactivity out of their chemicals. Continuous flow reactors naturally emerged as a pivotal element in this transition. The possibilities offered by flow in terms of reactivity and selectivity improvement, waste reduction, process automation, environmental footprint and scale-up potential make it suitable for the REACH Regulation’s requirements.

#### 1.4.1.1. Structure of continuous flow reactors

Reactors employed for continuous flow chemistry consist of tubing with microscopic dimensions or plates in which microchannels are carved (Figure 29). The inner volumes range from  $\mu\text{L}$  (microfluidic) to mL (mesofluidic) and are the key parameter that offers it singularity to flow chemistry.

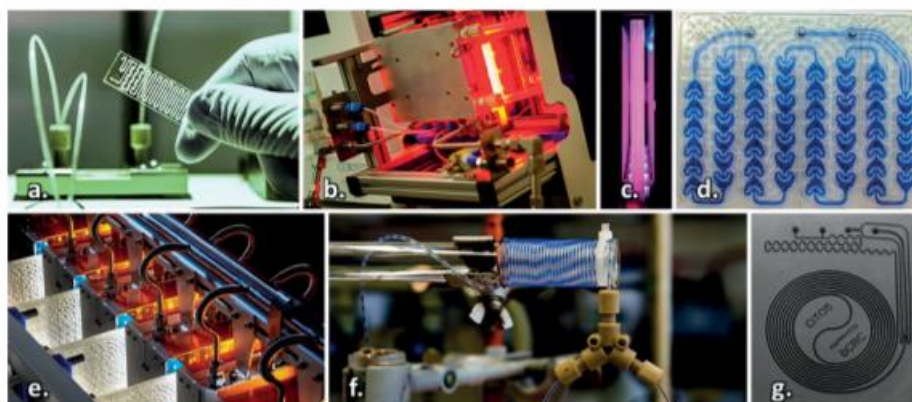


Figure 29 – Different types of continuous flow reactors: a. Glass chip microfluidic reactor (FutureChemistry Proprietary). b. Lab-scale Corning Advanced-Flow Lab Photo Reactor (Corning Proprietary). c. Cross view of a glass module irradiated between two LED panels (Corning Proprietary). d. Pilot-scale mesofluidic glass module (Corning Proprietary). e. Pilot-scale mesofluidic Corning Advance-Flow G1 photo Reactor (Corning Proprietary). f. Microfluidic reactor made of a PFA tubing and HPLC-type connectors. (CiTOS proprietary). g. Zircon microfluidic reactor manufactured by Belgian Ceramic Research Centre (BCRC). Adapted from *Eur. J. Org. Chem.*, 2018, 20-21, 2301-2351. Copyright 2018 Wiley-VCH Verlag GmbH & Co. KGaA, Weinheim

Flow reactors can be manufactured in different materials depending on the reaction intrinsic requirements. A photochemical reaction needs to be performed in a transparent reactor made out of glass, fused silica or transparent polymer. Highly exothermic reactions, above 200 °C, or reactions under high pressure are preferably performed in metallic reactors (stainless steel, titanium, copper...) to benefit from their performances in heat exchange and robustness. Corrosives and harsh reactants

can be handled inside tubing made out of chemically inert polymers or preferably Silicon Carbide. If a solid has to be involved in the reaction, some reactors can be equipped with a packed-bed column containing a solid quencher/catalyst<sup>75,76</sup> or can have their inner side coated or functionalized<sup>77,78</sup>. Furthermore, Oscillatory Flow Reactors (OFCs) have been developed to improve mixing by adding a symmetrical oscillation to the flow movement. OFCs can thus handle biphasic systems where the solid is dispersed in solution or slurry flows.<sup>79</sup>

Typically, a complete continuous flow setup consists of an assembly of different parts that can be added, moved or exchanged regarding of the necessity of their role in the reaction. At the beginning of the setup, solutions or pure liquid reagents are injected by highly accurate dosing systems that can handle either liquids, slurries or gas. The control over the residence time allowed by the accuracy of the pumps plays a major role in the enhancement of the selectivity. Feeds mixing is then ensured by dedicated equipment that can be intrinsic to the reactor or found as external pieces implemented before the entry of the reactor. Embedded static mixers are more commonly found in commercial plate reactors such as in Corning® Advance-Flow Reactors™ (Figure 30A). In each Corning flow module is carved a circuit of heart-shaped cells that induces intense passive mixing along the reaction path. External mixers can also be utilized, such as Y and T mixers, that combine reactant feeds before they enter the reactor. Different shapes can be found but the more common have a Y (Figure 30B), T, arrow-head or cross shape.

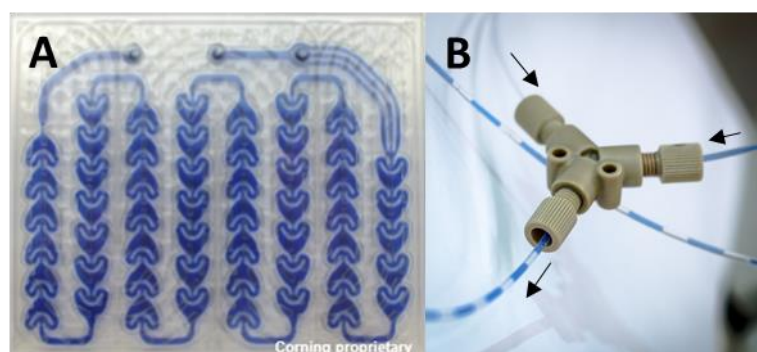


Figure 30 – Examples of different mixers. A – Intrinsic mixers, heart-shaped integrated to a mesofluidic glass module (Corning Proprietary), B – IDEX/ Upchurch Scientific Y-connector as external static mixer (CiTOS Proprietary).

The outlet of the reactor is also the place to install various downstream auxiliaries dedicated to the purification and/or the analysis of the reaction. Phases can be separated with an in-line liquid-liquid separator that works with a membrane only permeable to one of the phases. Quenching reactions is also feasible by adding a supplementary feed injecting the quenching solution or by adding a scavenger in a packed bed column. Nowadays, almost every classic analysis technique has been adapted to flow<sup>80–82</sup> so that the reactor can be equipped with an in-line NMR<sup>83</sup>, IR<sup>84</sup>, fluorescence<sup>85,86</sup>, absorbance<sup>86</sup>, UV-Vis<sup>87</sup>, Raman<sup>88</sup> spectrometers or be adapted for on-line mass spectrometer<sup>89</sup> and HPLC<sup>90</sup>. While the whole reaction stream flows through in-line analyzers, on-line devices automatically take samples of the stream to perform the analysis.

#### 1.4.1.2. Reactivity and selectivity increase

In chemical reactions, a good selectivity is achieved if all molecules undergo the same chemical transformation under identical process conditions. This is only possible if the reaction time and conditions are homogeneous for the whole medium. In continuous flow, the accuracy of the dosing system favors a high selectivity. Flow rates can precisely be tuned to the  $\mu\text{L min}^{-1}$  scale. This ensures a fine control of the residence time, as well as the local stoichiometry, so that the reaction can be carried on for a time strictly limited to the time necessary for the reaction to be complete. Molecules that

already underwent the reaction can be directly removed from the reaction medium, avoiding further transformation and, thus, side reactions. Furthermore, homogeneity of reaction conditions (temperature, pH, irradiation, etc.) is highly dependent on the mixing efficiency and is harder to control as the reactor volume increases. The low surface to volume ratio that characterizes batch vessels is responsible for a poor heat and mass transfer. This inhomogeneity of temperature and concentration often lead to a lower purity and yield while more waste have to be treated. This inherent problem is exacerbated in industrial scale processes in which reactors can reach impressive dimensions while a small switch from a round bottom flask of 5 mL to the same flask of 250 mL is sufficient to decrease the interfacial surface area from 107 to 35  $\text{m}^2\text{m}^{-3}$  (Figure 31).<sup>91</sup>

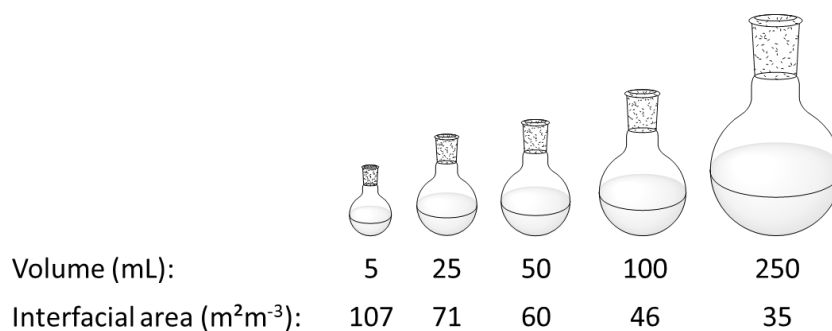


Figure 31 – Loss in interfacial area for classic round-bottom flasks. Adapted from *Org. Process Res. Dev.* 2016, 20, 327–360.

In microreactors, the narrow dimensions of the channels in which the chemicals flow ensure the quality of the heat and mass transfer. A better reactivity and homogeneity are achieved thanks to the strong mixing governed by the flow pattern inside the channel (Figure 32).

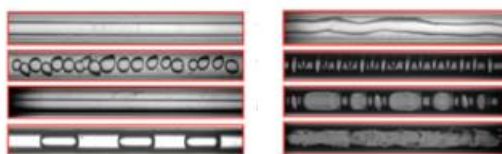


Figure 32 – Example of different gas-liquid flow patterns. Adapted with permission from *Ind. Eng. Chem. Res.* 2012, 51, 1015–1026. Copyright 2012 American Chemical Society.

The flow pattern is of tremendous importance for the reaction as it fixes the interfacial surface area, it establishes the way the reagents interact with each other inside the reactor as well as the exchanges between the potential different phases. For common tubular reactors, the interfacial surface area values range from 50 to 2000  $\text{m}^2\text{m}^{-3}$  but can reach 18 000  $\text{m}^2\text{m}^{-3}$  for some gas-liquid microchannels.<sup>91,92</sup> The internal pressure also influences the flow pattern and is controlled by a back-pressure regulator (BPR) positioned at the outlet of the reactor.

#### 1.4.1.3. Environmental footprint and safety

Continuous flow reactors can also help reducing the environmental footprint of chemical research by lowering the production of chemical waste. This reduction can be due to different phenomena depending on the purpose of the flow reaction. In research and development, it is mainly the low volumes required to perform one test in a microreactor (a few  $\mu\text{L}$  to a few mL) that will decrease the waste appearance. For production runs, it is mostly the gain in selectivity provided by the excellent heat and mass transfer that will avoid the formation of undesired products.

When it comes to safety, one problematic aspect to be dealt with is the quantity of potentially dangerous compounds involved in the reaction. A significant number of industrial reactions rely on the use of hazardous and/or unstable chemicals. In case of control loss, the amount of chemical at stake is crucial and will play a major role in the outcome of the incident. In flow reactors, the control over the temperature due to the quality of heat exchange allows the handling of exothermic and/or hazardous reactions<sup>93</sup>. The system can be cooled down quickly and easily and the reaction stopped by shutting down feed injection. If control should be lost anyway, an explosion of a reactor containing only a few  $\mu\text{L}$  or  $\text{mL}$  of a chemical compound should cause less damages than the volume that can be contained in a batch vessel.

#### 1.4.1.4. Numbering-up and scaling-out

The reduced quantity of reactant processed inside a flow reactor per unit of time does not preclude large scale operation since flow reactors are operated continuously (Figure 33).<sup>94</sup>

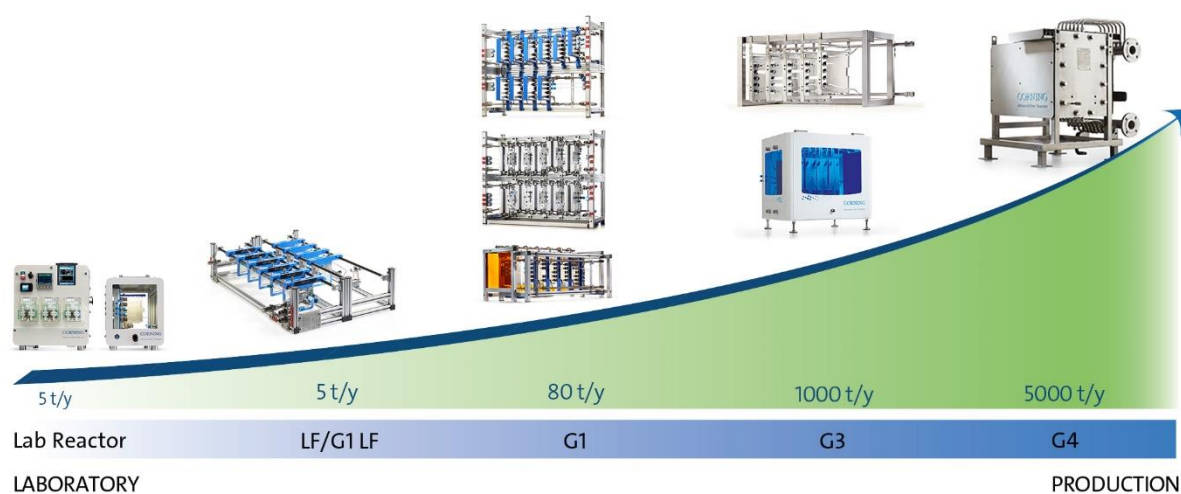


Figure 33 – Production scale of Corning® flow reactors from Lab Reactor™ to G4™ (Corning® Proprietary).

Pumps deliver fresh reagents inside the reactor in a continuous way as long as there is enough feed solution. As flow reactors are rather compact, they can be used in parallel, starting multiple reactors at the same time (numbering-up).<sup>95–99</sup> Kim *et al.* assembled a total of 25 microreactors made of stainless steel and copper for the high-throughput synthesis of Rufinamide, an anticonvulsant drug.<sup>100</sup> The optimization of the synthesis was first conducted in a single metallic microreactor of 1.571 mL of internal volume ( $V_i$ ) kept at 110 °C. The reactor was supplied with 2 feeds containing a mixture of 2,6-difluorobenzyl azide (0.29 M) and ascorbic acid (0.3 equiv.) in DMSO (Feed A) and a solution of propiolamide (2.8 M) in DMSO (Feed B). Feeds were pumped at 416.6  $\text{mL min}^{-1}$  and 63.4  $\text{mL min}^{-1}$  respectively which fixed the residence time at 3.3 min. Rufinamide was obtained with a 77% yield and at the productivity of  $\sim 1.3 \text{ g h}^{-1}$  (Figure 34A). The authors intensified their production by assembling 25 copper reactors in parallel. Feeds were pumped at 10.4  $\text{mL min}^{-1}$  and 1.6  $\text{mL min}^{-1}$  respectively. With only a slight decrease of the yield (73%), the productivity reached  $\sim 31.8 \text{ g h}^{-1}$  (Figure 34B).



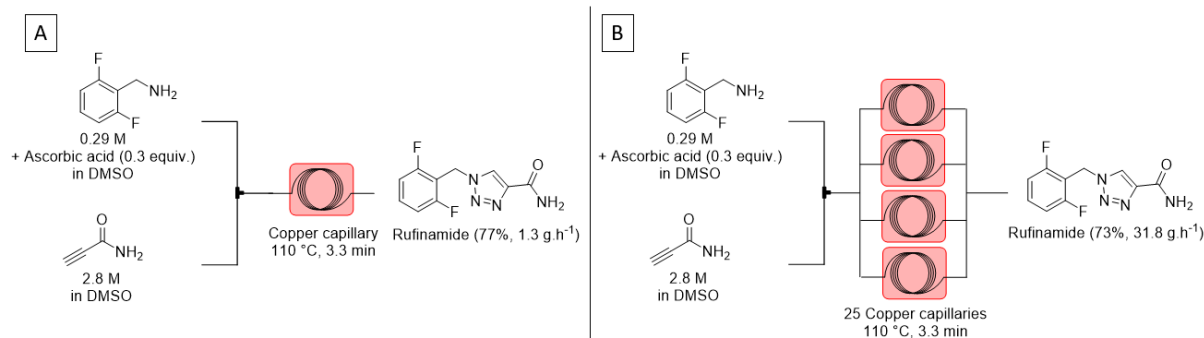


Figure 34 – High-throughput synthesis of Rufinamide by numbering-up copper capillaries reactors. A – Synthesis in a single reactor. B – Synthesis in 25 reactors in parallel (only 4 are represented for clarity).<sup>100</sup>

If the volume delivered by the reactor on which the reaction was first optimized is not sufficient for production, transitioning to a larger one (scaling-out) does only require minor readjustments for the reaction conditions to be transposed to the new reactor volume. This potential for seamless scale-up accelerates the development of industrial processes.<sup>93,94,101,102</sup>

Recently, Lévesque *et al.* constructed a low footprint flow photoreactor for a kilogram scale photoredox C-N coupling between 4-bromobenzotrifluoride and pyrrolidine.<sup>103</sup> The photoreactor was built up from inexpensive components and was placed in a 21 L aquarium that contained the thermal exchange liquid. The 725 mL reactor was irradiated with 400 nm LEDs. The authors aimed at the performance of their setup in terms of productivity. In the configuration resulting in full conversion of the reactants, 10 kg day<sup>-1</sup> of product could be obtained. Although this production is already significant, the authors desired to enhance the production even more. An increase of flow rates impacted the conversion as it reduced the residence time. However, under the conditions leading to 50% of conversion, up to 50 kg day<sup>-1</sup> of product could be delivered. This option would be favored for processes in which cheap starting material is handled and conversion can be sacrificed for productivity (Figure 35).

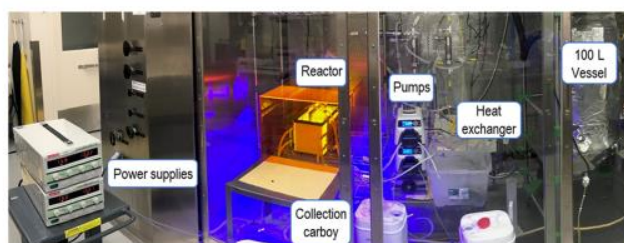
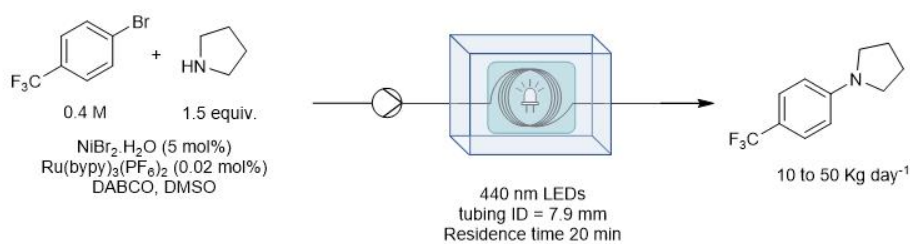


Figure 35 – Flow setup for a kilogram scale C-N coupling. Adapted with permission from *Org. Process. Res. Dev.*, 2020, just accepted. DOI: 10.1021/acs.oprd.0c00373. Copyright 2020 American Chemical Society.

Monbaliu *et al.*, scaled out the hydroxylation of tertiary ketones to provide high value-added compounds among which photoinitiators Darocure 1173 and Irgacure 184 and a ketamine precursor.<sup>104</sup> The optimization phase was conducted in a PFA coil, in which high conversion and selectivities were obtained in impressively short residence time (Figure 36A). Because of the incompatibility of KOH with glass, a Corning® Advanced-Flow™ G1 SiC reactor was employed for the hydroxylation intensification. With high flow rates and a residence time of 7.5 s only, a productivity of 12 kg day<sup>-1</sup> of  $\alpha$ -ketol was achieved (Figure 36B).

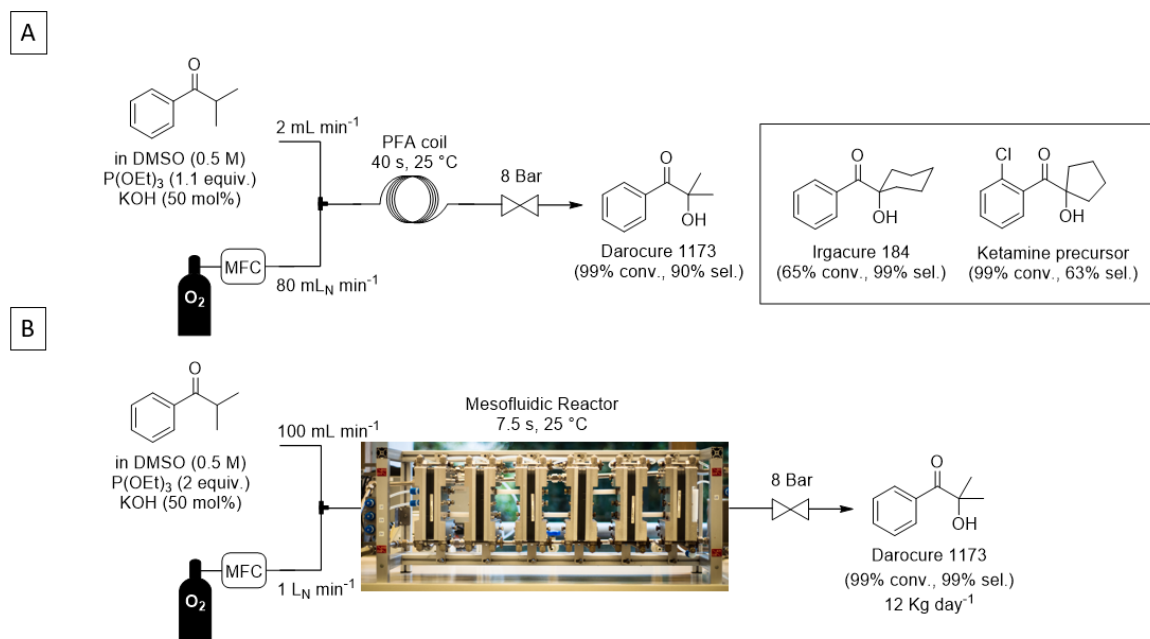


Figure 36 – Hydroxylation of tertiary ketones. A – Optimization in a PFA coil reactor. B – Scale out in a pilote scale Corning® Advanced-Flow™ G1 SiC reactor with 6 fluidic modules (Courtesy of Corning).<sup>104</sup>

#### 1.4.1.5. Multi-step reaction telescoping

Flow devices open possibilities for the telescoping of consecutive reactions by connecting reactors each dedicated to a specific reaction or elementary operation. In the best case, the outlet of a first reactor flows directly into the inlet of the second one, suppressing the need to isolate the product of the first reaction as it is immediately consumed downstream.<sup>105</sup> When a purification or a solvent change is required, some additional work up devices, such as extraction membranes, can be added between the units (Figure 37).

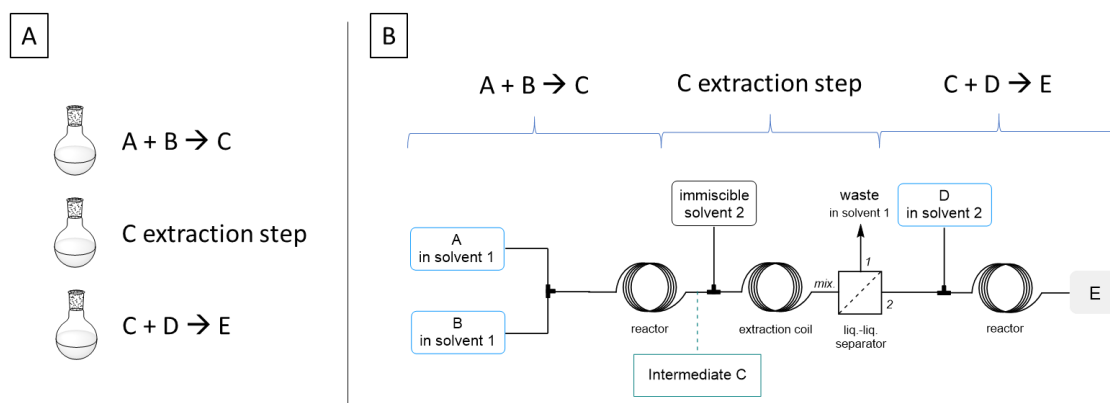


Figure 37 – A – Example of a multi-step reaction in batch involving the isolation of an intermediate. B – Telescoping of the same multi-step reaction in flow.

Automation of chemical reaction with such concatenated reactors also highly reduces the likelihood and the exposure time of the operator to the potentially harmful chemicals.

### 1.4.2. Gas-liquid reactions in flow

Multiphase processes such as gas-liquid reactions are frequent in chemistry. Gas can represent an advantageous choice for organic synthesis as an affordable and commercially available reagent, with a high atom economy. However, it remains relatively complex to handle and to contain. The reactor and gas lines chosen for the reaction needs to resist rather high pressure to avoid explosions.

In conventional batch chemistry, there are different ways to introduce a gas in a chemical reaction. If the gas is chosen to keep an inert atmosphere, a balloon filled with the inert gas (Ar, N<sub>2</sub>) connected to the reaction vessel by a needle is the most practical technique. The gas can also be loaded into a gas-tight syringe instead of a balloon. If the gas is used as a reagent (O<sub>2</sub>, CO<sub>2</sub>, ...), the most common technique is to inject the gas directly into the reaction medium by connecting a gas cylinder to a mass flow controller (MFC) and to “bubble it” through the solution until completion of the reaction. Under appropriately high pressure, part of the gas can also be dissolved into the liquid phase but not all reactors can stand such mechanical stress and the quantity of gas dissolved decreases significantly when the temperature increases. However, if the gas is a short-lived species, such as <sup>1</sup>O<sub>2</sub>, it is mandatory to generate it *in-situ*<sup>106</sup>. The *in-situ* generation of gas can also respond to safety concerns for toxic or hazardous gases. For these gases, such as CO<sup>107–109</sup>, H<sub>2</sub><sup>110</sup> or Cl<sub>2</sub><sup>111</sup>, CH<sub>2</sub>N<sub>2</sub><sup>112</sup> efficient precursors have been developed but often need to be promoted by a metallic catalyst.

The efficiency of a gas liquid reaction depends on the exchange between the two phases. The size of the gas bubbles depends on the pressure but also on the mixing system (Figure 32). Small bubbles lower the diffusional distances and ease the mass transfer which is why the control of their size is so important to improve mass transfer. In this regard, flow chemistry can highly improve the mass transfer and the control on bubbles sizes both at low or high pressure.

Many examples of implementation of gas-liquid reactions in flow can be found in the literature. They are typically performed on 3 types of reactor: A – a tubular reactor with a segmented<sup>113</sup> or annular<sup>114,115</sup> flow of gas, B – a tube-in-tube reactor<sup>116–119</sup> consisting of 2 concentric tubes where the wall of the inner one, made of Teflon AF-2400, is permeable to gas only, allowing the gas to diffuse in the liquid phase, C – a falling film reactor<sup>120</sup> where the gas can flow upstream or downstream the liquid flow (Figure 38).

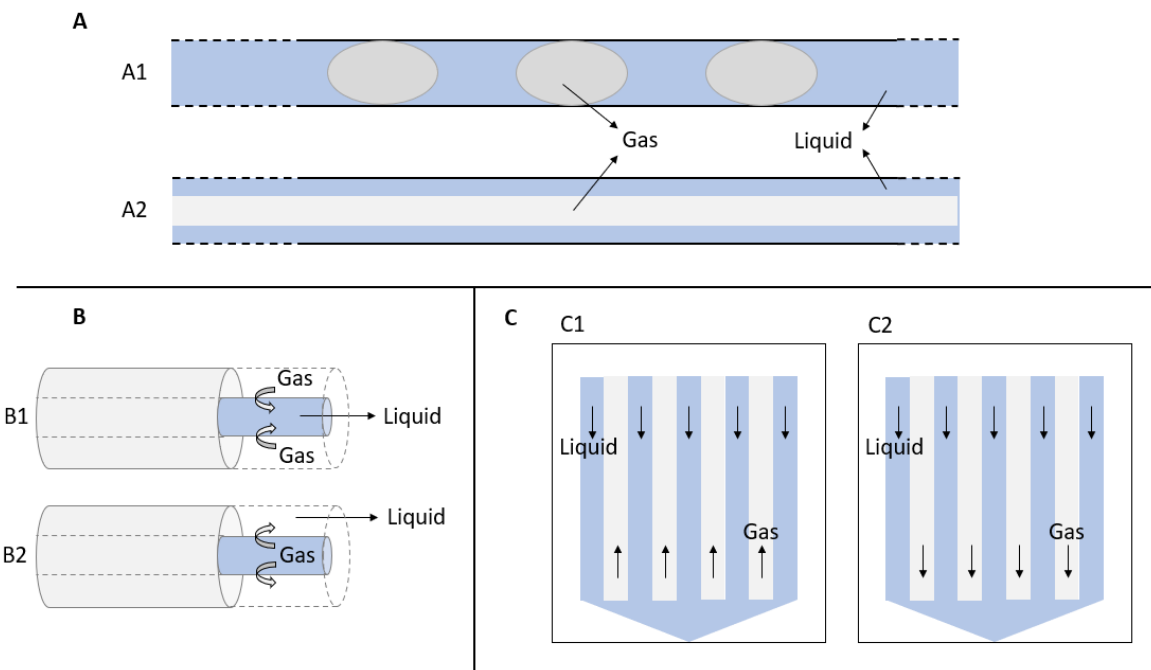


Figure 38 – A – Tubular reactor with segmented (A1) or annular (A2) flow. B – Tube-in-tube reactor, conventional (B1) or reverse (B2). C – Falling film reactor, conventional (C1) or reverse (C2).

In 2011, D-P. Kim and coworkers developed a membrane-based microreactor<sup>106,121–123</sup> where a gas permeable poly(dimethylsiloxane) (PDMS) membrane separates the gas and liquid phases but ensures an excellent interfacial area. This reactor was first used to perform photooxidation<sup>121</sup> and to carry out a Heck reaction<sup>122</sup>.

All these reactors have been successfully used to implement gas-liquid reaction in flow. Still, the most practical technique is the segmented flow in a tubular tube. Tubular tubes are readily available, inexpensive and easy to manipulate. It is the adequate flow material for beginners in flow or when the reaction has not been tested yet and parameters need to be optimized. A segmented flow of gas, also called a Taylor flow, is advantageous in terms of mass transfer.<sup>113</sup> This is indeed a gas-liquid flow type which maximizes the interfacial surface area between the two phases. The inside streams of both phases favor exchanges which enhance the mass transfer<sup>91</sup> (Figure 39).

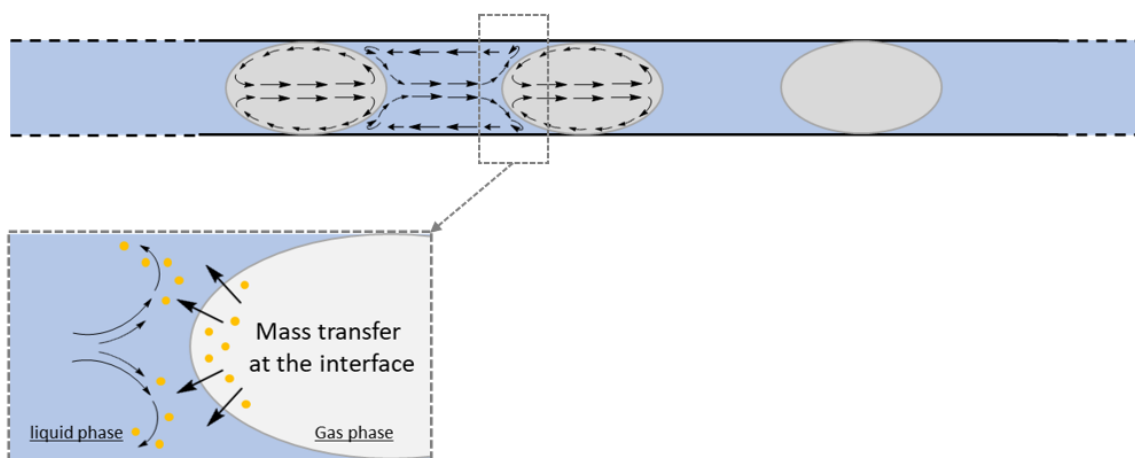


Figure 39 – Mass transfer between phases in a Taylor flow pattern.<sup>124</sup>

#### 1.4.2.1. Use of oxygen in flow

Gaseous oxygen is involved in a plethora of chemical transformations. The success of oxygen is due to its efficiency as an oxidant, combined to inherent benefits that meet the current tendency to transition to greener processes. This cheap and readily available gas is environmentally harmless. However, in addition to being prone to explosion such as every pressurized gas, oxygen is highly inflammable. The handling of large volumes of oxygen for industrial batch production represents an important risk. Hence, for the past few years, the development of oxygenation processes in continuous flow has gained a considerable interest in the scientific community.

Recently, Loubière *et al.*, selected the photooxidation of  $\alpha$ -terpinene into ascaridole with RB in EtOH to conduct a rigorous study of the reaction parameters when performed with a segmented gas-liquid regime.<sup>125</sup> Among these parameters, particular attention was given to the structure of the Taylor flow. The reaction was performed in an E-Series UV-150 photoreactor from Vapourtec®. The alternation of gas and liquid segments entered the coil reactor from the bottom, circulating up to its top. By comparing two runs in reactors of different internal volume, 2 mL and 5 mL, with the same residence time of 0.66 min, the authors demonstrated the effect of a more intense mixing on the quality of the mass transfer. For the residence time to be conserved in a longer reactor, the total flow rate has to increase. This increase has a direct impact on the bubbles by accelerating their internal motion, ensuring an increased interfacial contact, hence increasing the exchanges between the two phases. The conversion obtained were systematically better for the longer reactor. It has to be noted that for these experiments, the volumetric ratio between gas and liquid slugs was kept constant to remove this parameter from the equation.

Park *et al.*, conducted in 2015 a comparative study of a Pd-catalyzed oxidative Heck/dehydrogenation in two different microreactors, a capillary reactor and a tube-in-tube system.<sup>126</sup> The optimized reaction in a batch reactor took 36 h but the residence time was reduced to ~120 min under microfluidic conditions (130 min for a tube-in-tube). Park and co-workers used the larger tube-in-tube device to transpose the reaction to gram scale. Both reactors gave similar yields for similar substituents on the second aromatic ring: 85% yield in tubular reactor and 84% in tube-in-tube for R = OMe (Figure 40).

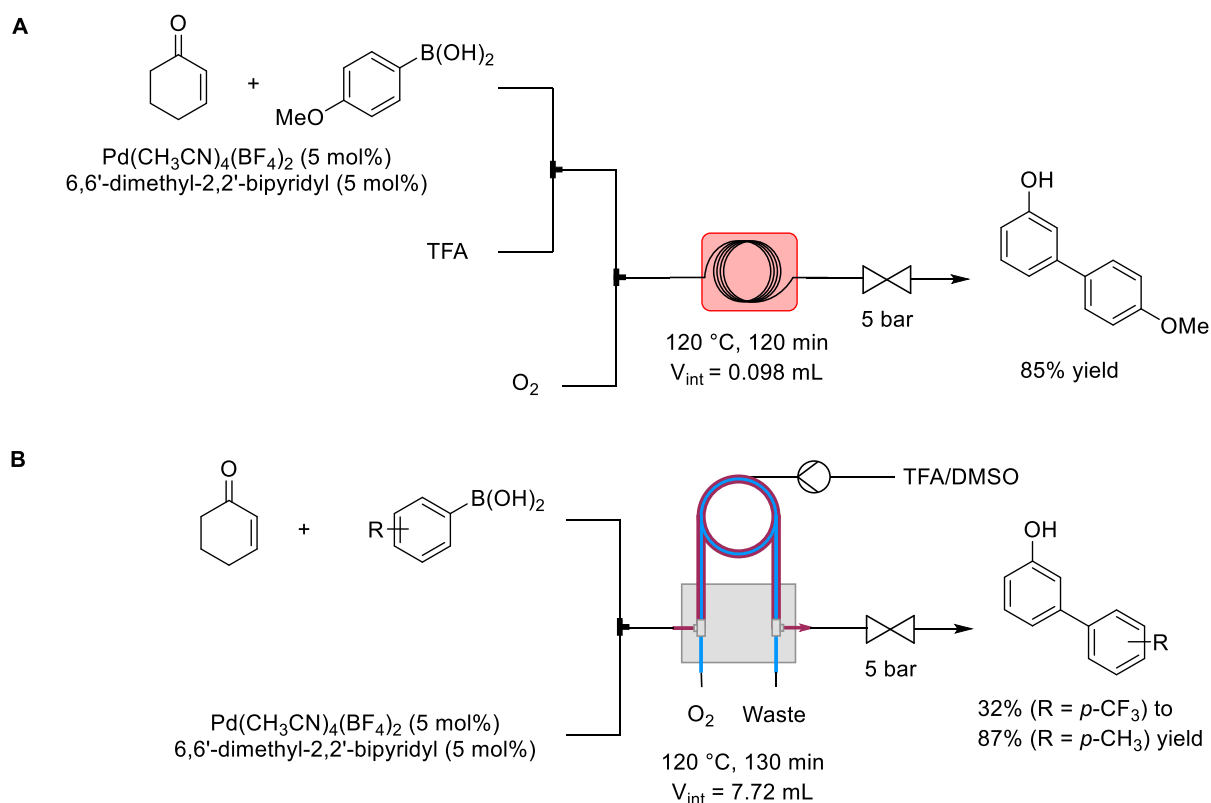


Figure 40 – Comparison of a Pd-catalyzed oxidative Heck/dehydrogenation. A – Tubular reactor. B – Tube-in-tube reactor.

LaPorte and co-workers explored the scale-up of the synthesis of 6-hydroxybuspirone, a metabolite of buspirone, an anxiolytic pharmaceutical ingredient.<sup>127</sup> They first worked with pure oxygen at -10 °C in a CPC CYTOS microreactor with stacked plates (Figure 41A). The system allowed a production of 0.3 kg day<sup>-1</sup> of 6-hydroxybuspirone which is still far below their 7.53 kg day<sup>-1</sup> batch production for the same reaction.<sup>95,128</sup> To increase this production, another reactor was devised (Figure 41B). This trickle bed reactor could be cooled down to -38 °C and involved a system in which the oxygen flows counterflows the liquid stream. To surpass the batch production, 4 of these reactors were started in parallel and allowed a total throughput of 15.8 kg day<sup>-1</sup>.

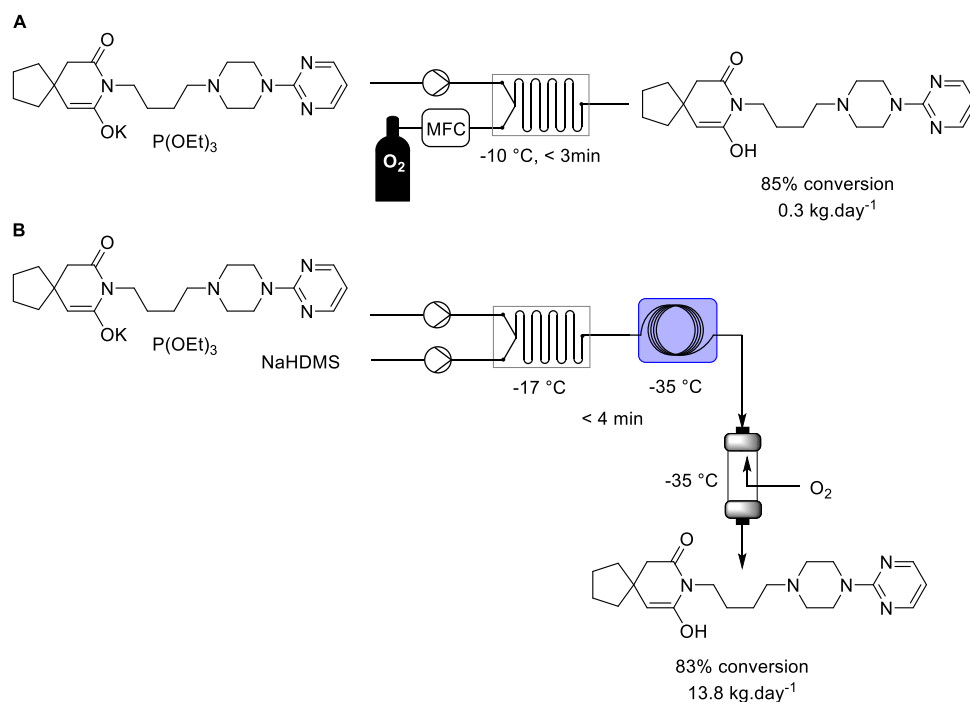


Figure 41 – Scale-up of the 6-hydroxybuspirone synthesis. A – CPC CYTOS microreactor. B – Trickle bed reactor.

The scaled-out hydroxylation of tertiary ketones developed by Monbaliu *et al.*, was already discussed in section 1.4.1.4 and is another example of the efficiency of fluidic devices to reach commercial challenges.<sup>104</sup> In a previous paper, the authors demonstrated a concatenated three-steps process for the sustainable preparation of ketamine.<sup>129</sup> In the first step, the hydroxylation required the use of molecular oxygen. The gas did not preclude the complete telescoping of the three reactions as a surge vial was placed at the outlet of the second step to collect the effluent and release the excess of oxygen before entering the final part of the reactor affording ketamine and analogs with excellent conversions and selectivities (Figure 42).

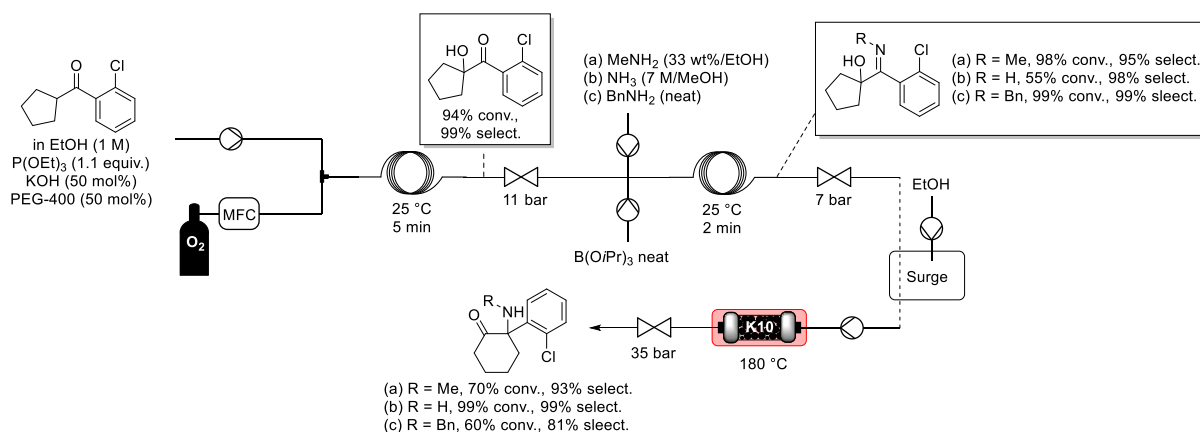


Figure 42 – Flow setup for the concatenated synthesis of racemic ketamine and analogs.<sup>129</sup>

Beside all these relevant examples of the use of molecular oxygen in continuous flow devices, gaseous oxygen is also required for oxidation reactions under its excited state, singlet oxygen, which is generated by photochemistry. Photochemistry is indeed one of the reaction types that can benefit the most from a transposition to flow.

### 1.4.3. Photochemistry in continuous flow

#### 1.4.3.1. General considerations

As introduced in previous sections of this dissertation, photochemistry is a powerful tool to access a diversified panel of chemical compounds. However, intensification of photochemical processes for industrial development in macroscopic batch reactors faces inherent limitations. Those issues can thus not be solved in batch reaction vessel and justify the need of transition to continuous flow reactors.

The most impactful issue of photochemistry in batch is related to its internal dimensions. Photochemistry is ruled by the Beer-Lambert law which details how the incident light will be absorbed by the molecules of the reaction for a given concentration and path length.<sup>130</sup> The equation is written as following:

$$A = \log \left( \frac{I_0}{I} \right) = -\log T = \epsilon C l \quad (\text{Equation 3})$$

In this equation:

A is the absorbance,

$I_0, I$  represent the initial and the transmitted light intensity respectively,

T is the light transmittance,

$\epsilon$  is the molar extinction coefficient ( $\text{L}\cdot\text{mol}^{-1}\cdot\text{cm}^{-1}$ ) which is proportional to the ability of a molecule to absorb light and is influenced by parameters such as temperature, pressure, pH and solvent.

C is the concentration (M),

l is the path length crossed by light ( $\text{cm}^{-1}$ ).

For a given photochemical system, Beer-Lambert law illustrates that the light transmission decreases when the thickness of solution to cross increases (Figure 43). When the incident light passes through the first layers of solution, a given quantity of photon is already absorbed, which reduces the remaining intensity of light for the other layers and this phenomenon worsen with the number of layers that light has to go through. External layers act like hiding screens to internal ones.

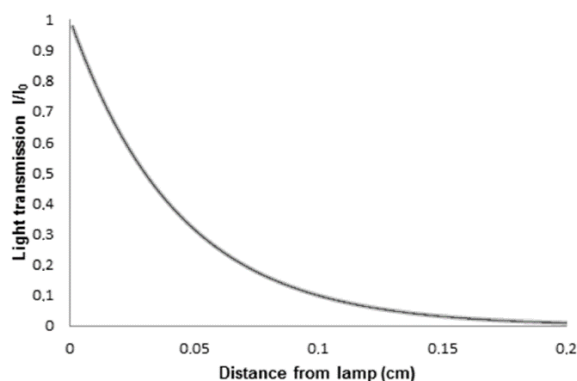


Figure 43 – Graph of a theoretical system subject to Beer-Lambert law. Values plotted here are not experimental.

The common way to scale-up batch processes to industrial production is to perform the reaction in reactors of larger volume. In such reactors, the uniformity of irradiation is almost impossible to obtain. A strong mixing can help refreshing the layer facing the light source but it is not granted that each molecule will spend the necessary time under irradiation. To ensure that the whole reactant has been converted in the expected product, the only solution is to keep the light source working for an extended duration. This can result in the formation of unexpected products from secondary reactions and/or degradation with consequences on reaction's selectivity (Figure 44A).



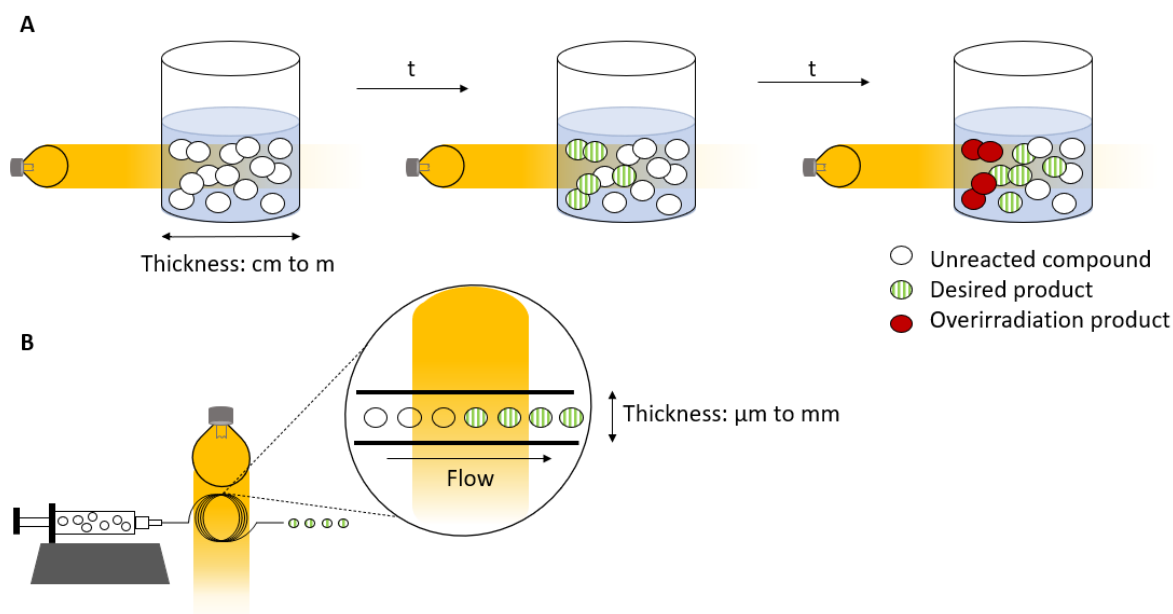


Figure 44 – Comparison of a batch vs Flow reactor for photochemical reactions. Illustration of the selectivity issue due to the reactor's dimension.

In 2014, Sanofi researchers presented a batch scaled-up process for the synthesis of artemisinin, an anti-malaria drug.<sup>131</sup> The complete synthesis of artemisinin includes a hydrogenation, an acid activation and a photooxidation that triggers a series of rearrangements in the presence of an acid (Figure 45). Their method was run in authentic industrial units, including a photoreactor. The authors discussed the challenges of implementing such a large photoreactor acknowledging the fact that photochemistry is often avoided for production scale manufactures due, among other points, to the complexity of light transmission. With a Hg vapor lamp and tetraphenylporphyrin (TPP) as a PS in  $\text{CH}_2\text{Cl}_2$ , they obtained artemisinin in an overall yield of 55%.

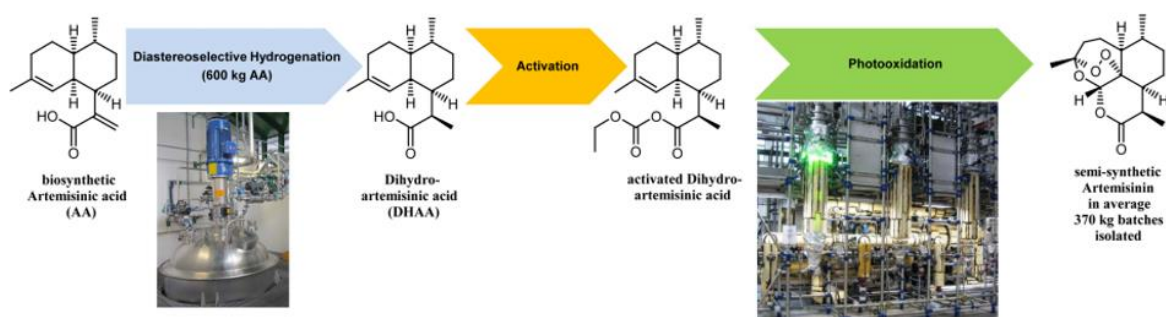


Figure 45 – Synthesis of artemisinin in industrial scale. Adapted with permission from *Org. Process Res. Dev.* 2014, 18, 417–422. Copyright 2014 American Chemical Society.

Seeberger *et al.* also published interesting papers on the manufacture of artemisinin and derivatives in the last decade.<sup>132–136</sup> Their work was oriented toward flow chemistry to address the light penetration problematic met in batch photoreactors. Seeberger developed a first flow setup that could deliver artemisinin from Dihydroartemisinic acid (DHAA) with a 40% yield.<sup>132</sup> This prototype was quickly improved one year later with another photoreactor.<sup>133</sup> The initial Hg lamp was replaced with more monochromatic LEDs (60 LEDs, 420 nm) and TPP was replaced with 9,10-dicyanoanthracene (DCA) which does not suffer from pH variation and can endure the acid required for the ring closure. The complete setup was composed of 3 units (Figure 46). The photoreactor, first unit, was composed of a

tubing ( $V_i = 7.5$  mL) wrapped in 2 layers around glass, immersed in a transparent cooling bath kept at  $-20$  °C and paced in front of the LEDs. The photoreactor was then followed by 2 units ( $V_i = 10$  mL and 30 mL respectively) that slowly reheat the solution at 10 °C and RT respectively to perform the final rearrangement reactions. With a residence time of 11.5 min only, they obtained pure artemisinin in 65% yield which represent one of the best yields reported in the literature for artemisinin manufacturing at that time.

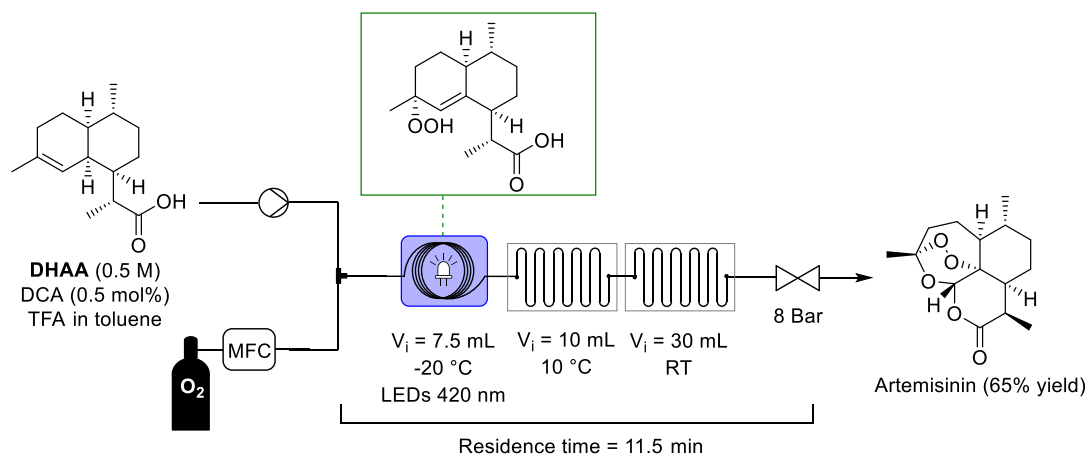


Figure 46 – Continuous flow setup for the preparation of artemisinin.

These results encourage chemists to develop new continuous flow photoreactors as this technology brings practical solutions to batch limitations. The internal dimension of the tubing (or channel) in which the reaction is occurring is so narrow that the layer of solution that is crossed by light only has an insignificant influence on its intensity. Furthermore, the irradiation time can be accurately controlled by tuning the flow rate and as the solution is continuously flowing through the reactor. The continuous nature of these reactors ensures that molecules that have already reacted are rapidly removed from the reactor. The segment of solution under irradiation is continuously refreshed reducing the probability of secondary reactions or degradation (Figure 44B).

The transition to flow is also inscribed in the spirit of thinking chemical processes with a greener approach. Flow reactors in general are already a step forward in terms of green chemistry<sup>137,138</sup> but flow photochemistry in particular reduces purification steps by increasing the selectivity and by limiting the irradiation time to the necessary duration.

#### 1.4.3.2. Photooxidation in flow

**N.B:** A more detailed literature concerning sulfides treated in this PhD manuscript can be find in each dedicated chapter.

Noël *et al.* reported the detailed construction of a cheap and flexible photoreactor for the oxidation of thiols in disulfides.<sup>139</sup> The microreactor was built with PFA capillaries wrapped around a classic plastic syringe surrounded by white LEDs strips. The photooxidation occurred through the activation of oxygen by Eosin Y into  $^1O_2$ . Both disulfides were obtained in excellent yields (Figure 47A). The same year, the authors worked on the reaction scale by numbering-up their home-made photoreactor.<sup>97</sup> 2 to 8 photoreactors were run in parallel with a common reagent feed. Pressurized air was blown on the setup to keep the temperature at about 22 °C. The gas/liquid ratio was kept at 3:1 and the segmented flow was settled in a first PFA tubing before being distributed in each photoreactor. Although, the authors identified a small deviation in yield and flow rates in each separated coil, the transition from 1 to 8 coils almost did not affect the overall yield (Figure 47B).

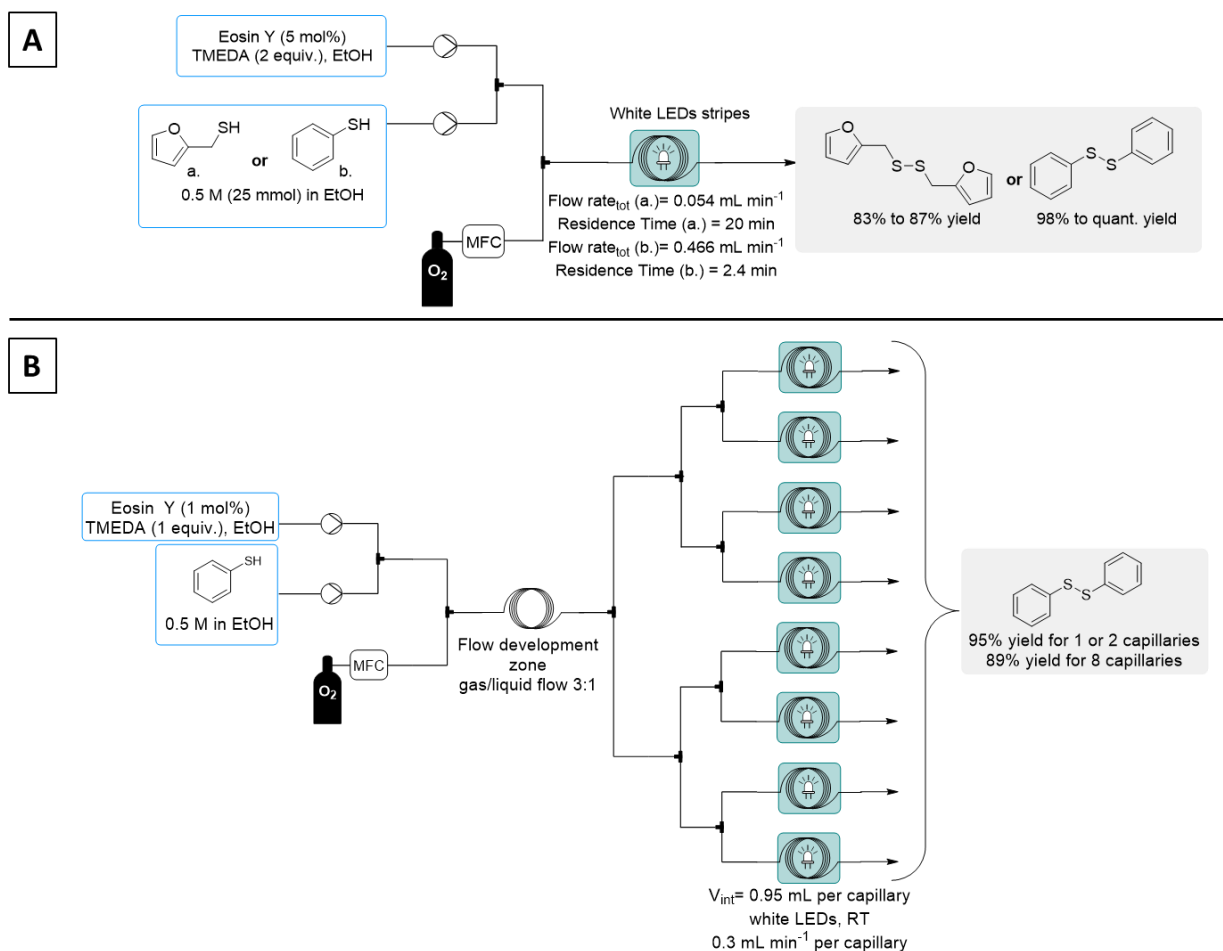


Figure 47 – A – Flow photooxidation of thiols in disulfide in a homemade photoreactor. B - Photoreactor numbering-up.

Noël and his team also took the opportunity of this work to test a heterogeneous photocatalyst for the same oxidation of thiols into disulfides.<sup>140</sup> Their previous PS, Eosin Y, was efficient but as all homogeneous PS, it required an additional purification step to isolate the disulfide. To adapt this disulfide bonding to peptides, the authors decided to change for  $\text{TiO}_2$ . Particles of  $\text{TiO}_2$  are too large to be pumped in the reactor and would cause clogging. Therefore, the metallic particles were placed in a packed bed glass column. It should be noted that  $\text{TiO}_2$  was mixed with small glass beads to create enough spacing in the packed-bed for the solution and oxygen to pass through without causing an excessive pressure drop. The packed-bed was also flushed with a basic solution before the reaction to aggregate  $\text{TiO}_2$  particles and ensure to avoid potential leaching in the reactor. The 2 liquid feeds ( $8.3 \mu\text{L min}^{-1}$  each) were mixed with oxygen feed ( $50 \mu\text{L min}^{-1}$ ) before entering the catalyst glass column irradiated by visible light. In this configuration, several disulfides could be synthesized in extremely short reaction time comparing to their batch similar synthesis (Figure 48).

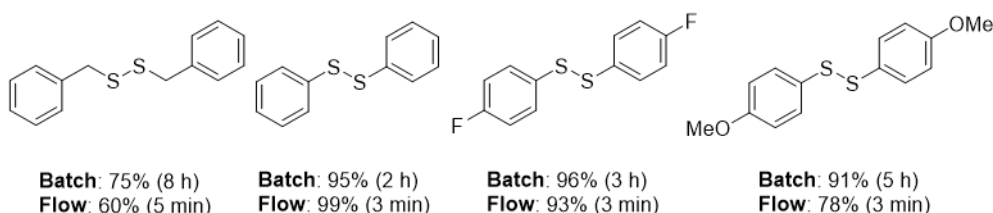
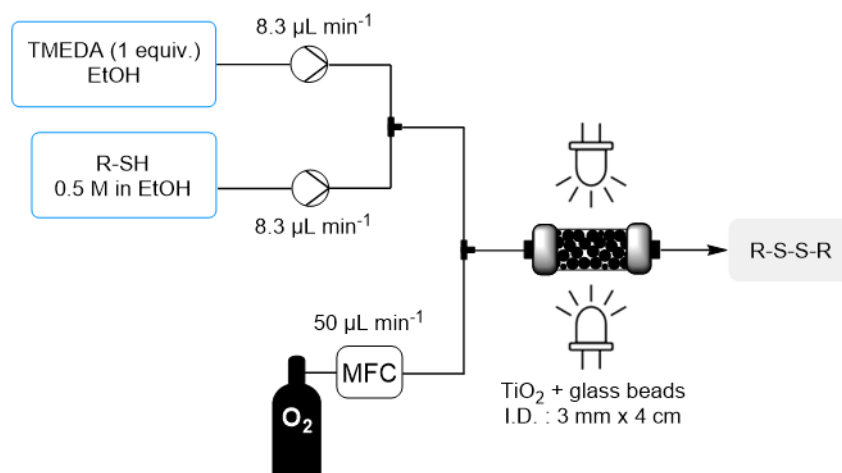


Figure 48 – Flow photoreactor including a  $\text{TiO}_2$  packed-bed for the oxidation of thiols into disulfides.

Vilela *et al.* demonstrated the feasibility of  $^1\text{O}_2$  generation by natural sunlight for the photooxidation of  $\alpha$ -terpinene into ascaridole.<sup>141</sup> Their catalyst, 2,1,3-benzothiadiazole (BTZ), was synthesized under three different forms: gel, beads and monoliths. Oxidations with those catalysts were conducted in batch and in flow except for the gel BTZ which was impracticable in a flow reactor. For beads-BTZ,  $\alpha$ -terpinene (1 mmol) was mixed with the catalyst in chloroform and strongly sonicated to disperse the particles. A Vapourtec equipment designed for photochemistry was employed at 420 nm and the solution and air circulated in the reactor several time for a total duration of 60 min. Ascaridole was produced at  $136 \text{ mg h}^{-1}$  (Figure 49A). Monoliths of BTZ were not compatible with the narrow dimensions of the injection tubing and was therefore packed in a glass column. By replacing air with pure oxygen, lowering the reactant concentration and flow rates, one passage through the photoreactor was sufficient to obtain full conversion (Figure 49B). To assess the stability of their catalyst, the reactor was run for 600 min. No decrease in conversion could be detected. The authors finally placed samples of solution with BTZ in the sunlight and observed a full oxidation in ascaridole in 60 min for beads-BTZ.

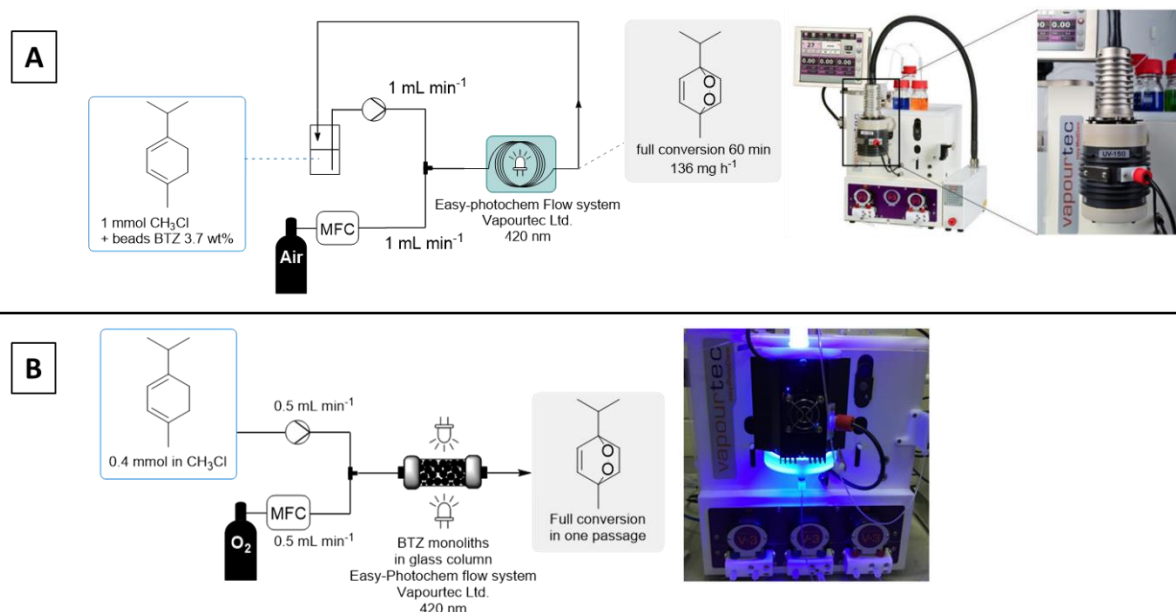


Figure 49 – Flow photooxidation of ascaridole with A - BTZ beads, B – BTZ monoliths as PS in Easy-Photochem flow system from Vapourtec Ltd. Adapted with permission from ACS Catal. 2017, 7, 4602–4612. Copyright 2017 American Chemical Society.

#### 1.4.3.3. Photooxidation of sulfides to sulfoxides in continuous flow

Aleman *et al.* succeeded in selectively oxidizing various aliphatic and aromatic sulfides with a Pt(II) coordination complex that served as a robust photocatalyst under visible light irradiation in harmless solvents both in batch and in flow.<sup>142</sup> This metal-catalyst favored oxidation through the superoxide radical anion pathway. Typically, for the batch procedure, 0.3 mmol of the sulfide was dissolved in a mixture of EtOH/H<sub>2</sub>O (1:1) with 2 mol% of the catalyst and the solution was irradiated under blue light for 10 h to 48 h depending on the structure of the sulfide. Sulfides with electron-poor aryl groups required a longer irradiation to be oxidized. Total conversion into sulfoxide was achieved for alkyl or electron-rich aryl sulfides but the conversion dropped to 70% for the sulfide bearing a benzonitrile group even after 48 h of irradiation. A modest scale-up on 3 mmol of 4-methylthioanisole was attempted but required to expand the irradiation time from 10 h to 25 h. The implementation of this process in flow required a few adaptations. An oxygen gas cylinder was connected to the reactor (between 0.04 and 0.1 mL min<sup>-1</sup>) and 0.3 mmol of sulfides were sonicated with 1 mol% of the platinum catalyst in a mixture of EtOH/H<sub>2</sub>O 9:1 and 3.2 equivalents of dioxane before being loaded in a loop. Both gas and liquid feeds were mixed with a T-mixer before entering a 4.1 mL coil reactor irradiated under blue light. Corresponding sulfoxides were obtained with 50% to total conversion and residence time varying from 10.5 to 82 min (Figure 50).

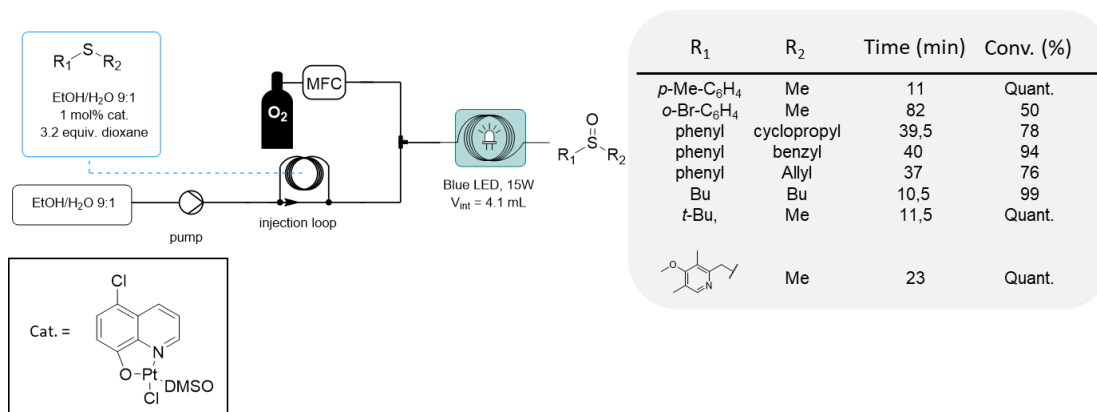


Figure 50 – Photooxidation of various sulfides in a flow reactor with a Pt(II) catalyst.

Gupton *et al.* opted for a heterogeneous photocatalyst by using a packed bed containing polymer-supported Rose Bengal.<sup>143</sup> The reagents were pumped through the packed bed under irradiation of green LEDs (530-580 nm) and underwent subsequent <sup>1</sup>O<sub>2</sub> oxidation. Although the main part of the publication was dedicated to the synthesis of anti-malarial drug artemisinin, the authors briefly described the photooxidation of several model compounds, among which, hydroxyethyl ethyl sulfide. 98% of conversion was achieved with a 10:1 mixture of sulfoxide and sulfone that the authors did not try to improve (Figure 51). However, in this packed-bed setup, RB was more resistant to photobleaching and the photooxidation could run for 10 h before detecting a loss of conversion.

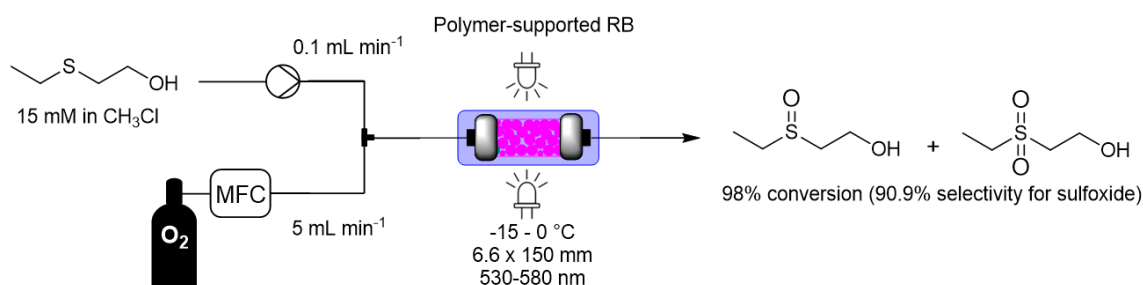


Figure 51 – Packed-bed photoreactor for the photooxidation of EtSEtOH.

In 2019, Noël and his team reported the photooxidation of several substrates, among which, methionine,  $\alpha$ -terpinene and dihydroartemisinic acid with a novel type of photoreactor.<sup>144</sup> The described photoreactors, luminescent solar concentrator-photomicroreactors (LSC-PMs), are able to harvest sunlight and concentrate photons to the reactor tubing. Three different LSC-PMs were available for red, green and blue irradiation. All consisted of PFA tubing embedded in a PMMA matrix with luminophore dopants and were constructed in 3 different internal volumes (177, 707 and 1590  $\mu$ L). First experiments were conducted with simulated indoor sunlight. Substrates were simply pumped into the reactor with oxygen and only methionine required the use of a back-pressure regulator (80 psi). All reaction tested occurred between 8 s and 20 min and led to good productivities (Figure 52). Methionine oxidation, as a safe reaction, was selected for the first test under outdoor solar irradiation on a larger scale (although the authors do not specify the exact scale). In the red LSC-PM, methionine sulfoxide was selectively obtained in 80% yield. The same experiment was reproduced on dihydroartemisinic acid, precursor of anti-malarial drug artemisinin, with the LSC-PM let on a window ledge on 2 different sunny days of June. The yield, followed by HPLC, varied depending on the time of day. This is explainable as the luminosity arriving from the sun is not always constant due to cloud passing. The yield, monitored at every 30 min interval, varied from 69% to 78% which is honorable considering the fluctuations and the “diluted” irradiation.

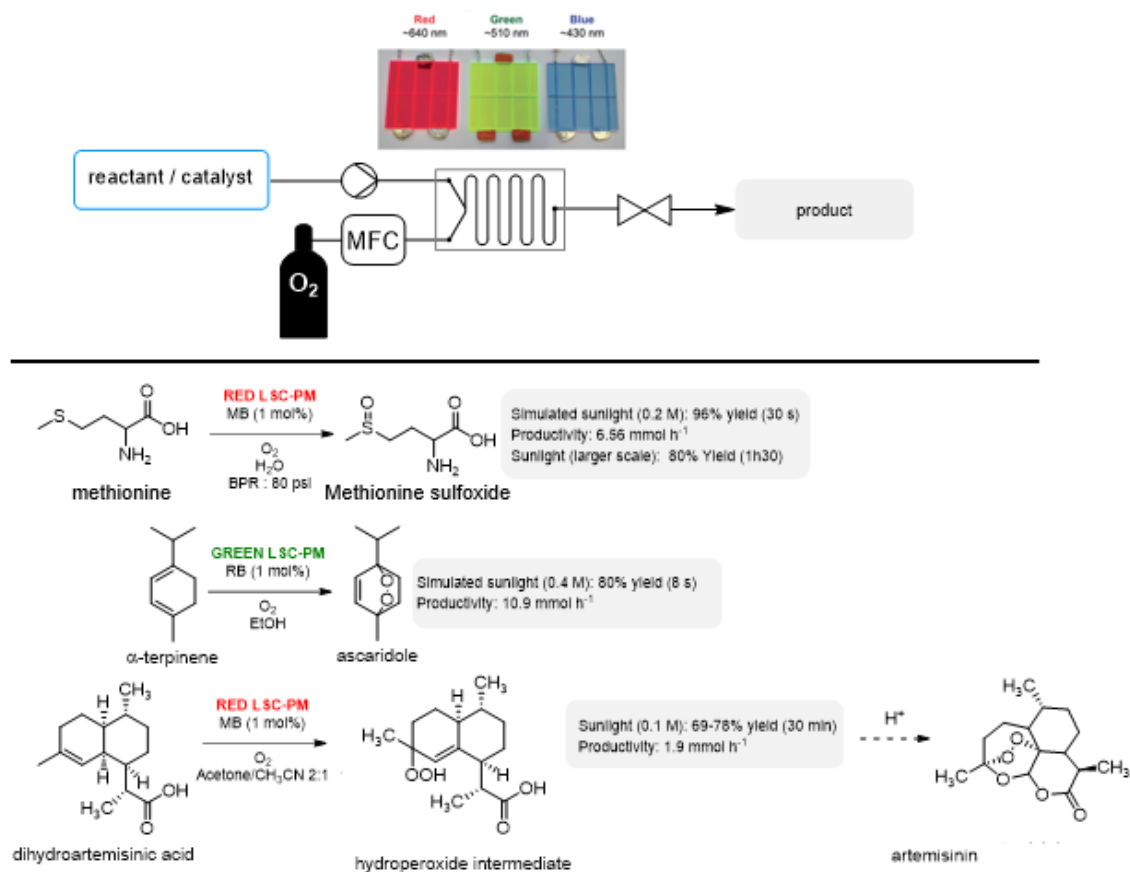
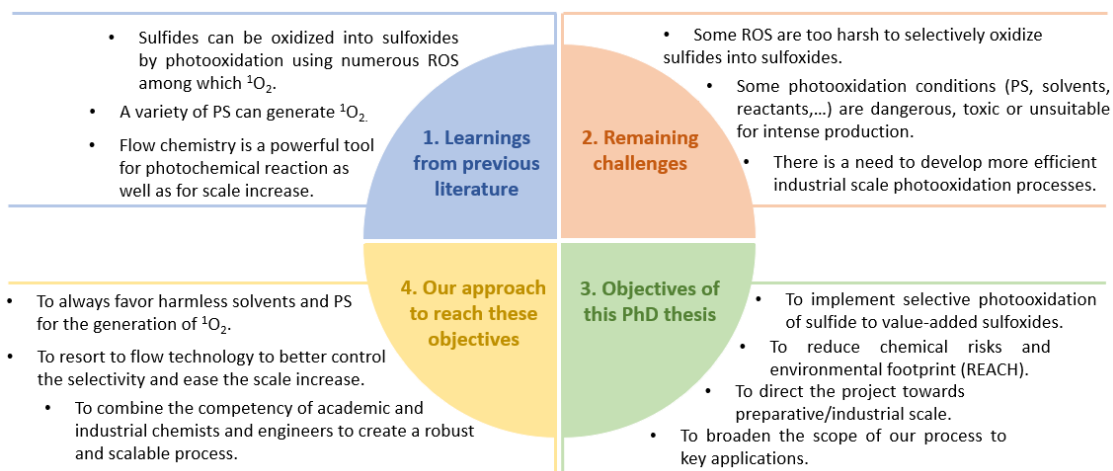


Figure 52 – Luminescent solar concentrators (LSCs) based Photoreactors for the photooxidation of various compounds with simulated and real light. Photography of the LSC-PMs belongs to Wiley-VCH Verlag GmbH & Co. KGaA, Weinheim.

These results encourage for more research in the field of singlet oxygen flow photooxidation to access new production scale of sulfoxides.

## 1.5. Aim of the thesis

The global context and objectives of this PhD thesis have been summarized in the diagram below:



Regarding the existing literature, it is undeniable that the oxidation of sulfides into sulfoxides is achievable under various conditions (solvent, oxidant, PS, light source, ...). Hydrogen peroxide remains the most frequently used oxidant but peroxides present chemical risk and can be too harsh for a controlled oxidation. Concerning photooxidations of sulfides, a plethora of organic and inorganic PS have already been studied for the generation of different ROS. However, the main challenges remain the lack of selectivity and scale increase. Even with milder oxidant, the obtention of pure sulfoxide is not easily achievable. Most of the selective photooxidation procedures were performed on small quantities ( $\mu\text{mol}$  to  $\text{mmol}$ ) and descriptions of preparative scale production of sulfoxides are too scarce. This PhD thesis aims at implementing the selective photooxidation of sulfides to value-added sulfoxides with singlet oxygen in continuous flow reactors. All photooxidation processes will be designed with the main objectives of reducing chemical risk and the overall environmental footprint within the context of increasingly restrictive legislations (e.g. REACH). Harmless reagents and solvents will be favored and the use of recent technologies will help achieving automation of the processes and potential scalability. This interdisciplinary project relies on the complementarity between chemistry and chemical engineering and is oriented toward preparative/pilot applications.

Our work aims at the development of selective oxidation protocols targeting sulfoxides with an industrial interest or with high societal impact. The results in this manuscript are organized in chapters regarding of the molecule(s) undergoing photooxidation. Chapter 2, divided in 3 publications, covers the very first experiments that shaped our oxidation protocol on the amino acid methionine in batch, the technique and challenges for a successful transposition to flow and how flow enabled the production of methionine sulfoxide at pilot scale under sustainable conditions. In the last publication of this chapter, the photooxidation was performed with a heterogeneous catalyst, opening the potential for PS protection and recovery. The pilot scale production of ascaridole and rose oxide, commercially relevant anthelmintic and fragrance respectively, is also described in this section. In Chapter 3, the employment of flow photooxidation in the battle against chemical warfare agents is described with the safe and sustainable neutralization of a mustard gas simulant in a mobile flow reactor that can be transported and operated on field. Chapter 4 proposes a total synthesis of modafinil, a drug used to treat narcolepsy and enhance cognitive functions. The complete synthesis was implemented in both batch and flow and involve a sulfoxidation step. Modafinil is an FDA approved eugeroic and a nootropic that is less likely to create addiction which raised the interest of NASA and the Army.



## 1.6. References

- 1 L. B. Josefsen and R. W. Boyle, *Met. Based. Drugs*, DOI:10.1155/2008/276109.
- 2 R. L. Edelson, *Sci. Am.*, 1988, **259**, 68–75.
- 3 K.K Rohatgi-Mukherjee, *Fundamentals of Photochemistry (Revised edition)*, 3rd edn., 2014.
- 4 V. Balzani and F. Scandola, *Quim. Nova*, 1996, **19**, 542–548.
- 5 B. Wardle, *Principles and Applications of Photochemistry*, Wiley, 2009.
- 6 P. Klán and J. Wirz, *Photochemistry of Organic Compounds. From Concepts to Practice.*, Wiley, 2009.
- 7 M. C. DeRosa and R. J. Crutchley, *Coord. Chem. Rev.*, 2002, **233–234**, 351–371.
- 8 S. Beutner, B. Bloedorn, T. Hoffmann and M. Hans-Dieter, *Methods Enzymol.*, 2000, **319**, 226–241.
- 9 M. Bregnhøj, M. Westberg, F. Jensen and P. R. Ogilby, *Phys. Chem. Chem. Phys.*, 2016, **18**, 22946–22961.
- 10 N. J. Turro, V. Ramamurthy, K.-C. Liu, A. Krebs and R. Kemper, *J. Am. Chem. Soc.*, 1976, **98**, 6758–6761.
- 11 A. M. Held, D. J. Halko and J. K. Hurst, *J. Am. Chem. Soc.*, 1978, **100**, 5732–5740.
- 12 C. S. Foote, S. Wexler, A. Wataru and R. Higgins, *J. Am. Chem. Soc.*, 1967, **90**, 975–981.
- 13 J. M. Aubry, *J. Am. Chem. Soc.*, 1985, **107**, 5844–5849.
- 14 W. Fudickar and T. Linker, *ChemPhotoChem*, 2018, **2**, 548–558.
- 15 H. G. Jeong and M. S. Choi, *Isr. J. Chem.*, 2016, **56**, 110–118.
- 16 C. E. Diaz-Uribe, M. C. Daza, E. A. Páez-Mozo, F. Martínez O., C. L. B. Guedes and E. Di Mauro, *J. Photochem. Photobiol. A Chem.*, 2013, **259**, 47–52.
- 17 A. P. Demchenko, *Methods Appl. Fluoresc.*, 2020, **8**, 0–43.
- 18 R. Bonnett and G. Martinez, *Tetrahedron*, 2001, **57**, 9513–9547.
- 19 W. C. Sun, K. R. Gee, D. H. Klaubert and R. P. Haugland, *J. Org. Chem.*, 1997, **62**, 6469–6475.
- 20 M. Varol, *Methods Mol. Biol.*, 2020, **2109**, 241–250.
- 21 M. Hirose, Y. Yoshida, K. Horii, Y. Hasegawa and Y. Shibuya, *Arch. Oral Biol.*, 2021, **122**, 105024.
- 22 J. Wang, H. Liu, D. Ma, Y. Wang, G. Yao, Q. Yue, B. Gao, S. Wang and X. Xu, *Chemosphere*, 2020, **268**, 128796.
- 23 S. Parcell, *Altern. Med. Rev.*, 2002, **7**, 22–44.
- 24 S. Hewlings and D. Kalman, *Ec Nutr.*, 2019, 785–791.
- 25 M. Kazemi, S. Sajjadifar, A. Aydi and M. M. Heydari, *J. Med. Chem. Sci.*, 2018, **1**, 1–4.
- 26 P. Das, M. D. Delost, M. H. Qureshi, D. T. Smith and J. T. Njardarson, *J. Med. Chem.*, 2019, **62**, 4265–4311.

- 27 N. Farrell, D. M. Kiley, W. Schmidt and M. P. Hacker, *Inorg. Chem.*, 1990, **29**, 397–403.
- 28 T. Andersson, K. Röhss, E. Bredberg and M. Hassan-Alin, *Aliment. Pharmacol. Ther.*, 2001, **15**, 1563–1569.
- 29 J. Dent, *Aliment. Pharmacol. Ther. Suppl.*, 2003, **17**, 5–9.
- 30 C. M. Den Hoed and E. J. Kuipers, *Expert Rev. Gastroenterol. Hepatol.*, 2010, **4**, 679–695.
- 31 G.-Q. Lin, Q. You and J.-F. Cheng, *Chiral Drugs : Chemistry and Biological Action*, Wiley, 2011.
- 32 I. Agranat and H. Marom, *ACS Med. Chem. Lett.*, 2020, **11**, 91–98.
- 33 B. M. Trost, M. C. Ryan and M. Rao, *Beilstein J. Org. Chem.*, 2016, **12**, 1136–1152.
- 34 S. E. Ammann, W. Liu and M. C. White, *Angew. Chemie - Int. Ed.*, 2016, **55**, 9571–9575.
- 35 B. M. Trost and M. Rao, *Angew. Chemie - Int. Ed.*, 2015, **54**, 5026–5043.
- 36 M. Stadlmeier, J. Bogena, M. Wallner, M. Wühr and T. Carell, *Angew. Chemie - Int. Ed.*, 2018, **57**, 2958–2962.
- 37 Z. He, G. J. P. Perry and D. J. Procter, *Chem. Sci.*, 2020, **11**, 2001–2005.
- 38 T. Stopka, M. Niggemann and N. Maulide, *Angew. Chemie - Int. Ed.*, 2017, **56**, 13270–13274.
- 39 T. Yoshida, M. Kito, M. Tsujii and T. Nagasawa, *Biotechnol. Lett.*, 2001, **23**, 1217–1222.
- 40 A. S. Surur, L. Schulig and A. Link, *Arch. der Pharm. Chem. Life Sci.*, 2019, **352**, 1–11.
- 41 J. S. Ballon and D. Feifel, *J. Clin. Psychiatry*, 2006, **67**, 554–566.
- 42 C. J. Loland, M. Mereu, O. M. Okunola, J. Cao, T. E. Prinszano, S. Mazier, T. Kopajtic, L. Shi, J. L. Katz, G. Tanda and A. Hauck Newman, *Biol. Psychiatry*, 2012, **72**, 405–413.
- 43 T. Klejch, D. T. Keough, M. Chavchich, J. Travis, J. Skácel, R. Pohl, Z. Janeba, M. D. Edstein, V. M. Avery, L. W. Guddat and D. Hocková, *Eur. J. Med. Chem.*, 2019, **183**, 111667.
- 44 A. Reale, S. Brogi, A. Chelini, M. Paolino, A. Di Capua, G. Giuliani, A. Cappelli, G. Giorgi, G. Chemi, A. Grillo, M. Valoti, L. Sautebin, A. Rossi, S. Pace, C. La Motta, L. Di Cesare Mannelli, E. Lucarini, C. Ghelardini and M. Anzini, *Bioorganic Med. Chem.*, 2019, **27**, 115045.
- 45 Z. Chen, C. Liu, J. Liu, J. Li, S. Xi, X. Chi, H. Xu, I. H. Park, X. Peng, X. Li, W. Yu, X. Liu, L. Zhong, K. Leng, W. Huang, M. J. Koh and K. P. Loh, *Adv. Mater.*, 2020, **32**, 1–8.
- 46 A. G. Moaser, A. Ahadi, S. Rouhani, B. B. Mamba, T. A. M. Msagati, S. Rostamnia, T. Kavetsky, S. Dugheri, S. Khaksar, A. Hasanzadeh and M. Shokouhimehr, *J. Mol. Liq.*, 2020, **312**, 113388.
- 47 M. Radko, A. Kowalczyk, P. Mikrut, S. Witkowski, W. Mozgawa, W. MacYk and L. Chmielarz, *RSC Adv.*, 2020, **10**, 4023–4031.
- 48 J. M. Campos-Martin, G. Blanco-Brieva and J. L. G. Fierro, *Angew. Chemie - Int. Ed.*, 2006, **45**, 6962–6984.
- 49 Y. Zhang, X. Yang, H. Tang, D. Liang, J. Wu and D. Huang, *Green Chem.*, 2020, **22**, 22–27.
- 50 C. Li, N. Mizuno, K. Murata, K. Ishii, T. Suenobu, K. Yamaguchi, K. Suzuki and K. Suzuki, *Green Chem.*, 2020, **22**, 3896–3905.
- 51 C. Ren, R. Fang, X. Yu and S. Wang, *Tetrahedron Lett.*, 2018, **59**, 982–986.
- 52 L. Q. Wei and B. H. Ye, *ACS Appl. Mater. Interfaces*, 2019, **11**, 41448–41457.

- 53 W. Zhao, C. Yang, J. Huang, X. Jin, Y. Deng, L. Wang, F. Su, H. Xie, P. K. Wong and L. Ye, *Green Chem.*, 2020, **22**, 4884–4889.
- 54 M. B. Colombo Migliorero, V. Palermo, G. P. Romanelli and P. G. Vázquez, *Catal. Today*, , DOI:10.1016/j.cattod.2020.10.034.
- 55 S. Klaine, N. Fung Lee, A. Dames and R. Zhang, *Inorganica Chim. Acta*, 2020, **509**, 119681.
- 56 F. Jensen, A. Greer and E. L. Clennan, *J. Am. Chem. Soc.*, 1998, **120**, 4439–4449.
- 57 S. M. Bonesi, M. Fagnoni, S. Monti and A. Albini, *Photochem. Photobiol. Sci.*, 2004, **3**, 489–493.
- 58 M. Scholz, R. Dedic, T. Breitenbach and J. Hala, *Photochem. Photobiol. Sci.*, 2013, **51**, 51-2070-51–2070.
- 59 S. Clement, M. Sobhan, W. Deng, E. Camilleri and E. M. Goldys, *J. Photochem. Photobiol. A Chem.*, 2017, **332**, 66–71.
- 60 E. Wolcan, *Inorganica Chim. Acta*, 2020, **509**, 119650.
- 61 T. S. A. Heugebaert, C. V. Stevens and C. O. Kappe, *ChemSusChem*, 2015, **8**, 1648–1651.
- 62 J. P. Tardivo, A. Del Giglio, C. S. De Oliveira, D. S. Gabrielli, H. C. Junqueira, D. B. Tada, D. Severino, R. De Fátima Turchiello and M. S. Baptista, *Photodiagnosis Photodyn. Ther.*, 2005, **2**, 175–191.
- 63 O. V. Ovchinnikov, M. S. Smirnov, T. S. Kondratenko, A. S. Perepelitsa, I. G. Grevtseva and S. V. Aslanov, *Opt. Spectrosc.*, 2018, **125**, 107–112.
- 64 Z. Amara, J. F. B. Bellamy, R. Horvath, S. J. Miller, A. Beeby, A. Burgard, K. Rossen, M. Poliakoff and M. W. George, *Nat. Chem.*, 2015, **7**, 489–495.
- 65 I. Pibiri, S. Buscemi, A. Palumbo Piccionello and A. Pace, *ChemPhotoChem*, 2018, **2**, 535–547.
- 66 Y. Zhang, J. Lou, M. Li, Z. Yuan and Y. Rao, *RSC Adv.*, 2020, **10**, 19747–19750.
- 67 H. Guo, H. Xia, X. Ma, K. Chen, C. Dang, J. Zhao and B. Dick, *ACS Omega*, 2020, **5**, 10586–10595.
- 68 Y. Gao, H. Xu, S. Zhang, Y. Zhang, C. Tang and W. Fan, *Org. Biomol. Chem.*, 2019, **17**, 7144–7149.
- 69 C. Ye, Y. Zhang, A. Ding, Y. Hu and H. Guo, *Sci. Rep.*, 2018, **8**, 1–6.
- 70 S. Biswas, M. Kumar, A. M. Levine, I. Jimenez, R. V. Ulijn and A. B. Braunschweig, *Chem. Sci.*, 2020, **11**, 4239–4245.
- 71 F. Yang, X. Chu, J. Sun, Y. Zhang, Z. Li, H. Liu, L. Bai, Y. Qu and L. Jing, *Chinese Chem. Lett.*, 2020, **31**, 2784–2788.
- 72 J. Wang, X. Xu, Y. Liu, Z. Wang, P. Wang, Z. Zheng, H. Cheng, Y. Dai and B. Huang, *ChemSusChem*, 2020, **13**, 3488–3494.
- 73 L. P. Li and B. H. Ye, *Inorg. Chem.*, 2019, **58**, 7775–7784.
- 74 COMMUNICATION FROM THE COMMISSION TO THE EUROPEAN PARLIAMENT, THE COUNCIL, THE EUROPEAN ECONOMIC AND SOCIAL COMMITTEE AND THE COMMITTEE OF THE REGIONS - *Chemicals Strategy for Sustainability Towards a Toxic-Free Environment*, European Commission, Brussels, 2020.
- 75 A. Polyzos, M. O'Brien, T. P. Petersen, I. R. Baxendale and S. V. Ley, *Angew. Chemie - Int. Ed.*, 2011, **50**, 1190–1193.

- 76 J. F. Ng, Y. Nie, G. K. Chuah and S. Jaenicke, *J. Catal.*, 2010, **269**, 302–308.
- 77 F. Carvalho, M. P. C. Marques and P. Fernandes, *Catalysts*, DOI:10.3390/catal7020042.
- 78 A. L. Liu, Z. Q. Li, Z. Q. Wu and X. H. Xia, *Talanta*, 2018, **182**, 544–548.
- 79 P. Bianchi, J. D. Williams and C. O. Kappe, *J. Flow Chem.*, 2020, **10**, 475–490.
- 80 B. J. Reizman and K. F. Jensen, *Acc. Chem. Res.*, 2016, **49**, 1786–1796.
- 81 J. Yue, J. C. Schouten and T. Alexander Nijhuis, *Ind. Eng. Chem. Res.*, 2012, **51**, 14583–14609.
- 82 V. Sans and L. Cronin, *Chem. Soc. Rev.*, 2016, **45**, 2032–2043.
- 83 B. Picard, B. Gouilleux, T. Lebleu, J. Maddaluno, I. Chataigner, M. Penhoat, F. X. Felpin, P. Giraudeau and J. Legros, *Angew. Chemie - Int. Ed.*, 2017, **56**, 7568–7572.
- 84 P. Koos, U. Gross, A. Polyzos, M. O’Brien, I. Baxendale and S. V. Ley, *Org. Biomol. Chem.*, 2011, **9**, 6903–6908.
- 85 S. Krishnadasan, R. J. C. Brown, A. J. DeMello and J. C. DeMello, *Lab Chip*, 2007, **7**, 1434–1441.
- 86 R. M. Maceiczky, L. Bezinge and A. J. Demello, *React. Chem. Eng.*, 2016, **1**, 261–271.
- 87 H. Lu, M. A. Schmidt and K. F. Jensen, *Lab Chip*, 2001, **1**, 22–28.
- 88 S. Mozharov, A. Nordon, D. Littlejohn, C. Wiles, P. Watts, P. Dallin and J. M. Girkin, *J. Am. Chem. Soc.*, 2011, **133**, 3601–3608.
- 89 N. Holmes, G. R. Akien, R. J. D. Savage, C. Stanetty, I. R. Baxendale, A. J. Blacker, B. A. Taylor, R. L. Woodward, R. E. Meadows and R. A. Bourne, *React. Chem. Eng.*, 2016, **1**, 96–100.
- 90 J. P. McMullen, M. T. Stone, S. L. Buchwald and K. F. Jensen, *Angew. Chemie - Int. Ed.*, 2010, **49**, 7076–7080.
- 91 C. J. Mallia and I. R. Baxendale, *Org. Process Res. Dev.*, 2016, **20**, 327–360.
- 92 M. B. Plutschack, B. Pieber, K. Gilmore and P. H. Seeberger, *Chem. Rev.*, 2017, **117**, 11796–11893.
- 93 R. Gérardy, N. Emmanuel, T. Toupy, V. E. Kassin, N. N. Tshibalonza, M. Schmitz and J. C. M. Monbaliu, *European J. Org. Chem.*, 2018, **2018**, 2301–2351.
- 94 M. Berton, J. M. de Souza, I. Abdiaj, D. T. McQuade and D. R. Snead, *J. Flow Chem.*, 2020, **10**, 73–92.
- 95 D. J. Watson, E. D. Dowdy, J. S. DePue, A. S. Kotnis, S. Leung and B. C. O’Reilly, *Org. Process Res. Dev.*, 2004, **8**, 616–623.
- 96 A. Yavorsky, O. Shvydkiv, N. Hoffmann, K. Nolan and M. Oelgemöller, *Org. Lett.*, 2012, **14**, 4342–4345.
- 97 Y. Su, K. Kuijpers, V. Hessel and T. Noël, *React. Chem. Eng.*, 2016, **1**, 73–81.
- 98 K. P. L. Kuijpers, M. A. H. Van Dijk, Q. G. Rumeur, V. Hessel, Y. Su and T. Noël, *React. Chem. Eng.*, 2017, **2**, 109–115.
- 99 M. Qiu, L. Zha, Y. Song, L. Xiang and Y. Su, *React. Chem. Eng.*, 2019, **4**, 351–361.
- 100 G. N. Ahn, T. Yu, H. J. Lee, K. W. Gyak, J. H. Kang, D. You and D. P. Kim, *Lab Chip*, 2019, **19**, 3535–3542.

- 101 V. Hessel, D. Kralisch, N. Kockmann, T. Noël and Q. Wang, *ChemSusChem*, 2013, **6**, 746–789.
- 102 T. Noël, *Discov. Futur. Mol. Sci.*, 2014, **9783527335**, 137–164.
- 103 M. J. Di Maso, K. Narsimhan, M. K. Wismer and J. R. Naber, , DOI:10.1021/acs.oprd.0c00373.
- 104 V. E. H. Kassin, T. Toupay, G. Petit, P. Bianchi, E. Salvadeo and J. C. M. Monbaliu, *J. Flow Chem.*, 2020, **10**, 167–179.
- 105 R. Gérardy, M. Winter, A. Vizza and J. C. M. Monbaliu, *React. Chem. Eng.*, 2017, **2**, 149–158.
- 106 C. A. Hone and C. O. Kappe, *Chem. - A Eur. J.*, 2020, **26**, 13108–13117.
- 107 T. Morimoto, K. Fuji, K. Tsutsumi and K. Kakiuchi, *J. Am. Chem. Soc.*, 2002, **124**, 3806–3807.
- 108 A. Więckowska, R. Fransson, L. R. Odell and M. Larhed, *J. Org. Chem.*, 2011, **76**, 978–981.
- 109 T. Ueda, H. Konishi and K. Manabe, *Angew. Chemie - Int. Ed.*, 2013, **52**, 8611–8615.
- 110 J. W. Yang, M. T. Hechavarria Fonseca and B. List, *Angew. Chemie - Int. Ed.*, 2004, **43**, 6660–6662.
- 111 F. J. Strauss, D. Cantillo, J. Guerra and C. O. Kappe, *React. Chem. Eng.*, 2016, **1**, 472–476.
- 112 M. Wernik, P. Poehlauer, C. Schmoelzer, D. Dallinger and C. O. Kappe, *Org. Process Res. Dev.*, 2019, **23**, 1359–1368.
- 113 Y. Zhou, C. Yao, P. Zhang, X. Zhang, H. Lü and Y. Zhao, *Ind. Eng. Chem. Res.*, 2020, **59**, 9279–9292.
- 114 P. W. Miller, N. J. Long, A. J. De Mello, R. Vilar, J. Passchier and A. Gee, *Chem. Commun.*, 2006, 546–548.
- 115 J. R. Breen, G. Sandford, D. S. Yufit, J. A. K. Howard, J. Fray and Bhairavi Patel, *Beilstein J. Org. Chem.*, 2011, **7**, 1048–1054.
- 116 M. O'Brien, I. R. Baxendale and S. V. Ley, *Org. Lett.*, 2010, **12**, 1596–1598.
- 117 M. Brzozowski, M. O'Brien, S. V. Ley and A. Polyzos, *Acc. Chem. Res.*, 2015, **48**, 349–362.
- 118 M. Ramezani, M. A. Kashfipour and M. Abolhasani, *J. Flow Chem.*, 2020, **10**, 93–101.
- 119 S. Han, M. A. Kashfipour, M. Ramezani and M. Abolhasani, *Chem. Commun.*, 2020, **56**, 10593–10606.
- 120 K. Jähnisch, M. Baerns, V. Hessel, W. Ehrfeld, V. Haverkamp, H. Löwe, C. Wille and A. Guber, *J. Fluor. Chem.*, 2000, **105**, 117–128.
- 121 C. P. Park, R. A. Maurya, J. H. Lee and D. P. Kim, *Lab Chip*, 2011, **11**, 1941–1945.
- 122 B. T. Ramanjaneyulu, N. K. Vishwakarma, S. Vidyacharan, P. R. Adiyala and D. P. Kim, *Bull. Korean Chem. Soc.*, 2018, **39**, 757–772.
- 123 T. Noël and V. Hessel, *ChemSusChem*, 2013, **6**, 405–407.
- 124 J. Jovanović, E. V. Rebrov, T. A. Nijhuis, V. Hessel and J. C. Schouten, *Ind. Eng. Chem. Res.*, 2010, **49**, 2681–2687.
- 125 R. Radjagobalou, J. F. Blanco, O. Dechy-Cabaret, M. Oelgemöller and K. Loubière, *Chem. Eng. Process. - Process Intensif.*, 2018, **130**, 214–228.
- 126 J. H. Park, C. Y. Park, M. J. Kim, M. U. Kim, Y. J. Kim, G. H. Kim and C. P. Park, *Org. Process Res.*

- Dev.*, 2015, **19**, 812–818.
- 127 T. L. LaPorte, M. Hamed, J. S. DePue, L. Shen, D. Watson and D. Hsieh, *Org. Process Res. Dev.*, 2008, **12**, 956–966.
- 128 C. A. Hone and C. O. Kappe, *The Use of Molecular Oxygen for Liquid Phase Aerobic Oxidations in Continuous Flow*, Springer International Publishing, 2019, vol. 377.
- 129 V. E. H. Kassin, R. Gérardy, T. Toupay, Di. Collin, E. Salvadeo, F. Toussaint, K. Van Hecke and J. C. M. Monbaliu, *Green Chem.*, 2019, **21**, 2952–2966.
- 130 F. Darvas, G. Dorman and V. Hessel, *Flow Chemistry. Volume 2: Applications*, Walter de Gruyter GmbH, 2014.
- 131 J. Turconi, F. Griollet, R. Guevel, G. Oddon, R. Villa, A. Geatti, M. Hvala, K. Rossen, R. Göller and A. Burgard, *Org. Process Res. Dev.*, 2014, **18**, 417–422.
- 132 F. Lévesque and P. H. Seeberger, *Angew. Chemie - Int. Ed.*, 2012, **51**, 1706–1709.
- 133 D. Kopetzki, F. Lévesque and P. H. Seeberger, *Chem. - A Eur. J.*, 2013, **19**, 5450–5456.
- 134 K. Gilmore, D. Kopetzki, J. W. Lee, Z. Horváth, D. T. McQuade, A. Seidel-Morgenstern and P. H. Seeberger, *Chem. Commun.*, 2014, **50**, 12652–12655.
- 135 S. Budde, F. Goerdeler, J. Floß, P. Kreitmeier, E. F. Hicks, O. Moscovitz, P. H. Seeberger, H. M. L. Davies and O. Reiser, *Org. Chem. Front.*, 2020, **7**, 1789–1795.
- 136 S. Triemer, K. Gilmore, G. T. Vu, P. H. Seeberger and A. Seidel-Morgenstern, *Angew. Chemie - Int. Ed.*, 2018, **57**, 5525–5528.
- 137 D. Dallinger and C. O. Kappe, *Curr. Opin. Green Sustain. Chem.*, 2017, **7**, 6–12.
- 138 B. Gutmann and C. O. Kappe, *J. Flow Chem.*, 2017, **7**, 65–71.
- 139 N. J. W. Straathof, Y. Su, V. Hessel and T. Noël, *Nat. Protoc.*, 2016, **11**, 10–21.
- 140 C. Bottecchia, N. Erdmann, P. M. A. Tijssen, L. G. Milroy, L. Brunsveld, V. Hessel and T. Noël, *ChemSusChem*, 2016, **9**, 1781–1785.
- 141 J. M. Tobin, T. J. D. McCabe, A. W. Prentice, S. Holzer, G. O. Lloyd, M. J. Paterson, V. Arrighi, P. A. G. Cormack and F. Vilela, *ACS Catal.*, 2017, **7**, 4602–4612.
- 142 A. Casado-Sánchez, R. Gómez-Ballesteros, F. Tato, F. J. Soriano, G. Pascual-Coca, S. Cabrera and J. Alemán, *Chem. Commun.*, 2016, **52**, 9137–9140.
- 143 C. J. Kong, D. Fisher, B. K. Desai, Y. Yang, S. Ahmad, K. Belecki and B. F. Gupton, *Bioorganic Med. Chem.*, 2017, **25**, 6203–6208.
- 144 D. Cambié, J. Dobbelaar, P. Riente, J. Vanderspikken, C. Shen, P. H. Seeberger, K. Gilmore, M. G. Debije and T. Noël, *Angew. Chemie - Int. Ed.*, 2019, **58**, 14374–14378.

## Chapter 2. Scalable and selective photooxidation of methionine with singlet oxygen in a continuous flow reactor

### 2.1. Introduction

Among the amino acid class of biogenic compounds, sulfur-bearing residues such as methionine (Met) or cysteine are the most susceptible to undergo redox reactions in proteins. Methionine is sensitive to several type of oxidants, resulting in the formation of methionine sulfoxide (MetO) which in turn can be reduced under the action of methionine sulfoxide reductases (Msr's).<sup>1</sup> Several studies showed that the amount of MetO can be related to the age of the protein<sup>2-4</sup> and that the activity of one Msr, the MsrA, could have a significant influence on the lifespan of the fruit fly *Drosophila*<sup>5</sup> or rats<sup>6</sup>. The effect of MetO on some age-related diseases, such as Alzheimer, has driven a lot of attention from the scientific community. The decline of MsrA activity in damaged brain cells result in an increased amount of MetO.<sup>3</sup> However, Lee *et al.* demonstrated that MetO could also help fighting Alzheimer's disease by preventing the aggregation of  $\beta$ -amyloid peptides.<sup>7</sup> Those peptides tend to form oligomers that are known to be involved in the loss of memory and cognitive abilities of the patient.<sup>8</sup> The authors used methylene blue as a photosensitizer to oxidize methionine residues in  $\beta$ -amyloid peptides and showed that the oxidized monomers would not form toxic aggregates. This application could open a possibility of a painless treatment for patients but the oxidation needs to be controlled as the sulfone behaves just as the sulfide and also results in aggregation.<sup>9</sup>

Outside of peptide science and neurodegenerative studies, Met oxidation into MetO is also required in material science<sup>10</sup> because of the influence of MetO on the hydrophobicity of a material and in organic chemistry for enantiopure synthesis<sup>11</sup> or as a cheap starting material for the synthesis of a high value added compound: vinylglycine, an unsaturated amino acid with antibacterial properties.<sup>12</sup>

In 2008, Carofiglio *et al.* described the photooxidation of methionine methyl ester in D<sub>2</sub>O in a flow reactor.<sup>13</sup> A functionalized fulleropyrrolidine-SiO<sub>2</sub> hybrid (Si-C<sub>60</sub>) was used as a heterocatalyst and allowed the conversion into the corresponding sulfoxide in 33 s. The impressively short residence time can be explained by the deuterated solvent which enhance the <sup>1</sup>O<sub>2</sub> lifetime. However, this procedure can only deliver 0.5 mmol per day of sulfoxide (Figure 53).

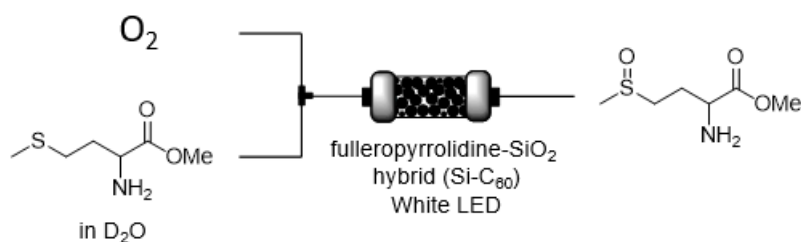


Figure 53 – Photocatalytic oxidation of methionine methyl ester in D<sub>2</sub>O with Si-C<sub>60</sub>.

In 2016, Casado-Sánchez *et al.* used a platinum complex to catalyze the photooxidation of methionine but only performed the oxidation of the latter in a batch reactor on a 0.3 mmol scale.<sup>14</sup>

Another metallic catalyst was studied by Vaquero *et al.* for the photooxidation of methionine.<sup>15</sup> The authors opted for metallic complexes as those catalysts are more resistant to photodegradation and can be easily tuned regarding of the reaction requirements and the irradiation source. Ir<sup>III</sup> complexes were synthesized and used as a photocatalyst for the oxidation of several sulfides involving methionine (Figure 54). The total reaction took 18 h to reach total and selective oxidation in d<sub>6</sub>-DMSO/D<sub>2</sub>O for a 10 mM methionine solution.

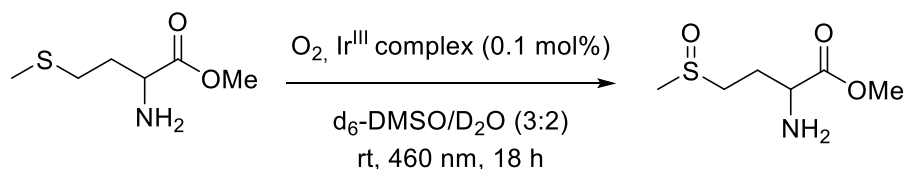
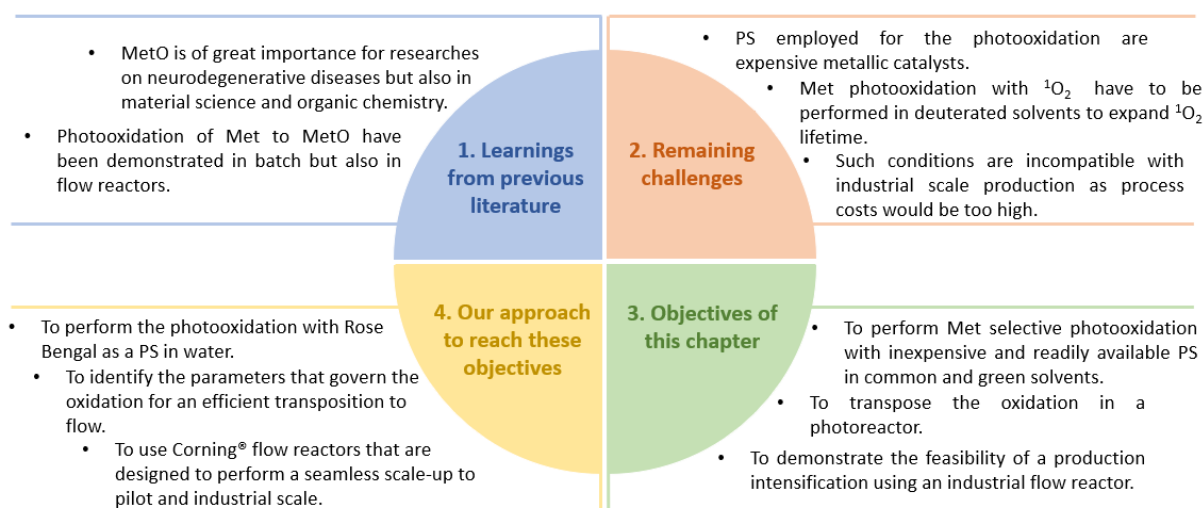


Figure 54 – Photooxidation of methionine methyl ester with an iridium catalyst.

The context and objectives of this chapter are summarized in the diagram below:



Although Met photooxidation to MetO with <sup>1</sup>O<sub>2</sub> have been reported in batch and in flow, the experimental conditions are not compatible with large production scale. Expensive metallic catalysts added to deuterated solvents prevent productions exceeding mmol scale. In this work, Met was oxidized in MetO using Rose Bengal as a photosensitizer for the *in-situ* production of <sup>1</sup>O<sub>2</sub> in water. Rose Bengal was selected for its well-known ability to generate <sup>1</sup>O<sub>2</sub>, its low toxicity and its affordable price. The replacement of deuterated solvents by regular solvents was enabled by the irradiation assets of flow photoreactors. The oxidation parameters were first optimized in a batch photoreactor before being transposed to a continuous flow setup consisting of a PFA tubing wrapped around a lamp. A scale-up of the reaction was then implemented in a commercial mesofluidic setup (Corning Lab Reactor) and could lead to a production of 6 T y<sup>-1</sup> in a G3 reactor.



### 2.1.1. References

- 1 E. R. Stadtman, H. Van Remmen, A. Richardson, N. B. Wehr and R. L. Levine, *Biochim. Biophys. Acta - Proteins Proteomics*, 2005, **1703**, 135–140.
- 2 I. Petropoulos, J. Mary, M. Perichon and B. Friguet, 2001, **825**, 819–825.
- 3 S. P. Gabbita, M. Y. Aksenov, M. A. Lovell and W. R. Markesbery, *J. Neurochem.*, 1999, **73**, 1660–1666.
- 4 L. R. Walker, A. B. Shiels, L. R. Walker and A. B. Shiels, *Landslide Ecol.*, 2013, **5**, 83–137.
- 5 H. Ruan, X. D. Tang, M. L. Chen, M. L. A. Joiner, G. Sun, N. Brot, H. Weissbach, S. H. Heinemann, L. Iverson, C. F. Wu and T. Hoshi, *Proc. Natl. Acad. Sci. U. S. A.*, 2002, **99**, 2748–2753.
- 6 E. R. Stadtman, J. Moskovitz, B. S. Berlett and R. L. Levine, *Mol. Cell. Biochem.*, 2002, **234–235**, 3–9.
- 7 B. Il Lee, Y. S. Suh, Y. J. Chung, K. Yu and C. B. Park, *Sci. Rep.*, 2017, **7**, 1–10.
- 8 I. Benilova, E. Karran and B. De Strooper, *Nat. Neurosci.*, 2012, **15**, 349–357.
- 9 P. Maiti, R. Piacentini, C. Ripoli, C. Grassi and G. Bitan, *Biochem. J.*, 2011, **433**, 323–332.
- 10 J. D. Seixas, M. F. A. Santos, A. Mukhopadhyay, A. C. Coelho, P. M. Reis, L. F. Veiros, A. R. Marques, N. Penacho, A. M. L. Gonçalves, M. J. Romão, G. J. L. Bernardes, T. Santos-Silva and C. C. Romão, *Dalt. Trans.*, 2015, **44**, 5058–5075.
- 11 S. G. Li, F. Portela-Cubillo and S. Z. Zard, *Org. Lett.*, 2016, **18**, 1888–1891.
- 12 N. Lamborelle, J. F. Simon, A. Luxen and J. C. M. Monbaliu, *Org. Biomol. Chem.*, 2015, **13**, 11602–11606.
- 13 T. Carofiglio, P. Donnola, M. Maggini, M. Rossetto and E. Rossi, *Adv. Synth. Catal.*, 2008, **350**, 2815–2822.
- 14 A. Casado-Sánchez, R. Gómez-Ballesteros, F. Tato, F. J. Soriano, G. Pascual-Coca, S. Cabrera and J. Alemán, *Chem. Commun.*, 2016, **52**, 9137–9140.
- 15 M. Vaquero, A. Ruiz-Riaguas, M. Martínez-Alonso, F. A. Jalón, B. R. Manzano, A. M. Rodríguez, G. García-Herbosa, A. Carbayo, B. García and G. Espino, *Chem. - A Eur. J.*, 2018, **24**, 10662–10671.

## 2.2. Transitioning from conventional batch to microfluidic processes for the efficient singlet oxygen photooxygenation of methionine

### 2.2.1. General information and authors contributions

This chapter is published:

Mendoza, C.; Emmanuel, N.; Páez, C. A.; Dreesen, L.; Monbaliu, J-C. M.; Heinrichs, B. Transitioning from conventional batch to microfluidic processes for the efficient singlet oxygen photooxygenation of methionine. *Journal of Photochemistry and Photobiology A: Chemistry*. 2018, 356, 193–200. 8 citations (08 December 2020)

C. M. designed the chemistry, performed the experiments, analyzed the results, calculated the kinetics and wrote the manuscript. N. E. designed the chemistry, performed the experiments, analyzed the results and wrote the manuscript. C. A. P. designed the chemistry, analyzed the results, calculated the kinetics. L. D. revised the manuscript and secured funding for the project. J.-C. M. M. designed the chemistry, analyzed the results, supervised the project, wrote and revised the manuscript and secured funding for the project. B. H. designed the chemistry, analyzed the results, calculated the kinetics, supervised the project, revised the manuscript and secured funding for the project.

The figures, tables and references numbering of the section 2.2.2 correspond to the numbering of the article as published online.

### 2.2.2. Templated copy of the article

The content of this section, including figures, is copyrighted (Elsevier B.V. 2017).

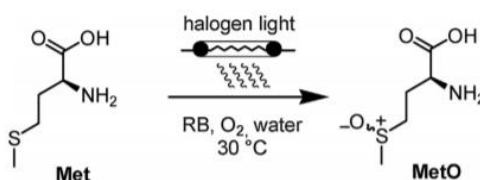
#### Introduction

Singlet oxygen ( $^1\text{O}_2$ ) has received considerable attention over the last decade in several areas: depollution [1–5], disinfection [6,7] and photodynamic applications such as blood sterilization, sunlight-activated herbicides and insecticides, as well as photodynamic cancer therapy (PDT) [8–11]. As a powerful oxidizer,  $^1\text{O}_2$  has also been extensively studied for the production of high-value added organic molecules [12–20]. There are various methodologies for the production of singlet oxygen, among which the most popular involves a photoinduced electronic energy transfer from an excited state of a catalytic photosensitizer (PS) to triplet oxygen ( $^3\text{O}_2$ ). Rose Bengal (RB) is a popular, non-toxic photosensitizer that has been widely utilized for the production of  $^1\text{O}_2$  upon visible light aerobic irradiation. The amino acids tyrosine, tryptophan, methionine, histidine and cysteine constitute one of the most relevant families among the photooxidizable biological substrates due to their areas of high electron density because of double bonds or sulfur moieties [21]. Of particular interest is the photooxidation of methionine (**Met**) to methionine sulfoxide (**MetO**) (Scheme 1). In general, sulfoxides are frequently used in organic synthesis, pharmaceutical science, biochemistry and material science [22,23]. However, the classical methods to oxidize sulfides to sulfoxides present a high risk of overoxidation to sulfones [24]. In particular, **MetO** is a particularly valuable synthetic intermediate [23,25,26] with applications ranging from peptide sciences [27– 29], material sciences [30,31], to organic synthesis [32,33]. In 1977, Sysak & Foote reported for the first time the reaction of **Met** via  $^1\text{O}_2$  to yield **MetO** [34,35]. In 1981, Wilkinson and Brummer reported the equations to determinate the

rate constants of this reaction [36] as a function of solvent, pH, dye and substrate oxidized where  $^1\text{O}_2$  was included (Eq. (1)).

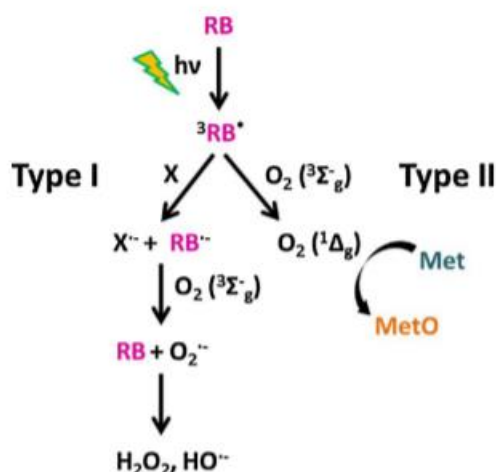
$$-\frac{d[\text{Met}]}{dt} = -\frac{d[\text{O}_2]}{dt} = \frac{d[\text{MetO}]}{dt} = k_t^A [^1\text{O}_2][\text{Met}] \quad (1)$$

In this work, we describe the process by calculating a pseudo first-order kinetic model where some parameters like  $\text{O}_2$  concentration, quantum yield of Rose Bengal, non-radiative decay rate constant of  $^1\text{O}_2$  or quenching are included in the apparent kinetic constant to facilitate the transitioning to microfluidic systems. The oxidation of **Met** can occur via two distinct mechanisms that essentially depend on the oxidant. Radicals such as  $\text{HO}^\bullet$  and metal ions such as  $\text{Fe}^{\text{III}}$  and  $\text{Cu}^{\text{II}}$  oxidize **Met** through a one-electron oxidation (Type I). This oxidation yields highly unstable sulfide radical cations that produce posttranslational protein modifications [37–39]. Oxidants such as  $\text{HOCl}$ ,  $\text{O}_2^-$ ,  $\text{H}_2\text{O}_2$ , and  $^1\text{O}_2$ , in contrast, directly oxidize **Met** to **MetO** through a formal oxygen transfer via a two-electron oxidation (Type II) (Scheme 2) [37,38].



**Scheme 1.** Aerobic photocatalytic oxidation of **Met** to **MetO**.

$\text{HOCl}$  as an oxidant presents an important risk of overoxidation to methionine sulfone **MetO<sub>2</sub>** that needs to be avoided during the photooxygenation process. This highlights  $^1\text{O}_2$  as a good candidate to oxidize **Met**: despite its high reactivity, it has a short life time in solution. Accurately managing the light source and the irradiation time are thus efficient ways to control its oxidative power, and ensure chemoselective reactions. Initially, the reaction of  $^1\text{O}_2$  with a sulfide generates a persulfoxide intermediate. The chemistry of the persulfoxide is highly dependent on the nature of the sulfide and the solvent. In water, a rapid hydration of the persulfoxide is most likely, where the product hydroperoxysulfurane will either oxidize a second sulfide or eliminate hydrogen peroxide. The reaction of  $^1\text{O}_2$  with free **Met** yields azasulfonium salts, which subsequently hydrolyze to **MetO**. Interestingly, this mechanism does not operate with the dipeptide **Met–Met**, which undergoes a clean oxidation to the disulfoxide, **MetO–MetO** [37]. Photochemical reactions utterly depend on the penetration of light in the reaction medium, which is superficial in macroscopic reactors, thus leading to low efficiency. Such an inherent limitation is nowadays overcome by utilizing microreactor technology, and many examples illustrating the assets of continuous-flow photochemistry have been published, including an improved light penetration, an accurate control of the irradiation time, and seamless scalability [12]. Different studies of catalytic photosensitized oxygenation were carried out either in batch [13,40], or in microfluidic devices [13,41]. In 2002, the photooxidation of  $\alpha$ -terpinene by RB-sensitized to obtain ascaridole and *p*-cymene as byproduct was studied using a glass microchip device with etched channels [42,43]. In 2013, a similar reaction was reported using a microphotoreactor reaching greater results compared to a batch reactor [44]. In 2014, pinocaryone was synthesized from a TPP-sensitized microflow photooxidation of  $\alpha$ -terpinene [14]. Ziegenbald described a microreactor that was fabricated to synthesize ascaridole from RB-sensitized microflow photooxidation of  $\alpha$ -terpinene [45]. More recently, Alemán et al. reported a microfluidic procedure utilizing Pt(II) coordination complexes for the visible light photooxidation of various sulfides [13]. To date, only one report described the catalytic photooxidation of **Met** methyl ester in  $\text{D}_2\text{O}$  using a microfluidic setup in the presence of supported [60] fullerene PS [41]. We recently reported a continuous-flow process for the large scale photocatalytic oxidation of unprotected **Met** [20].



**Scheme 2.** Overview of the two types of photosensitization processes in combination with **Met** photooxygenation.

In this paper, we report on the optimization of various reaction parameters for selectively producing **MetO** from **Met** through RB sensitization. The intrinsic reaction kinetics were studied as a function of the RB concentration, the light intensity and the O<sub>2</sub> flow. Apparent first-order kinetic constants, initial rates and spacetime yields were calculated obtaining the best results with a low loading of RB (0.45 mM) as photocatalyst, a high light intensity (5360 W m<sup>-2</sup>) and 15 mL min<sup>-1</sup> of pure O<sub>2</sub>, at room temperature. Next, optimized reaction parameters were transposed to a microfluidic reactor for the photocatalytic oxidation of **Met** under continuous-conditions.

## Experimental

### General

The photooxygenation rates for the <sup>1</sup>O<sub>2</sub>-oxidation of **Met** toward **MetO** were determined in macroscopic batch and microfluidic systems. All experiments were carried out in thermostated reactor setups at 30 °C with 15 mL min<sup>-1</sup> of pure O<sub>2</sub> (Alphagaz™ 1 grade) excluding the section about the influence of the O<sub>2</sub> source where air and O<sub>2</sub> (Alphagaz™ 1 grade) were used. The light source was a linear halogen Osram R7S Haloline (230 W, 114.2 mm). The emission spectrum of the halogen lamp was measured with a Mini-Spectrometer (Hamamatsu Photonics), apparatus previously described by Pàez et al. [46]. The RB spectra were obtained by UV-vis on a Genesys 10S UV-vis (Thermo Scientific) in order to calculate the %T as a function of the distance through the Bouguer-Lambert-Beer law. The evolution in the concentration of **Met** and **MetO** was measured by <sup>1</sup>H NMR with a Bruker Avance III 400 MHz in D<sub>2</sub>O by monitoring the appearance and disappearance of characteristic signals (Fig. S.1).

### Chemicals

Chemicals were obtained from commercial sources, and used without further purification: (L)-Methionine (CAS 63-68-3, >99.0%, TCI) and Rose Bengal (CAS 632-69-9, TCI).

### Batch system

The photooxygenation was carried out in a batch reactor setup (1 L) with a radial light path of 8 cm, equipped with a quartz double-walled immersion well (Fig. 1a) connected to a Lauda Proline RP 845 thermostat. The O<sub>2</sub> source was bubbled through a glass frit in a 0.1 M aqueous solution of (L)-methionine (700 mL) containing RB. The effect of RB concentration on the photooxygenation of **Met** was studied using 0, 0.006, 0.029, 0.044, 0.073, 0.147, 0.293 and 0.586 mM of RB. The halogen lamp

was used at different percentage of voltage, 0, 25, 50, 75 and 100%, corresponding to 0, 320, 1590, 3460 and 5360 W m<sup>-2</sup>, respectively. Finally, the source of O<sub>2</sub> as well as the gas flow was studied with air and pure O<sub>2</sub> at 5, 10 and 15 mL min<sup>-1</sup> at atmospheric pressure. The RB concentration, irradiance and O<sub>2</sub> flow were fixed at 0.45 mM, 5360 W m<sup>-2</sup> and 15 mL min<sup>-1</sup>, respectively, for the microreactor section.

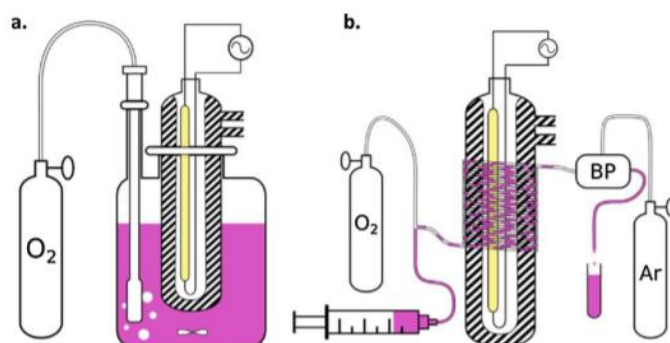


**Fig. 1.** (a) Macroscopic batch setup. (b) Microfluidic setup for the photocatalytic oxidation of methionine

### Microreactor system

The continuous-flow photomicroreactor was constructed from high purity PFA capillaries (800mm internal diameter) wrapped in coils around the photochemical quartz double-walled immersion well (Fig. 1b) connected to a Lauda Proline RP 845 thermostat. The light source was the same halogen lamp as for the batch reactor experiments. Air and the liquid feed solution were injection through a static mixer (T-Mixer, IDEX-Upchurch, natural PEEK 1/4- 28 thread for 1/16" o.d. tubing, 0.02" through hole) placed upstream the irradiation coil. Chemyx Nexus 6000 syringe pumps were used to handle the 0.1 M aqueous solution of (L)-methionine containing RB (loaded into a 20 mL plastic Luer Lock syringe). The syringe pump was set at 0.5 mL min<sup>-1</sup>. O<sub>2</sub> was delivered with a Bronkhorst F210CTM mass flow controller. A Zaiput Flow Technologies dome-type back-pressure regulator (BPR) was inserted downstream and connected to a cylinder of compressed Argon (set point: 7 bar). The residence (irradiation) time in the microfluidic reactor was modified with the length using PFA tubes of 10, 20, 40, 60 and 200 cm.

## Results and discussion

### Effect of RB concentration

The concentration in photocatalyst (RB) has also an important effect in the transmission of the light, with a drastic decrease when using concentrations up to 0.45 mM due to the high absorbance and the decrease in the light penetration (Fig. S.2). Thus, reducing the internal size of the reaction vessel might indeed be highly beneficial for such photocatalytic process. Initially, the reaction order with respect to the substrate (**Met**) needs to be validated. Two assumptions, including the pseudo first-order reaction and the pseudo second-order reaction were made using the integration method for the lowest RB concentration (0.06 mM) obtaining a better correlation coefficient with the first-order assumption (Fig. S.3). Pseudo first-order reaction rates of **Met** photooxygenation were evaluated at 30 °C as a function of the RB concentration in the batch setup described in Fig. 1a, with RB concentrations ranging from 0.060 to 0.586 mM. pH values between 4.4 and 5.1 were recorded for every solution. The control tests confirmed that **Met** is not oxidized in the absence of light or in the absence of RB. The variation of **Met** concentration ( $[\text{Met}]/[\text{Met}]_0$ ) as a function of time was calculated following the pseudo first-order kinetic law (Eq. (2)).

$$r = k_{app} \cdot [Met] \left( = -\frac{d[Met]}{dt} \right) \quad (2)$$

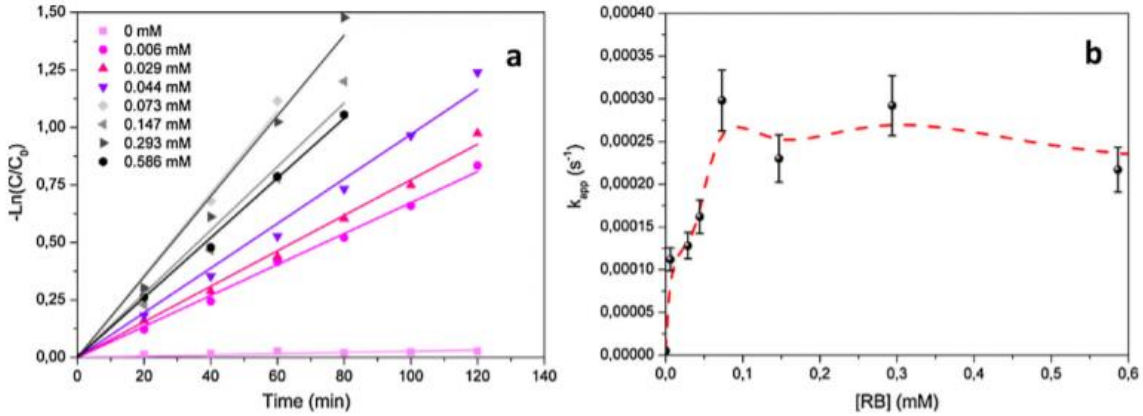


**Fig. 2.** (a) Pseudo first-order relationship  $-\ln([Met]/[Met]_0) = k_{app}t$  as a function of RB concentration. (b)  $k_{app}$  as function of RB concentration ( $[Met]_0 = 0.1$  M, irradiance =  $5360$  W m<sup>-2</sup>, O<sub>2</sub> flow =  $15$  mL min<sup>-1</sup> and T =  $30$  °C).

After integration, Eq. (3) is obtained:

$$-\ln \frac{[Met]}{[Met]_0} = k_{app} \cdot t \quad (3)$$

Where  $r$  is the reaction rate (mol L<sup>-1</sup> s<sup>-1</sup>),  $k_{app}$  is the apparent first order constant and  $t$  the reaction time (s). In all cases, a linear correlation was obtained by fitting the curves with a slope of  $k_{app}$ . For each experiment, the initial rate of photooxygenation of **Met**,  $r_0$ , was calculated by multiplying the obtained  $k_{app}$  by the initial **Met** concentration ( $[Met]_0$ ) (Eq. (4)).

$$r_0 = k_{app} \cdot [Met]_0 \quad (4)$$

Additionally, the space-time yield (STY), that refers to amount of **MetO** produced (mmol) during the illumination ( $n$ ) (Eq. (5));  $V_R$  is the reactor volume and  $t$  is the time) was also determined for both reactor configurations. In batch reactor, the time used was the reaction time necessary to obtain complete conversion ( $t$ ), while in microreactor was the residence time ( $t_R$ ).

$$STY (mmol \cdot L^{-1} \cdot min^{-1}) = \frac{n}{V_R \cdot t} \quad (5)$$

All these parameters of conversion of **Met** into **MetO** were calculated in order to obtain the optimum concentration of RB in the system. As shown in Fig. 2a, a linear fit was plotted for each experiment to obtain the  $k_{app}$  from the slope with acceptable  $r^2$  values (Table S.1). Fig. 2b includes the evolution of  $k_{app}$  with increasing RB concentrations. No significant conversion was observed without photosensitizer. As expected, kinetic rates of the process were improved with a larger amount of RB. For low RB concentrations (ranging from 0 to 0.073 mM),  $k_{app}$  values presented a linear growth due to the Lambert-Beer law. Then, the kinetic rates plateaued at 0.073 mM, and stayed constant for higher RB concentrations. Concentrations higher than 0.6 mM would likely decrease the efficiency of the system because of the decrease of the light penetration. Based upon this loss of efficiency at the highest RB concentration and in order to assure that we were working in good conditions avoiding the region of linear growth where the variation of kinetics is very sensitive, the value chosen as optimum for **Met** photooxygenation was  $[RB] = 0.45$  mM. This value will be utilized in the following experiments. Results of the kinetic parameters as a function of RB concentration are collected in Table 1.

**Table 1**  
Kinetic parameters of the photooxygenation of **Met** in batch for different RB concentrations.

[RB] (mM)	$k_{app}$ ( $\times 10^3$ s $^{-1}$ )	$r_0$ ( $\times 10^3$ mol L $^{-1}$ s $^{-1}$ )	STY $\times 10^{-5}$ (mol MetO L $^{-1}$ min $^{-1}$ )
0	0	0	0
0.06	11.2	1.1	45.2
0.029	12.8	1.3	49.7
0.044	16.2	1.6	56.8
0.073	29.8	2.9	95.9
0.147	23.0	2.3	76.7
0.293	29.2	2.9	77.6
0.586	21.7	2.2	69.7

### Effect of the light intensity

The light source plays an important role in this kind of processes, modifying the effectiveness of the process with the type of lamp, the distance between the light source and the PS, the emission spectrum and the intensity of the light. During all the experiments, the center of the batch reactor was located at 4 cm from the lamp and the furthest point of the reactor was located at 8 cm. The irradiance decreases drastically with the distance even without RB or liquid inside the batch reactor (Fig. S.4). 5 different voltages were applied to show the effect on **Met** conversion corresponding to irradiances of 0, 320, 1590, 3460 and 5360 W m $^{-2}$  at the center of the batch reactor (4 cm). As shown in Fig. 3a, the conversion of **Met** is faster with higher irradiances: conversions of 0, 4, 44, 78 and >99% were obtained at 120 min for 0, 320, 1590, 3460 and 5360 W m $^{-2}$ , respectively. In a batch setup, the photooxygenation of **Met** required 120 min to reach completion with the highest irradiance.  $k_{app}$  values and initial rates were calculated from the slope of the pseudo first order equation (Fig. 3b) with [RB] = 0.45 mM. Table 2 collects the kinetic parameters as a function of the irradiance.

### Effect of the O<sub>2</sub> flow

Mass transfer phenomena are related with the photooxygenation rate of **Met** into **MetO** and the concentration of O<sub>2</sub> is a key parameter in the production of <sup>1</sup>O<sub>2</sub>. The source of O<sub>2</sub> as well as the gas flow was studied with air and pure O<sub>2</sub> at 5, 10 and 15 mL min $^{-1}$  (1 bar) and pseudo first-order kinetics calculated (Fig. 4). The concentration of O<sub>2</sub> is crucial in photooxygenation processes providing a higher conversion of **Met** using pure O<sub>2</sub>. Conversions obtained with air as O<sub>2</sub> source are coherent with the content of O<sub>2</sub>. 15 mL min $^{-1}$  of pure O<sub>2</sub> was found as an optimized gas flow for the photooxygenation of **Met**. Table 3 shows the kinetic parameters  $k_{app}$ ,  $r_0$  and STY as a function of the O<sub>2</sub> source and gas flow.

### PFA microfluidic reactor

Mass transfer of O<sub>2</sub> is a key parameter in photooxygenation processes and its limitation can be described with the Hatta number, which allows evaluating the extent of mass transfer limitations. The mass transfer rate of oxygen from the gas phase to the liquid phase is low in batch reactors due to its low surface-to-volume ratio. On the other hand, there are no mass transfer limitations when conducting this kind of reactions in a capillary microreactor [48]. This means that the reaction process occurs inside the bulk phase due to the fast supply of the oxidant from the gas to the liquid phase using segmented flow and high pressure ( $Ha < 0.3$ ). Noël et al. reported that the value of  $Ha$  could be even as low as 0.06 in the fast photo-catalytic aerobic oxidation of thiols using a capillary microreactor and a Taylor flow regime. The low values of  $Ha$  demonstrate the advantages of using microreactors for the measurement of intrinsic reaction kinetics as one can avoid mass transfer limitations [49]. The microcapillary reactor allows a better determination of intrinsic kinetics of the methionine photooxygenation because gas/liquid mass transfer limitation can be excluded and the gas/liquid absorption equilibrium can be assumed to be achieved at any stage of the reaction. The residence time in a microphotoreactor corresponds to the irradiation time, and is thus an important parameter during the transition from macroscopic batch to microreactor technology. The individual flow rates of liquid and O<sub>2</sub> feeds were fixed at 0.5 mL min $^{-1}$  and 15 mL min $^{-1}$  respectively, in order to calculate the kinetic

parameters; the space time was varied by altering the length of the PFA capillary assuming the increasing irradiated area. 10, 20, 40, 60 and 200 cm were employed to calculate the photooxygenation rate. The linear fit in this case presented an apparent first-order constant,  $k_{app}$ , of 305.2 ( $\times 10^5 \text{ s}^{-1}$ ) and an initial rate of photooxygenation,  $r_0$ , of 29.3 ( $\times 10^5 \text{ mol L}^{-1} \text{ s}^{-1}$ ).

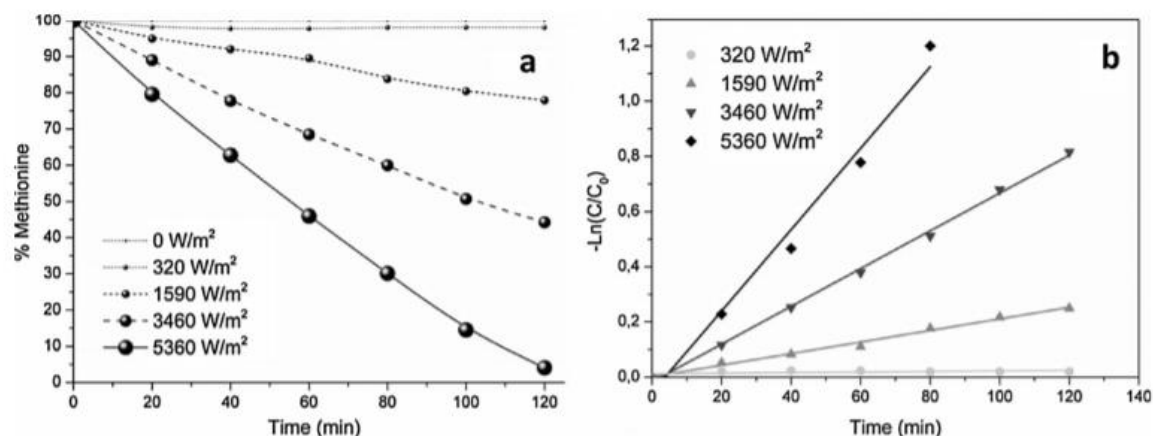


**Fig. 3.** (a) Residual **Met** (%) upon photooxygenation over 0–120 min. (b) Pseudo first-order relationship  $-\ln([Met]/[Met]_0) = k_{app}t$  as a function of irradiance (0, 320, 1590, 3460 and 5360  $\text{W m}^{-2}$ ).

**Table 2**  
Kinetic parameters of the photooxygenation of **Met** for different irradiances.

Irradiance ( $\text{W m}^{-2}$ )	$k_{app}$ ( $\times 10^5 \text{ s}^{-1}$ )	$r_0$ ( $\times 10^5 \text{ mol L}^{-1} \text{ s}^{-1}$ )	STY $\times 10^{-5}$ ( $\text{mol MetO L}^{-1} \text{ min}^{-1}$ )
0	0	0	0
320	0.2	0.01	1.6
1590	3.5	0.3	17.6
3460	11.4	1.1	44.5
5360	24.6	2.4	76.6

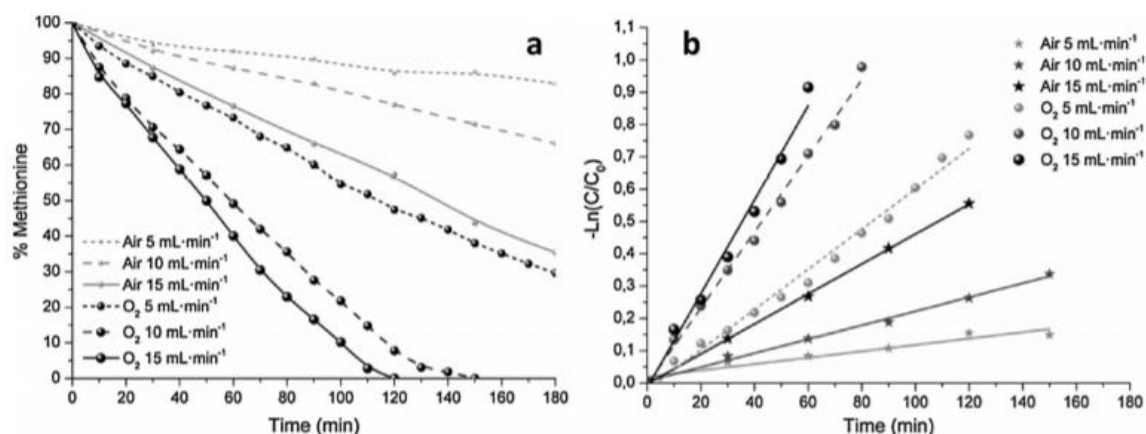


**Fig. 4.** (a) Residual **Met** (%) upon photooxidation over 0–180 min and (b) Pseudo first-order relationship  $-\ln([Met]/[Met]_0) = k_{app}t$  as a function of  $\text{O}_2$  flow.

**Table 3**  
Kinetic parameters of the photooxygenation of **Met** for different irradiances.

Source of $\text{O}_2$	$\text{O}_2$ ( $\text{mL min}^{-1}$ )	$k_{app}$ ( $\times 10^5 \text{ s}^{-1}$ )	$r_0$ ( $\times 10^5 \text{ mol L}^{-1} \text{ s}^{-1}$ )	STY $\times 10^{-5}$ ( $\text{mol MetO L}^{-1} \text{ min}^{-1}$ )
Air	1	1.6	0.2	9.1
	2	3.6	0.4	18.2
	3	7.7	0.7	34.3
$\text{O}_2$	5	10.4	0.9	38.1
	10	19.6	1.9	63.7
	15	24.6	2.4	76.6



Macroscopic batch and microfluidic reactors provided complete conversions of **Met** into **MetO** at different times, 120 min of reaction time ( $t$ ) and 5 min of space time ( $t_R$ ) for batch and microreactor, respectively. Pseudo first-order relationship  $-\ln(C/C_0) = k_{app} t$  of both systems is plotted in Fig. 5.

As shown in Fig. 5,  $-\ln([Met]/[Met]_0)$  increases with the residence time for both configurations. The slope ( $k_{app}$ ) calculated by linear fit of the data was 24.6 and 305.2 ( $\times 10^5 \text{ s}^{-1}$ ) for batch and microreactor conditions, respectively. The initial photooxygenation rates were obtained multiplying these constants by the initial **Met** concentration  $[Met]_0$ . The kinetic values for the catalytic photooxygenation of **Met** under continuous-flow microreactor are remarkable, since apparent first-order constants and reaction rates are about 10-fold faster than under batch conditions due to the absence of mass transfer limitations. Fig. 6 summarizes the obtained results with batch and microreactor setups in terms of STY.

In the case of STY, the difference between both systems is lower, but stays worthy of consideration with a STY 3.12 times higher, similar to the improvement obtained for the synthesis of pinocaryone from a TPP-sensitized microflow photooxygenation of  $\alpha$ -terpinene [14].

The incident photon flux density was evaluated as a function of reactor geometry and specifications. Table 4 summarizes the photochemical process parameters utilized for the photooxygenation of methionine under batch and microreactor conditions, as well as the kinetics obtained for each technology. As summarized in Table 4, the calculated photon flux density was  $0.0247 \text{ einstein m}^{-3} \text{ s}^{-1}$  for the batch reactor and  $17.3 \text{ einstein m}^{-3} \text{ s}^{-1}$  for the microreactor setup. Similar figures were reported by Loubière et al. while comparing batch ( $0.033 \text{ einstein m}^{-3} \text{ s}^{-1}$ ) and microreactor ( $5.02 \text{ einstein m}^{-3} \text{ s}^{-1}$ ) setups for an intramolecular [2 + 2] photocycloaddition. [50] The higher incident photon flux density in microreactors accounts for the substantial acceleration of photochemical reactions compared to batch setups. The photon flux strongly affects the intrinsic reaction rate of photochemical processes: the higher the photon flux, the faster the reaction will be completed. Besides, the accurate control of the irradiation time in microreactors avoids overexposure, and hence, side reactions. It has also been reported that the photonic efficiency ( $j$ ) is about one order of magnitude higher in microreactors (typ.  $j = 0.0262$ ) than in batch reactors (typ.  $j = 0.0086 - 0.0042$ ) [51]. For instance, Meyer et al. reported that the photonic efficiency was doubled while transitioning from a batch setup to a microreactor setup for the photosensitized oxidation of citronellol [52]. Besides, the space-time yield (STY) was about one order of magnitude higher for the microreactor, similar to the improvement obtained in this work.

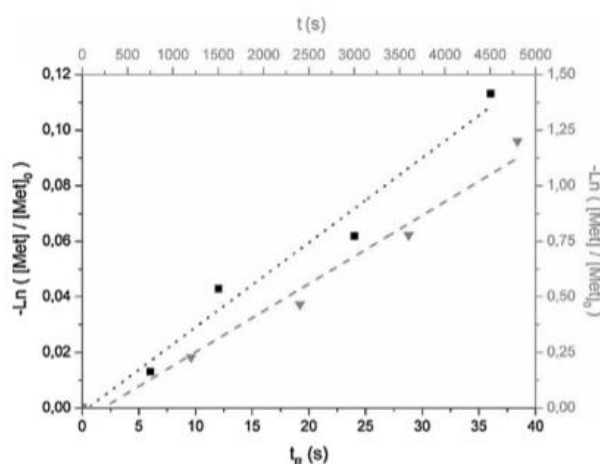


**Fig. 5.** Pseudo first-order relationship  $-\ln([Met]/[Met]_0) = k_{app}t$  for batch using the reaction time ( $t$ ) (black squares and dotted line) and microreactor using the residence time ( $t_R$ ) (gray triangles and dashed line).

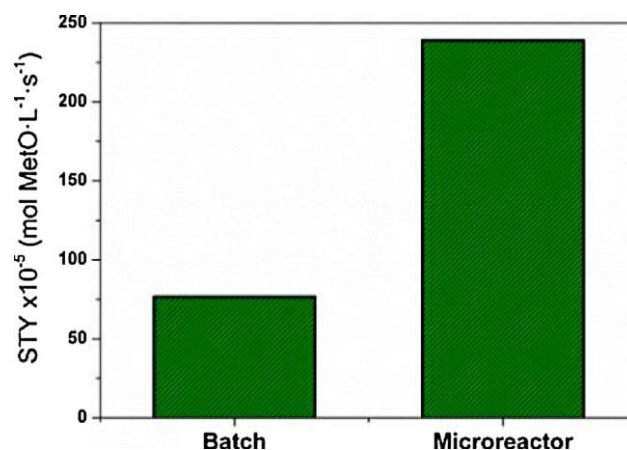


**Fig. 6.** Comparison between the batch reactor and microreactor in terms of STY.

**Table 4**

Photochemical process parameters and kinetics obtained in batch and microreactor.

Parameters	Batch	Microreactor
Depth of light penetration (cm)	8	0.08
Irradiated area (cm <sup>2</sup> )	63	40
Irradiated volume (cm <sup>3</sup> )	700	1
Irradiated area/volume ratio (cm <sup>2</sup> cm <sup>-3</sup> )	0.09	40
Photon flux density (einstein m <sup>-3</sup> s <sup>-1</sup> )	0.0247	17.3
k <sub>app</sub> (10 <sup>5</sup> s <sup>-1</sup> )	24.6	305.2
r <sub>0</sub> (10 <sup>5</sup> mol L <sup>-1</sup> s <sup>-1</sup> )	2.4	29.3
STY (10 <sup>5</sup> mol MetO L s <sup>-1</sup> )	76.6	239

The importance of the light source and reactor geometry optimization was shown by Lapkin et al. [14]. However, there are still some limitations associated with the use of <sup>1</sup>O<sub>2</sub>. The lifetime of <sup>1</sup>O<sub>2</sub> is highly solvent dependent and a large light exposition can lead to the formation of undesired by-products or the degradation of the photosensitizer. These limitations can be overcome by the implementation of microreactor technology [47]. The light penetration (%T) as well as the higher O<sub>2</sub> transfer are pivotal assets of microfluidic reactors as illustrated with the much faster conversion of **Met**. These results show an important enhancement of the STY and emphasize the wide variety of possibilities that microreactor technology offers for these photosensitized processes. Additionally, the immobilization of the PS, the modification of the wavelength or the use of tube-in-tube systems could lead to enhanced photocatalytic oxygenations

## Conclusion

This work reports the technological transition of the catalytic photooxygenation of methionine from macroscopic batch to microreactor. RB concentration, light intensity and O<sub>2</sub> flow have been evaluated in batch reactor showing that the light penetration as well as mass transfer limitations play important roles in this photosensitized process as limiting parameters with an important impact on the production of methionine sulfoxide via <sup>1</sup>O<sub>2</sub>. Pseudo first-order kinetics and space-time yields have been also calculated in both technologies obtaining an enhancement of 12 and 3-fold for r<sub>0</sub> and STY, respectively when using continuous-flow microreactor. Further works are in progress in order to avoid some issues like the RB photodegradation and its immobilization in solid supports.

## References

- [1] M.L. Marin, L. Santos-Juanes, A. Arques, A.M. Amat, M.A. Miranda, Organic photocatalysts for the oxidation of pollutants and model compounds, *Chem. Rev.* 112 (2012) 1710–1750.
- [2] D. Gryglik, J.S. Miller, S. Ledakowicz, Singlet molecular oxygen application for 2-chlorophenol removal, *J. Hazard. Mater.* 146 (2007) 502–507.
- [3] E. Pepe, O. Abbas, C. Rebufa, M. Simon, S. Lacombe, M. Julliard, Supported photosensitizers for the visible light activation of phenols towards oxygen, *J. Photochem. Photobiol. A* 170 (2005) 143–149.
- [4] R. Gerdes, D. Whrle, W. Spiller, G. Schneider, G. Schnurpfeil, G. Schulz-ekloff, Aqueous solutions by different photosensitizers, *J. Photochem. Photobiol. A* 111 (1997) 65–74.
- [5] K. Ozoemena, N. Kuznetsova, T. Nyokong, Comparative photosensitized transformation of polychlorophenols with different sulphonated metallophthalocyanine complexes in aqueous medium, *J. Mol. Catal. A-Chem.* 176 (2001) 29–40.
- [6] A.K. Benabbou, C. Guillard, S. Pigeot-rémy, C. Cantau, T. Pigot, P. Lejeune, Water disinfection using photosensitizers supported on silica, *J. Photochem. Photobiol. A* 219 (2011) 101–108.
- [7] M. Wainwright, P. Pr, Photodynamic antimicrobial chemotherapy (PACT), *J. Antimicrob. Chemother.* 42 (1998) 13–28.
- [8] A.A. Ghogare, A. Greer, Using singlet oxygen to synthesize natural products and drugs, *Chem. Rev.* 116 (2016) 9994–10034.
- [9] Y. Shen, A.J. Shuhendler, D. Ye, J.-J. Xu, H.-Y. Chen, Two-photon excitation nanoparticles for photodynamic therapy, *Chem. Soc. Rev.* 45 (2016) 6725–6741.
- [10] S. Nonell, C. Flores, Singlet oxygen: applications in biosciences and nanosciences, *R. Soc. Chem.* 1 (2016).
- [11] M.C. DeRosa, R.J. Crutchley, Photosensitized singlet oxygen and its applications, *Coord. Chem. Rev.* 233–234 (2002) 351–371.
- [12] D. Cambie, C. Bottecchia, N.J.W. Straathof, V. Hessel, T. Noel, Applications of continuous-flow photochemistry in organic synthesis material science, and water treatment, *Chem. Rev.* 116 (2016) 10276–10341.
- [13] A. Casado-Sánchez, R. Gómez-Ballesteros, F. Tato, F.J. Soriano, G. Pascual-Coca, S. Cabrera, J. Alemán, Pt(ii) coordination complexes as visible light photocatalysts for the oxidation of sulfides using batch and flow processes, *Chem. Commun.* 52 (2016) 9137–9140.
- [14] K.N. LoPONOV, J. Lopes, M. Barlog, E.V. Astrova, A.V. Malkov, A.A. Lapkin, Optimization of a scalable photochemical reactor for reactions with singlet oxygen, *Org. Process Res. Dev.* 18 (2014) 1443–1454.
- [15] F. Lévesque, P.H. Seeberger, Highly efficient continuous flow reactions using singlet oxygen as a green reagent, *Org. Lett.* 13 (2011) 5008–5011.
- [16] S. Criado, S.G. Bertolotti, N.A. García, Kinetic aspects of the rose bengalsensitized photo-oxygenation of tryptophan alkyl esters. Ground state and photopromoted dye-tryptophan derivative interactions, *J. Photochem. Photobiol. B* 34 (1996) 79–86.

- [17] V. Rizzi, I. Losito, A. Ventrella, P. Fini, A. Fraix, S. Sortino, A. Agostiano, F. Longobardi, P. Cosma, Rose Bengal-photosensitized oxidation of 4- thiothymidine in aqueous medium: evidence for the reaction of the nucleoside with singlet state oxygen, *Phys. Chem. Chem. Phys.* 17 (2015) 26307–26319.
- [18] T.S.A. Heugebaert, C.V. Stevens, C.O. Kappe, Singlet-oxygen oxidation of 5- hydroxymethylfurfural in continuous flow, *ChemSusChem* 8 (2015) 1648– 1651.
- [19] D. Kalaitzakis, M. Triantafyllakis, M. Sofiadis, D. Noutsias, G. Vassilikogiannakis, Photooxygenation of furylalkylamines: easy access to pyrrolizidine and indolizidine scaffolds, *Angew. Chem. Int. Edit.* 55 (2016) 4605–4609.
- [20] N. Emmanuel, C. Mendoza, M. Winter, C. Horn, A. Vizza, L. Dreesen, B. Heinrichs, J.-C.M. Monbaliu, Scalable photocatalytic oxidation of methionine under continuous-flow conditions, *Org. Process Res. Dev.* 21 (2017) 1435– 1438.
- [21] S. Criado, S.G. Bertolotti, N.A. García, Kinetic aspects of the rose bengalsensitized photo-oxygenation of tryptophan alkyl esters. Ground state and photopromoted dye-tryptophan derivative interactions, *J. Photochem. Photobiol. B* 34 (1996) 79–86.
- [22] S. Matsuoka, Y. Mizoguchi, H. Itoh, K. Okura, N. Shinohara, M. Inoue, The effect of sulfur stereochemistry of L-b,b-dimethylmethionine S-oxide on the physicochemical properties of truncated polytheonamides, *Tetrahedron. Lett.* 51 (2010) 4644–4647.
- [23] S. Yamada, K. Ikkyu, K. Iso, M. Goto, T. Endo, Facile synthesis of polymethionine oxides through polycondensation of activated urethane derivative of  $\alpha$ -amino acid and their application to antifouling polymer against proteins and cells, *Polym. Chem.* 6 (2015) 1838–1845.
- [24] F. Lazzaro, M. Crucianelli, F. De Angelis, V. Neri, R. Saladino, A novel oxidative side-chain transformation of  $\alpha$ -amino acids and peptides by methyltrioxorhenium/H<sub>2</sub>O<sub>2</sub> system, *Tetrahedron Lett.* 45 (2004) 9237–9240.
- [25] S. Ng, E. Lin, P.I. Kitov, K.F. Tjhung, O.O. Gerlits, L. Deng, B. Kasper, A. Sood, B.M. Paschal, P. Zhang, C.C. Ling, J.S. Klassen, C.J. Noren, L.K. Mahal, R.J. Woods, L. Coates, R. Derda, Genetically encoded fragment-based discovery of glycopeptide ligands for carbohydrate-binding proteins, *J. Am. Chem. Soc.* 137 (2015) 5248–5251.
- [26] M. Hellwig, K. Löbmann, T. Orywol, A. Voigt, Model studies on the oxidation of benzoyl methionine in a carbohydrate degradation system, *J. Agric. Food Chem.* 62 (2014) 4425–4433.
- [27] M. Kukowska, M. Kukowska-Kaszuba, K. Dzierzbicka, A study on the protection of methionine and the reduction of methionine sulfoxide in methioninecontaining analogues of the growth-modeling factor Gly-His-Lys, *Tetrahedron Lett.* 56 (2015) 525–528.
- [28] P.W.R. Harris, R. Kowalczyk, S.H. Yang, G.M. Williams, M.A. Brimble, An important side reaction using the thiol 3,6-dioxa-1,8-octanedithiol (DODT), in 9-fluorenylmethoxycarbonyl-based solid phase peptide synthesis, *J. Pept. Sci.* 20 (2014) 186–190.
- [29] Y. Zhang, T. Li, X. Li, Synthesis of human growth hormone-releasing hormone via three-fragment serine/threonine ligation (STL), *Org. Biomol. Chem.* 11 (2013) 5584.
- [30] S.M.M. Reddy, P. Dorishetty, A.P. Deshpande, G. Shanmugam, Hydrogelation induced by change in hydrophobicity of amino acid side chain in fmocfunctionalised amino acid: significance of sulfur on hydrogelation, *ChemPhysChem* 17 (2016) 2170–2180.

- [31] J.D. Seixas, M.F.A. Santos, A. Mukhopadhyay, A.C. Coelho, P.M. Reis, L.F. Veiros, A.R. Marques, N. Penacho, A.M.L. Gonçalves, M.J. Romão, G.J.L. Bernardes, T. Santos-Silva, C.C. Romão, A contribution to the rational design of Ru(CO)<sub>3</sub>Cl<sub>2</sub>L complexes for in vivo delivery of CO, *Dalton Trans.* 44 (2015) 5058–5075.
- [32] S.G. Li, F. Portela-Cubillo, S.Z. Zard, A Convergent synthesis of enantiopure open-chain, cyclic, and fluorinated amino acids, *Org. Lett.* 18 (2016) 1888–1891.
- [33] N. Lamborelle, J.F. Simon, A. Luxen, J.-C. Monbaliu, Continuous-flow thermolysis for the preparation of vinylglycine derivatives, *Org. Biomol. Chem.* 13 (2015) 303.
- [34] P.K. Sysak, C.S. Foote, T.-Y. Ching, Chemistry of singlet oxygen—XXV. Photooxygenation of methionine, *J. Photochem. Photobiol.* 26 (1977) 19–27.
- [35] M.J. Thomas, C.S. Foote, Chemistry of singlet oxygen—XXVI. Photooxygenation of phenols, *J. Photochem. Photobiol.* 27 (1978) 683–693.
- [36] F. Wilkinson, J. Brummer, Rate constants for the decay and reactions of the lowest electronically excited singlet state of molecular oxygen in solution. An expanded and revised compilation, *J. Phys. Chem. Ref. Data* 10 (1981) 809–999.
- [37] C. Schöneich, Methionine oxidation by reactive oxygen species: reaction mechanisms and relevance to Alzheimer's disease, *BBA-Proteins Proteom.* 1703 (2005) 111–119.
- [38] A. Drazic, J. Winter, The physiological role of reversible methionine oxidation, *BBA-Proteins Proteom.* 1844 (2014) 1367–1382.
- [39] T. Nauser, J. Pelling, C. Schneich, C. Scho, Thiyl radical reaction with amino acid side chains: rate constants for hydrogen transfer and relevance for posttranslational protein modification, *Chem. Res. Toxicol.* 17 (2004) 1323–1328.
- [40] X. Gu, X. Li, Y. Chai, Q. Yang, P. Li, Y. Yao, A simple metal-free catalytic sulfoxidation under visible light and air, *Green. Chem.* 15 (2013) 357–361.
- [41] T. Carofiglio, P. Donnola, M. Maggini, M. Rossetto, E. Rossi, Fullerene-promoted singlet-oxygen photochemical oxygenations in glass-polymer microstructured reactors, *Adv. Synth. Catal.* 350 (2008) 2815–2822.
- [42] M.C. Mitchell, V. Spikmans, A.J. De Mello, Microchip-based synthesis and analysis: control of multicomponent reaction products and intermediates, *Analyst* 126 (2001) 24–27.
- [43] S. Sirichai, A.J. De Mello, A capillary electrophoresis microchip for the analysis of photographic developer solutions using indirect fluorescence detection, *Analyst* 125 (2000) 133–137.
- [44] K.S. Elvira, R.C.R. Wootton, N.M. Reis, M.R. Mackley, J. Andrew, Through-wall mass transport as a modality for safe generation of singlet oxygen in continuous flows, *ACS Sustain. Chem. Eng.* 1 (2013) 209–213.
- [45] D. Ziegenbalg, G. Kreisel, D. Weis, D. Kralisch, OLEDs as prospective light sources for microstructured photoreactors, *Photochem. Photobiol. Sci.* 13 (2014) 1005–1015.
- [46] T. Carofiglio, P. Donnola, M. Maggini, M. Rossetto, E. Rossi, Fullerene-promoted singlet-oxygen photochemical oxygenations in glass-polymer microstructured reactors, *Adv. Synth. Catal.* 350 (2008) 2815–2822.

[47] C.A. Páez, D.Y. Lique, C. Calberg, S.D. Lambert, I. Willems, A. Germeau, J. Pirard, B. Heinrichs, Study of photocatalytic decomposition of hydrogen peroxide over ramdellite-MnO<sub>2</sub> by O<sub>2</sub>-pressure monitoring, *Catal. Commun.* 15 (2011) 132–136.

[48] H.P.L. Gemoets, Y. Su, M. Shang, V. Hessel, R. Luque, T. Noël, Liquid phase oxidation chemistry in continuous-flow microreactors, *Chem. Soc. Rev.* 45 (2016) 83–117.

[49] J. Fischer, T. Lange, R. Boehling, A. Rehfinger, E. Klemm, Uncatalyzed selective oxidation of liquid cyclohexane with air in a microcapillary reactor, *Chem. Eng. Sci.* 65 (2010) 4866–4872.

[50] T. Aillet, K. Loubiere, O. Dechy-Cabaret, L. Prat, Photochemical synthesis of a cage compound in a microreactor: rigorous comparison with a batch photoreactor, *Chem. Eng. Process.* 64 (2013) 38–47.

[51] Y. Su, N. Straathof, V. Hessel, T. Noël, Photochemical transformations accelerated in continuous-flow reactors: basic concepts and applications, *Chem. Eur. J.* 20 (2014) 10562–10589.

[52] S. Meyer, D. Tietze, S. Rau, B. Schäfer, G. Kreisel, Photosensitized oxidation of citronellol in microreactors, *J. Photochem. Photobiol.* 186 (2007) 248–253.

### Supporting information

The oxidation reaction was monitored by following the disappearance of the triplet at 2.55 ppm (**Met**) and the appearance of the singlet at 2.65 ppm (**MetO**).

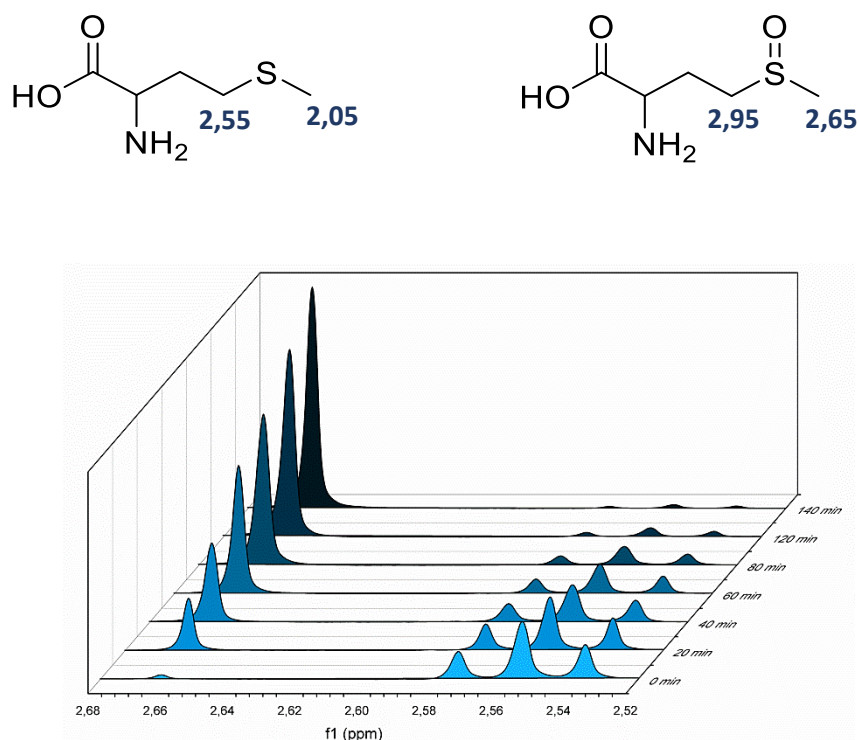


**Fig. S.1.** Evolution of the <sup>1</sup>H NMR spectra from the initial concentration of methionine until its complete oxidation in the batch reactor

The Lambert-Beer law rationalizes the attenuation effect of the photon transport in the liquid media, and according to this law, the radiation distribution is not uniform in a reactor due to the absorption effects of the PS (and any other chromophore). The transmission of the light is also reduced drastically with the distance from the light source, and with the liquid path to cross due to dispersion. This

equation shows a clear correlation between the absorption and the extinction coefficient ( $\epsilon$ ) of the light absorbing molecules, their concentration ( $c$ ), and the path length of the light propagation ( $l$ ). Transmission percentage (%T) was calculated as a function of the path length, in order to evaluate the effect of the light propagation inside of a batch/microreactor as a function of the photosensitizer concentration. The percentage of transmittance at 540 nm was calculated for RB solutions with 0.05, 0.1 0.45 and 1 mM as a function of the path length. By plotting this relationship between transmission and distance (Fig. S.2), the impact of the path length can be rationalized.

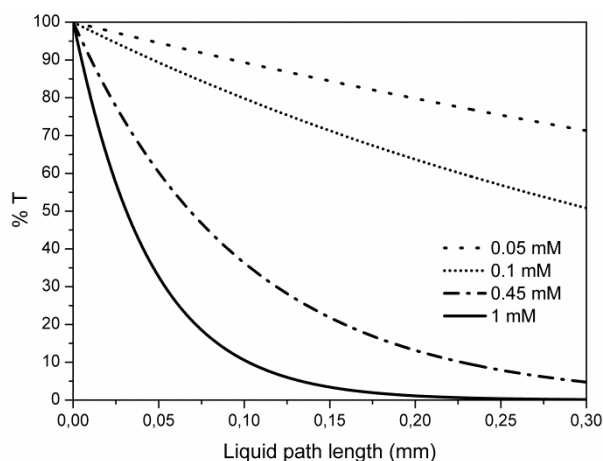


**Fig. S.2.** %T as a function of the path length inside of the liquid medium for free RB solutions at the maximum absorption of the dye (540 nm).

**Table S.1** Apparent kinetic constant ( $k_{app}$ ) and coefficient of determination ( $r^2$ ) for different RB concentrations in batch.

RB (mM)	$k_{app}$ (s <sup>-1</sup> )	$r^2$
0	0.000005	0.89409
0.006	0.000112	0.99848
0.029	0.000128	0.99777
0.044	0.000162	0.99587
0.073	0.000298	0.99483
0.147	0.000230	0.98844
0.293	0.000292	0.99435
0.586	0.000217	0.99875

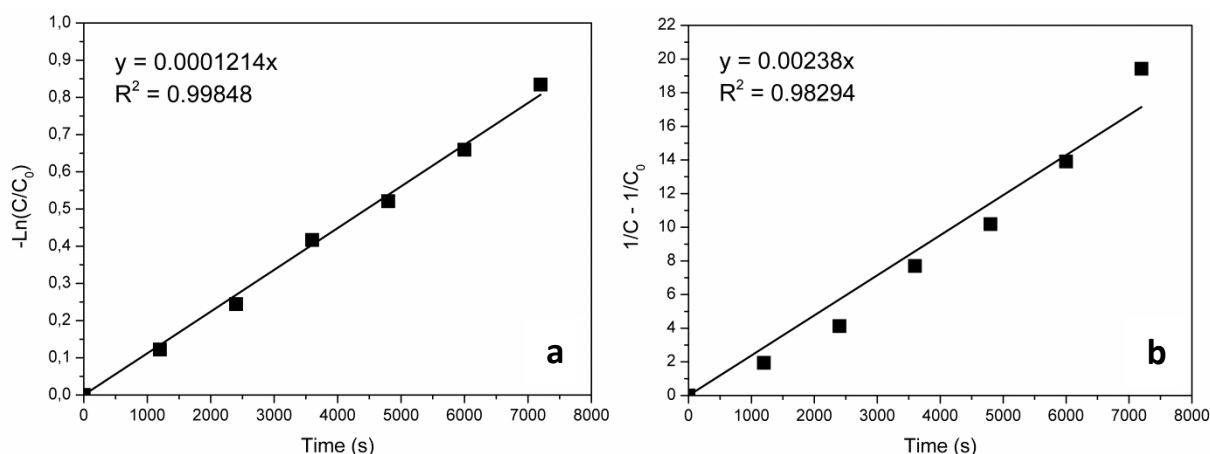


**Fig. S.3.** Validation of the reaction order with respect to the substrate (**Met**) **(a)** Pseudo first-order and **(b)** Pseudo second-order

The light was characterized in order to understand the effect of the light on the **Met** photooxygenation. Emission spectrum was recorded from 200 to 1000 nm (Fig. S.4a) and the irradiance ( $\text{W}\cdot\text{m}^{-2}$ ) was also measured at different distances (Fig. S.4b).

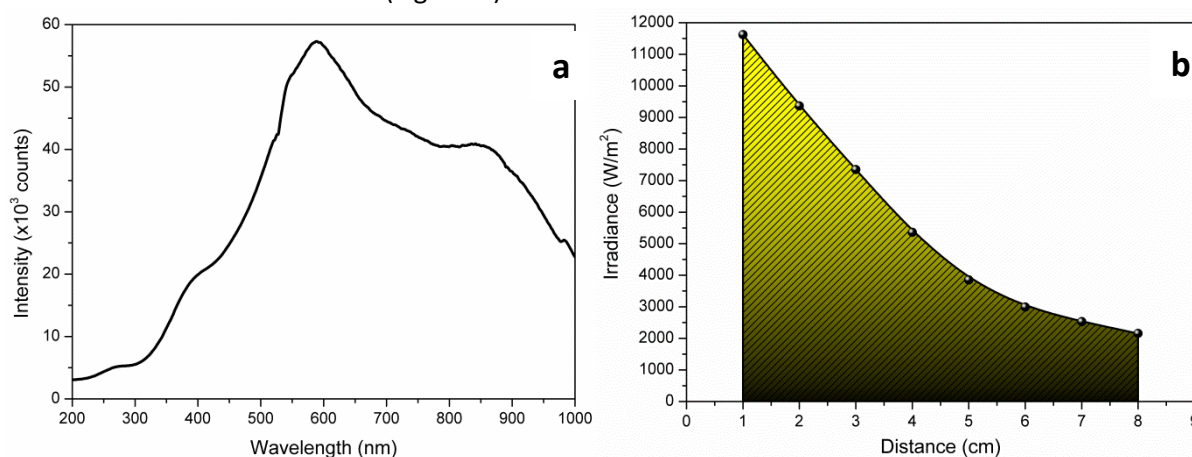


**Fig. S.4.** **(a)** Emission spectrum of the halogen lamp and **(b)** Irradiance of the halogen lamp as a function of the distance.

**Table S.2** Apparent kinetic constant ( $k_{\text{app}}$ ) and coefficient of determination ( $r^2$ ) for different irradiances in batch.

$\text{W}\cdot\text{m}^{-2}$	$k_{\text{app}}$	$r^2$
320	0.000002	0.14797
1590	0.000035	0.97549
3460	0.000114	0.98839
5360	0.000246	0.99722



**Table S.3** Apparent kinetic constant ( $k_{app}$ ) and coefficient of determination ( $r^2$ ) for different  $O_2$  flows in batch.

	$mL \cdot min^{-1}$	$k_{app}$	$r^2$
Air	5	0.000016	0.90458
	10	0.000036	0.99332
	15	0.000077	0.99945
$O_2$	5	0.000104	0.98658
	10	0.000196	0.99460
	15	0.000246	0.99722

## 2.3. Scalable Photocatalytic Oxidation of Methionine under Continuous-Flow Conditions

After methionine selective photooxidation was proven feasible in flow with singlet oxygen, the next challenge was to intensify the production of methionine sulfoxide. For this purpose, the process was transposed into a Corning Lab Photo Reactor. Corning photoreactors are designed to cover a large panel of scales. The transition from a lab scale to a pilot and an industrial scale reactor requires minimal readjustments which enables to predict the production of larger reactors from an optimization at lab scale.

### 2.3.1. General information and authors contributions

This chapter is published:

Emmanuel, N.; Mendoza, C.; Winter, M.; Horn, C. R.; Vizza, A.; Dreesen, L.; Heinrichs, B.; Monbaliu, J.-C. M. Scalable Photocatalytic Oxidation of Methionine under Continuous-Flow Conditions. *Org. Process Res. Dev.* 2017, 21, 1435–1438. 50 citations (08 December 2020)

N. E. designed the chemistry, performed the experiments, analyzed the results and wrote the manuscript. C. M. revised the manuscript. M. W. designed the chemistry, provided the equipment, supervised the experiments, analyzed the results and revised the manuscript. C. R. H. provided the equipment, supervised the experiments, analyzed the results and revised the manuscript. A. V. provided the equipment and revised the manuscript. L. D. revised the manuscript and secured funding for the project. B. H. revised the manuscript and secured funding for the project. J.-C. M. M. designed the chemistry, analyzed the results, supervised the project, wrote the manuscript and secured funding for the project.

The figures, tables and references numbering of the section 2.3.2 correspond to the numbering of the article as published online.

### 2.3.2. Templated copy of the article

The content of this section, including figures, is copyrighted (American Chemical Society 2017).

#### Introduction

Oxidation reactions are one of the most ubiquitous chemical transformations in living matter and chemical laboratories, and a huge palette of oxidizers, that is, chemicals prone to extract electrons from other substrates, are available to the chemist.<sup>1</sup> In the context of developing more sustainable chemical processes, molecular oxygen is most likely the cheapest, the most widely available, and greenest oxidant. Oxidation reactions using ground state triplet oxygen [ $X^3\Sigma_g$ ] often require high pressure and/or coordination complexes, increasing safety and environmental concerns at a larger scale.<sup>2</sup> Compared to triplet oxygen, singlet oxygen [ $a^1\Delta_g$ ] shows a much higher reactivity that usually alleviates the use of drastic process conditions but, on the downside, that could also trigger a variety of side reactions if not tamed appropriately. Singlet oxygen is conveniently generated via an energy transfer to triplet oxygen from catalytic metal-free or metal-based photosensitizers (PS) upon exposure to UV or visible light. The association of light (in particular visible light), a widely accessible and environmentally benign gas, a catalyst, and mild process conditions is setting essential foundations whereupon sustainable and green oxidation processes can be designed.<sup>3,4</sup> However, the inherent

limitations of catalytic photosensitized oxidations, that is, light penetration in macroscopic reaction media, gas–liquid mass transfer, solubility of oxygen in solution, and the transient nature of singlet oxygen, impose long irradiation/reaction times, consequent energy input for active mixing, large excess of oxygen, and the use of noxious solvents or additives, hence challenging process sustainability and efficiency.<sup>3,5</sup> Photochemistry in continuous-flow microreactors is now widely recognized as an enabling combination,<sup>6–9</sup> providing major process assets arising from a much improved light penetration and accurate control of irradiation time, high mass and heat transfer, safe and efficient handling of transient species, and seamless scalability. Many organic substrates have been successfully oxidized with singlet oxygen in microfluidic devices.<sup>6,10–14</sup> For instance, Aleman et al. reported a microfluidic procedure utilizing Pt(II) coordination complexes for the visible light photooxidation of various sulfides.<sup>10</sup>

Sulfoxides are found in many natural products<sup>15</sup> and are important organic building blocks with tremendous applications in organic synthesis, pharmaceutical sciences, biochemistry, and material sciences.<sup>16,17</sup> Sulfoxides are traditionally obtained from the oxidation of sulfides with peroxides,<sup>18</sup> peracids,<sup>19</sup> or periodates,<sup>20</sup> with optionally metal catalysts,<sup>21</sup> but these methods suffer from a high risk of overoxidation to sulfones.<sup>22</sup> The recent developments in catalytic photosensitized oxidations have led to robust and chemoselective oxidation procedures, either in batch<sup>3,10</sup> or in microfluidic devices.<sup>10,23</sup> Methionine sulfoxide **2a** (Figure 1), that is, the sulfoxide of essential amino acid methionine (**1a**) has attracted considerable attention over the past few years.<sup>17,24–26</sup> It has numerous applications in studying the pathogenesis of neurodegenerative diseases,<sup>27,28</sup> cell aging and oxidative stress,<sup>29</sup> peptide sciences,<sup>30–32</sup> material sciences,<sup>33,34</sup> and in organic synthesis.<sup>35,36</sup> To date, only one report described the catalytic photooxidation of **1a** methyl ester in D<sub>2</sub>O using a microfluidic setup in the presence of supported [60]fullerene PS.<sup>23</sup> This process took advantage of <sup>1</sup>O<sub>2</sub> longer lifetime and faster oxidation kinetics in deuterated solvents,<sup>26</sup> with a quantitative conversion in 33 s residence time. The output remained, however, at a slender 0.5 mmol d<sup>-1</sup> scale. In this communication, we report for the first time the development of a scalable continuous-flow strategy for the photocatalytic oxidation of methionine **1a** toward methionine sulfoxide **2a** under mild, chemoselective, atom-economic, safe and sustainable process conditions (Figure 1). The best results (1 mol day<sup>-1</sup>) were obtained with an extremely low loading of Rose Bengal (RB, 0.1 mol %) as a photocatalyst, at room temperature under white light irradiation (4000K) and a slight excess of oxygen (1.1 equiv). This was enabled by innovative reactor design combining high mixing and irradiation efficiencies. Other classical organic substrates such as  $\alpha$ -terpinene **1b** and citronellol **1c** were oxidized under similar conditions with excellent performances (Figure 1).

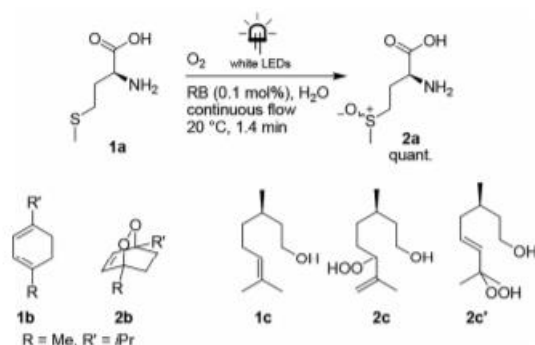


**Figure 1.** L-methionine (**1a**),  $\alpha$ -terpinene (**1b**), and citronellol (**1c**) and the corresponding catalytic photooxidation products (**2a–c'**) (see Supporting Information for details).

## Experimental section

### Continuous-Flow Setup

The continuous-flow setup (Figure 2) involved a compact commercial glass mesofluidic module (Corning Lab Reactor, 155 × 125 mm size, 400 μm I.D. reaction path, 2.6 mL internal volume) integrated with static mixers and sandwiched in a high-capacity heat exchanger (2 layers, 22 mL, 1 W mL<sup>-1</sup> K<sup>-1</sup>). The integrated static mixers were designed to optimize multiphase mass transfer.<sup>37,38</sup> LED panels were mounted on both sides of the fluidic module (40 mm from the center of the reaction path). Each LED panel was equipped with multiple wavelengths (20 LEDs for each wavelength) and a heat exchanger (T = 10 °C). The continuous-flow reactor was alimented in aqueous **1a** through a FLOM HPLC pump (0.01–100 mL min<sup>-1</sup>) and with industrial grade oxygen (99.99%, ALPHAGAZ 1, Air Liquide) through a Bronkhorst mass flow controller (MFC). A Zaiput Flow Technologies dome-type back-pressure regulator (BPR) was inserted downstream (set point: 8 barg). An analysis of the reactor effluent was carried out by in- and off-line NMR (Supporting Information).

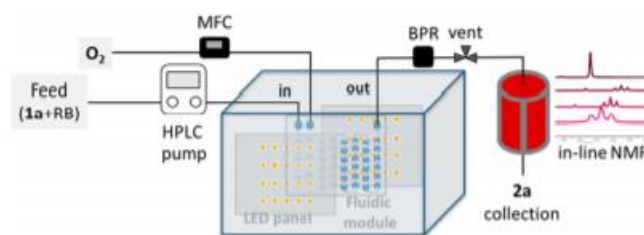


**Figure 2.** Continuous-flow setup for the catalyzed photooxidation of **1a**. The fluidic module and the LED panels are integrated with heat exchangers (omitted for clarity).

### Feed Preparation

The feed solutions of **1a–c** were prepared in D.I. water or in methanol containing 0.1 mol % of PS and stored in brown bottles.

### Typical Run

The HPLC pump used to deliver the aqueous solution of **1a** (0.3 M) and RB (0.1 mol %) was set to 1 mL min<sup>-1</sup>, and the oxygen flow was set to 7.5 mL min<sup>-1</sup> with the MFC; both fluids were conveyed to the continuous-flow photoreactor through perfluoroalkoxyalkane (PFA) tubing (1/8" O.D.). Mixing and irradiation (white LED, 100% intensity) occurred along the entire reaction channel (2.6 mL internal volume, 1.4 min residence time) under 8 barg of pressure. Conversion: >99%; selectivity: >99%; output: 132 g day<sup>-1</sup>.

## Results and discussion

Water-soluble metal-free Rose Bengal (RB), Methylene Blue (MB), and tetrakis(4-carboxyphenyl)porphyrin (TCPP) sensitizing dyes were selected for dye-sensitized generation of singlet oxygen.<sup>38</sup> These PS are harmless and widely available and can be photodegraded as an additional postreaction treatment.<sup>39,40</sup> Two competitive mechanisms are generally accepted for photocatalytic oxidations of organic substrates: (a) an oxidative process involving the unique reactivity of singlet oxygen via an energy transfer and (b) an oxidative process involving radical intermediates such as the superoxide radical anion.<sup>10,26</sup> The prevalence of the singlet oxygen or the radical mechanism essentially depends on the PS and on the reaction medium.<sup>10,26,41</sup> In the case of sulfides, both mechanisms result in the formation of sulfoxides.<sup>41</sup>

Preliminary experiments were designed to set the boundary conditions for the PS effective concentration (0.1 mol %) and oxygen excess to ensure total conversion within short reaction times (Supporting Information). Controlled experiments were run in the absence of light, PS, or oxygen, and **2a** was not detected in the reactor effluent. The reaction temperature had no notable effect on the conversion, and the temperature was set at 20 °C for all experiments. The concentration in **1a** of the feed solution had a significant impact on the reaction: at saturation (0.3 M), completion was obtained within a residence time of 1.4 min, while at lower concentrations, the residence time to reach completion dropped to 0.6 min (0.1 M), with 0.1 mol % PS and a 1.1:1 O<sub>2</sub>/**1a** ratio (Table 1). Upon optimization, the O<sub>2</sub>/**1a** ratio was decreased from 12.9 to 1.1, still affording complete conversion in 1.4 min residence time. The oxygen excess (equiv) was thus successfully reduced from 3.8 to 0.1. The best set of conditions involved a liquid flow of 1 mL min<sup>-1</sup> and a gas flow of 7.5 mL N min<sup>-1</sup> of oxygen, corresponding to an estimated residence time of 1.4 min. The consumption of oxygen could be visually monitored through the glass continuous-flow reactor.

The light intensity had a profound impact on the conversion (Table 1). With white light LEDs (4000K) and in the presence of RB ( $\lambda_{\text{max}} = 550 \text{ nm}$ ), the conversion was still complete with 80% intensity and then dropped to 54% with 20% intensity. The lower conversion observed at lower irradiation intensity reflects the lower amount of singlet oxygen available in the system. Changing white LEDs to monochromatic LEDs affected more severely the conversion with 4% at 622 nm and 63% at 385 nm, although complete conversion was obtained with blue (405 nm) LEDs under the same conditions (Table 1).

The nature of the photosensitizer had also a profound impact on the oxidation efficiency. Stock solutions were prepared with MB and TCPP (0.1 mol % each), and handled as described above. The optimal conditions for the photooxidation of **1a** with RB (1.4 min residence time, 1.1 equiv of O<sub>2</sub>, room temperature, white LEDs) only led to partial conversion when the photooxidation was carried out with MB ( $\lambda_{\text{max}} = 610 \text{ nm}$ )<sup>42</sup> as a photocatalyst. Shifting to orange LEDs (622 nm) increased the conversion, but the optimum required a larger excess of oxygen (1.5 equiv). The light intensity also impacted the conversion (Supporting Information). At 80 and 50% intensity, the conversion dropped to 91 and 65%, respectively. Changing the LEDs to 385 nm expectantly reduced the conversion (13%). TCPP ( $\lambda_{\text{max}} = 405 \text{ nm}$ )<sup>43</sup> performed even less under white light irradiation, with a mere 25% conversion under the optimized conditions with white LEDs. Adjusting the wavelength to 405 nm together with an increase of the residence time to 1.4 min and 1.5 equiv of oxygen led to full conversion. Decreasing light intensity also led to lower conversions (88% conversion at 50% intensity), similarly to RB.

**Table 1.** Optimization of the Photocatalytic Oxidation of **1a** under Continuous-Flow Conditions in the Presence of Rose Bengal.

entry	[ <b>1a</b> ] (M)	feed 1 (mL min <sup>-1</sup> )	feed 2 (mL <sub>O<sub>2</sub></sub> min <sup>-1</sup> )	T (°C)	res. time (min)	LEDs (intensity)	conv. (%)
1	0.1	2.5	15	rt	0.6	white (100%)	quant.
2	0.2	1.5	7.5	rt	1	white (100%)	quant.
3	0.3	1	7.5	rt	1.4	white (100%)	quant.
4	0.1	2.5	15	10	0.6	white (100%)	quant.
5	0.1	2.5	15	50	0.6	white (100%)	quant.
6	0.2	1.5	7.5	rt	1	white (50%)	89
7	0.2	1.5	7.5	rt	1	white (20%)	54
8	0.3	1	7.5	rt	1.4	622 nm (100%)	4
9	0.3	1	7.5	rt	1.4	385 nm (100%)	63
10	0.3	1	7.5	rt	1.4	405 nm (100%)	quant.

These results emphasized RB as a superior sensitizer for the photooxidation of **1a** under sustainable process conditions.<sup>3</sup> Various production campaigns (8 h runs) emphasized a stable reactor operation and provided consistent results. Decompression after the BPR released the excess oxygen. The downstream treatment of reactor effluents included the filtration of the solution on activated charcoal to remove the PS, concentration of the solution, and antisolvent recrystallization (slow addition of *i*-PrOH), giving **2a** in 79% isolated yield (99% purity). Similar conditions were amenable to other organic substrates (Figure 1 and Supporting Information). In particular,  $\alpha$ -terpinene (**1b**) and citronellol (**1c**) are very common model organic substrates for assessing photocatalytic singlet oxygen process efficiency.<sup>27,44</sup> For solubility reasons, methanol was utilized for these trials. Feed solutions of **1b** with concentrations of up to 1 M were submitted to photocatalytic oxidation using white light and a slightly larger excess of oxygen (1.4 equiv). The total conversion was observed with 2.2 min of residence time, with no detectable traces of *p*-cymene, giving a productivity of up to 273 g d<sup>-1</sup> (1.6 mol d<sup>-1</sup>). Quantitative photocatalytic oxidation of **1c** (0.1 M) was obtained within 1 min residence time with 3 equiv of oxygen, yielding a 3:2 ratio of peroxides **2c,c'** (Supporting Information). Out-scaling the best conditions for the catalytic photooxidation of **1a** with RB (0.3 M, 1.1 equiv of O<sub>2</sub>, room temperature and residence time of 1.4 min) with a similar light input and surface to volume ratio in a Corning advanced-flow G1 photoreactor would allow to process ca. 72 mL min<sup>-1</sup> (daily productivity of 31.1 mol day<sup>-1</sup> or 5.1 kg day<sup>-1</sup>). A Corning advanced-flow G3 reactor with similar process conditions would increase the productivity up to 6 T y<sup>-1</sup>. In conclusion, we have developed a scalable catalytic photooxidation process for the production of methionine sulfoxide under sustainable process conditions. By contrast to previously reported catalytic photooxidation processes where a large excess of oxygen is required, the integration of static mixers along the reactor path ensured an excellent mass transfer and, hence, fast oxidation rates despite the moderate solubility of oxygen in the reaction medium. The conditions are amenable to other organic substrates and provided high productivities within a short residence time for ascaridole **2b** and Rose oxide synthetic intermediates **2c,c'**.

## References

- (1) Guo, Z.; Liu, B.; Zhang, Q.; Deng, W.; Wang, Y.; Yang, Y. *Chem. Soc. Rev.* 2014, 43, 3480–3524.
- (2) Correa, P. E.; Hardy, G.; Riley, D. P. *J. Org. Chem.* 1988, 53, 1695–1702.
- (3) Gu, X.; Li, X.; Chai, Y.; Yang, Q.; Li, P.; Yao, Y. *Green Chem.* 2013, 15, 357–361.
- (4) Alsters, P. L.; Jary, W.; Nardello-Rataj, V.; Aubry, J.-M. *Org. Process Res. Dev.* 2010, 14, 259–262.
- (5) Elvira, K. S.; Wootton, R. C. R.; Reis, N. M.; Mackley, M. R.; DeMello, A. J. *ACS Sustainable Chem. Eng.* 2013, 1, 209–213.
- (6) Cambie, D.; Bottecchia, C.; Straathof, N. J. W.; Hessel, V.; Noel, T. *Chem. Rev.* 2016, 116, 10276–10341.
- (7) Levesque, F.; Seeberger, P. H. *Org. Lett.* 2011, 13, 5008–5011.
- (8) Ciriminna, R.; Delisi, R.; Xu, Y.; Pagliaro, M. *Org. Process Res. Dev.* 2016, 20, 403–408.
- (9) Mallia, C. J.; Baxendale, I. R. *Org. Process Res. Dev.* 2016, 20, 327–360.
- (10) Casado-Sanchez, A.; Gómez-Ballesteros, R.; Tato, F.; Soriano, F. J.; Pascual-Coca, G.; Cabrera, S.; Aleman, J. *Chem. Commun.* 2016, 52, 9137–9140. (11)
- (11) Heugebaert, T. S. A.; Stevens, C. V.; Kappe, C. O. *ChemSusChem* 2015, 8, 1648–1651.
- (12) Maurya, R. A.; Park, C. P.; Kim, D. P. *Beilstein J. Org. Chem.* 2011, 7, 1158–1163.
- (13) Wootton, R. C. R.; Fortt, R.; De Mello, A. J. *Org. Process Res. Dev.* 2002, 6, 187–189.
- (14) Loponov, K. N.; Lopes, J.; Barlog, M.; Astrova, E. V.; Malkov, A. V.; Lapkin, A. A. *Org. Process Res. Dev.* 2014, 18, 1443–1454.
- (15) Imae, Y.; Takada, K.; Okada, S.; Ise, Y.; Yoshimura, H.; Morii, Y.; Matsunaga, S. *J. Nat. Prod.* 2013, 76, 755–758.
- (16) Matsuoka, S.; Mizoguchi, Y.; Itoh, H.; Okura, K.; Shinohara, N.; Inoue, M. *Tetrahedron Lett.* 2010, 51, 4644–4647.
- (17) Yamada, S.; Ikkyu, K.; Iso, K.; Goto, M.; Endo, T. *Polym. Chem.* 2015, 6, 1838–1845.
- (18) Gan, S.; Yin, J.; Yao, Y.; Liu, Y.; Chang, D.; Zhu, D.; Shi, L. *Org. Biomol. Chem.* 2017, 15, 2647–2654.
- (19) Mello, R.; Olmos, A.; Alcalde-Aragones, A.; Díaz-Rodríguez, A.; Gonzalez Nunez, M. E.; Asensio, G. *Eur. J. Org. Chem.* 2010, 32, 6200–6206.
- (20) Leonard, N. J.; Johnson, C. R. *J. Org. Chem.* 1962, 27, 282–284.
- (21) Arterburn, J. B.; Nelson, S. L. *J. Org. Chem.* 1996, 61, 2260–2261.
- (22) Lazzaro, F.; Crucianelli, M.; De Angelis, F.; Neri, V.; Saladino, R. *Tetrahedron Lett.* 2004, 45, 9237–9240.

- (23) Carofiglio, T.; Donnola, P.; Maggini, M.; Rossetto, M.; Rossi, E. *Adv. Synth. Catal.* 2008, 350, 2815–2822.
- (24) Ng, S.; Lin, E.; Kitov, P. I.; Tjhung, K. F.; Gerlits, O. O.; Deng, L.; Kasper, B.; Sood, A.; Paschal, B. M.; Zhang, P.; et al. *J. Am. Chem. Soc.* 2015, 137, 5248–5251.
- (25) Hellwig, M.; Löbmann, K.; Orywol, T.; Voigt, A. *J. Agric. Food Chem.* 2014, 62, 4425–4433.
- (26) Liu, F.; Liu, J. *J. Phys. Chem. B* 2015, 119, 8001–8012.
- (27) Taniguchi, A.; Sasaki, D.; Shiohara, A.; Iwatsubo, T.; Tomita, T.; Sohma, Y.; Kanai, M. *Angew. Chem., Int. Ed.* 2014, 53, 1382–1385.
- (28) Schöneich, C. *Biochim. Biophys. Acta, Proteins Proteomics* 2005, 1703, 111–119.
- (29) Gennaris, A.; Ezraty, B.; Henry, C.; Agrebi, R.; Vergnes, A.; Oheix, E.; Bos, J.; Leverrier, P.; Espinosa, L.; Szweczyk, J.; et al. *Nature* 2015, 528, 409–412.
- (30) Kukowska, M.; Kukowska-Kaszuba, M.; Dzierzbicka, K. *Tetrahedron Lett.* 2015, 56, 525–528.
- (31) Harris, P. W. R.; Kowalczyk, R.; Yang, S. H.; Williams, G. M.; Brimble, M. A. *J. Pept. Sci.* 2014, 20, 186–190.
- (32) Zhang, Y.; Li, T.; Li, X. *Org. Biomol. Chem.* 2013, 11 (34), 5584.
- (33) Reddy, S. M. M.; Dorishetty, P.; Deshpande, A. P.; Shanmugam, G. *ChemPhysChem* 2016, 17, 2170–2180.
- (34) Seixas, J. D.; Santos, M. F. A.; Mukhopadhyay, A.; Coelho, A. C.; Reis, P. M.; Veiros, L. F.; Marques, A. R.; Penacho, N.; Goncalves, A. M. L.; Romao, M. J.; et al. *Dalt. Trans.* 2015, 44, 5058–5075.
- (35) Li, S. G.; Portela-Cubillo, F.; Zard, S. Z. *Org. Lett.* 2016, 18, 1888–1891.
- (36) Lamborelle, N.; Simon, J. F.; Luxen, A.; Monbaliu, J.-C. *Org. Biomol. Chem.* 2015, 13, 11602–11606.
- (37) Jeong, H. G.; Choi, M. S. *Isr. J. Chem.* 2016, 56, 110–118.
- (38) Cherfan, D.; Verter, E. E.; Melki, S.; Gisel, T. E.; Doyle, F. J.; Scarcelli, G.; Yun, S. H.; Redmond, R. W.; Kochevar, I. E. *Invest. Ophthalmol. Visual Sci.* 2013, 54, 3426–3433.
- (39) Chesneau, E.; Neckers, D. C. *J. Photochem. Photobiol., A* 1988, 42, 269–281.
- (40) Bonesi, S. M.; Manet, I.; Freccero, M.; Fagnoni, M.; Albinì. *Chem. - Eur. J.* 2006, 12, 4844–4857.
- (41) Heger, D.; Jirkovsky, J.; Klá n, P. *J. Phys. Chem. A* 2005, 109, 6702–6709.
- (42) Cherian, S.; Wamser, C. C. *J. Phys. Chem. B* 2000, 104, 3624–3629.
- (43) Ziegenbalg, D.; Wriedt, B.; Kreisel, G.; Kralisch, D. *Chem. Eng. Technol.* 2016, 39, 123–134.
- (44) Ronzani, F.; Costarramone, N.; Blanc, S.; Benabbou, A. K.; Behec, M. L.; Pigot, T.; Oelgemöller, M.; Lacombe, S. *J. Catal.* 2013, 303, 164–174.



## Supporting information

The section numbering of this supporting information corresponds to the numbering of the supporting information found online.

### 1 Continuous-flow setup

#### 1.1 Generalities

A HPLC pump from FLOM Corporation was used ( $0.01 - 100 \text{ mL min}^{-1}$ ; wetted-parts: PTFE, PCTFE, FFKM and ruby). The feed solution was conveyed to the HPLC pump through a section of  $1/8''$  PFA tubing (Swagelok®) equipped with a filter frit and with  $1/8''$  PFA connectors (Swagelok®). The gas flow rate was controlled with a Bronkhorst® F210CTM mass flow controller (MFC). A Zaiput Flow Technologies® dome-type back-pressure regulator (BPR) was inserted downstream and connected to a cylinder of compressed Argon (set point: 8 barg). LAUDA® Proline RP 845TM thermostats were used for the thermoregulation of the mesofluidic reaction glass modules and the LED illumination setup (Corning® Advanced-Flow™ Lab Photo Reactor). In-line NMR analysis was carried out with a 43 MHz Spinsolve™ Carbon NMR spectrometer from Magritek® equipped with the flow-through module.

#### 1.2 Pictures of the continuous-flow setup

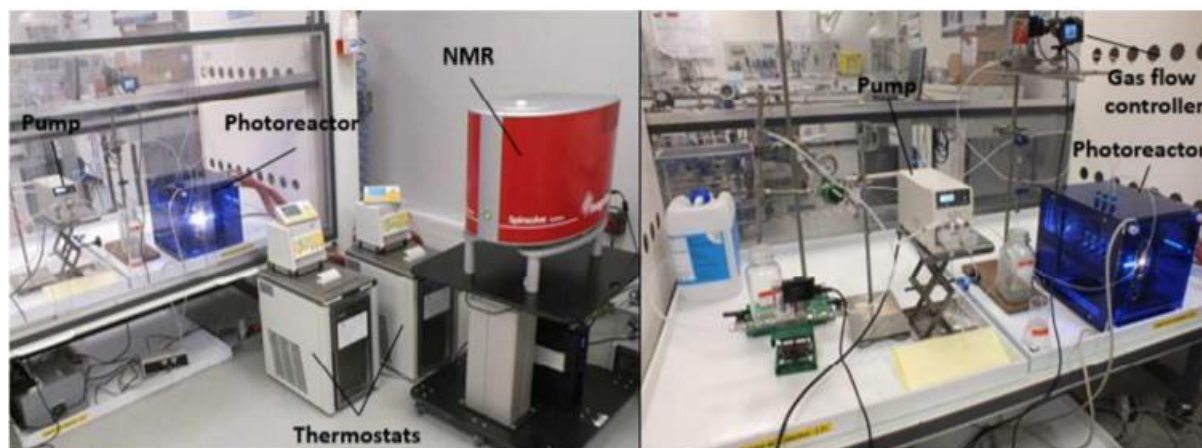


**Figure S1.** Detailed setup for the continuous-flow preparation of methionine sulfoxide **1a**. Corning® proprietary.

#### 1.3 Residence time calculation

The residence time is calculated according to Equation S1:

$$\text{Residence Time (min)} = \frac{\text{Internal volume (mL)}}{\text{Flow rate (mL min}^{-1}\text{)}} \quad \text{(Equation S1)}$$

The total flow rate combines the individual flow rates of all fluids fed into the reactor. The actual gas flow rate is calculated from the flow rate measured by the MFC according to Equations S2-3:

$$n_{\text{O}_2} = \frac{P_{\text{N}}(\text{atm})V_{\text{N}}(\text{L})}{R(\text{L atm mol}^{-1}\text{K}^{-1})T_{\text{N}}(\text{K})} \quad \text{(Equation S2)}$$

$$V_{\text{real}} = \frac{n_{\text{O}_2}RT_{\text{real}}}{P_{\text{real}}} \quad \text{(Equation S3)}$$

For example, the actual volume of O<sub>2</sub> delivered under 8 barg and 30 °C when the MFC is set at 15 mL min<sup>-1</sup> is 1.9 mL min<sup>-1</sup> (see Equations S4-5):

$$n_{O_2} = \frac{P_N(\text{atm})V_N(\text{L})}{R(\text{L} \cdot \text{atm} \cdot \text{mol}^{-1} \cdot \text{K}^{-1})T_N(\text{K})} = \frac{1 * 0.015}{0.082 * 273.15} = 0.67 \text{ mmol (Equation S4)}$$

$$V_{\text{real}} = \frac{n_{O_2}RT_{\text{real}}}{P_{\text{real}}} = \frac{0.00067 * 0.082 * 303.15}{8.8} = 1.9 \text{ mL (Equation S5)}$$

## 2 Supplemental experimental data

### 2.1 Chemicals

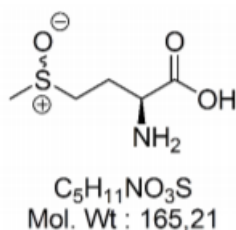
- (L)-Methionine (CAS 63-68-3, >99.0%, TCI, [MSDS](#))
- α-terpinene (CAS 99-86-5, >90%, TCI, [MSDS](#))
- Citronellol (CAS 106-22-9, 95%, Sigma-Aldrich, [MSDS](#))
- Methanol (CAS 67-56-1, ≥99.9%, Sigma-Aldrich, [MSDS](#))
- Rose Bengal (CAS 632-69-9, TCI, [MSDS](#))
- TCPP (CAS 14609-54-2, 97%, TCI, [MSDS](#))
- Methylene Blue (CAS 122965-43-9, 82%, Sigma-Aldrich, [MSDS](#))

### 2.2 Nuclear magnetic resonance (NMR)

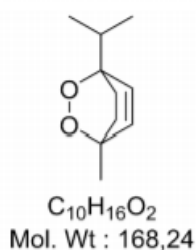
#### 2.2.1 Generalities

Qualitative in-line reaction monitoring was carried out by <sup>1</sup>H NMR with a 43 MHz Spinsolve<sup>TM</sup> Carbon NMR spectrometer from Magritek<sup>®</sup> equipped with the flow-through module. Analytical samples were collected and analyzed by <sup>1</sup>H NMR at 400 MHz on a Bruker Avance III HD spectrometer (9.4 Tesla). The chemical shifts are reported in ppm relative to TMS as internal standard or to solvent residual peak.

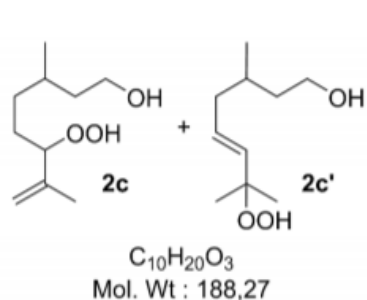
#### 2.2.2 NMR data and characterization for compounds **2a-c**'



Methionine sulfoxide (**2a**). <sup>1</sup>H NMR (D<sub>2</sub>O, 400 MHz): δ = 3.79 (m, 1H), 2.81-3.08 (m, 2H), 2.66 (s, 3H), 2.23 (m, 2H) ppm. The NMR data matched the data obtained for commercial methionine sulfoxide. ESI HRMS m/z C<sub>5</sub>H<sub>12</sub>O<sub>3</sub>NS [M+H]<sup>+</sup> : calcd 166.05324. Found: 166.05330.



Ascaridole (**2b**). <sup>1</sup>H NMR (CD<sub>3</sub>OD, 400 MHz): δ = 6.5 (dd, 2H), 1.97 (d, 1H), 1.88 (m, 1H), 1.56 (d, 1H), 1.34 (s, 3H), 1.00 (m, 6H). NMR data matched those reported in the literature.<sup>1,2</sup> ESI HRMS m/z C<sub>10</sub>H<sub>16</sub>O<sub>2</sub>Na [M+Na]<sup>+</sup> : calcd 191.10425. Found: 191.10418.



Peroxides of citronellol (**2c,c'**). 1:1 mixture of two isomers.  $^1\text{H}$  NMR ( $\text{CD}_3\text{OD}$ , 400 MHz):  $\delta = 7.59$  (s, 2H), 5.61 (m, 2H), 4.62 (brs, 4H), 4.21 (t, 1H), 3.61 (m, 4H), 2.09 (m, 1H), 1.93 (m, 1H), 1.72 (s, 3H), 1.32-1.68 (m, 8H), 1.30 (s, 6H), 1.13 (m, 2H), 0.92 (m, 6H) ppm. NMR data matched those reported in the literature.<sup>2</sup> ESI HRMS  $m/z$   $\text{C}_{10}\text{H}_{20}\text{O}_3\text{Na}$   $[\text{M}+\text{Na}]^+$  : calcd 211.13047. Found: 211.13047.

### 2.2.3 Determination of the conversion of **1a** to **2a**

The oxidation of **1a** was easily monitored by  $^1\text{H}$  NMR. Conversion of **1a** into **2a** was monitored by following the disappearance of signal at 2.55 ppm (triplet, 2H, **1a**) and the appearance of the signal 2.65 ppm (singlet, 3H, **2a**) as illustrated in Figure S2. The conversion was calculated by using Equation S6 ( $I$  is the normalized integration of the corresponding signals):

$$\text{Conversion} = 100 * \frac{\frac{I(2.65 \text{ ppm})}{3}}{\frac{I(2.65 \text{ ppm})}{3} + \frac{I(2.55 \text{ ppm})}{2}} \quad (\text{Equation S6})$$

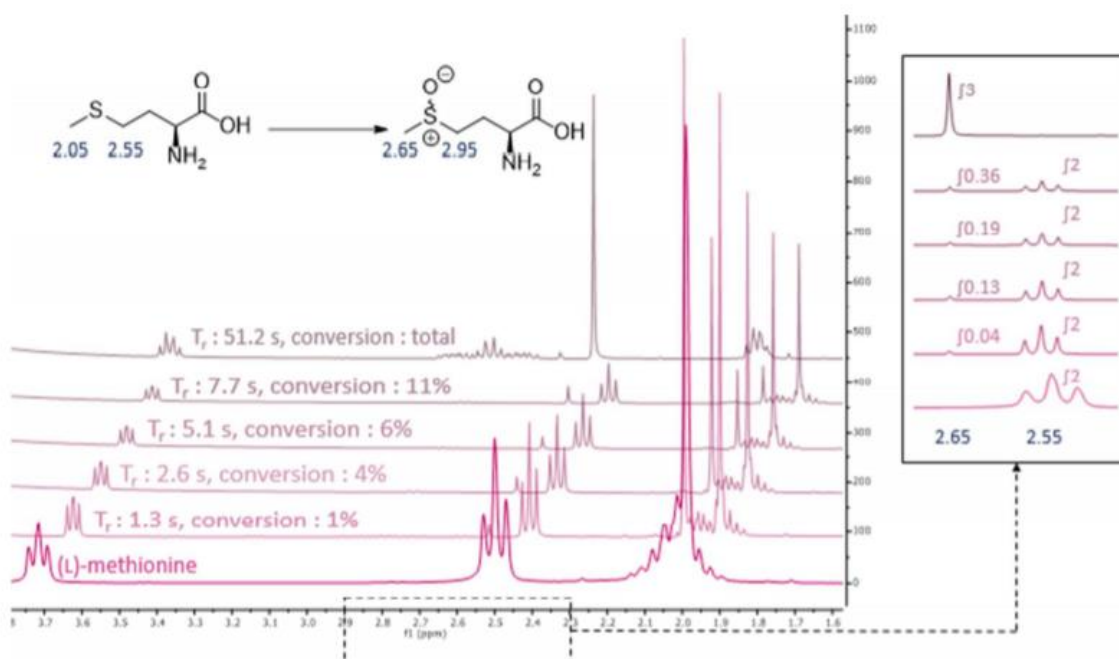


**Figure S2.**  $^1\text{H}$  NMR reaction monitoring for the preparation of **2a**.

## 2.3 Typical runs

### 2.3.1 Continuous-flow preparation of ascaridole **2b**

The HPLC pump used to deliver a solution of **1b** (1 M in methanol) and RB (1 mol%) was set to  $0.25 \text{ mL min}^{-1}$  and the oxygen flow was set to  $7.5 \text{ mL min}^{-1}$  with the MFC, and both fluids were conveyed to the continuous-flow photoreactor through perfluoroalkoxyalkane (PFA) tubing ( $1/8''$  O.D.). Mixing and irradiation (white LED, 100% intensity) occurred along the entire reaction channel (2.6 mL internal volume, 2.2 min residence time) under 8 barg of pressure. Process and reaction parameters such as concentration, temperature and residence time were optimized (Table S1).

**Table S1.** Process optimization for the preparation of ascaridole **2b** using white light (100% intensity).

Entry	1b (M)	Flow rate (mL min <sup>-1</sup> )		T (°C)	Res. time (min)	Conversion (%)
		Feed 1 (mL min <sup>-1</sup> )	Feed 2 (mL <sub>N</sub> min <sup>-1</sup> )			
1	0.18	1.25	7.5	RT	1.3	quant.
2	0.18	1.5	7.5	RT	1	quant.
3	0.18	2	7.5	RT	0.9	quant.
4	1	0.5	15	RT	1.1	67
5	1	0.25	7.5	RT	2.2	quant.
6	0.18	0.5	7.5	RT	1.8	quant.
7	0.18	0.25	7.5	RT	2.2	92
8	0.18	0.25	7.5	30	2.2	quant.
9	0.18	0.25	7.5	50	2.2	quant.

### 2.3.2 Continuous-flow preparation of citronellol peroxides **2c,c'**

The HPLC pump used to deliver a solution of **1c** (0.1 M in methanol) and RB (5 mol%) was set to 1.5 mL min<sup>-1</sup> and the oxygen flow was set to 10 mL min<sup>-1</sup> with the MFC, and both fluids were conveyed to the continuous-flow photoreactor through perfluoroalkoxyalkane (PFA) tubing (1/8" O.D.). Mixing and irradiation (white LED, 100% intensity) occurred along the entire reaction channel (2.6 mL internal volume, 1 min residence time) under 8 barg of pressure. Process and reaction parameters such as concentration, temperature and residence time were optimized (Table S2).

**Table S2.** Process optimization for the preparation of citronellol peroxides **2c,c'** using white light (100% intensity) at 20 °C.

Entry	1c (M)	Flow rate (mL min <sup>-1</sup> )			Conversion (%)		
		Feed 1 (mL min <sup>-1</sup> )	Feed 2 (mL <sub>N</sub> min <sup>-1</sup> )	Res. time (min)	2c	2c'	Remaining reactant (%)
1	0.1	0.5	15	1.1	52	48	0
2	0.1	0.5	7.5	1.8	30	22	48
3	0.1	0.5	10	1.5	51	49	0
4	0.1	0.25	10	1.8	51	49	0
5	0.1	1	10	1.2	58	42	0
6	0.1	0.75	10	1.3	55	45	0
7	0.1	2	10	0.8	24	20	56
8	0.1	1.5	10	1	56	44	0
9	0.1	1.25	10	1.1	56	44	0

### 2.3.3 Off-line purification of methionine sulfoxide **2a**

The effluent of the reactor was collected and treated with activated charcoal. The resulting mixture was stirred for 2 min at reflux, filtered and then concentrated under reduced pressure or recrystallized with i-PrOH as an antisolvent. Methionine sulfoxide (**2a**) was obtained as a white solid (79%).

## 2.4 Overlap between RB absorption and LED emission

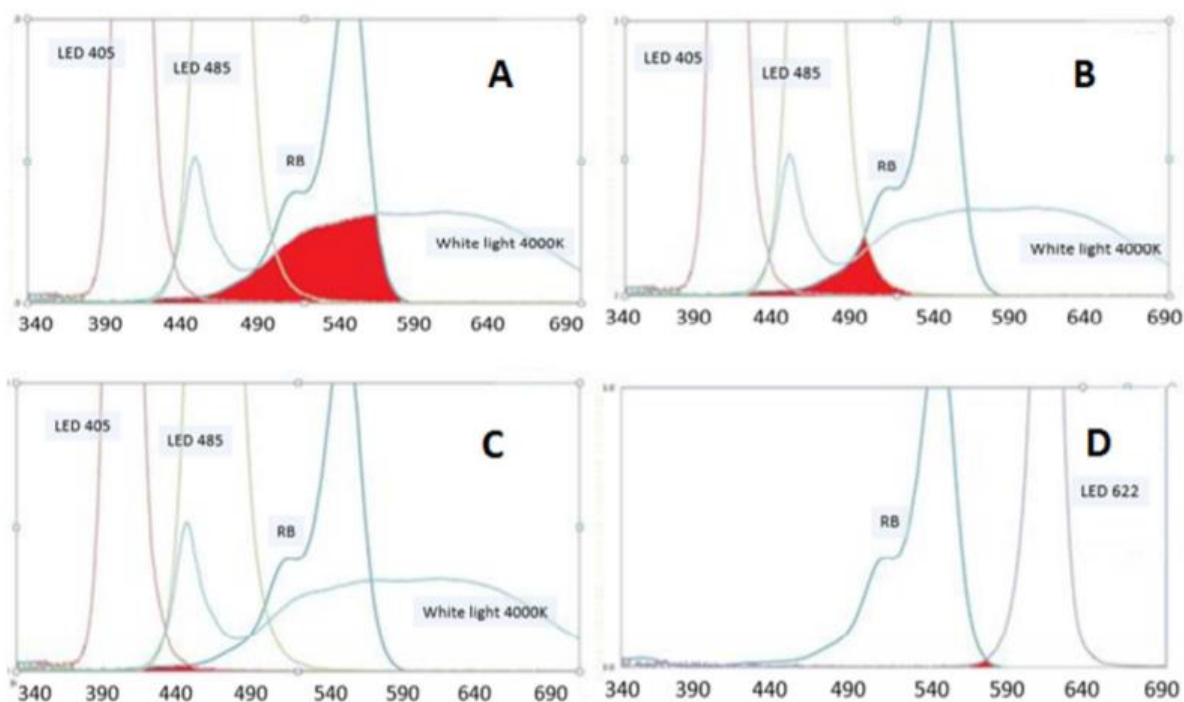


**Figure S3.** A: Overlap between RB absorption and white light emission spectra, B: Overlap between RB absorption and LED 485 emission spectra, C: Overlap between RB absorption and LED 405 emission spectra, D: Overlap between RB absorption and LED 622 emission spectra.

## 2.5 Representative $^1\text{H}$ NMR spectra

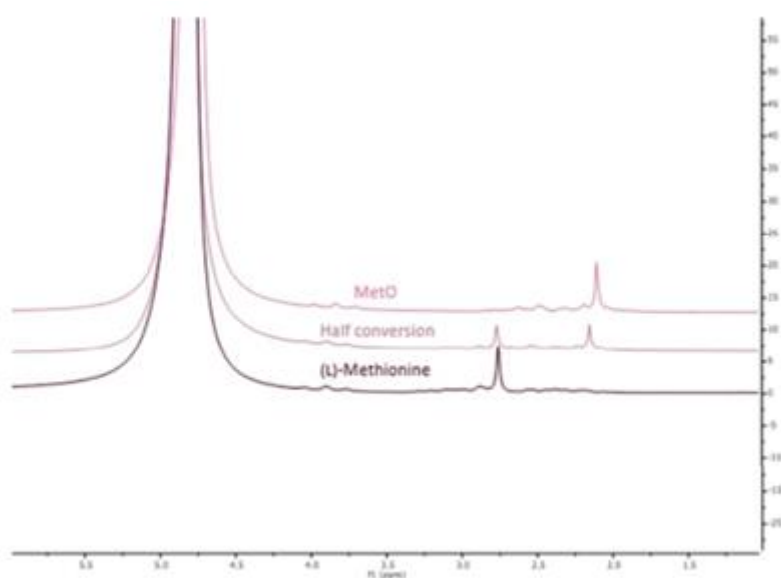


**Figure S4.** Typical in-line  $^1\text{H}$  NMR (45 MHz) spectra for **2a**. (L)-Methionine and MetO spectra were inverted on the figure.

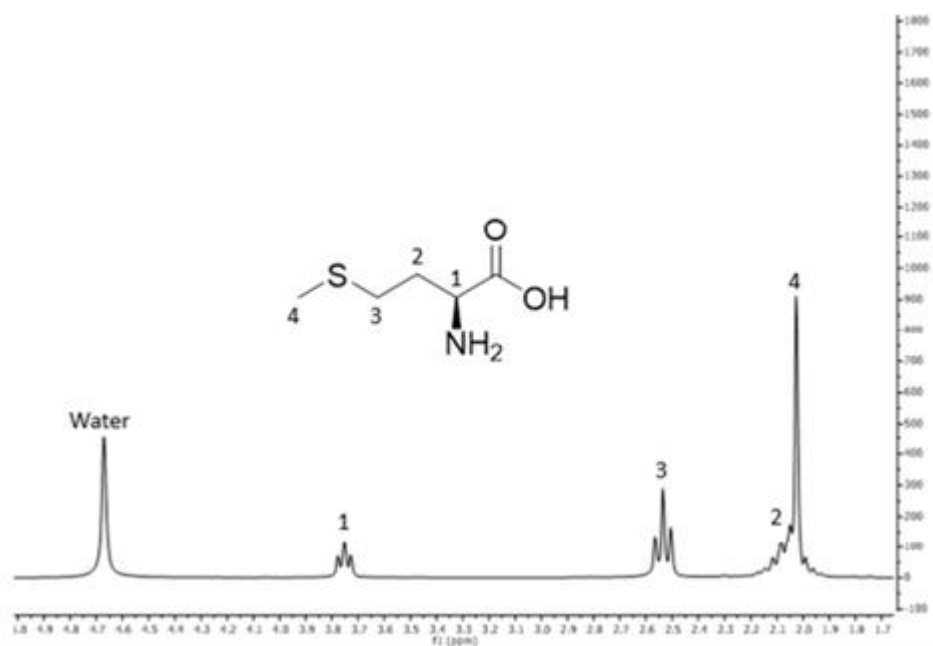


**Figure S5.** <sup>1</sup>H NMR spectrum (400 MHz) of (L)-methionine **1a** in D<sub>2</sub>O.

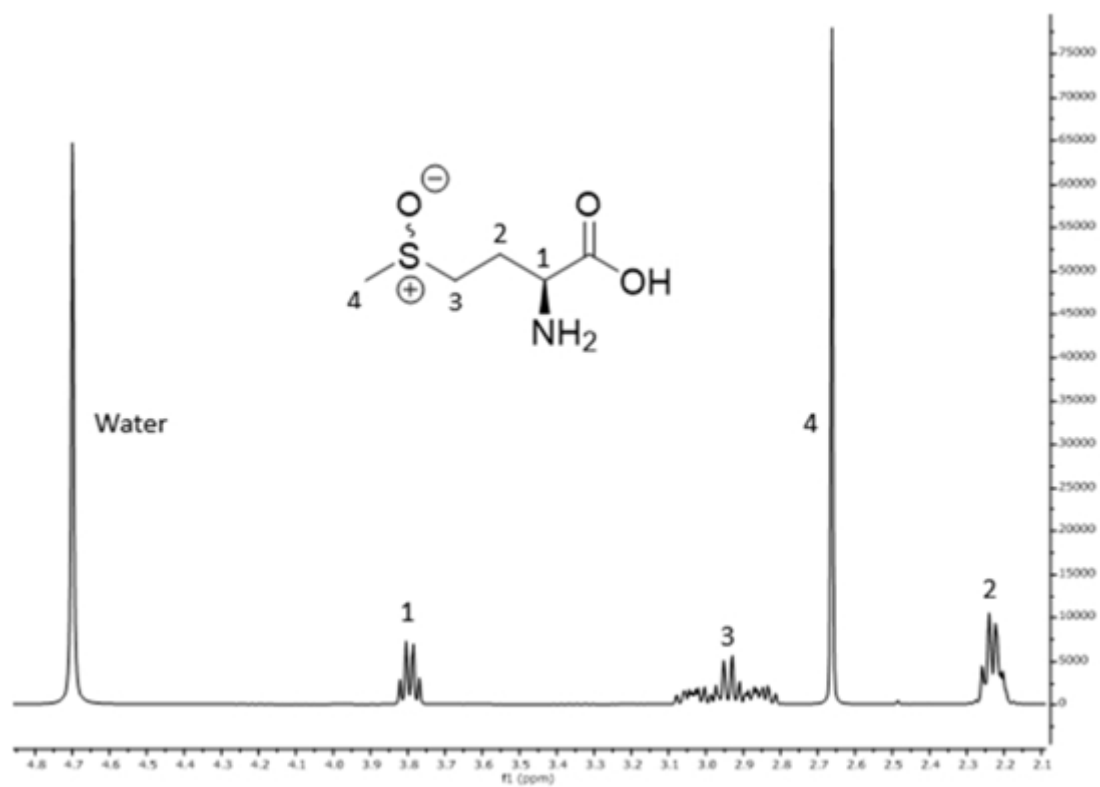


**Figure S6.** <sup>1</sup>H NMR spectrum (400 MHz) of methionine sulfoxide **2a** in D<sub>2</sub>O.

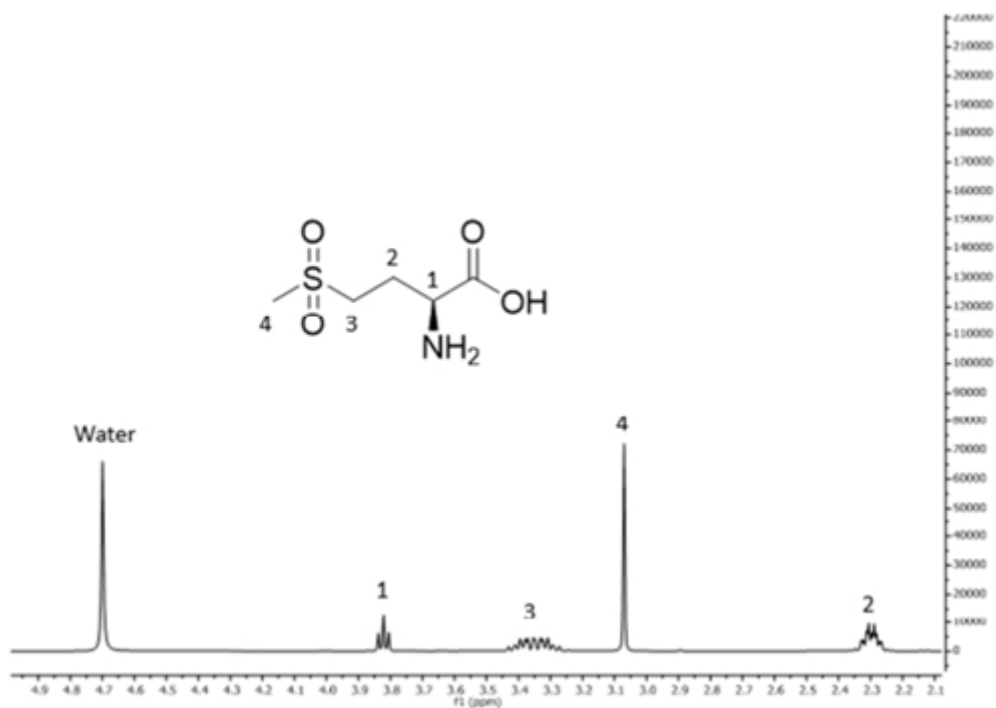


Figure S7.  $^1\text{H}$  NMR spectrum (400 MHz) of methionine sulfone in  $\text{D}_2\text{O}$ .

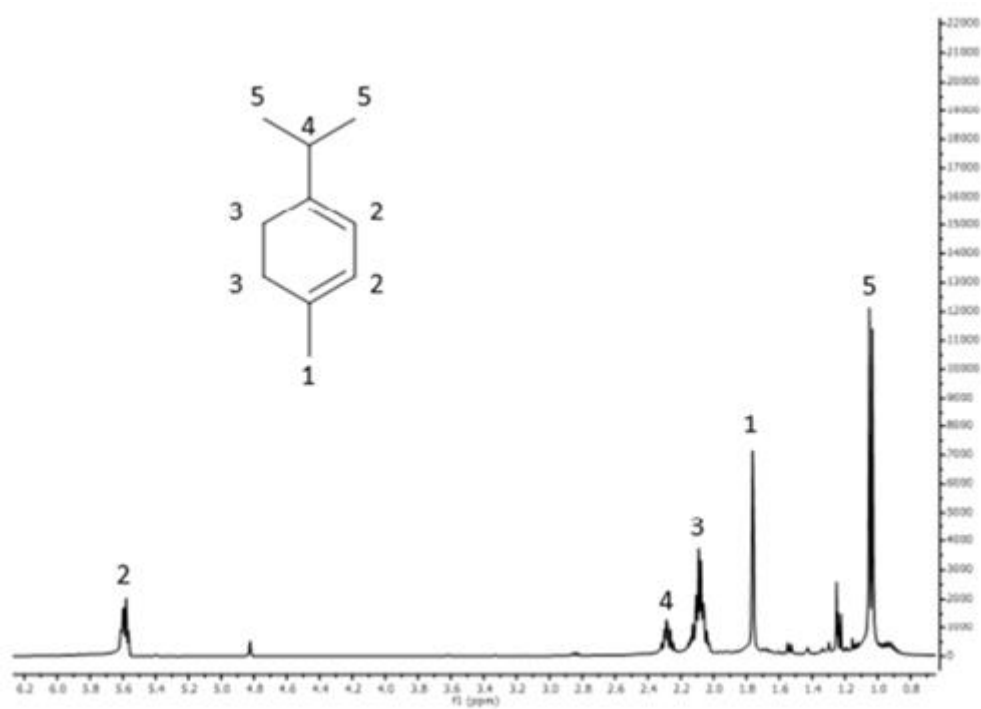
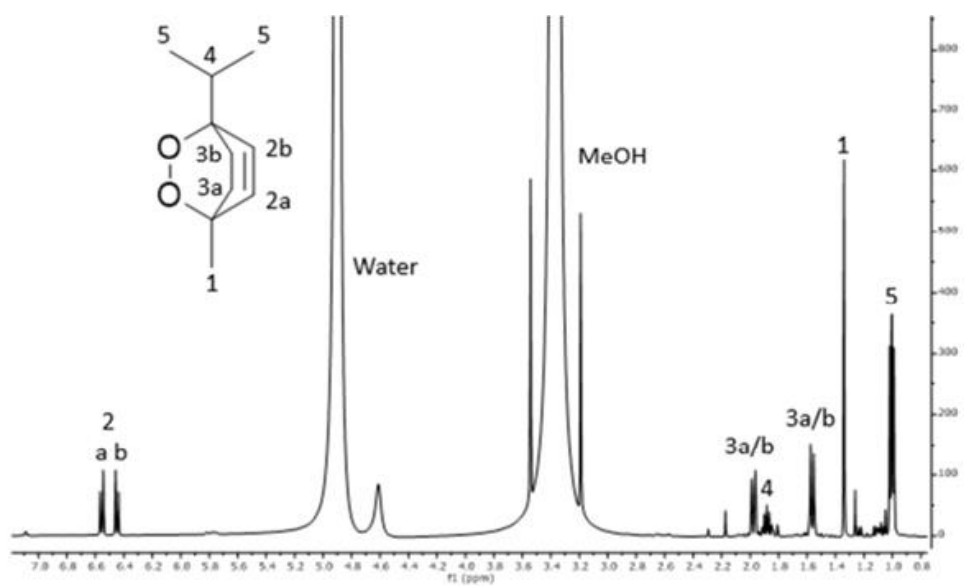
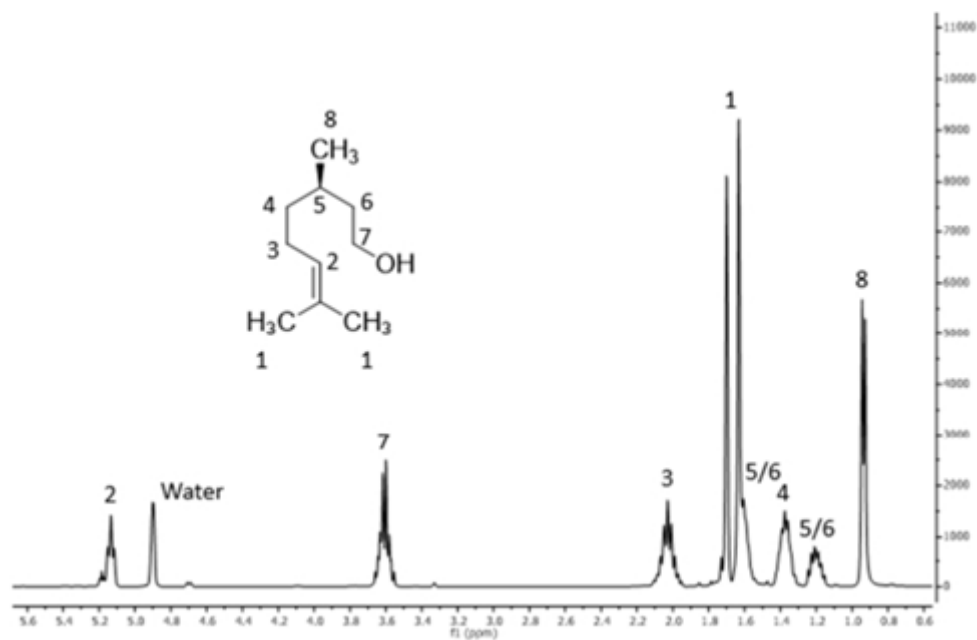


Figure S8.  $^1\text{H}$  NMR spectrum (400 MHz) of  $\alpha$ -terpinene **1b** in  $\text{CD}_3\text{OD}$ .



**Figure S9.** <sup>1</sup>H NMR spectrum (400 MHz) of ascaridole **2b** in CD<sub>3</sub>OD.



**Figure S10.** <sup>1</sup>H NMR spectrum (400 MHz) of citronellol **1c** in CD<sub>3</sub>OD.



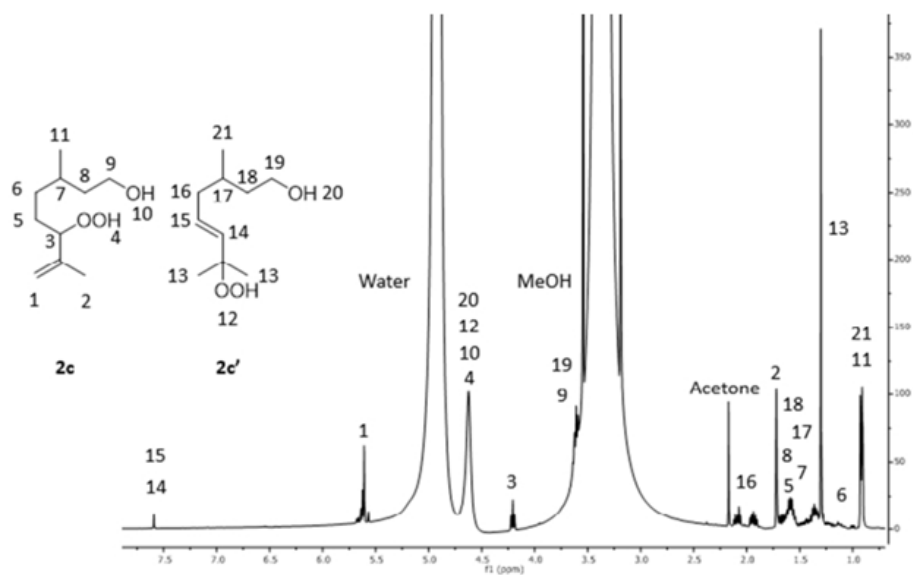


**Figure S11.**  $^1\text{H}$  NMR spectrum (400 MHz) of peroxides **2c,c'** in  $\text{CD}_3\text{OD}$ .

### 3 References

- (1) Wootton, R. C. R.; Fortt, R.; De Mello, A. J. *Org. Process Res. Dev.* 2002, 6 (2), 187–189.
- (2) Levesque, F.; Seeberger, P. H. *Org. Lett.* 2011, 13 (19), 5008–5011.

## **2.4. Improving Continuous Flow Singlet Oxygen Photooxygenations with Functionalized Mesoporous Silica Nanoparticles**

Homogeneous photocatalysis was selected for our experiments as it is the more straightforward catalysis technique and the easiest to perform, especially in flow where clogging is an issue. However, RB in homogeneous phase might not be the optimal catalyst for a robust process for the synthesis of methionine sulfoxide. To separate RB from the final product, activated charcoal was added to the solution and boiled for a few minutes before filtration. This purification was successfully performed during our experiments but has not been tested on industrial production scale with large quantities of RB. Furthermore, RB undergoes photobleaching when exposed to light and is thus irreversibly degraded. The purification technique coupled to this degradation makes it impossible to recycle RB for more than one oxidation in homogeneous phase.

Those advantages justify why the use of heterocatalysts for photooxidation is so widely reported. Although silica-supported RB and other metal-free heterocatalysts have already been described, their utilization in flow reactors is often limited to packed-bed catalysts to avoid clogging issues and to ease their recovering for multiple uses. However, we believe that clogging issue can be avoided by dispersing the particles in a sufficiently stable suspension.

The publication here under describes the preparation of mesoporous silica nanoparticles in which RB was incorporated, their use for flow photooxidation as well as their recycling for several consecutive oxidations. Hidden inside the porous shell, RB is indeed protected from excessive photobleaching which is also translated by a lower efficiency due to the difficulty for light to reach the catalyst. This efficiency loss was also reported in publications studying RB in heterocatalysts. Beside the recycling potential, this new catalyst could be functionalized to be grafted to the reactor walls and be removed from the feed solution.

### **2.4.1. General information and authors contributions**

This chapter is published:

Mendoza, C.; Emmanuel, N.; Páez, C. A.; Dreesen, L.; Monbaliu, J-C. M.; Heinrichs, B. Improving Continuous Flow Singlet Oxygen Photooxygenations with Functionalized Mesoporous Silica Nanoparticles. *ChemPhotoChem*. 2018, 2, 890-897. 8 citations (8 December 2020)

C. M. designed the chemistry, synthesized and characterized the nanoparticles, performed the experiments, analyzed the results and wrote the manuscript. N. E. designed the chemistry, performed the oxidation experiments, analyzed the results and wrote the manuscript. C. A. P. designed the chemistry, analyzed the results. L. D. revised the manuscript and secured funding for the project. J.-C. M. M. designed the chemistry, analyzed the results, supervised the project, wrote the manuscript and secured funding for the project. B. H. designed the chemistry, analyzed the results, supervised the project, revised the manuscript and secured funding for the project.

The figures, tables and references numbering of the section 2.4.2 correspond to the numbering of the article as published online.

## 2.4.2. Templated copy of the article

The content of this section, including figures, is copyrighted (2018 Wiley-VCH Verlag GmbH & Co. KGaA, Weinheim).

### Introduction

Despite its short-lived, metastable status, singlet oxygen ( $^1\text{O}_2$ ) has found applications in numerous areas ranging from depollution to photodynamic applications<sup>[1]</sup>.  $^1\text{O}_2$ -based photocatalytic oxidations have also emerged as model transformations in green and solar chemistry.<sup>[2]</sup>  $^1\text{O}_2$  is a convenient reagent for compound oxidation that easily forms carbon–oxygen and heteroatom–oxygen bonds. Photocatalytic oxygenations with a synthetic/preparative interest are receiving increasing attention, and have been implemented in conventional batch setups or under continuous flow conditions.<sup>[3,4]</sup>  $^1\text{O}_2$  is an electronically excited form of molecular dioxygen and is a powerful oxidant that usually has a short life time in solution.<sup>[1,5]</sup> Although different strategies do exist for the preparation of  $^1\text{O}_2$ , the most common method involves ground state triplet oxygen ( $^3\text{O}_2$ ), light and a photosensitizer (PS). PSs are commonly organic dyes bearing a (hetero)aromatic core such as Rose Bengal, Methylene Blue, Erythrosin B, porphyrins,<sup>[6]</sup> phthalocyanines, and related tetrapyrroles. Transition metal complexes such as  $[\text{Ru}(\text{bpy})_3]$  or Pt(II)-complexes have been reported as efficient PSs as well.<sup>[7,8]</sup>

Rose Bengal (RB) is a metal-free, non-toxic, and popular PS that shows intense absorption bands in the green region of the visible spectrum (480-550 nm), and is renowned for its high quantum yield ( $\phi_{\Delta} = 0.75$  in water) for the generation of  $^1\text{O}_2$ .<sup>[9]</sup> Despite its assets, RB suffers from extensive photobleaching/degradation under prolonged irradiation, and is usually difficult to remove from reactor effluents.<sup>[10,11]</sup> Regarding the use of RB under continuous flow photocatalytic conditions and the configuration of the flow setup, three main strategies emerge from the literature based on the use of (a) homogeneous PSs,<sup>[9,12]</sup> (b) packed-bed photoreactors with heterogeneous PSs embedded on the packing material<sup>[13]</sup> and (c) heterogeneous PSs concomitantly fed with the substrate.<sup>[14]</sup> Although each strategy comes with assets and drawbacks, the use of free flowing heterogeneous PSs is supposedly the most interesting option as far as (a) they are readily prepared, (b) do not accumulate within the micro/mesoreactor channels or cause clogging and (c) are easily removed downstream.

The recent literature has witnessed the development of various nanoparticles (NPs) such as  $\text{Ag}@\text{SiO}_2$  and  $\text{Au}@\text{SiO}_2$  core-shell NPs for the production of  $^1\text{O}_2$ ,<sup>[15,16]</sup> including examples where a PS is anchored on the NPs.<sup>[17]</sup> Mesoporous silica nanoparticles (MSNs) and hollow silica nanoparticles have attracted considerable attention over the last decade in particular for medical applications. Among the nanocarriers used in nanomedicine, MSNs can be used as drug delivery systems for the PS and they are of great interest in targeted photodynamic therapy (PDT) owing to their biocompatibility, high PS loading capacity, and ease of surface functionalization.<sup>[18]</sup> Moreover, the porous silica structure does not only act as a suitable carrier for hydrophobic molecules, but may also protect the loaded molecules from degradation. More specifically, the functionalization of MSNs with RB ( $\text{RB}@\text{MSNs}$ ) was demonstrated to increase resistance toward photobleaching and to reduce the formation of deleterious ground-state complexes,<sup>[19,20]</sup> and was successfully employed for photodynamic cancer therapy (PDT).<sup>[10,17,21]</sup> Both the heterogenization of the PS and its protection against extensive photobleaching are interesting assets for continuous flow photooxygenations. Either non-covalent or covalent anchorage can be utilized for PSs onto MSNs, although PS leakage remains a threat upon reaction for the former.<sup>[21]</sup>

We describe herein a unique approach combining the assets of continuous flow photochemistry with the advantages of heterogeneous, nanoparticle-supported photosensitizers for  $^1\text{O}_2$ -based oxygenations of organic substrates of preparative/synthetic value. RB@MSNs were prepared through the conjugation of amino-functionalized MSNs ((3-aminopropyl)triethoxysilane linker) and activated RB (HATU coupling). Both photocatalytic activity and stability were evaluated by comparing homogeneous RB and with RB@MSNs on model organic substrates. The results confirmed the assets of RB@MSNs for photocatalytic oxidation reactions of organic molecules under continuous flow conditions with a significant reduction of the photodegradation of the PS and a significant improvement for downstream processing. Various model organic substrates were tested, including bio-sourced methionine (**1a**)<sup>[9,22]</sup> and  $\alpha$ -terpinene (**1b**)<sup>[23]</sup> as well as 2-furoic acid (**1c**)<sup>[24]</sup> triphenylphosphine (**1d**)<sup>[13]</sup> citronellol (**1e**)<sup>[25]</sup> and cyclopentadiene (**1f**)<sup>[26]</sup>.

## Results and discussion

### 1. Synthesis and Characterization of RB@MSNs

MSNs were obtained according a procedure adapted from Planas et al<sup>[17]</sup>, and the covalent anchorage of RB toward RB@MSNs was carried out according a procedure adapted from Martins-Stevão et al<sup>[21]</sup> (see Experimental Section). RB@MSNs suspensions were completely stable without addition of any stabilizer. Bare MSNs showed a density of  $2.06 \text{ g}\cdot\text{cm}^{-3}$ . This value is lower than the theoretical density of  $\text{SiO}_2$  ( $2.65 \text{ g}\cdot\text{cm}^{-3}$ ) due to the absence of thermal treatment. Nitrogen adsorption isotherms were recorded for all the samples to analyze the filler of RB inside of the pores, as well as the pore size distribution (see Supporting Information, **Fig. S9**). The specific surface, pore volume and pore diameter are shown in Table 1.

Material	$S_{\text{BET}}$ [ $\text{m}^2\text{g}^{-1}$ ]	$V_p$ [ $\text{cm}^3\text{g}^{-1}$ ]	$d_p$ [nm]
MSNs	926.63	1.6296	2.96
RB@MSNs	256.77	0.8064	1.26

Dense  $\text{SiO}_2$  nanostructures commonly present a type II isotherm without hysteresis loop, while the MSNs obtained herein exhibited a typical type IV isotherm with a well-defined and narrow hysteresis loop, indicating its well-ordered mesostructure. The specific surface area of MSNs, calculated by the Brunauer-Emmett-Teller (BET) equation, was  $926.63 \text{ m}^2\cdot\text{g}^{-1}$ . The specific surface area ( $S_{\text{BET}}$ ) decreased in functionalized RB@MSNs by comparison to bare MSNs, as shown in Table 1. This reduction indicates that RB occupies the mesoporous channels of RB@MSNs, thus decreasing the total pore volume without complete clogging of the pores. The percentage of RB grafted to MSNs was estimated by thermogravimetric analysis<sup>[27-30]</sup> (see Supporting Information, Fig. S9b) after thorough washing sequences to remove any non-grafted RB (Soxhlet). RB@MSNs samples were preheated at  $350 \text{ }^\circ\text{C}$ , and the mass loss was measured between  $400 \text{ }^\circ\text{C}$  and  $800 \text{ }^\circ\text{C}$ . A low mass loss of 4.5% was measured with unfunctionalized MSNs, and this value was used as reference to obtain the actual concentration of RB in functionalized RB@MSNs. The latter showed an increased mass loss of 8% (corrected) in all cases due to the presence covalently anchored RB. This value corresponds to a concentration of  $82 \text{ }\mu\text{mol}\cdot\text{g}^{-1}$  and this concentration of 8 wt.% was used as an estimation to calculate the concentration of RB in the next experiments. The appearance of  $\text{CO}_2$  was followed by mass spectrometry and recorded in order to follow the disappearance of the attached RB, which occurred between  $450$  and  $650 \text{ }^\circ\text{C}$ . The heat flow gave information about the differences in the linkage between

SiO<sub>2</sub> and RB. Fig. 1 shows the recorded heat flow of RB@MSNs before washing between 200 and 700 °C.

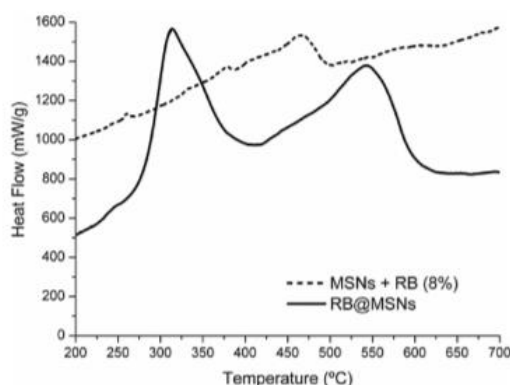


**Figure 1.** Heat flow of MSNs and RB (8%) without functionalization and RB@MSNs before washing in the thermogravimetric analysis.

The heat flow presented an individual exothermic peak at 465 °C when MSNs and 8% of RB are mixed mechanically (thus, without covalent link), while RB@MSNs produced 2 exothermic peaks. The first peak between 275 and 400 °C correspond to adsorbed RB that was removed after extensive washing, while the second peak between 430 and 626 °C (with a maximum at 544 °C) indicates the presence of a stable bond between RB and MSNs. <sup>13</sup>C Cross Polarization Magic Angle Spinning (CP MAS) NMR was used in order to confirm that RB preserves its integrity inside RB@MSNs and is chemically attached (Fig. 2a).

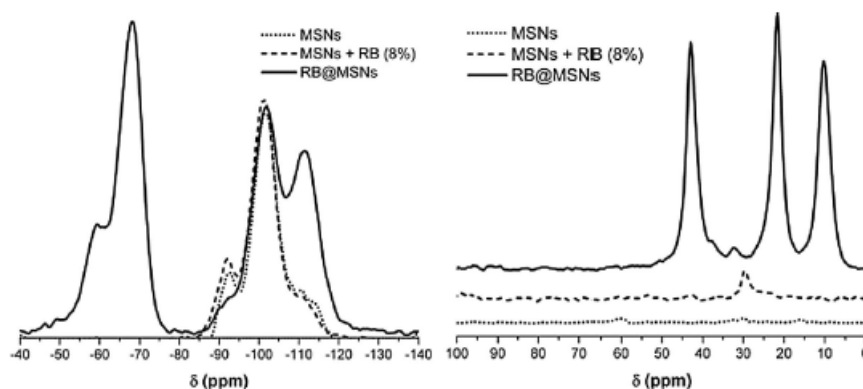


**Figure 2.** Solid state MAS NMR characterization of RB@MSNs. a) <sup>29</sup>Si MAS NMR and b) <sup>13</sup>C MAS NMR of unfunctionalized MSNs, unfunctionalized MSNs with RB (8%) and RB@MSNs.

The <sup>29</sup>Si MAS NMR spectrum of MSNs exhibits an individual band at -101 ppm attributed to Q<sup>3</sup> (Si(OH)(OSi)<sub>3</sub>) (Fig. 2b). For RB@MSNs, Q<sup>3</sup> is also present and Q<sup>4</sup> (Si(OSi)<sub>4</sub>) at 110 ppm indicates a link between SiO<sub>2</sub> and Si from APTES. The band at -65 ppm is assigned to T<sup>3</sup>-type silicon species having a Si-C covalent bond which is characteristic of APTES. In the 180 to -20 ppm range for the <sup>13</sup>C MAS NMR spectrum (Fig. 2a), no significant peaks were found in MSNs, while in RB@MSNs, the appearance of 5 signals confirmed the presence of RB. The peak assigned to carbonyl groups was at ~165 ppm, and the signal assigned to C-NH was at 43 ppm, thus confirming a covalent bond between the APTES linker and RB. The peak at 32 ppm corresponds to RB according to previously reported data.<sup>[21]</sup> The peaks at 22

and 8 ppm can be attributed to CH<sub>2</sub>-CH<sub>2</sub>-Si of the APTES precursor. No residual DMF was observed in RB@MSNs. The presence of the covalent bond was confirmed by FTIR spectroscopy (Fig. 3a), which showed the presence of a signal at 1413 cm<sup>-1</sup> attributed to the C-N stretching mode of amide II. C=O stretch of COO<sup>-</sup> was identified at 1393 cm<sup>-1</sup>. RB was also measured to discard the peaks corresponding to the dye. UV-Vis normalized spectra presented a bathochromic shift from 550 to 561 nm corresponding to RB and RB@MSNs, this shift to higher wavelengths indicated a different configuration of RB grafted to MSNs.

Representative TEM pictures are presented in Fig. 4, where it is possible to differentiate mesoporous structures of SiO<sub>2</sub> NPs. Their sizes were calculated in several areas of the sample obtaining an average of 43.7±0.9 and 44.1±0.7 nm for MSNs and RB@MSNs, respectively. The structure of the MSNs and RB@MSNs was also investigated by low angle powder X-ray diffraction (XRD) to demonstrate that mesoporous structure kept constant after functionalization (Supporting Information). As-synthesized MSNs exhibited one high-intensity reflection at 2θ = 0.55° and two additional higher-angle reflections in the region of 2θ close to 1.26 and 1.89 indexed as (100), (110) and (200), respectively (Fig. S10). After functionalization of RB at the inner and outer surface of MSNs, RB@MSNs showed similar diffraction peaks excepting (110), which disappeared when RB is attached to SiO<sub>2</sub>.

EPR/TEMP was then measured with RB (0.45 mM) in solution and RB@MSNs using the same amount of RB and irradiated with a halogen lamp. No TEMPO signal was detected with MSNs. However, RB and RB@MSNs showed three characteristic peaks of TEMPO (Fig. 5), which are related with <sup>1</sup>O<sub>2</sub> production. Intensity of the peaks was similar for RB and RB@MSNs samples, thus showing the generation of <sup>1</sup>O<sub>2</sub> with heterogeneous systems.

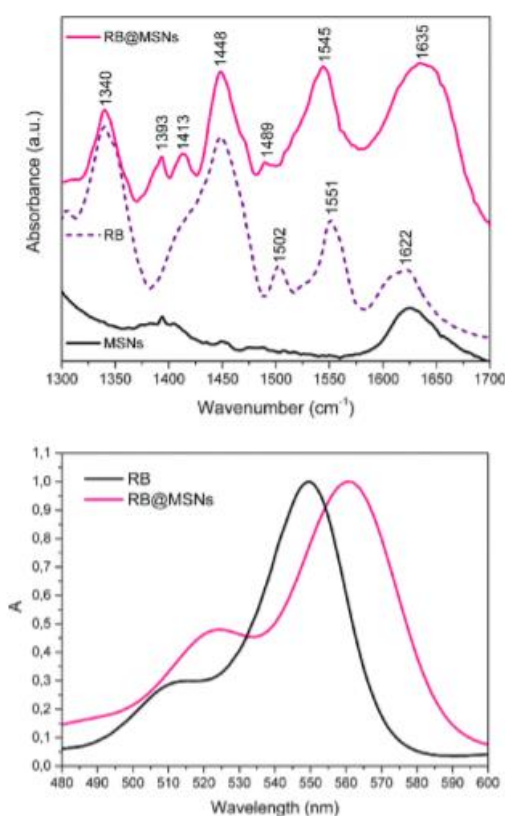


**Figure 3.** a) FTIR spectra and b) UV-Vis spectra of RB and RB@MSNs.

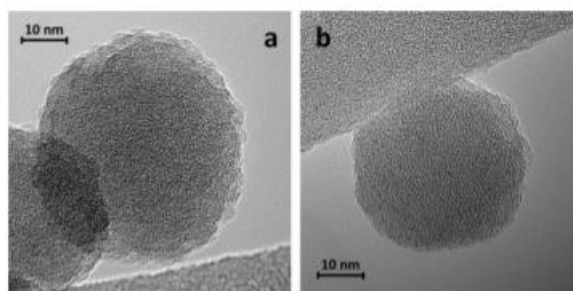


**Figure 4.** TEM images of a) MSNs, b) RB@MSNs.

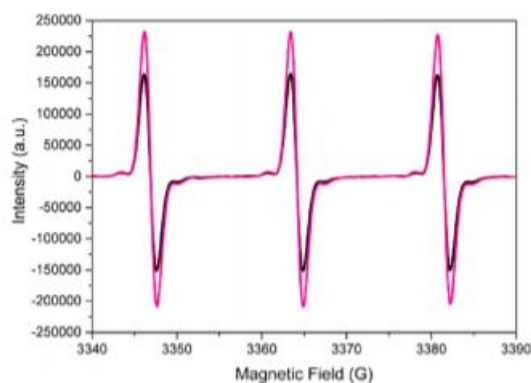


**Figure 5.** EPR/TEMP spectra for aqueous solutions (0.45 mM) of a) free RB (black line) and b) RB@MSNs (pink line).

## 2. Study of the photodegradation of free RB and RB@MSNs

Four different samples were prepared, and irradiated at 540 nm under aerobic conditions for up to 240 min. The first solution contained free RB in water (Fig. 6a), the second was similar to the previous one but in this case with a concentration of 0.1 M of **1a** (Fig. 6b).<sup>[22]</sup> The third solution was prepared with RB@MSNs in water (Fig. 6c) and the last suspension with RB@MSNs and 0.1 M of **1a** (Fig. 6d). It is worth mentioning that RB@MSNs colloidal suspensions were stable without addition of any stabilizer. The concentration of RB was similar in all cases (0.001 mM).

The absorption maximum of RB in a 0.001 mM aqueous solution was localized at 549 nm with a shoulder at 512 nm. As shown in Fig. 6a, free RB in water was completely photodegraded after 3 h, giving an orange solution. The characterization of the side products was not attempted. The photodegradation occurred rapidly when **1a** was added to the RB solution (Fig. 6b), with a complete degradation in 60 min, leading to a transparent solution. It could be explained with the formation of ground state complexation between **1a** and RB, similarly to what was reported for tryptophan-RB.<sup>[20]</sup> The absorption maximum and the shoulder were shifted to 560 nm and 523 nm, respectively for RB in RB@MSNs and molar extinction coefficient decreased from 130.000 to 17.000 M<sup>-1</sup>·cm<sup>-1</sup> for RB and RB@MSNs, respectively due to Rayleigh dispersion, which decreased the absorbance maximum. Most importantly, the photodecomposition of RB was significantly reduced: only 78% of photodegradation was measured after 4 h of irradiation of a suspension of RB@MSNs (Fig. 6c). After irradiation, the solution kept a bright pink color, thus supporting the reduced photobleaching and the protection effect of SiO<sub>2</sub>. Fig. 6d corresponds to the evolution of the UV spectra of a **1a** solution (0.1 M) in the presence of suspension with RB@MSNs (0.001 mM of RB), for which neither degradation nor change of color were observed after 2 h irradiation.

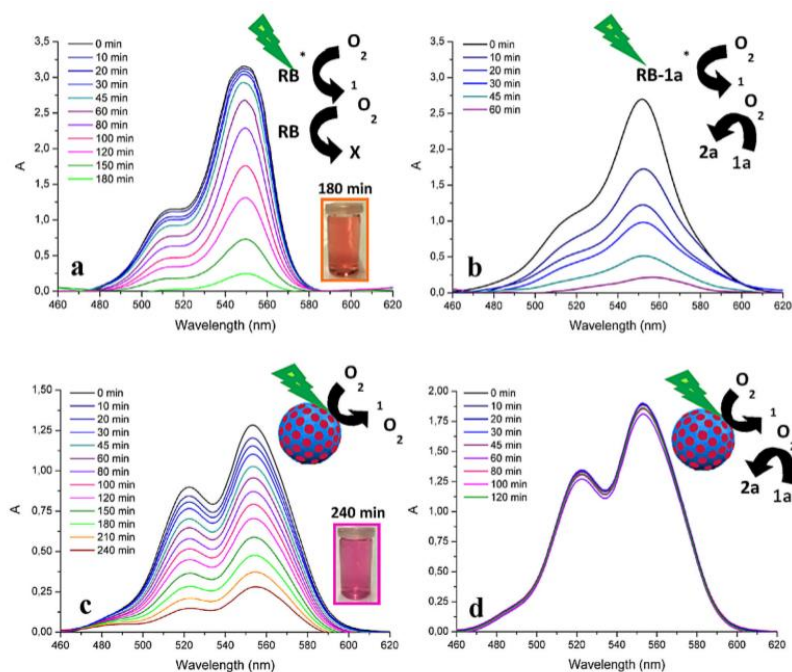


**Figure 6.** Evolution of the UV-Vis spectra as a function of the time for aqueous solutions of a) free RB b) free RB with **1a**, c) RB@MSNs and d) RB@MSNs with **1a**.

### 3. Photocatalytic singlet oxygen oxidation under microfluidic conditions

Building upon these promising results, the photocatalytic oxygenation of **1a** using RB@MSNs was attempted under continuous flow conditions in a microfluidic setup (see full description in the experimental section) constructed from PFA capillaries and using green LEDs as light source. The irradiation setup featured 12 green LEDs (see Experimental Section for details) mounted on 4 heat exchangers surrounding the PFA capillary coil. A pressure regulator (set point: 8.5 bar) was inserted downstream the irradiation module. The microfluidic device was operated at room temperature. The first trials were attempted with a simplified setup (Figure 7).

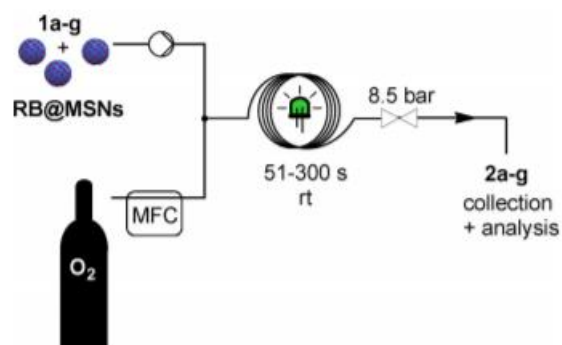


**Figure 7.** Microfluidic setup for the heterogeneous photooxygenations. MFC stands for mass flow controller. See Table 2 for detailed experimental conditions

The photocatalytic oxidation of **1a** to **2a** under aerobic conditions was used as a model reaction<sup>[22]</sup> to evaluate the viability and the efficiency of RB@MSNs for the production of  $^1\text{O}_2$  in water (Table 2, Entry 1). The performance of the reaction with RB@MSNs was compared with the homogeneous conditions using unsupported RB. The degradation of RB and the conversion of **1a** were monitored by UV-Vis and  $^1\text{H}$  NMR, respectively (Fig. 8).



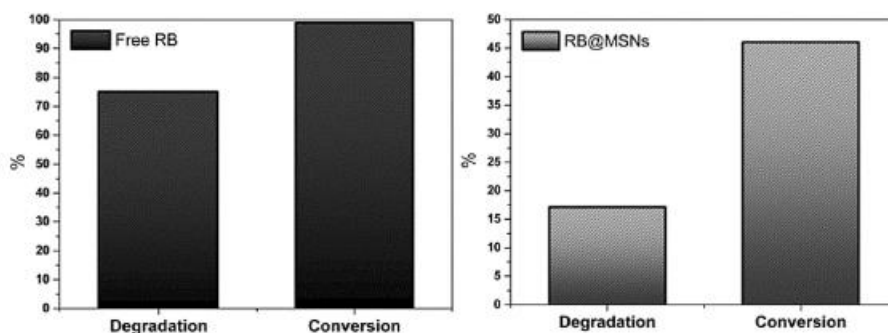


**Figure 8.** RB degradation and **1a** conversion for free RB and RB immobilized in MSNs using a residence time of 72 s under continuous flow microfluidic conditions

**Table 2.** Residence time and photooxygenation conversion obtained for the different substrates ([RB] = 0.45 mM).

Entry	Substrate	Product	$t_R$ [s]	Conv. [%]
1 <sup>[a]</sup>	methionine <chem>CSCCC(N)C(=O)O</chem>	methionine sulfoxide <chem>CSC(=O)CC(N)C(=O)O</chem>	72	47
2 <sup>[b]</sup>	<b>1 a</b> $\alpha$ -terpinene <chem>CC1=CC=C(C)C=C1</chem>	<b>2 a</b> ascaridole <chem>CC1=CC=C(C)C=C1</chem>	72	90
3 <sup>[b]</sup>	<b>1 b</b> 2-furoic acid <chem>O=C(O)c1ccoc1</chem>	<b>2 b</b> 5-hydroxy-2(5H)-furanone <chem>O=C(O)c1cc(O)oc1</chem>	72	8
4 <sup>[c]</sup>	<b>1 c</b> triphenylphosphine <chem>P(c1ccccc1)(c1ccccc1)c1ccccc1</chem>	<b>2 c</b> triphenylphosphine oxide <chem>P(=O)(c1ccccc1)(c1ccccc1)c1ccccc1</chem>	300	55
5 <sup>[b]</sup>	<b>1 d</b> citronellol <chem>CC(C)=CC(C)CO</chem>	<b>2 d</b> allyl hydroperoxide <chem>CC(C)=CC(C)OO</chem>	72	26
6 <sup>[b]</sup>	<b>1 e</b> cyclopentadiene <chem>C1=CC=CC1</chem>	<b>2 e</b> <i>cis</i> -2-cyclopentene-1,4-diol <chem>O=C1C=CC(O)C1O</chem>	51	quant.
	<b>1 f</b> <chem>C1=CC=CC1</chem>	<b>2 f</b> <chem>O=C1C=CC(O)C1O</chem>		

[a] H<sub>2</sub>O; [b] MeOH; [c] (CH<sub>3</sub>)<sub>2</sub>CO.

Regarding the conversion of **1a** to **2a**, the reaction was completed within 72 s of residence time using homogeneous conditions (free RB, 0.1 M solution of **1a**). Under these conditions, however, RB underwent extensive photodegradation (Fig. 8a). With RB@MSNs, a lower efficiency of photooxygenation was observed under the same microfluidic conditions, as a consequence of the reduction of the light absorption (Fig. 8b). The photostability of RB on RB@MSNs was however much improved, with a significant reduction from of photobleaching from 75 to 17%, emphasizing the protective effect of the incorporation of RB into MSNs. The solutions collected at the outlet were also centrifuged in order to demonstrate that RB did not leach and remained anchored on RB@MSNs (see Supporting Information).

The next set of trials was attempted in methanol on  $\alpha$ -terpinene (**1b**), the photooxidation of which led to ascaridole (**2b**), biologically active nature bicyclic monoterpene. The photooxygenation of **1b** into **2b** provided a higher conversion (90%) than for **1a** under similar conditions (Table 2, Entry 2). In order to assess potential recyclability and durability of the RB@MSNs, a series of photooxidations were attempted while recovering and reusing the same RB@MSNs. The reactor effluent was collected, and processed to recover the RB@MSNs, which were next reused for carrying out a new photooxidation run. Conversion toward **2b**, as well as photodegradation of RB, were determined after each cycle. A series of four photooxygenation runs were carried on with the same recycled RB@MSNs, and Fig. 9 summarizes both conversion and photodegradation. Complete photodegradation occurred after a 72 s fourth run.

The conversion remained almost constant for the two first cycles, i.e. 90% and 86% respectively, and dropped to 62% for the third cycle. Compound **2b** was not be detected during the fourth oxygenation cycle. The RB degradation obtained after the first cycle was 45% and it increased to 63% and 77% after the second and third cycles, respectively. Comparing with **1a** experiments, RB degradation was higher in this case and this increase is related with the improvement in the conversion. The production of **2b** remains high during the third cycle, while the degradation is 77%. It could indicate an initial photodegradation of the RB attached to the surface of MSNs and the protection of the RB that is filling the mesopores during the first cycles. In addition, it should be noted that RB@MSNs were centrifuged and dried after each cycle of photooxygenation that could have affected to the dispersion of the NPs producing their agglomeration and therefore the decrease of their efficiency. These results highlight the reusable character of the RB@MSNs allowed by their protective spot inside mesopores which lower photodegradation for at least two photooxygenation cycles.

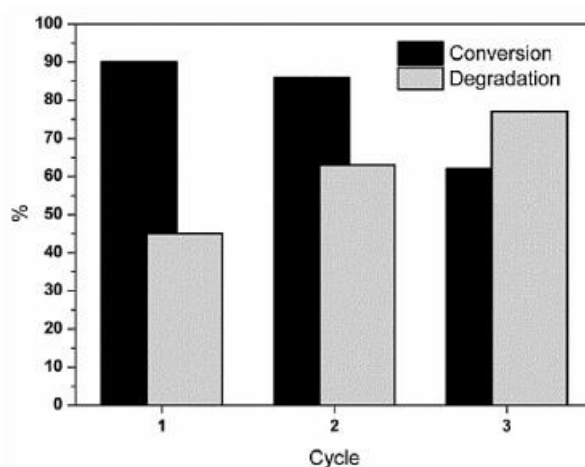


**Figure 9.** Conversion of  $\alpha$ -terpinene and RB photodegradation after 1, 2 and 3 cycles

The same model reaction was next evaluated in a more complex setup including in-line, downstream membrane separation (Figure 10). The setup included two pumps for the injection of the substrate (**1b**, 0.1 M in toluene) and for the colloidal suspension of RB@MSNs (0.45 mM in water), respectively. Both liquid feeds were mixed through a T-static mixer upstream the reactor, leading to a **2b** stable Taylor flow. Oxygen was injected next, before the irradiation module, through a mass-flow controller. A pressure regulator was inserted between the irradiation module and the membrane separator equipped with a hydrophobic 0.5  $\mu\text{m}$  porous membrane. Liquid separation occurs through differential wettability of the membrane, and the organic stream (toluene) was continuously separated from the aqueous stream containing the RB@MSNs. The breakthrough of water in the organic stream is typically as low as 20 ppm (Karl Fisher titration). Since the aqueous stream containing the RB@MSNs does not cross the membrane, there is limited risk of clogging, and the membrane separator could be operated

for several hours, affording ascaridole in toluene free from RB and nanoparticles. The excess oxygen was eliminated with the aqueous stream. The conversion of **1b** to ascaridole (**2b**) reached completion within 180 s of residence time upon irradiation at 540 nm.

Various substrates were used to evaluate the photooxygenation efficiency of RB@MSNs (Table 2, Entry 3-6) (**1a-1f**). Table 2 collects the conversion obtained as a function of the molecular structure of the substrates and products. The nature of the substrate had a profound impact on the photooxygenation efficiency. The photooxygenation of **1e** provided a mixture of allyl hydroperoxide isomers **2e** (26% conversion for both), peroxides that could lead to rose oxide after additional steps. For **1b**, the endoperoxide **2b** was produced. However, **1f** photooxygenation reaction was performed to yield **2f** in the presence of thiourea to reduce in situ the unstable endoperoxide intermediate inducing the reduction of the peroxide bond and the production of the two alcohol groups. These results emphasized RB@MSNs as a superior heterogeneous photosensitizer for the photooxygenation of **1a**, **1b**, **1d** and **1f**, which can be recovered from the microreactor effluent and recycled as shown in the durability test.

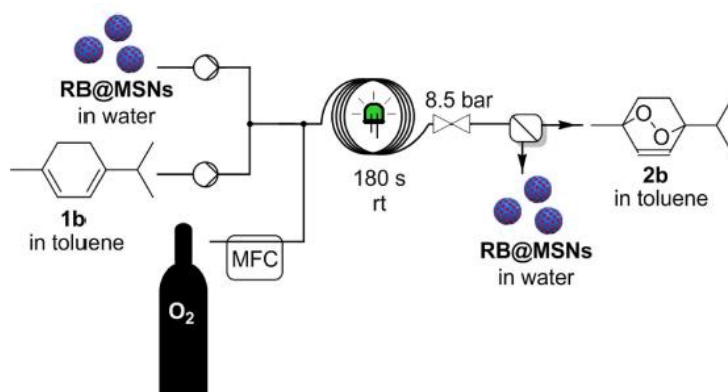


**Figure 10.** Microfluidic setup for the heterogeneous photooxygenations featuring in-line, continuous membrane separation.

## Conclusion

The results herein document the use of covalently anchored RB on mesoporous silica nanoparticles for applications under photocatalytic microfluidic conditions. The results emphasize that covalent anchorage of RB on silica nanoparticles decreases its sensitivity to photobleaching, while maintaining high levels of photooxidation. The heterogenization of RB significantly improves the processability of the reactor effluent, and eases the separation process. The separation process can be automated with a membrane separator, providing convenient alternative to manual downstream separation. In addition of the ease of recovery, RB@MSNs are reusable to some extent. Various organic substrates of synthetic or preparative value were photooxidized with moderate to excellent yield within 72 to 300 s of residence time.

## Experimental section

### 1. Functionalized Mesoporous SiO<sub>2</sub>-RB NPs

To obtain RB@MSNs, the methods adapted from Planas<sup>[17]</sup> and Martins-Stevao<sup>[21]</sup> were utilized. A solution of CTAB (cetyltrimethylammonium bromide, 5.81 g, 16.9 mmol) was prepared in a mixture of 130 mL of deionized H<sub>2</sub>O, 25 mL of EtOH, and 250 mL NH<sub>3</sub> (30% aq.), and was stirred for 30 min at 488 °C. Then, 15 mL of TEOS (tetraethyl orthosilicate, 67.2 mmol) were added dropwise, and the solution was stirred during 2 h at r.t. The resulting suspension was kept without stirring for 24 h at room

temperature, and the template was removed with 40 mL of HCl (wt. 37%). MSNs were centrifuged for 30 min at 6000 rpm and washed three times with 50 mL EtOH. Afterwards, MSNs were dispersed in 50 mL of isopropanol, and 1 mL of APTES ((3-aminopropyl)triethoxysilane, 4.27 mmol) was added. The resulting solution was stirred 24 h to obtain a complete amino-functionalization. MSNs-NH<sub>2</sub> were centrifuged and washed twice with ethanol. MSNs-NH<sub>2</sub> were next dispersed in 100 mL of DMF (dimethylformamide). This solution was then mixed with 200 mL of a RB (0.19 mmol) solution in DMF. 0.075 g of HATU ((1-[bis(dimethylamino)methylene]-1H-1,2,3-triazolo[4,5-b]pyridinium 3-oxid hexafluorophosphate, 0.20 mmol) and 80 mL of DIPEA (diisopropylethylamine, 0.46 mmol) were added to induce the coupling, and the resulting reaction mixture was stirred for 24 h. RB@MSNs were recovered by centrifugation and washed with acetone to remove unreacted RB until a colorless supernatant was obtained.

## 2. Characterization of RB@MSNs

The density of RB@MSNs was measured by helium pycnometry using an Accupyc II 1330 pycnometer. The textural features of unfunctionalized MSNs and of functionalized RB@MSNs were assessed by nitrogen adsorption-desorption data acquired on a Micromeritics ASAP 2420 MP. Prior to measurements, the samples were degassed at 300 °C to remove unreacted Rose Bengal. The specific surface area was calculated using the Brunauer-Emmet-Teller (BET) method. The total pore volume was determined from the amount of gas adsorbed at a relative pressure of 0.99 and the pore size distribution was obtained using the Barret-Joyner-Halenda (BJH) desorption method. All calculations were determined from the DFT method, provided with the software of the apparatus. Thermogravimetric measurements were performed on a Setaram Sensys Evo microbalance under air with a heating flow rate of 3 °C min<sup>-1</sup> to estimate the functionalization ratio of RB@MSNs (Figure S9). Unfunctionalized MSNs, unfunctionalized MSNs with RB (8%) and RB@MSNs were also characterized by solid state Nuclear Magnetic Resonance (ss<sup>13</sup>C and <sup>29</sup>Si NMR) recorded on a Bruker Avance III 400 MHz spectrometer. FTIR measurements were carried out using a Perkin Elmer Spectrum One FTIR Spectrometer in a wavelength range of 4000–450 cm<sup>-1</sup>. Transmission electron microscopy pictures were collected using a FEI Tecnai G2 20 TWIN instrument operating at 200 kV, which enabled size calculation for MSNs and RB@MSNs. Mesoporous structure of MSNs and RB@MSNs was also investigated by low angle powder X-ray diffraction (XRD) on a Siemens D-5000 diffractometer (Cu K- $\alpha$  radiation, 40 kV, 40 mA). EPR was employed to evaluate the photogeneration of <sup>1</sup>O<sub>2</sub>, which reacts with 2,2,6,6-tetramethylpiperidine (TEMP) leading to the paramagnetic 2,2,6,6-tetramethyl-4-piperidone-N-oxyl radical (TEMPO). RB, and RB@mSiO<sub>2</sub> solutions were prepared with the same amount of RB (0.045 mM). The samples were irradiated with an halogen lamp (Figure S11b) measured under normal conditions, with 100 kHz magnetic field modulation, 22 mW microwave power and 1.0 G modulation amplitude in a Bruker EMX Plus spectrometer.

## 3. Photodegradation of Free RB and RB@MSNs

Photobleaching of RB was monitored by UV-Vis (Genesys 10S UV-Vis spectrometer) on free RB and RB@MSNs exposed to 540 nm irradiation (green LEDs) (Figure S8) under aerobic conditions in a batch setup. The setup consisted of a 50 mL vessel irradiated with 12 green LEDs (540 nm, LZ1-00G102, Led Engin) mounted on 4 heat exchangers. The reactor was fed with a stream of pure O<sub>2</sub> (1 bar, and 15 mL min<sup>-1</sup> of O<sub>2</sub>). The photodegradation of RB was tested in the presence of model substrate **1a**. Four aqueous samples were prepared a) free RB, b) RB and 0.1 M **1a**, c) RB@MSNs and d) RB@MSNs and 0.1 M **1a**. All samples were prepared with a similar concentration of RB (0.001 mM), and their UV-Vis spectra were recorded at different irradiation times.

#### 4. Continuous Flow Setup and General Procedure for the Photocatalytic $^1\text{O}_2$ Oxygenation of Organic Substrates under Continuous Flow Conditions

The continuous flow setup for the photocatalytic  $^1\text{O}_2$  oxygenation of organic substrates was constructed from high purity PFA capillaries (800  $\mu\text{m}$  internal diameter) wrapped in coils around a reflective, thermoregulated aluminum cylinder (Figure 12 in the Supporting Information). The PFA coils were surrounded by 4 adjustable heat-sink integrated pillars each supporting 3 high power LEDs (540 nm, LZ1-00G102, Led Engin) (Figure S8). The LEDs were mounted to face towards the PFA coil wrapped around the central cylinder. Oxygen (AirLiquide, Alphagaz 1) and the liquid feed solution were injected through a static mixer (T-Mixer, IDEXUpchurch, natural PEEK 1/4-28 thread for 1/16" o.d. tubing, 0.02" through hole) placed upstream the irradiation coil. Chemyx Nexus 6000 syringe pumps were used to handle the suspension containing the organic substrate and RB@MSNs (loaded into a 20 mL SS Chemyx syringe). The syringe pump was set at the appropriate flow rate, and  $\text{O}_2$  was delivered with a Bronkhorst F210CTM mass flow controller. A dome-type back-pressure regulator (BPR, Zaiput Flow Technologies) was inserted downstream and connected to a cylinder of compressed Argon (set point: 8.5 bar). A membrane separator (Zaiput Flow Technologies) equipped with a 0.5  $\mu\text{m}$  PTFE hydrophobic membrane was inserted downstream in some experiments.

##### 4.1. Photocatalytic Oxygenation of Methionine

The photocatalytic oxygenation of methionine **1a** to methionine sulfoxide **2a** was used as model reaction to evaluate the efficiency in the production of  $^1\text{O}_2$  using RB@MSNs in a microfluidic reactor setup operated in continuous flow. A feed solution containing a 0.1 M aqueous solution of L-methionine **1a** and RB@MSNs (0.45 mM RB) was employed. Typically, the feedstock solution was prepared by dissolving L-methionine (TCI, >99%, 1.49 g) in 100 mL of D.I. water, and then mixed with 8 mL of a RB@MSNs aqueous suspension (13  $\text{mg mL}^{-1}$ ). The stock solution with 1  $\text{mg mL}^{-1}$  of RB@MSNs was loaded into a 20 mL 316 Stainless Steel syringe. The syringe pump was set at 0.1  $\text{mL min}^{-1}$  and the gas controller at 12  $\text{mL min}^{-1}$ . The solution was collected at the end of the reactor and was then centrifuged to separate RB@MSNs from the supernatant. The reaction was monitored by off-line  $^1\text{H}$  NMR recorded on a Bruker Avance III 400 MHz spectrometer (See Supporting Information for details).

##### 4.2. Photocatalytic Oxygenation of $\alpha$ -Terpinene

The general procedure described above was followed. A 0.1 M solution of  $\alpha$ -terpinene **1b** in methanol containing 0.45 mM of RB@MSNs was loaded in a 20 mL SS syringe, and injected in the reactor at a flow rate of 0.1  $\text{mL min}^{-1}$  along with pure  $\text{O}_2$  delivered at 12  $\text{mL min}^{-1}$ . The solution was collected at the end of the reactor and was then centrifuged to separate RB@MSNs from the supernatant. The reaction was monitored by off-line  $^1\text{H}$  NMR recorded on a Bruker Avance III 400 MHz spectrometer (See Supporting Information for details). In a series of experiences dedicated to recycling the RB@MSNs, the reactor effluent was collected and centrifuged to separate RB@MSNs from the supernatant (Figure S11). The RB@MSNs were washed twice with pure methanol, and then reutilized for another photocatalytic oxygenation.

##### 4.3. Photocatalytic Oxygenation of $\alpha$ -Terpinene, Including Downstream In-Line Continuous Membrane Separation

The general procedure described above was modified as follow: a 0.1 M solution of  $\alpha$ -terpinene **1b** in toluene and a colloidal suspension of RB@MSNs in water were loaded in two separate 20 mL SS syringes. Both solutions were injected at a flow rate of 0.1  $\text{mL min}^{-1}$ , and then mixed with a pure stream of  $\text{O}_2$  delivered at 2  $\text{mL min}^{-1}$ . The multiphasic mixture was then reacted within a PFA coil upon irradiation at 540 nm for 180 s. The two outlets of the membrane separator were connected to

collection vials, and the organic stream was processed and analyzed by off-line  $^1\text{H}$  NMR recorded on a Bruker Avance III 400 MHz spectrometer (See Supporting Information for details).

#### 4.4. Photooxygenation of Other Substrates of Synthetic/Preparative Value

0.1 M solutions of **1c**, **1d**, **1e** and **1f** were prepared in different solvents (see Table 2) containing 0.45 mM of RB attached to MSNs as described previously and the collected suspension was analyzed by offline  $^1\text{H}$  NMR to obtain the conversion of the different tests. A back-pressure regulator (BPR) set at 8.5 bar was inserted downstream.

#### References

- [1] M. C. DeRosa, R. J. Crutchley, *Coord. Chem. Rev.* 2002, 233–234, 351–371.
- [2] H. P. L. Gemoets, Y. Su, M. Shang, V. Hessel, R. Luque, T. Nol, *Chem. Soc. Rev.* 2016, 45, 83–117.
- [3] D. Cambie, C. Bottecchia, N. J. W. Straathof, V. Hessel, T. Nol, *Chem. Rev.* 2016, 116, 10276–10341.
- [4] A. A. Ghogare, A. Greer, *Chem. Rev.* 2016, 116, 9994–10034.
- [5] P. R. Ogilby, *Chem. Soc. Rev.* 2010, 39, 3181–3209.
- [6] M. Lismont, L. Dreesen, B. Heinrichs, C. A. Paez, *Photochem. Photobiol.* 2016, 92, 247–256.
- [7] S. Kobayashi, H. Miyamura, R. Akiyama, T. Ishida, *J. Am. Chem. Soc.* 2005, 127, 9251–9254.
- [8] A. Casado-Sanchez, R. Gomez-Ballesteros, F. Tato, F. J. Soriano, G. Pascual-Coca, S. Cabrera, J. Aleman, *Chem. Commun.* 2016, 52, 9137–9140.
- [9] N. Emmanuel, C. Mendoza, M. Winter, C. R. Horn, A. Vizza, L. Dreesen, B. Heinrichs, J.-C. M. Monbaliu, *Org. Process Res. Dev.* 2017, 21, 1435–1438.
- [10] E. Gianotti, B. Martins Estevao, F. Cucinotta, N. Hioka, M. Rizzi, F. Reno, L. Marchese, *Chem. Eur. J.* 2014, 20, 10921–10925.
- [11] C. Whitmire, *Photosensitizers: Types, Uses and Selected Research*, 2016, Nova Science Publishers.
- [12] K. N. Loponov, J. Lopes, M. Barlog, E. V. Astrova, A. V. Malkov, A. A. Lapkin, *Org. Process Res. Dev.* 2014, 18, 1443–1454.
- [13] C. J. Kong, D. Fisher, B. K. Desai, Y. Yang, S. Ahmad, K. Belecki, B. F. Gupton, *Bioorg. Med. Chem.* 2017, 25, 6203–6208.
- [14] T. Carofiglio, P. Donnola, M. Maggini, M. Rossetto, E. Rossi, *Adv. Synth. Catal.* 2008, 350, 2815–2822.
- [15] M. Lismont, C. A. Paez, L. Dreesen, *J. Colloid Interface Sci.* 2015, 447, 40–49.
- [16] H. H. Lin, I. C. Chen, *J. Phys. Chem. C.* 2015, 119, 26663–26671.
- [17] O. Planas, N. Macia, M. Agut, S. Nonell, B. Heyne, *J. Am. Chem. Soc.* 2016, 138, 2762–2768.
- [18] B. J. Jankiewicz, D. Jamiola, J. Choma, M. Jaroniec, *Adv. Colloid Interface* 2012, 170, 28–47.
- [19] T. Nakamura, A. Son, Y. Umehara, T. Ito, R. Kurihara, Y. Ikemura, K. Tanabe, *Bioconjugate Chem.* 2016, 27, 1058–1066.
- [20] S. Criado, S. G. Bertolotti, N. A. Garcia, *J. Photochem. Photobiol. B* 1996, 34, 79–86.

- [21] B. Martins Estevao, F. Cucinotta, N. Hioka, M. Cossi, M. Argeri, G. Paul, L. Marchese, E. Gianotti, *Phys. Chem. Chem. Phys.* 2015, 17, 26804–26812.
- [22] C. Mendoza, N. Emmanuel, C. A. Paez, L. Dreesen, J.-C. M. Monbaliu, B. Heinrichs, J. Photochem. Photobiol. A 2018, 356, 193–200.
- [23] F. Ronzani, N. Costarramone, S. Blanc, A. K. Benabbou, M. Le Behec, T. Pigot, M. Oelgemöller, S. Lacombe, *J. Catal.* 2013, 303, 164–174.
- [24] M. Drhova, S. Hejda, J. Kristal, P. Kluson, *Procedia Eng.* 2012, 42, 1365–1372.
- [25] S. Meyer, D. Tietze, S. Rau, B. Schäfer, G. Kreisel, *J. Photochem. Photobiol. A* 2007, 186, 248–253.
- [26] B. K. Jähnisch, U. Dingerdissen, *Chem. Eng. Technol.* 2005, 426–427.
- [27] W. Li, Y. Xu, Y. Zhou, W. Ma, S. Wang, Y. Dai, *Nanoscale Res. Lett.* 2012, 7, 485.
- [28] D. Sarma, K. Gawlitza, K. Rurack, *Langmuir* 2016, 32, 3717–3727.
- [29] I. Rosa-Pardo, M. Roig-Pons, A. A. Heredia, J. V. Usagre, A. Ribera, R. E. Galian, J. Pérez-Prieto, *Nanoscale* 2017, 9, 10388–10396.
- [30] Y. Y. Ma, H. X. Huang, M. Chen, D. J. Qian, *J. Lumin.* 2018, 203, 277–285.

## Supporting information

The figure numbering of these supporting information corresponds to the numbering of the supporting information found online.

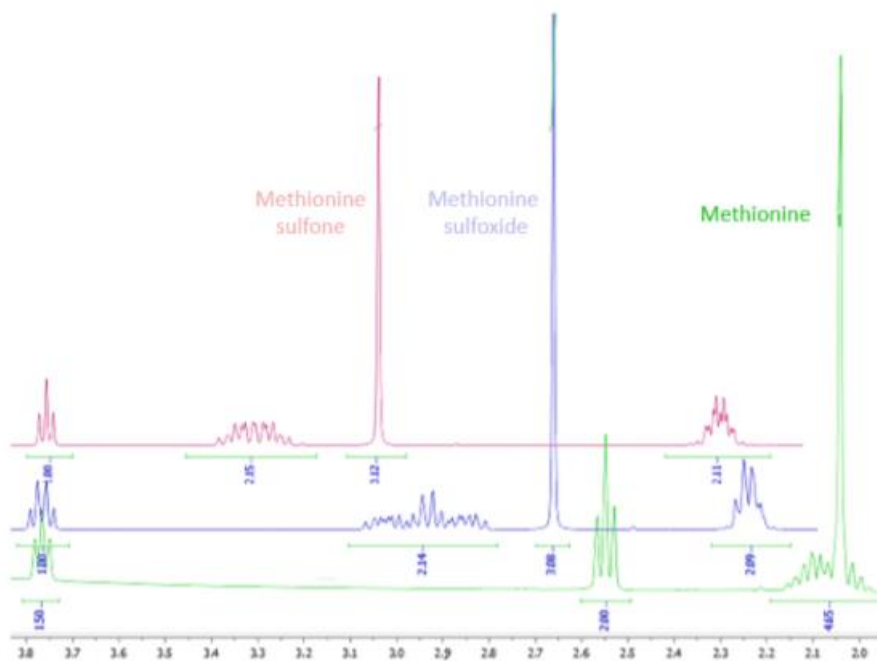


Fig. S1. <sup>1</sup>H NMR spectra (400 MHz, D<sub>2</sub>O) of **1a**, **2a** and methionine sulfone



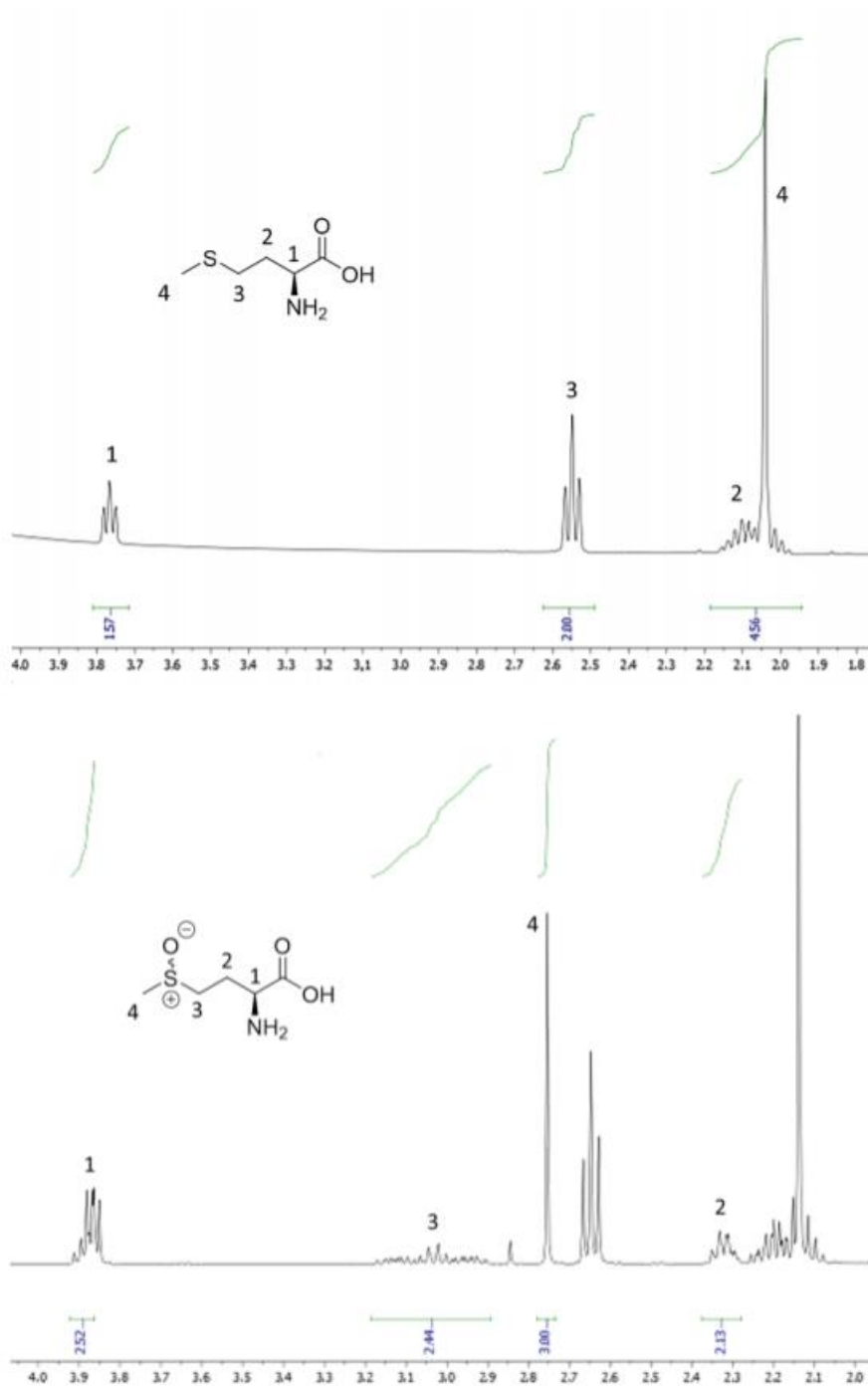


Fig. S2.  $^1\text{H}$  NMR spectra (400 MHz,  $\text{D}_2\text{O}$ ) of substrate **1a** and product **2a**

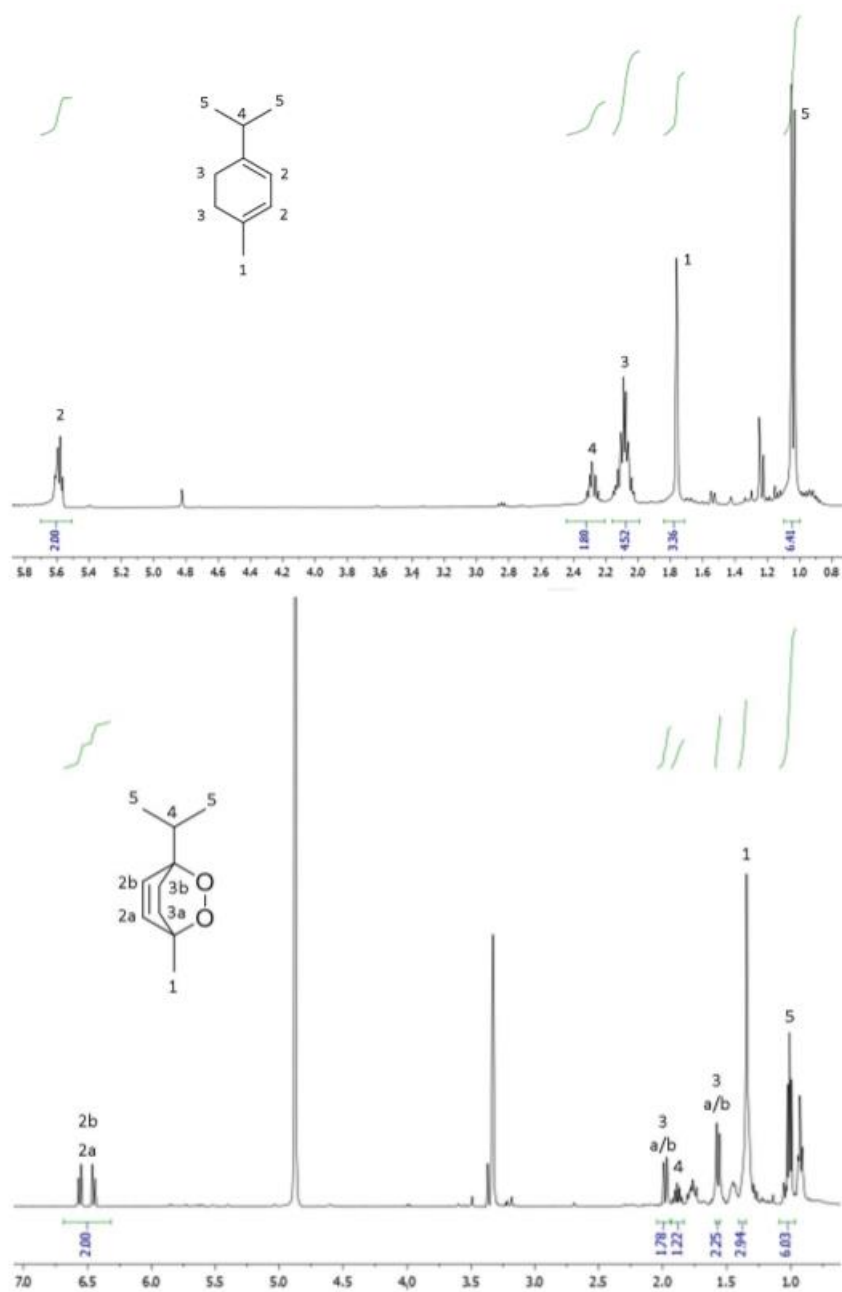


Fig. S3. <sup>1</sup>H NMR spectra (400 MHz, CD<sub>3</sub>OD) of substrate **1b** and product **2b**

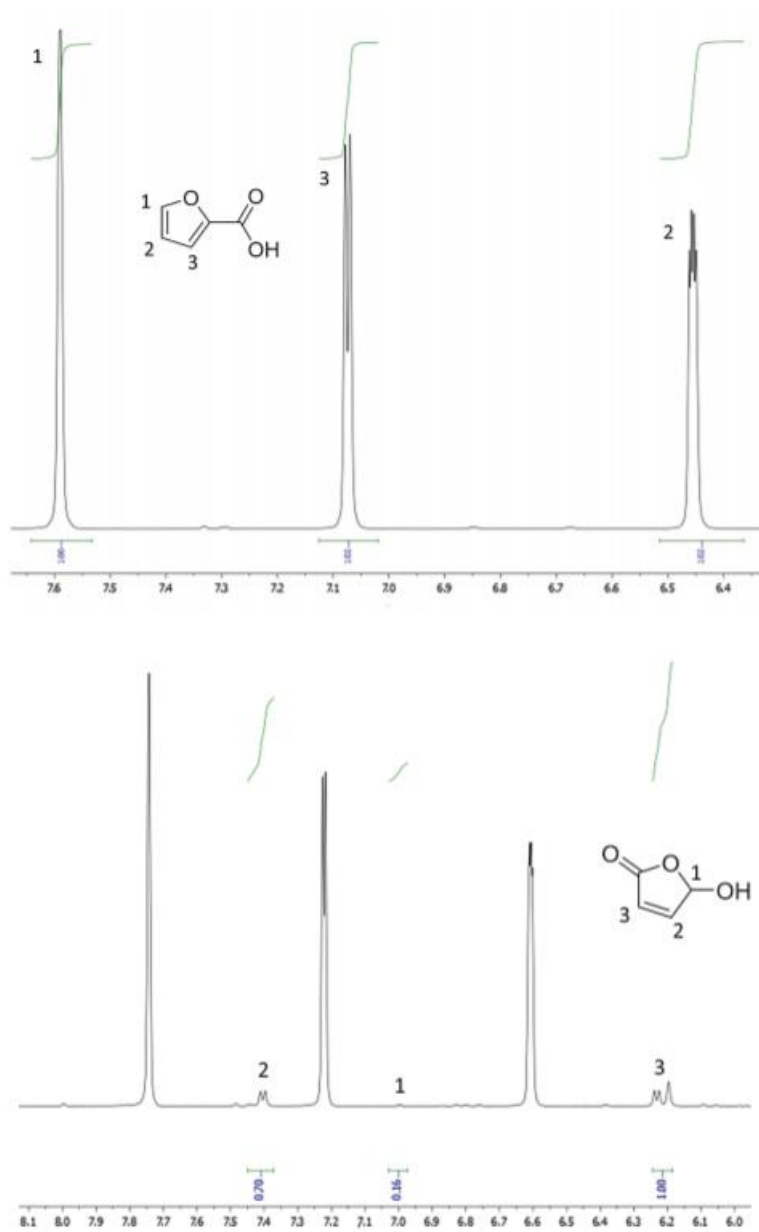


Fig. S4. <sup>1</sup>H NMR spectra (400 MHz, CD<sub>3</sub>OD) of substrate **1c** and product **2c**

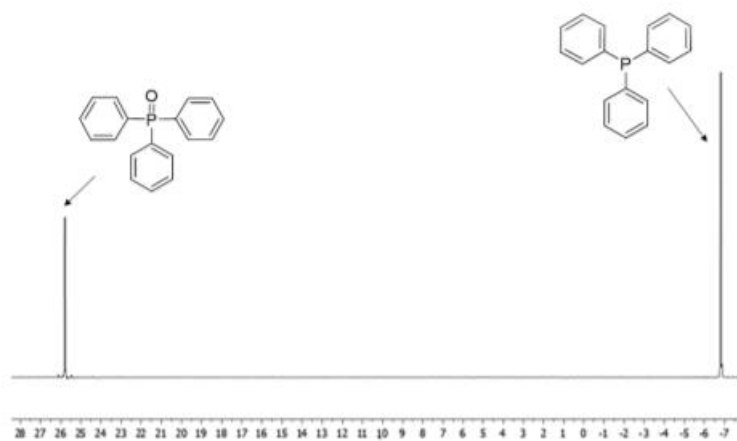


Fig. S5.  $^{31}\text{P}$  NMR spectrum (161 MHz,  $d_6$ -DMSO) of a reaction mixture showing substrate **1d** and product **2d**

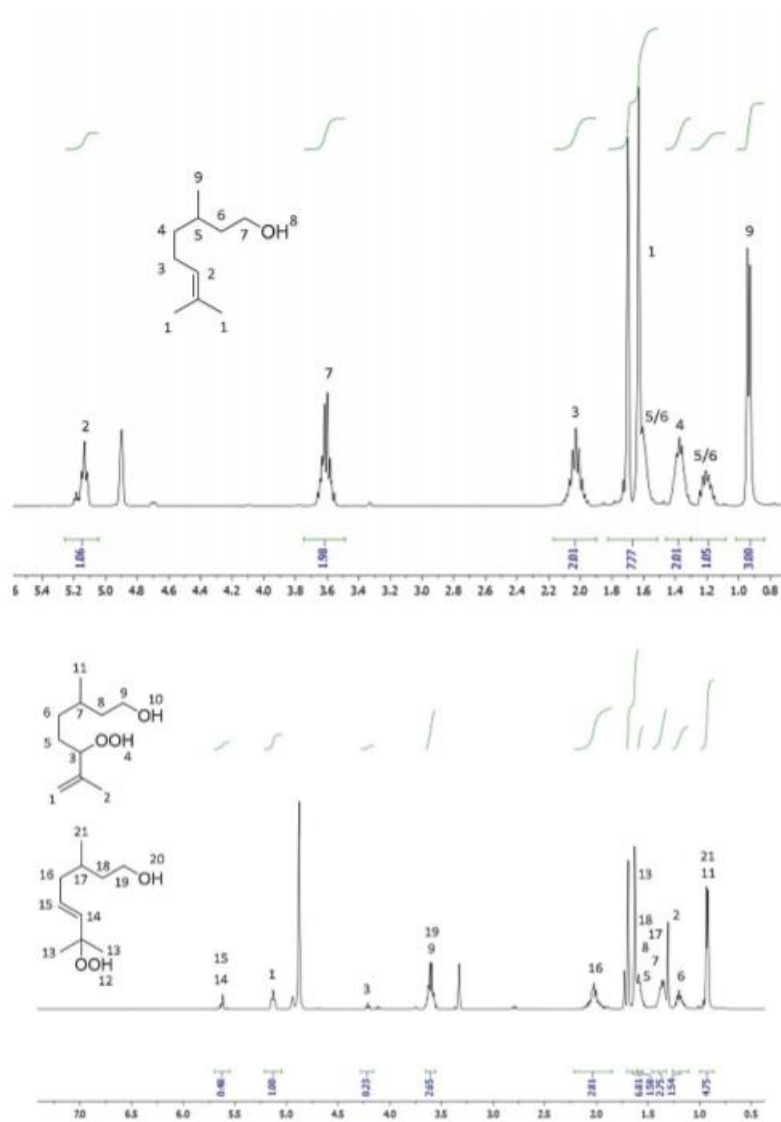


Fig. S6.  $^1\text{H}$  NMR spectra (400 MHz,  $\text{CD}_3\text{OD}$ ) of substrate **1e** and product **2e**

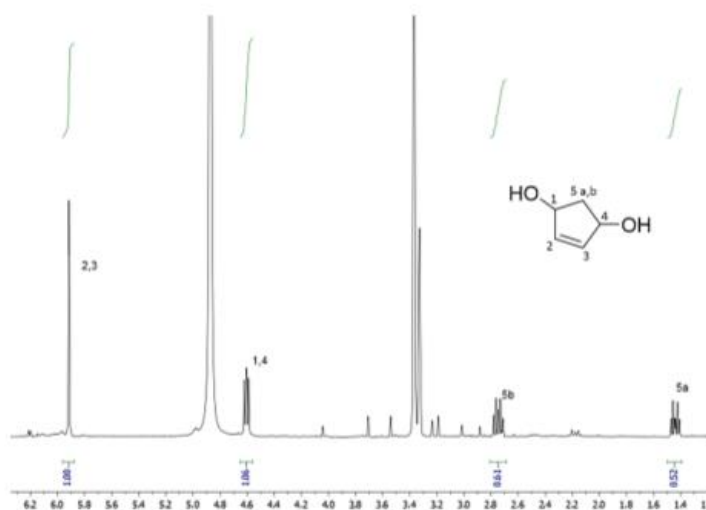
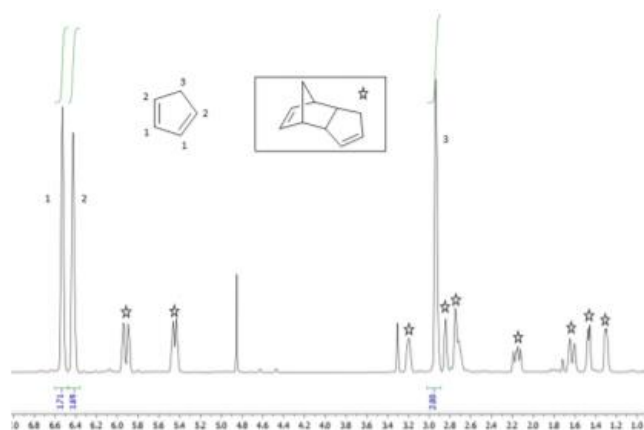


Fig. S7.  $^1\text{H}$  NMR spectrum (400 MHz,  $\text{CD}_3\text{OD}$ ) of substrate **1f** and product **2f**

LEDs were characterized in order to understand the effect of the light on the photooxygenation reactions. Emission spectrum was recorded from 200 to 1000 nm (Fig. S8a) and the irradiance ( $\text{W}\cdot\text{m}^{-2}$ ) was also measured at different distances (Fig. S8b).

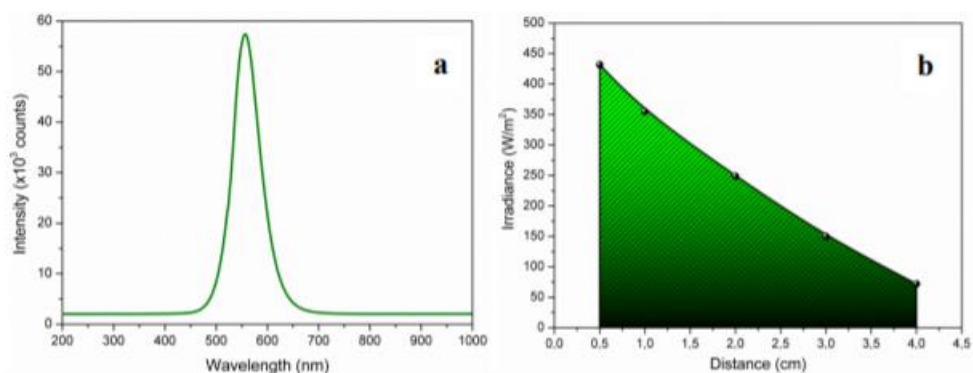


Fig. S8. a) Emission spectrum of the green LEDs b) Irradiance of the green LEDs as a function of the distance

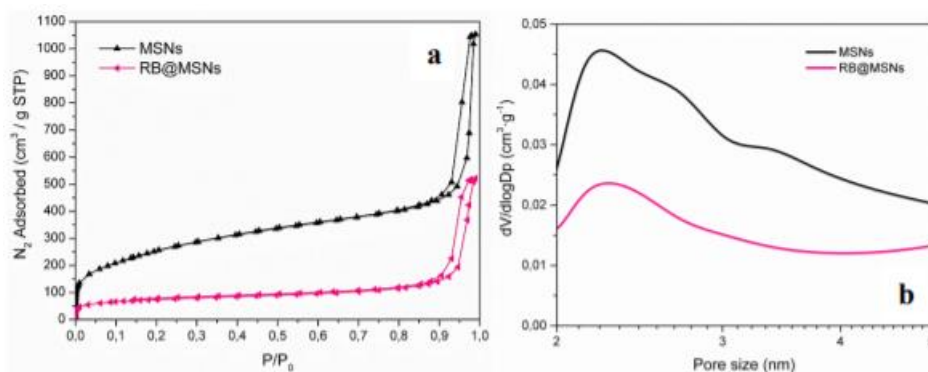


Fig. S9. a)  $N_2$  isotherms and b) Pore size distribution of MSNs and RB@MSNs

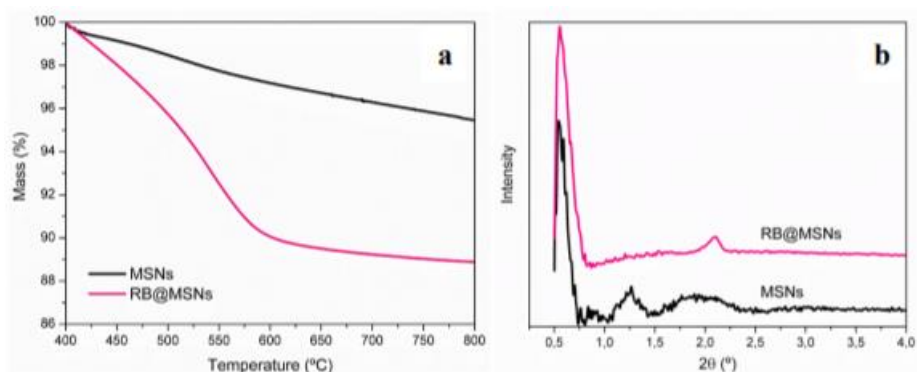


Fig. S10 a) Thermogravimetric analysis of MSNs and RB@MSNs and b) Low angle powder XRD of MSNs and RB@MSNs

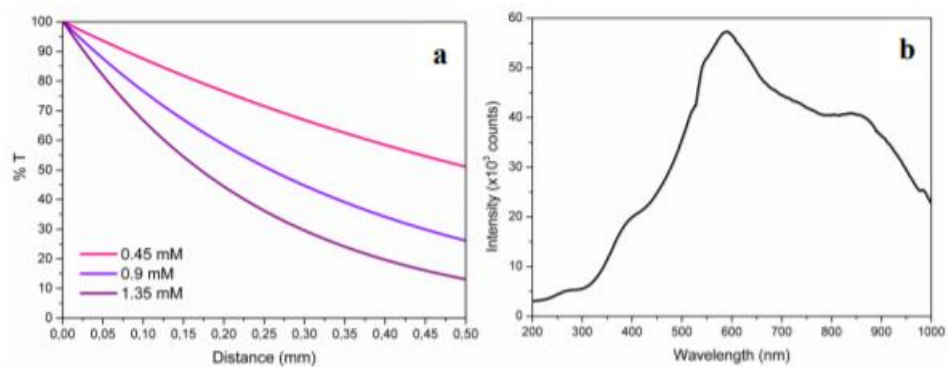


Fig. S11. %T vs. light pathlength of RB@MSNs suspensions with 0.45, 0.9 and 1.35 mM of RB and b) Emission spectrum of the halogen lamp

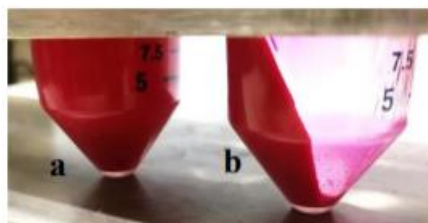


Fig. S12. a) Feed solution of Met-RB@MSNs b) Centrifuged suspension after reaction



Fig. S13. Details of the irradiation setup for microfluidic photooxygenations

## Chapter 3. A safe and compact flow platform for the neutralization of a mustard gas simulant with air and light

### 3.1. Introduction: Chemical Warfare Agents

Chemical warfare agents (CWAs) are generally utilized in conflicts to rapidly generate a maximum of casualties. Although World Wars I and II were the most infamous example of CWAs' usage, terrorists' groups around the world still frequently use such weapons on civilians. CWA stockpiles are also regularly discovered on land and under the sea and have to be dealt with safely. CWAs are generally categorized considering the sort of damage they create on human body as harassing, incapacitating or lethal agents.<sup>1</sup> However, the Chemical Weapon Convention embodied by the Organization for the Prohibition of Chemical Weapons (OPCW) created a CWA classification based on the quantity of compound that can be synthesized for legal usage. This list is divided in 3 schedules, schedule 1 gathering the controlled substances with the smallest tolerance to undeclared production, schedule 3 gathering substances that can have a large-scale legal use.<sup>2</sup> Mustard gas (HD) and derivatives, as well-known blistering and vesicant agents, belong to the schedule 1 along with nerve agents Sarin and VX.

Oxidation is one of the HD chemical neutralization techniques. The toxicity of HD comes from its ability to form a highly toxic episulfonium. Once in its sulfoxide (HDO) form, the equilibrium with the episulfonium is prevented. However, the corresponding sulfone (HDO<sub>2</sub>) can quickly transform into dangerous bis(vinyl)sulfone by loss of HCl and the toxicity of this sulfone is comparable to HD (Figure 55). This explains why the selectivity of HD oxidation is of major importance.

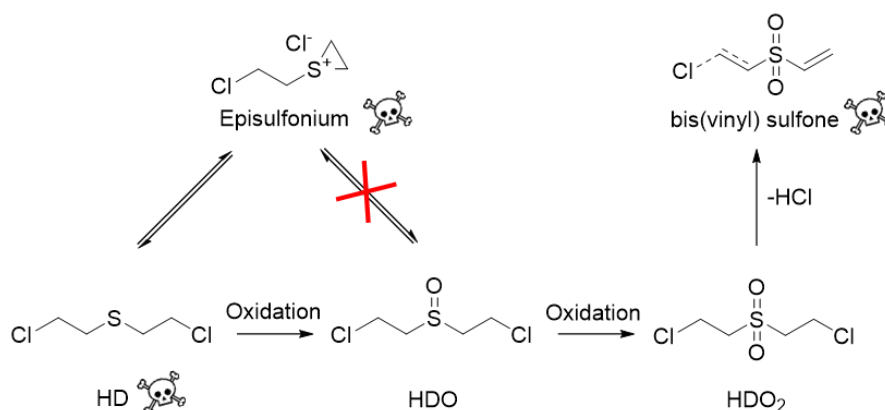


Figure 55 – Evolution of HD oxidation with representation of its toxic forms.

In 2018, Xi *et al.* reported the neutralization of chemical warfare agents including HD with peroxydicarbonate ( $\text{HCO}_4^-$ ) obtained by the activation of  $\text{H}_2\text{O}_2$  with  $\text{NaHCO}_3$ .<sup>3</sup> The authors reported the formation of many side products, including hydrolysis products and the corresponding toxic sulfone (Figure 56A). Two years later, Xi *et al.* studied the same oxidation with peroxytungstate ( $\text{MoO}_4^{2-}/\text{H}_2\text{O}_2$ ) instead of peroxydicarbonate.<sup>4</sup> However, thioanisole, that was selected as a mustard gas simulant was oxidized into both sulfoxide and sulfone. HD neutralization resulted again in a mixture including HDO<sub>2</sub> (Figure 56B). The authors did not provide selectivity values.



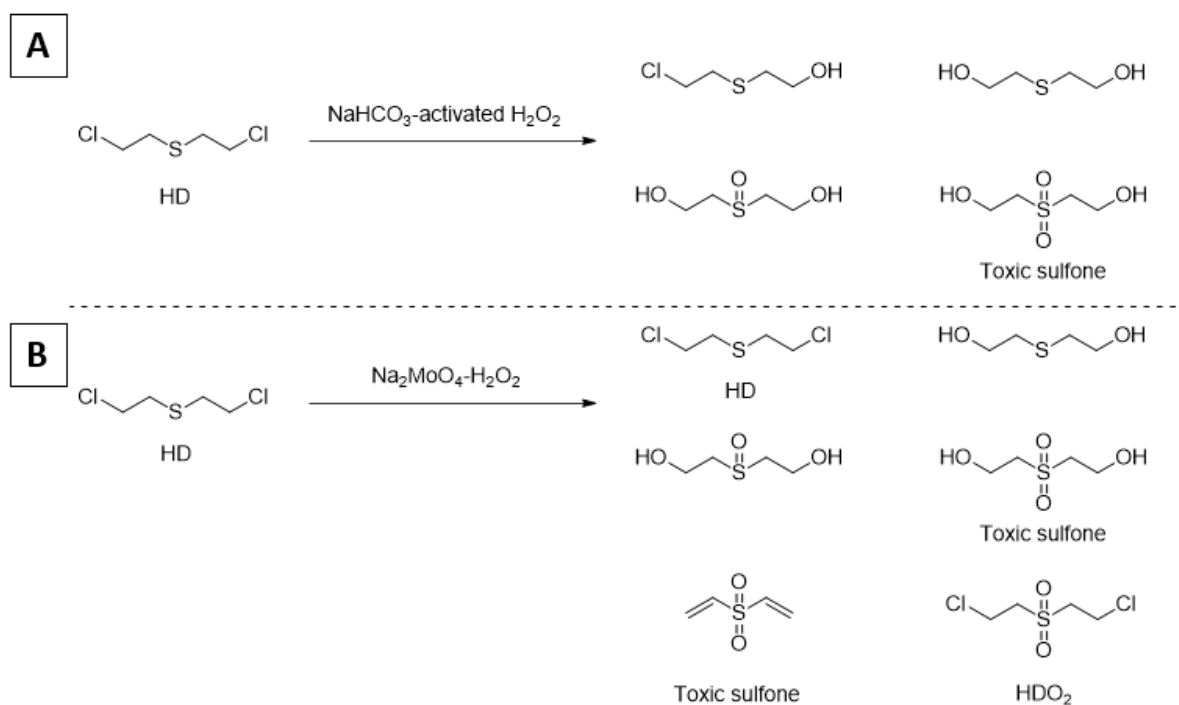
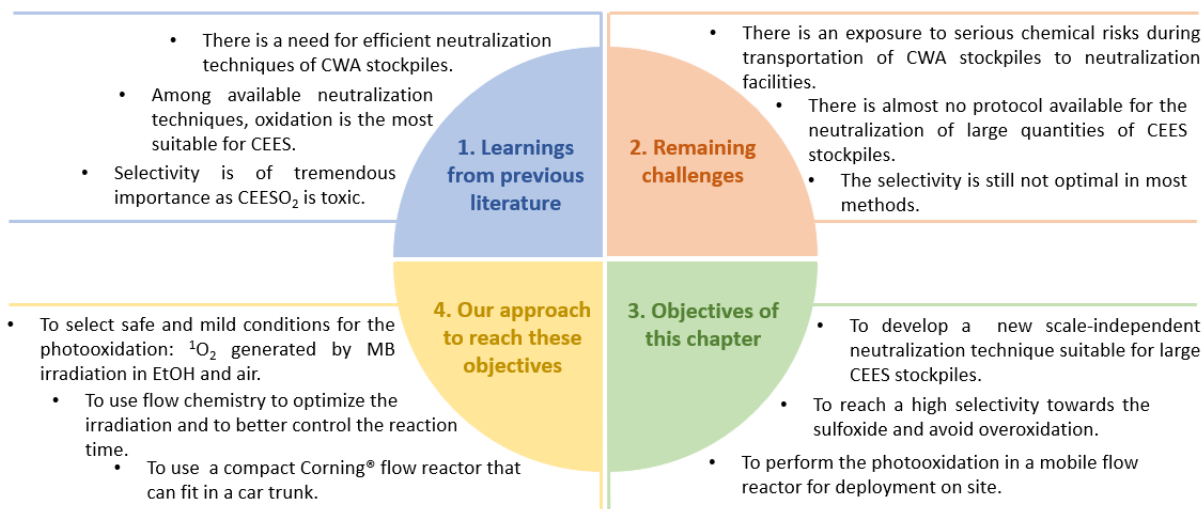


Figure S6 – HD neutralization with H<sub>2</sub>O<sub>2</sub> activated by A - NaHCO<sub>3</sub> or B – MoO<sub>4</sub><sup>2-</sup>.

Howarth *et al.* designed a new metal-organic framework (MOF) consisting of rare-earth cluster (Y(III)) nodes with tetratopic pyrene-based linkers (1,3,6,8-tetrakis(*p*-benzoic acid)pyrene).<sup>5</sup> The authors assessed the efficiency of their catalyst for the neutralization of chloroethyl ethyl sulfide (CEES), a mustard gas simulant. 0.2 mmol of CEES were suspended with the catalyst (0.9 mol%) in MeOH and purged with oxygen. After 30 min, the oxygen was stopped and the reactor was placed under UV LEDs (390-400 nm). After 15 min, CEES was fully oxidized into its sulfoxide CEESO with no trace of the toxic sulfone.

Neutralization of CEES was also studied by Hupp *et al.* with a singlet oxygen oxidation.<sup>6</sup> The authors compared two halogenated BODIPY (4,4-difluoro-4-bora-3a,4a-diaza-s-indacene) arranged in a porous organic polymer (POP). An initial H-BODIPY-POP was modified with *N*-bromo and *N*-iodosuccinimide to obtain Br-BODIPY-POP and I-BODIPY-POP as final photosensitizers. 0.2 mmol of CEES and BODIPYs (1 mol%) were mixed in MeOH under green LEDs irradiation and the reactor was purged with oxygen. Both halogenated BODIPYs allowed the full oxidation of CEES exclusively into its sulfoxide with a half-life of 3 min.

The context and objectives of this chapter are summarized in the diagram below:



The following publication illustrates our contribution to the research of safe and efficient methods to destroy CWAs by proposing a photooxidation with air of a mustard gas simulant in a mobile flow reactor compatible with a deployment on field.

### 3.1.1. References

- 1 M. Schwenk, *Toxicol. Lett.*, 2018, **293**, 253–263.
- 2 Organization for the Prohibition of Chemical Weapons, <https://www.opcw.org/chemical-weapons-convention/annexes/annex-chemicals/annex-chemicals>, (accessed 30 November 2020).
- 3 S. Zhao, H. Xi, Y. Zuo, Q. Wang, Z. Wang and Z. Yan, *J. Hazard. Mater.*, 2018, **344**, 136–145.
- 4 S. Zhao, Y. Zhu, H. Xi, M. Han, D. Li, Y. Li and H. Zhao, *J. Environ. Chem. Eng.*, 2020, **8**, 104221.
- 5 V. Quezada-Novoa, H. Titi, A. Sarjeant and A. Howarth, DOI:10.26434/chemrxiv.12355406.
- 6 A. Atilgan, M. M. Cetin, J. Yu, Y. Beldjoudi, J. Liu, C. L. Stern, F. M. Cetin, T. Islamoglu, O. K. Farha, P. Deria, J. F. Stoddart and J. T. Hupp, *J. Am. Chem. Soc.*, 2020, **142**, 18554–18564.

## 3.2. General information and authors contributions

This chapter is published:

Emmanuel, N.; Bianchi, P.; Legros, J.; Monbaliu, J-C. M. A safe and compact flow platform for the neutralization of a mustard gas simulant with air and light. *Green Chem.* 2020, **22**, 4105-4115.

N. E. designed the chemistry, performed the experiments, analyzed the results and wrote the manuscript. P. B. designed the chemistry, performed the experiments, analyzed the results and wrote the manuscript. J. L. revised the manuscript. J.-C. M. M. designed the chemistry, ran the computations and analyzed the results, supervised the project, wrote the manuscript and secured funding for the project.

The figures, tables and references numbering of the section 3.3 correspond to the numbering of the article as published online.

### 3.3. Templated copy of the article

The content of this section, including figures, is copyrighted (The Royal Society of Chemistry 2020).

#### Introduction

Chemical warfare agents (CWAs, Figure 1) were conceived in the darkest converging alleys of Science and Industry to optimize debilitating, incapacitant or lethal activity for maintaining military superiority.<sup>1</sup> World War II stressed the emergence of much more redoubtable nuclear warfare, even though large stockpiles of CWAs were maintained worldwide and new chemical agents were developed. Since WWII, CWAs were sporadically used for armed conflicts with the last reports dating back to 2017-2018 in the Middle East. The tragedy with CWAs remains that it also affects civilians who lack protection gears and antidotes.<sup>2</sup> The Chemical Weapons Convention (CWC) entered in force in 1997 with the ambition to prohibit the possession, manufacture and use of CWAs and was ratified by 193 countries.<sup>3</sup> Besides prohibition, it also aims at developing resources, procedures and capacities to treat the consequences of a CWA attack and to supervise the destruction of stockpiles, related equipment and infrastructure.<sup>2,4</sup> There are still large inventories of CWAs reminiscent of previous conflicts, either as a latent, still usable threat or as spoiled ammunitions. Besides, the availability of various chemicals on small to medium scale as well as emerging process technologies with a very low footprint have also raised significant concerns with the potential local production of CWAs for chemical terrorism.<sup>5</sup> Following the inception of the CWC, a total of 8 countries declared CWAs, 7 of which have now completed the destruction of 97% of the declared inventories worldwide. The USA has announced the destruction of 90% of its total inventory and aims at a complete destruction by 2023.<sup>6,7</sup>

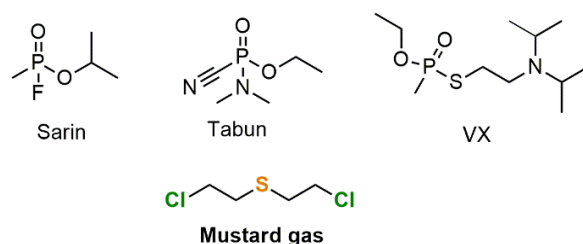
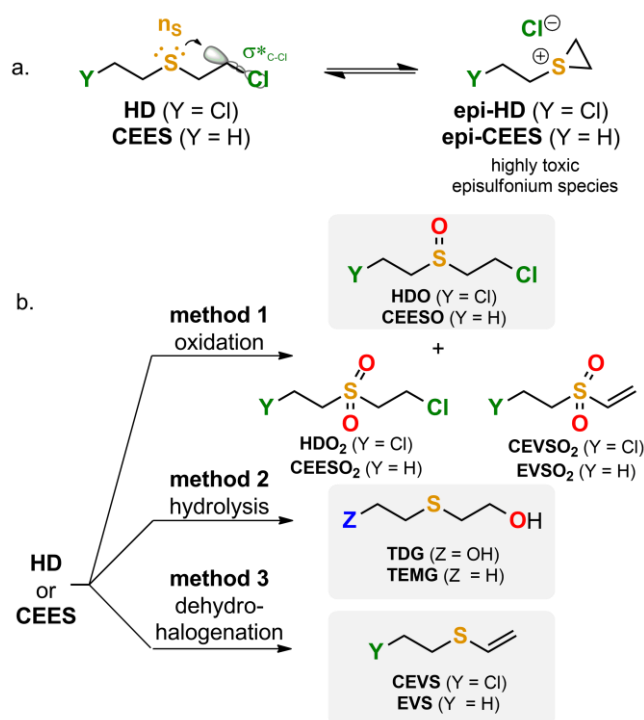


Fig. 1. Representative examples of Schedule I CWAs.

Among CWAs, 1-chloro-2-[(2-chloroethyl)sulfanyl]ethane (CAS 505-60-2) commonly referred to as mustard gas or **HD** is a Schedule I CWA with cytotoxic and vesicant properties.<sup>8</sup> **HD** is considered as the parent molecule of sulfur mustards. The unique reactivity and toxicity profile of sulfur mustards arise from the combination of donor lone pairs  $n_s$  on the sulfur atom in the vicinity of two  $\sigma^*_{C-Cl}$  acceptors, hence potentially forming strongly alkylating and toxic episulfonium species **epi-HD** (Figure 2a).<sup>9</sup> The most common method of destruction of **HD** relies on incineration,<sup>10,11</sup> although such a method raises significant safety concerns not only for the emission of toxic gaseous or liquid emissions upon thermal treatment but also for the transportation risk.<sup>12</sup> Chemical neutralization methods<sup>10,11</sup> (**methods 1-3**, Figure 2b) for sulfur mustards such as **HD** or its most common simulant **CEES** (2-chloroethyl ethyl sulfide) typically target either one of the lone pairs  $n_s$  on sulfur through selective oxidation towards a sulfoxide (**method 1**) or the  $\sigma^*_{C-Cl}$  acceptors through hydrolysis or displacement with a strong nucleophile (**method 2**).<sup>13</sup> A third alternative method of chemical neutralization relies on dehydrohalogenation protocols (**method 3**).



**Fig. 2. a.** Reactivity and toxicity of **HD**; **b.** General chemical neutralization methods for mustard gas (**HD**) and its most common simulant (**CEES**). **Method 1.** Oxidation; **Method 2.** Hydrolysis; **Method 3.** Dehydrohalogenation. Compounds with the light gray background are considered low-toxicity neutralized species.

Although these oxidative neutralization methods seem straightforward, the complex reaction profile of **HD/CEES** makes them very cumbersome. For instance, the overoxidation of **HD/CEES** leads to the formation of a strong Michael acceptor sulfone **CEVSO<sub>2</sub>/EVSO<sub>2</sub>**,<sup>14–16</sup> the toxicity of which is comparable to the parent mustard. In all instances, its formation must thus be limited to trace amounts. The selectivity of the oxidation is therefore a critical parameter for the validation of a neutralization method. The lipophilic nature of **HD/CEES** typically renders aqueous oxidation protocols inefficient, hence often imposing surfactants<sup>14</sup> or organic solvents as carriers.<sup>15</sup> Primary oxidizers typically include hydrogen peroxide,<sup>14,16–22</sup> peracids<sup>15</sup> or oxygen<sup>22–25</sup> in the presence of homogeneous<sup>26</sup> or heterogeneous catalysts.<sup>16–18,27–31</sup> Other oxidizers were also reported such as *N*-iodosuccinimide/water (Table 1).<sup>32</sup> The oxidative neutralization methods relying on reactive oxygen species are very attractive, especially when molecular oxygen is the primary oxidant source (Table 1). Zeolites<sup>2</sup> and MOF-based heterogeneous materials and fibers were also reported and successfully tested for the UV photooxidation of **CEES** and actual samples of **HD**.<sup>23,28,33–36</sup> These photooxidations typically proceed with complete conversion and high to complete selectivity towards the sulfoxide **HDO** with a catalytic amount (typ. 1–2 mol%).<sup>23,28</sup> The heterogeneous MOF photocatalyst can be easily recovered after neutralization and is potentially reusable.<sup>35</sup> Photoactive ferrocene-conjugated microporous polymers were also reported.<sup>24,25</sup> Despite excellent results, these methods have only been reported on the milligram scale and would face additional challenges for reaching larger scales. Organic homogeneous photosensitizers were also considered under aerobic conditions such as Riboflavin tetraacetate (RFTA) or riboflavin (vitamin B2).<sup>37,38</sup> Under irradiation with blue LEDs (450 nm) with 2 mol% RFTA at room temperature, **CEES** was quantitatively and selectively converted into **CEESO** in 10 min of irradiation. Boron-dipyrromethene (BODIPY) PSs were assessed for the photooxidation of **CEES** and actual samples of **HD** under blue light irradiation in solution or impregnated on PVDF films and textiles, providing **CEES** half-life down to 0.8 min.<sup>39</sup> Other critical parameters are the compactness, robustness and inherent

safety related to the neutralization method. Indeed, the neutralization setup must be transportable and compact for rapid deployment on site. It must also provide consistent neutralization with high selectivity yet relying on simple, non-toxic, cheap and widely available chemicals. While most of the oxidative procedures rely on batch setups, several authors have considered continuous flow conditions and flow reactors as process technologies endowed with unique inherent features that could be exploited for the efficient oxidation of **CEES** specifically for the use of oxygen and related reactive species.<sup>40–45</sup> In particular, photocatalysis in flow has attracted significant attention both for the preparation of advanced chemical structures and for the chemical destruction (neutralization) of pollutants.<sup>46</sup> Flow protocols relying on either homogeneous or heterogeneous photocatalysts<sup>47–52</sup> benefit from the synergistic combination of flow and photochemistry: uniform irradiation with accurately controlled irradiations times, hence leading to intensified reactions with shorter and more selective reaction pathways.<sup>46,53–55</sup> Flow conditions are also typically considered as scale-independent and easier to scale-up than conventional batch setups.<sup>46,53–56</sup>

**Table 1.** Selection of procedures for the neutralization of mustard gas **HD** and its simulant **CEES**

Entry	Author	Scale	Type	Catalyst	Oxidant	Solvent	Conditions
1	Jackowski <sup>57</sup>	5 mM	Batch <sup>a</sup>	<i>Rhodococcus R. IGTS8</i>	N.A.	H <sub>2</sub> O	30 °C, 14 d, quant. <sup>c</sup>
2	Landry <sup>29</sup>	5.4 mg	Batch <sup>b</sup>	V-mesoporous SiO <sub>2</sub> , 10%	<i>t</i> -BuOOH	CH <sub>2</sub> Cl <sub>2</sub>	r.t., 1 h, 97% <sup>d</sup>
3	Wynne <sup>30</sup>	0.85 mg	Batch <sup>b</sup>	ZnOPpC	Air	Neat	λ, 32–34 °C, 24 h, quant. <sup>e</sup>
4	Cibulka <sup>38</sup>	25 mg	Batch <sup>a</sup>	Riboflavin tetraacetate, 2 mol%	O <sub>2</sub>	MeCN/H <sub>2</sub> O	450 nm, r.t. 10 min; quant.
5	Farha <sup>28</sup>	25 mg	Batch <sup>b</sup>	NU-1000, 1 mol%	O <sub>2</sub>	MeOH	~400 nm, r.t., 15 min, quant. <sup>c</sup>
6	Legros <sup>20</sup>	~780 g day <sup>-1</sup>	Flow <sup>a</sup>	<i>Methanesulfonic acid urea-H<sub>2</sub>O<sub>2</sub> (UHP) adduct</i>		MeOH	r.t., 3.9 min, quant. <sup>c</sup>
7	Farha <sup>34</sup>	25 mg	Batch <sup>b</sup>	NU-1000-PCBA, 0.7 mol%	O <sub>2</sub>	MeOH	400 nm, 14 min, quant. <sup>c</sup>
8	Clarck <sup>26</sup>	28.7 mg	Batch <sup>b</sup>	Cu(hfac) <sub>2</sub> ·H <sub>2</sub> O, 4 mol%	<i>t</i> -BuOOH	CDCl <sub>3</sub>	r.t., 27 h, 50% <sup>c</sup>
9	Zhao <sup>22</sup>	10 mg	Batch <sup>a</sup>	—	H <sub>2</sub> O <sub>2</sub>	[BMim]HCO <sub>3</sub>	r.t., 30 min, quant. <sup>f</sup>
10	Karwacki <sup>39</sup>	172 mM	Batch <sup>a</sup>	BODIPYs	O <sub>2</sub>	<i>d</i> 4-MeOH	3–30 min, quant. <sup>g</sup>
11	Karwacki <sup>39</sup>	2.8 mg (HD)	Batch <sup>b</sup>	BODIPY-I in fabric, 0.1 mol%	Air	Neat	r.t. 30 min, quant. <sup>g</sup>
12	Farha <sup>33</sup>	25 mg	Batch <sup>b</sup>	PCN-222, UMCM-313, 1 mol%	O <sub>2</sub>	MeOH	395–420 nm 12–18 min, quant. <sup>c</sup>
13	Farha <sup>35</sup>	25 mg	Batch <sup>b</sup>	[Y(H9TPPA)(H <sub>2</sub> O) <sub>κ</sub> ]Cl <sub>2</sub> ·H <sub>2</sub> O	O <sub>2</sub>	MeOH	400–500 nm, 28 min, quant. <sup>c</sup>
14	Zafrani <sup>13</sup>	50 mg	Batch <sup>b</sup>	Me-DABCOF, 6–20 wt%	N.A.	H <sub>2</sub> O	36 min–24 h, quant. <sup>c</sup>
15	Estour <sup>21</sup>	116.5 mg	Batch <sup>b</sup>	MIP/porphyrin, 0.25 mol%	H <sub>2</sub> O <sub>2</sub>	MeOH/H <sub>2</sub> O	r.t., 2 h, 99.3% <sup>c</sup>
16	This work	~180 g day <sup>-1</sup>	Flow <sup>a</sup>	Methylene blue, 0.06 mol%	O <sub>2</sub> or air	EtOH	610 nm, r.t. 4 min, >99% <sup>h</sup>

<sup>a</sup> Homogeneous conditions; <sup>b</sup> heterogeneous conditions; <sup>c</sup> no sulfone detected; <sup>d</sup> **CEESO**/**CEESO**<sub>2</sub> ratio of 3.1; <sup>e</sup> trace amounts for long reaction time; <sup>f</sup> 6% of **CEESO**<sub>2</sub>; <sup>g</sup> trace amounts; <sup>h</sup> <1% of **CEESO**<sub>2</sub>

Seeberger was actually one of first to report the catalytic photooxidation of thiodiglycol **TDG** (0.25 M) under continuous flow conditions.<sup>58</sup> The authors used tetraphenylporphyrin (TPP, 2 mM) in chloroform as a photosensitizer. The reactor was operated at room temperature under 6.9 bar of counterpressure and under UV irradiation (450 W medium pressure mercury lamp). Analog **TDG** was oxidized with 95%, yielding to a 3:1 mixture of the corresponding sulfoxide and sulfone. Legros reported a compact flow process with an integrated in-line low field NMR<sup>20</sup>. The oxidation was carried out with the hydrogen peroxide/urea complex (UHP) in methanol with methanesulfonic acid as promotor. The authors reported complete and selective oxidation mustard gas simulant **CEES** within 3.9 min of residence time, and overoxidation to the sulfone was avoided by collecting the reaction effluents in a quenching solution. Despite its effectiveness, their procedure imposes the availability and transportation of explosive and corrosive reagents along with the reactor setup. Moreover, the use of UHP releases stoichiometric amounts of urea in the effluents to be further disposed. Based upon our expertise in the design of flow processes and in particular for the generation and handling of reactive oxygen species<sup>5,59–61</sup>, a compact flow system (L x W x H 94 x 42 x 40 cm) was devised for enabling rapid deployment on site and effective oxidative neutralization with frugal and benign resources. We report herein an advanced continuous flow setup for the selective oxidation of simulant **CEES** and further document the reactivity of such thioethers through MP2 and Natural Bond Order (NBO) computations. The combination of both experimental and theoretical approaches led to a more refined understanding of the unique features of the photooxidation of thioethers. This process is unique

compared to the prior Art (Table 1, entry 16) since (a) it relies on the unique features of a highly engineered continuous flow setup using intensified and user-friendly conditions; (b) it uses the powerful combination of oxygen (or air), visible light and trace amounts (0.06 mol%) of a non-toxic, cheap and widely available organic photosensitizer (Methylene Blue); (c) only environmental and user-friendly reagents are involved, including the solvent (EtOH); (d) the reactor setup is mobile and can be embarked on a vehicle for on-site neutralization with minimal resources and it can be integrated with in-line analysis for process monitoring and increased safety; (e) quantitative conversion of simulant **CEES** is obtained with high selectivity within 4 min of irradiation time under mild process conditions (20 °C, 9 bar) with unprecedented concentrations (1 M in ethanol); (f) the process is virtually scaled-independent since it relies on intensified flow conditions that can be transposed to much larger scales with larger commercial fluidic reactors. It provides the most cost effective, operator-friendly and low footprint process with high atom economy reported so far for the oxidative neutralization of mustard gas simulant **CEES**.

## Experimental section

### General information

Conversion, selectivity and yield were determined by Gas Chromatography coupled to Flame Ionization Detection (GC-FID) or Mass Spectrometry (GC-MS) or by High Performance Liquid Chromatography coupled to Diode-Array Detection (HPLC-DAD). GC and HPLC conversions and yields were determined using external calibration curves established with commercial standards (2-chloroethylethyl sulfide, 2-chloroethylethyl sulfone, ethyl vinyl sulfide, ethyl vinyl sulfone, methyl vinyl sulfone, methyl phenyl sulfide, methyl phenyl sulfoxide, methyl phenyl sulfone, dipropyl sulfide, dipropyl sulfone, thiodipropionic acid, dibenzyl sulfide, dibenzyl sulfoxide, dibenzyl sulfone, diphenyl sulfide, diphenyl sulfoxide, diphenyl sulfone, tetrahydrothiophene sulfide, tetrahydrothiophene sulfoxide, tetrahydrothiophene sulfone, benzyl phenyl sulfide, diethyl sulfide, benzyl methyl sulfide, benzyl methyl sulfone, dibenzothiophene, dibenzothiophene sulfone) or with synthesized reference samples following reported procedures (see Supporting Information Section 2.2.4 for experimental procedures).<sup>19,30,35,39</sup> Structural identity was confirmed by <sup>1</sup>H and <sup>13</sup>C NMR spectroscopy (400 MHz Bruker Avance spectrometer) in CDCl<sub>3</sub> (Supporting Information Sections 2.4 and 2.5). Ethanol, acetonitrile, water, Rose Bengal, Methylene Blue, 9,10-dicyanoanthracene, oxygen and air were obtained from commercial sources, and used without additional purification. **CAUTION:** 1-chloro-2-(ethylsulfanyl)ethane (**CEES**) is a highly toxic and severe vesicant. It must be handled with great care under a fume hood. The access to 1-chloro-2-[(2-chloroethyl)sulfanyl]ethane (mustard gas or **HD**) is subjected to military clearance under very strict conditions.

### Computations

Computations were performed at the MP2/6-31+G\*\* or B3LYP/6-31+G\*\* level of theory with the Gaussian 09 package of programs (Revision D.01) with implicit solvent (PCM,  $\epsilon = 24.852$ , ethanol). Stationary points were optimized with gradient techniques (tight optimization convergence). Transition states were localized using the Newton-Raphson algorithm, and the nature of the stationary points was determined by analysis of the Hessian matrix. Intrinsic reaction coordinate (IRC) calculations were performed on representative transition states. NBO calculations and population analysis were performed at the B3LYP/6-31+G\*\* level on the optimized structures (MP2/6-31+G\*\*). Graphical representations of the HOMO of thioethers were obtained through the FormChk utility in Gaussian 09.<sup>62</sup>

## Experimental setup

**Mesofluidic setup.** Mesofluidic experiments were carried with a Corning® Advanced-Flow™ Lab Photo Reactor (1 fluidic module, 2.6 mL internal volume) and in a Corning® Advanced-Flow™ LF/G1 skid Photo Reactor (5 fluidic modules integrated with static mixers and connected in series, 13 mL total internal volume). Feed and collection lines consisted of PFA tubing (1/8" o.d. or 1/4" o.d.) equipped with PFA or SS Swagelok connectors and ferrules. The liquid feed was handled with ThalesNano MicroHPLC pumps, and the gas feed (oxygen or air) was handled with a Bronkhorst EL FLOW Prestige mass flow controller. The reactor was maintained at reaction temperature with a LAUDA Integral XT 280 thermostat. The LED panels were maintained at 10 °C with a LAUDA RP845. Downstream pressure was regulated with a back pressure regulator from Zaiput Flow Technologies (BPR-10 or BPR-100). Optionally, an in-line IR (FlowIR™ from Mettler-Toledo equipped with a DTGS detector using HappGenzel apodization, a Silicon probe connected via a FlowIR™ sensor and a high pressure heated 10 µL cell) or NMR (43 MHz Spinsolve™ carbon NMR spectrometer from Magritek®) was inserted downstream (Supporting Information Section 2.3).

## Typical run

Continuous flow photochemical neutralization of CEES with oxygen. The pump used to deliver the solution of 2-chloroethyl ethyl sulfide (CEES, 1 M) and Methylene Blue (560 µM) in EtOH was set to 1 mL min<sup>-1</sup>. The mass flow controller used to deliver oxygen was set to 20 mL<sub>N</sub> min<sup>-1</sup>, and both streams were conveyed through PFA tubing to the first glass fluidic module of the Corning® Advanced-Flow™ LF/G1 skid Photo Reactor upon irradiation at 610 nm (full intensity, 300 LEDs) at 20° C (9 bar of counterpressure) (Figure 6). The reactor effluent was collected at steady state, diluted with EtOH and analyzed by GC/FID (99% conversion, 99% selectivity, see Table 1).

## Results and discussion

The photooxidation of thioethers has been widely discussed in the literature through mechanistic and computational studies, and various mechanisms were postulated and assessed.<sup>63–77</sup> Depending on the photosensitization, the oxidation can proceed either through the addition of the thioether substrate onto singlet oxygen or through electron transfer (ET) involving the superoxide anion.<sup>66,78</sup> The photooxidation of thioethers with singlet oxygen is consensually recognized as a complex reaction sequence leading to various oxidations products, among which the corresponding sulfoxides are typically the major product, along with variable amounts of sulfones and oxidative fragmentation products.<sup>65,69,74,76</sup> The process goes through the formation of several key intermediates (Figure 3), the first of which being a weakly bound peroxysulfoxide intermediate **A** that forms upon the addition of the nucleophilic thioether substrate onto electrophilic singlet oxygen. Intermediate **A** was actually never isolated. The fate of the later determines the output of the photochemical process. Intermediate **A** typically undergoes physical quenching in apolar aprotic solvents, while it is stabilized in protic solvents, hence drastically improving the efficiency of the photooxidation.<sup>73,79</sup> The exact nature of the second intermediate **B** has fed intense debate in the literature; advanced mechanistic and computations studies pointed towards hydroperoxysulfonium ylide **B**<sub>2</sub> rather than thiadioxirane **B**<sub>1</sub>.<sup>63–77</sup> The reaction of each molecule of singlet oxygen can potentially result in 2 equiv. of sulfoxide.<sup>64,73</sup>

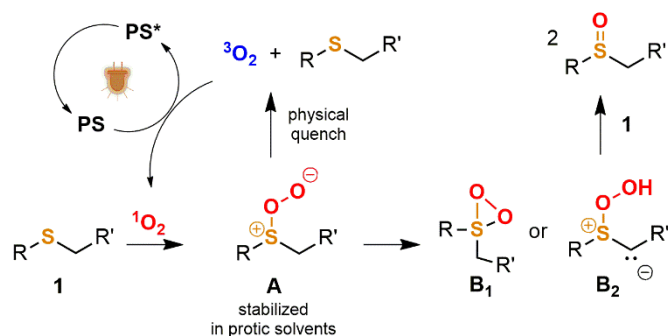


**Fig. 3.** Commonly accepted intermediates and mechanism for the reaction of thioethers with singlet oxygen under photosensitized conditions. Singlet oxygen is typically generated from ground state molecular oxygen upon irradiation in the presence of a photosensitizer (**PS**). A common organic **PS** is Methylene Blue.

The access to **HD** is subjected to military clearance under very strict conditions, while small inventories of its most widely accepted simulant (**CEES**) can be purchased. **CEES** is however still a very toxic and severe vesicant that must be handled with great care, hence precluding its direct use for large-scale optimization. Decision was made to undertake a preliminary computational study on the reactivity of **HD** and **CEES** towards singlet oxygen for comparison with other widely available non-toxic thioethers, the handling of which for preliminary experiments with singlet oxygen would not raise a significant safety hazard. Obviously, the model thioethers must echo the peculiar inherent reactivity of **HD/CEES** for enabling fast transposition with minimal readjustment to **CEES**. The rationale behind such an approach was to limit the exposure to extremely toxic chemicals upon the optimization of the process conditions. *In silico* modeling enables to compute quantitative or semi-quantitative models and data, which are particularly relevant when high toxicity chemicals are at stakes. The efficiency of singlet oxygen oxidation of thioethers is not only very sensitive to reaction conditions, but it also critically depends on the inherent structural and stereoelectronic features of the thioether substrate. The availability of the non-bonding  $n_s$  orbitals on the sulfur atom, which correlates to its intrinsic nucleophilicity, is thus paramount to ensure quick and efficient scavenging of singlet oxygen to form peroxy-sulfonium intermediate **A**. Any factor that potentially decreases the availability of the non-bonding  $n_s$  orbitals on the sulfur atom will therefore potentially reduce the efficiency of the reaction with singlet oxygen. As discussed in the Introduction (Figure 2a), the reactivity and toxicity profiles of sulfur mustards **HD** and **CEES** arise from the combination of a donor lone pair  $n_s$  on the sulfur atom in the vicinity of two  $\sigma^*_{C-Cl}$  acceptors; such stereoelectronic feature might thus impact the oxidative neutralization process. It is therefore critical to have access to a metric for assessing the extent of such stereoelectronic feature for supporting the rational selection of an appropriate non-toxic model thioether. In order to quantify the availability of the non-bonding  $n_s$  orbitals and thus to provide insights on the potential for reaction with singlet oxygen, a preliminary computational study was undertaken on a series of model thioethers with defined structural and stereoelectronic features (Figure 4). The selected model thioethers included **CEES** and **HD**, as well as other alkyl, aryl and benzyl thioethers (**1a-f**), more specifically, dipropyl sulfide (**1a**), (chloromethyl)(ethyl)sulfide (**1b**), benzyl methyl sulfide (**1c**) methyl phenyl sulfide (**1d**), diphenyl sulfide (**1e**) and dibenzothiophene (**1f**). Thus the selection of thioethers **1a-f** included thioethers with qualitatively expected high (**1a**), intermediate (**1c**, **1d**) and low (**1b**, **1e**, **1f**) availability of non-bonding  $n_s$  orbitals, thus mirroring a potentially decreasing reactivity towards electrophilic singlet oxygen. This qualitative scale relies on the structural analysis of the compounds **1a-f** and the identification of any potential strong stereoelectronic or delocalization effects, yet a more precise scale was required.



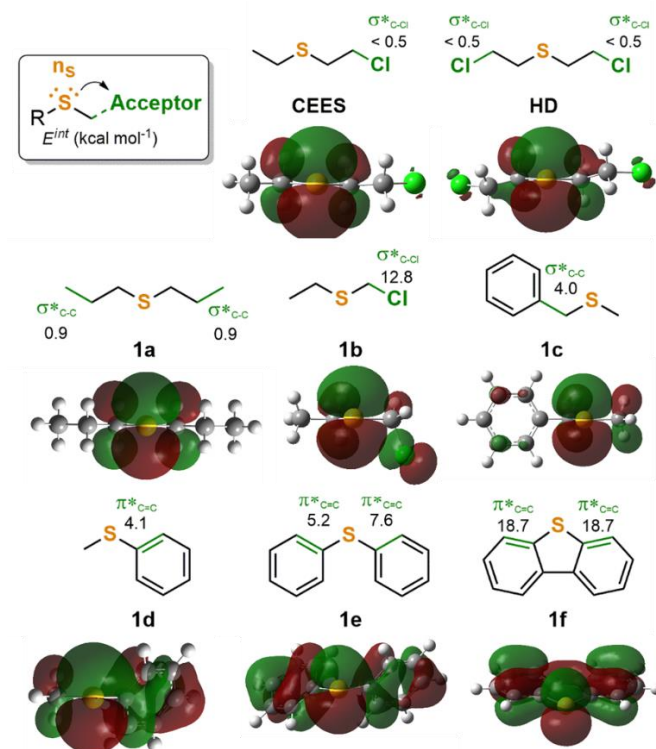


**Fig. 4.** Selection of model thioethers **1a-f** for the computational study. The stereoelectronic interaction between a donor non-bonding  $n_S$  and a vicinal acceptor ( $\sigma^*_{C-X}$  ( $X = C, Cl$ ) or  $\pi^*_{C=C}$ ) were looked at on the most stable conformers of **CEES**, **HD** and **1a-f** is expressed in kcal mol<sup>-1</sup>. HOMO (isovalue 0.02) are represented for thioethers **CEES**, **HD** and **1a-f**.

The structures of **HD**, **CEES** and **1a-f** were optimized at the MP2/6-31+G\*\* level of theory in ethanol. In order to have more precise information on the availability of the non-bonding  $n_S$  orbitals on the sulfur atom of each of these thioethers, NBO and electronic population analyses were carried out at the B3LYP/6-31+G\*\* level of theory on the optimized structures (MP2/6-31+G\*\*). A second order perturbation theory analysis of the Fock matrix in the NBO basis provided a convenient metric (Figure 4) to sense stereoelectronic features that are responsible for a decreased availability of the non-bonding  $n_S$  orbitals on the sulfur atom, thus indicating a lower efficiency for the reaction with singlet oxygen. Only the potential donor/acceptor interactions ( $E^{int}$ ) involving the non-bonding  $n_S$  and acceptors such as  $\sigma^*_{C-X}$  ( $X = C, Cl$ ) or  $\pi^*_{C=C}$  were looked at on the most stable conformers of **CEES**, **HD** and **1a-f**. From the NBO and population analyses (Figure 4), it can be seen that dialkyl sulfides such as **CEES**, **HD** and **1a** have well-localized HOMO centered on the sulfur atom and are characterized by low to negligible donor/acceptor interactions (Figure 4). By contrast, chloromethyl ethyl sulfide (**1b**) features a strongly interacting non-bonding  $n_S$  in the direct vicinity of a  $\sigma^*_{C-Cl}$  acceptor and a less localized HOMO. Benzyl methyl sulfide (**1c**) features a medium stereoelectronic effect ( $E^{int} = 4.0$  kcal mol<sup>-1</sup>) involving a neighboring  $\sigma^*_{C-C}$  orbital. Major differences appear for **1d** and to a larger extent to **1e,f**, where the delocalization of the non-bonding  $n_S$  orbitals to the aromatic ring drastically affects their availability. Dibenzothiophene **1f** comes with a very strong stereoelectronic interaction ( $E^{int} = 18.7$  kcal mol<sup>-1</sup> for each  $n_S$  orbital). The results from the NBO and population analyses are in agreement with the data from the literature, which emphasize that alkyl aryl and diaryl sulfides are considered as poor quenchers of singlet oxygen compared to dialkyl sulfides due to their HOMO only partially localized on the sulfur atom.<sup>67</sup> The transition state for the quenching of singlet oxygen by thioethers **1a**, **CEES** and **HD** towards the corresponding peroxysulfoxide intermediates **A** (**1Aa**, **CEESOO** and **HDOO**, respectively) were located at the MP2/6-31+G\*\* level of theory in ethanol. The structure of the

targeted sulfoxides (**2a**, **CEESO** and **HDO**) are illustrated for the sake of comparison (Figure 5). These TSs display an orthogonal approach of singlet oxygen relative to the thioether substrates and are structurally related (Supporting Information Section 4). The structural and energetic features of these TSs are in agreement with the work of Jensen and Clennan on other dialkyl thioethers.<sup>63–65,68,70,75–77</sup> The TSs connecting **1a**, **CEES** and **HD** (**TS<sup>1</sup><sub>1a</sub>**, **TS<sup>1</sup><sub>CEES</sub>** and **TS<sup>1</sup><sub>HD</sub>**, respectively) to the corresponding peroxy sulfoxide intermediates (**1Aa**, **CEESOO** and **HDOO**) feature a rather long S-O bond (1.85–1.87 Å) indicative of an early transition state and strong interactions between the non-bonding *n<sub>S</sub>* orbitals and singlet oxygen.<sup>77</sup> The slightly shorter S-O bond length for **TS<sup>1</sup><sub>HD</sub>** (1.85 Å) compared to **TS<sup>1</sup><sub>1a</sub>**, **TS<sup>1</sup><sub>CEES</sub>** (1.87 Å) reflects the presence of two electrons withdrawing Cl atoms. From the analysis of both NBO and TS structures, it appeared that both **1a** and **CEES** are potentially good structural mimics of the parent **HD** for such transformation, hence the results collected on the photooxidation of both **1a** and **CEES** are expected to be transposable on **HD**.

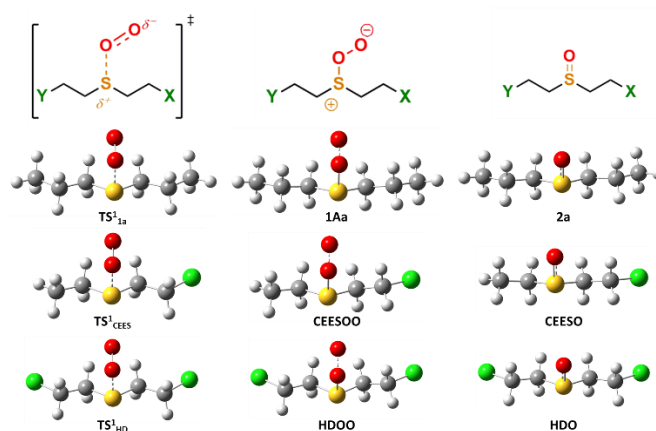


**Fig. 5.** Structural features of the transition states for the reaction of thioethers **1a**, **CEES**, and **HD** with singlet oxygen, of the corresponding peroxy sulfoxide intermediates **A** and of the final sulfoxides. See Supporting Information Section 4 for details. The corresponding S-O and O-O bond lengths are listed here (values in Å): **TS<sup>1</sup><sub>1a</sub>** (S-O: 1.88, O-O: 1.36), **TS<sup>1</sup><sub>CEES</sub>** (S-O: 1.87, O-O: 1.36), **TS<sup>1</sup><sub>HD</sub>** (S-O: 1.85, O-O: 1.36), **1Aa** (S-O: 1.63, O-O: 1.46), **CEESOO** (S-O: 1.63, O-O: 1.46), **HDOO** (S-O: 1.63, O-O: 1.46), **2a** (S-O: 1.54), **CEESO** (S-O: 1.54), and **HDO** (S-O: 1.54).

Based on the computational results, preliminary trials were carried out under photosensitized conditions to calibrate the singlet oxygen oxidation process. The flow setup is described in Figure 6. It consisted of 5 specialty glass fluidic modules (FMs) of 2.6 mL each connected in series for a total of 13 mL. Each glass FM features a succession of high performance static mixers to ensure high mass transfer efficiency between gaseous and liquid effluents. Each FM is integrated with a double layer heat exchanger and is sandwiched between two LED panels, each equipped with 30 high power LEDs of a defined wavelength (300 LEDs in total). The LED panels are integrated with a dedicated heat exchanger. The combination of high-efficiency static mixers and high power LEDs makes this reactor configuration particularly well suited for the generation of singlet oxygen in the presence of organic substrates.<sup>59</sup> The reactor setup was kept under 9 bar of counterpressure with a dome-type backpressure regulator (BPR). In-line low field NMR or IR spectrometers were optionally inserted downstream for qualitative process monitoring and samples were analyzed off-line either by GC or HPLC (Supporting Information Section 2.2.1).

Solutions of representative commercial thioethers were prepared in EtOH (1 M), unless solubility issues imposed a co-solvent or a lower concentration (Supporting Information Section 2.2.3), in the

presence of an organic photosensitizer (Figure 6 and Table 2). Methylene Blue (MB) was selected as organic photosensitizer for the singlet oxygen reaction with thioethers **1a-f** rather than Rose Bengal for its improved resistance to photobleaching and its overall better performances as an organic photosensitizer (Supporting Information Section 3.2.3). MB is a non-toxic, stable, widely available and affordable organic photosensitizer. The liquid feed solution was mixed with oxygen upon irradiation with the appropriate wavelength at 25 °C under 9 bar of counterpressure for a total estimated residence time of 10 min (see Supporting Information Sections 2.2.3 and 3.1 for details).

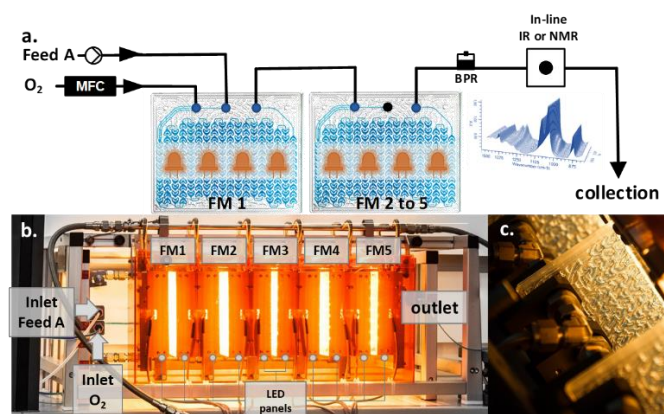


**Fig. 6.** **a.** Simplified flow chart for the photooxidation of thioethers including CEES (BPR = back pressure regulator; MFC = mass flow controller; FM = fluidic module; Feed A = substrate typically 1 M in EtOH with 0.06 mol% of an organic photosensitizer; heat exchange on the reactive path and LED panels are omitted for clarity). **b.** Photograph of the low footprint and mobile chemical neutralization technology for the oxidative neutralization of mustard gas simulant CEES upon irradiation at 610 nm (Corning® Advanced-Flow™ G1/LF skid Photo Reactor; Courtesy of Corning®). The footprint of the setup is L x W x H 94 x 42 x 40 cm. **c.** Details of a glass fluidic module with the LED panels removed.

Table 2 Calibration of the photooxidation process with singlet oxygen on model thioethers (see also Fig. 6 for the general setup)

Entry	Thioether substrate	Solvent (M)	Catalyst (mol%)	Conv. (%) <sup>c</sup>
1	1a	EtOH (1)	MB (0.06) <sup>a</sup>	>99 <sup>d</sup>
2	1c	EtOH (1)	MB (0.06) <sup>a</sup>	>99 <sup>e</sup>
3	1d	EtOH (1)	MB (0.06) <sup>a</sup>	>99 <sup>e</sup>
4	1e	EtOH (1)	MB (0.06) <sup>a</sup>	5 <sup>e</sup>
5	1f	EtOH : 2MeTHF (0.1)	MB (0.06) <sup>a</sup>	0 <sup>e</sup>
6	1e	CH <sub>3</sub> CN	DCA <sup>b</sup>	47
7	1f	CH <sub>3</sub> CN	DCA <sup>b</sup>	49

<sup>a</sup> MB = Methylene Blue, irradiation at 610 nm. <sup>b</sup> DCA = 9,10-dicyanoanthracene, irradiation at 395 nm. <sup>c</sup> Conditions (see Scheme 1): 25 °C, 10 min residence time, 9 bar; the selectivity towards the corresponding sulfoxides is given in the ESI (Table S3†). <sup>d</sup> Determined by GC-FID. <sup>e</sup> Determined by HPLC-DAD.

The first set of conditions involved MB (0.06 mol%) in conjunction with oxygen and irradiation at 610 nm (orange LEDs) for the generation of singlet oxygen (entries 1-5). Control experiments in the absence of light or in the absence of organic photosensitizer were carried out as well, and no conversion was detected. Compound **1b** was not tested since it reacted quickly with the solvent under these conditions. The experimental observations were analyzed in parallel with the computation data (Table 2). It can be concluded that thioethers **1a**, **1c** and **1d** that are characterized by a low stereoelectronic involvement of the non-bonding  $n_s$  orbitals ( $E^{int} \leq 4.1$  kcal mol<sup>-1</sup>) and a rather S-centered HOMO are

efficient quenchers of singlet oxygen under intensified flow conditions, and are converted selectively and quantitatively to the corresponding sulfoxides (Table 2, entries 1-3). No traces of sulfones or other oxidative fragmentation products were detected. By contrast, diaryl thioethers **1e,f** were barely reactive towards singlet oxygen (entries 4,5). Changing the photosensitizer to 9,10-dicyanoanthracene (0.06 mol%) in acetonitrile under irradiation at 395 nm (entries 6,7) led to 47 and 49% conversion for compounds **1e,f**. Such conditions are typically associated with the generation of a superoxide and an electron transfer mechanism for the oxidation of thioethers rather than a singlet oxygen oxidation,<sup>67,69,78</sup> hence emphasizing the differences in terms of mechanism and its implication for the oxidation of structurally diverse thioethers. The choice of the involved mechanism depends not only on the structural and stereoelectronic features of the thioether, but also on the nature of the photosensitizer, which was not evaluated with the computational approach, hence showing the interests for combining computational with experimental data.

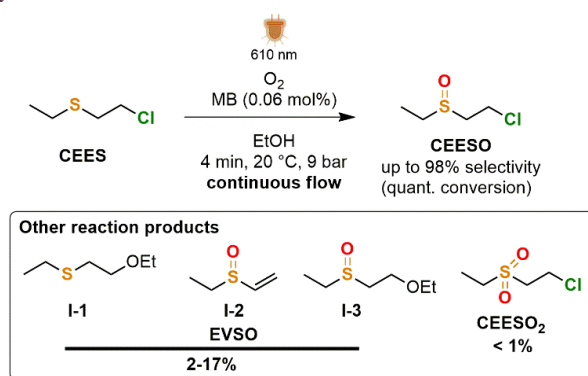
A stock solution of **CEES** (1 M) and MB (560  $\mu$ M) was prepared in EtOH (Supporting Information Section 2.2.3) and the process conditions were further optimized. Given the complex reactivity profile of **CEES**, a variety of side products are expected according to the data of the literature. Under the experimental conditions of this report, 4 impurities were detected (Scheme 1, Table 3), among which only **CEESO<sub>2</sub>** (the corresponding overoxidized sulfone) is considered as toxic since it potentially produces electrophilic ethyl vinyl sulfone **EVS** (Figure 2). Impurities **I-1** and **I-3** are formed through the addition of EtOH on **CEES** and **CEESO** and can therefore be considered as neutralized species. Impurity **I-2** is formed through the dechlorination of **CEESO** and is typically considered as a non-toxic chemical. The identity of all impurities was confirmed by GC, GC-MS or NMR with commercial or prepared samples. The impact of various process parameters (irradiation time, primary source of singlet oxygen, light intensity and nature) on the efficiency and the selectivity of the photooxidation was assessed (Table 3 and Supporting Information Section 3.2). In this process, the highest conversion of **CEES** must be reached within a short residence time, and the oxidation must be selective enough to produce low amounts of **CEESO<sub>2</sub>**. The emergence of other impurities such as **I-1**, **I-2** and **I-3** does not impact negatively the process, since they are considered as neutralized species as **CEESO**.

The irradiation time can be reduced from 10 to 4 min upon irradiation at 610 nm with full intensity in the presence of oxygen while still reaching almost quantitative conversion of **CEES** (entries 1 and 7, >99% and 92%, respectively) towards mainly **CEESO** and other minor impurities (Scheme 1). A further decrease to 2 min nevertheless left about 18% of unreacted **CEES** in the reactor effluent (82% conversion). The amount of **CEESO<sub>2</sub>** increased with the conversion of **CEES** to **CEESO**, yet it remained under 1%: 0.1% (2 min), 0.4% (4 min) and 0.9% (10 min). Impurities **I-1** (3%), **I-2** (1%) and **I-3** (3%) were present in the reactor effluent from the experiment at 4 min of irradiation time.

**Table 3** Optimization of the oxidative neutralization of CEES under continuous flow conditions (see also Scheme 1)

Entry	Oxidant	RT (min)	LEDs (nm)	Conv. <sup>c</sup> (%)	Reactor effluent composition (%) <sup>d</sup>					
					CEES	CEESO	CEESO <sub>2</sub>	I-1	I-2	I-3
1	O <sub>2</sub>	10	610	>99 <sup>a</sup>	0	95	1	0	1	3
2	O <sub>2</sub>	10	White	>99 <sup>a</sup>	0	96	1	0	2	1
3	O <sub>2</sub>	10	White	>99 <sup>a</sup>	0	95	1	0	1	3
4	Air	10	610	>99 <sup>a</sup>	0	84	1	0	1	15
5	Air	10	610	>99 <sup>b</sup>	0	85	0	0	1	14
6	O <sub>2</sub>	4	610	99 <sup>a</sup>	1	92	0	3	1	3
7	Air	4	610	51 <sup>a</sup>	81	14	0	4	0	0
8	O <sub>2</sub>	4	White	>99 <sup>a</sup>	0	98	1	0	2	0
9	Air	4	White	68 <sup>a</sup>	41	55	0	3	1	0
10	O <sub>2</sub>	2	610	82 <sup>a</sup>	28	68	0	2	1	0

<sup>a</sup> 1 M solution in EtOH with 0.06 mol% Methylene Blue (Rose Bengal for entry 3), processed at 20 °C under 9 bar of counterpressure. <sup>b</sup> 0.1 M solution in EtOH with 0.06 mol% methylene blue, processed at 20 °C under 9 bar of counterpressure. <sup>c</sup> Determined by GC with an external calibration on commercial CEES. <sup>d</sup> Ratio of compounds determined by GC. The references for compounds CEESO, CEESO<sub>2</sub>, I-1, I-2 and I-3 were either purchased from commercial sources or synthesized in the lab.



**Scheme 1.** Oxidative neutralization of CEES under optimized continuous flow conditions (see also Table 3).

At 10 min of irradiation time, only impurities I-2 (1%) and I-3 (3%) were detected besides CEESO<sub>2</sub>. It is expected that the longer irradiation time oxidized completely I-1 towards I-3. At the shortest residence time (2 min), impurity I-3 was not detected while impurities I-1 and I-2 reached 2% and 1%, respectively. These observations indicate a potential filiation between I-3 and I-1, as well as I-2 (EVSO) and CEESO, although other reaction paths might be incriminated (See Supporting Information Section 2.2.4). Impurity I-2 is also believed to arise from the specific reactivity of the corresponding hydroperoxysulfonium ylide B<sub>2</sub> intermediate (Figure 3).<sup>80</sup> Impurity I-1 most likely arises from a slow reaction between the substrate CEES and the solvent upon storage of the feed solution. Such reaction was not significant upon standing in the feed, and is likely to be accelerated in the flow reactor with the local heat generated by the LEDs (Supporting Information Section 2.2.4). The efficiency of the photooxidation is typically greater with pure oxygen rather than air. This is logical and explainable as the proportion of oxygen is simply lower in air. Within 4 min of irradiation at 610 nm (full intensity), the conversion of CEES reached 99% with pure oxygen while it decreased to 51% with air under the same conditions. For the longest irradiation time (10 min), either oxygen or air gave a similar conversion (99%). The reactor effluent from the experiment with air within 4 min of irradiation was exempt from CEESO<sub>2</sub>, although this is most likely related to the low conversion of CEES than to the nature of the primary source of singlet oxygen. The amount of impurity I-1, was slightly higher for the experiment with air (4%) than for the experiment with oxygen (3%). Impurity I-3 was absent from the reaction with air, while 3% were formed in the presence of oxygen. The intensity and the nature of the light source were also looked at (Supporting Information Section 3.2.4). Decreasing the LEDs intensity typically led to lower conversions, and the maximum intensity was used for most of the trials. With oxygen or air at the longest irradiation time (10 min), either orange LEDs (610 nm) or white LEDs

(4000K) provided >99.9% conversion of **CEES**. The reactor effluent from the experiment with the 610 nm LEDs contained 95% of **CEESO**, and traces of **CEESO<sub>2</sub>** (0.6%), **I-1** (0.5%), **I-2** (2%) and **I-3** (1%). The reactor effluent from the experiment with white LEDs had a similar composition with 96% of **CEESO**, and traces of **CEESO<sub>2</sub>** (1%), **I-2** (1%) and **I-3** (3%). Decreasing the residence time to 4 min still afforded quantitative conversion of **CEES** under white LEDs irradiation. In the latter case, the crude reactor effluent contained 98% of **CEESO** along with 0.5% of **CEESO<sub>2</sub>** and less than 2% of **I-2**. Pure oxygen could be replaced with air, although the concentration of the solution had to be decreased 10-fold to maintain full conversion within 10 min of residence time. Within 4 min of irradiation in the presence of air, white LEDs gave better photooxidation performances than the orange LEDs, affording 68% conversion in **CEES** (51% under irradiation at 610 nm). Both samples were free of **CEESO<sub>2</sub>**.

To summarize the optimization of the chemical oxidative neutralization of **CEES**, the best results involved process conditions relying on oxygen under 4 min irradiation either at 610 nm or under white light at room temperature and 9 bar of counterpressure. Under these conditions, only a trace amount of **CEESO<sub>2</sub>** is formed. Air can also be utilized for the neutralization of **CEES**, affording complete conversion of **CEES** yet with a longer irradiation time (10 min).

## Conclusions

This work illustrates the development of a low footprint, mobile, robust and frugal chemical neutralization technology for the oxidative neutralization of a mustard gas simulant. It relies on the unique features of a highly engineered continuous flow setup and robust conditions using non-toxic and widely available chemicals. The experimental work is also supported with a computational rationalization of the reactivity of selected thioethers towards singlet oxygen. The optimized conditions use concentrated solutions of **CEES** in ethanol with a trace amount of MB upon irradiation with orange or white light. Quantitative conversion was obtained within 4 min of irradiation time under mild process conditions (20 °C, 9 bar). Oxygen or air can be utilized as primary oxidant, although with air longer irradiation times or lower feed concentrations are typically required. Under optimized conditions, only trace amounts of toxic **CEESO<sub>2</sub>** are detected in the reactor effluent, hence providing an extremely cost effective, operator-friendly and low footprint process for the oxidative neutralization of **CEES**. The neutralization technology can be embarked on a vehicle for on-site interventions, localized at a neutralization facility or both. The ability to transpose these optimized conditions to larger scales with commercial Corning Advanced-Flow Reactors with minimal reoptimization definitively opens up new perspectives for the safe chemical neutralization of mustard gas with a minimal footprint under frugal conditions. Such a protocol of neutralization could possibly be further adapted to other S-based CWA from the V-series (VX, VR).

## Notes and references

- 1 [https://www.iss.europa.eu/content/preventing-re-emergence-chemical-weapons#\\_a\\_short\\_history\\_of\\_chemical\\_warfare](https://www.iss.europa.eu/content/preventing-re-emergence-chemical-weapons#_a_short_history_of_chemical_warfare)
- 2 B. Friedrich, D. Hoffmann, J. Renn, F. Schmaltz and M. Wolf, *One hundred years of chemical warfare: Research, deployment, consequences*, 2017.
- 3 <https://www.opcw.org/chemical-weapons-convention/download-convention>.
- 4 <https://www.opcw.org/about-us>
- 5 R. Gérardy, N. Emmanuel, T. Toupy, V. E. Kassin, N. N. Tshibalonza, M. Schmitz and J. C. M. Monbaliu, *Eur. J. Org. Chem.*, 2018, 2018, 2301–2351.
- 6 <https://www.armscontrol.org/factsheets/cbwprolif>
- 7 <https://www.opcw.org/media-centre/opcw-numbers>
- 8 <https://www.opcw.org/chemical-weapons-convention/annexes/annex-chemicals/schedule-1>
- 9 Q. Q. Wang, R. A. Begum, V. W. Day and K. Bowman-James, *Org. Biomol. Chem.*, 2012, 10, 8786–8793.
- 10 *Decontamination of Warfare Agents*, 2008.
- 11 B. Picard, I. Chataigner, J. Maddaluno and J. Legros, *Org. Biomol. Chem.*, 2019, 17, 6528–6537.
- 12 <https://www.opcw.org/our-work/eliminating-chemicalweapons>
- 13 N. Karton-Lifshin, S. Katalan, I. Columbus, R. Chen, L. Yehezkel, M. Madmon, S. Dagan, S. Elias, G. Fridkin and Y. Zafrani, *Chem. Commun.*, 2019, 55, 12471–12474.
- 14 G. W. Wagner, L. R. Procell, Y. C. Yang and C. A. Bunton, *Langmuir*, 2001, 17, 4809–4811.
- 15 S. R. Livingston and C. C. Landry, *J. Am. Chem. Soc.*, 2008, 130, 13214–13215.
- 16 F. Carniato, C. Bisio, R. Psaro, L. Marchese and M. Guidotti, *Angew. Chem., Int. Ed.*, 2014, 53, 10095–10098.
- 17 Y. Hou, H. An, Y. Zhang, T. Hu, W. Yang and S. Chang, *ACS Catal.*, 2018, 8, 6062–6069.
- 18 X. Li, J. Dong, H. Liu, X. Sun, Y. Chi and C. Hu, *J. Hazard. Mater.*, 2018, 344, 994–999.
- 19 J. Dong, J. Hu, Y. Chi, Z. Lin, B. Zou, S. Yang, C. L. Hill and C. Hu, *Angew. Chem., Int. Ed.*, 2017, 56, 4473–4477.
- 20 B. Picard, B. Gouilleux, T. Lebleu, J. Maddaluno, I. Chataigner, M. Penhoat, F. X. Felpin, P. Giraudeau and J. Legros, *Angew. Chem., Int. Ed.*, 2017, 56, 7568–7572.
- 21 S. Mohamed, S. Balieu, E. Petit, L. Galas, D. Schapman and J. Hardouin, *Chem. Commun.*, 2019, 55, 13243–13246.
- 22 Z. Wang, H. Xi, L. Kong, Y. Zuo, Z. Shi and S. Zhao, *Mol. Catal.*, 2017, 430, 1–8.
- 23 Y. Liu, A. J. Howarth, J. T. Hupp and O. K. Farha, *Angew. Chem., Int. Ed.*, 2015, 54, 9001–9005.
- 24 W. Q. Zhang, K. Cheng, H. Zhang, Q. Y. Li, Z. Ma, Z. Wang, J. Sheng, Y. Li, X. Zhao and X. J. Wang, *Inorg. Chem.*, 2018, 57, 4230–4233.

- 25 L. Ma, Y. Liu, Y. Liu, S. Jiang, P. Li, Y. Hao, P. Shao, A. Yin, X. Feng and B. Wang, *Angew. Chem., Int. Ed.*, 2019, 58, 4221–4226.
- 26 J. R. Hiscock, G. P. Bustone and E. R. Clark, *ChemistryOpen*, 2017, 6, 497–500.
- 27 H. K. Dong, M. Kim and S. Chang, *Org. Lett.*, 2005, 7, 5014–5018.
- 28 Y. Liu, C. T. Buru, A. J. Howarth, J. J. Mahle, J. H. Buchanan, J. B. Decoste, J. T. Hupp and O. K. Farha, *J. Mater. Chem. A*, 2016, 4, 13809–13813.
- 29 C. R. Ringenbach, S. R. Livingston, D. Kumar and C. C. Landry, *Chem. Mater.*, 2005, 17, 5580–5586.
- 30 R. T. Gephart, P. N. Coneski and J. H. Wynne, *ACS Appl. Mater. Interfaces*, 2013, 5, 10191–10200.
- 31 J. T. Rhule, W. A. Neiwert, K. I. Hardcastle, B. T. Do and C. L. Hill, *J. Am. Chem. Soc.*, 2001, 123, 12101–12102.
- 32 B. Smolkin, N. Levi, N. Karton-Lifshin, L. Yehezkel, Y. Zafrani and I. Columbus, *J. Org. Chem.*, 2018, 83, 13949–13955.
- 33 C. T. Buru, M. B. Majewski, A. J. Howarth, R. H. Lavroff, C. W. Kung, A. W. Peters, S. Goswami and O. K. Farha, *ACS Appl. Mater. Interfaces*, 2018, 10, 23802–23806
- 34 A. J. Howarth, C. T. Buru, Y. Liu, A. M. Ploskonka, K. J. Hartlieb, M. McEntee, J. J. Mahle, J. H. Buchanan, E. M. Durke, S. S. Al-Juaid, J. F. Stoddart, J. B. DeCoste, J. T. Hupp and O. K. Farha, *Chem. – Eur. J.*, 2017, 23, 214–218.
- 35 C. F. Pereira, Y. Liu, A. Howarth, F. Figueira, J. Rocha, J. T. Hupp, O. K. Farha, J. P. C. Tomé and F. A. A. Paz, *ACS Appl. Nano Mater.*, 2019, 2, 465–469.
- 36 K. Ma, T. Islamoglu, Z. Chen, P. Li, M. C. Wasson, Y. Chen, Y. Wang, G. W. Peterson, J. H. Xin and O. K. Farha, *J. Am. Chem. Soc.*, 2019, 141, 15626–15633.
- 37 J. Dad'ová, E. Svobodová, M. Sikorski, B. König and R. Cibulka, *ChemCatChem*, 2012, 4, 620–623.
- 38 T. Neveselý, E. Svobodová, J. Chudoba, M. Sikorski and R. Cibulka, *Adv. Synth. Catal.*, 2016, 358, 1654–1663.
- 39 H. Wang, G. W. Wagner, A. X. Lu, D. L. Nguyen, J. H. Buchanan, P. M. McNutt and C. J. Karwacki, *ACS Appl. Mater. Interfaces*, 2018, 10, 18771–18777.
- 40 T. S. A. Heugebaert, C. V. Stevens and C. O. Kappe, *ChemSusChem*, 2015, 8, 1648–1651.
- 41 C. A. Hone and C. O. Kappe, *The Use of Molecular Oxygen for Liquid Phase Aerobic Oxidations in Continuous Flow*, Springer International Publishing, 2019, vol. 377.
- 42 V. E. H. Kassin, R. Gérardy, T. Toupy, D. Collin, E. Salvadeo, F. Toussaint, K. Van Hecke and J. C. M. Monbaliu, *Green Chem.*, 2019, 21, 2952–2966.
- 43 V.-E. H. Kassin, T. Toupy, G. Petit, P. Bianchi, E. Salvadeo and J.-C. M. Monbaliu, *J. Flow Chem.*, 2020, 10, 167–179.



- 44 D. Cambié, J. Dobbelaar, P. Riente, J. Vanderspikken, C. Shen, P. H. Seeberger, K. Gilmore, M. G. Debije and T. Noël, *Angew. Chem., Int. Ed.*, 2019, 58, 14374–14378.
- 45 H. P. L. Gemoets, Y. Su, M. Shang, V. Hessel, R. Luque and T. Noël, *Chem. Soc. Rev.*, 2016, 45, 83–117.
- 46 D. Cambié, C. Bottecchia, N. J. W. Straathof, V. Hessel and T. Noël, *Chem. Rev.*, 2016, 116, 10276–10341.
- 47 L. Suhadolnik, A. Pohar, U. Novak, B. Likozar, A. Mihelič and M. Čeh, *J. Ind. Eng. Chem.*, 2019, 72, 178–188.
- 48 M. Krivec, A. Pohar, B. Likozar and G. Drazic, *AIChE J.*, 2015, 61, 572–581.
- 49 L. Suhadolnik, A. Pohar, B. Likozar and M. Čeh, *Chem. Eng. J.*, 2016, 303, 292–301.
- 50 D. Rackl, P. Kreitmeier and O. Reiser, *Green Chem.*, 2015, 18, 214–219.
- 51 D. C. Fabry, Y. A. Ho, R. Zapf, W. Tremel, M. Panthöfer, M. Rueping and T. H. Rehm, *Green Chem.*, 2017, 19, 1911–1918.
- 52 P. R. Adiyala, S. Jang, N. K. Vishwakarma, Y.-H. Hwang and D.-P. Kim, *Green Chem.*, 2020, 22, 1565–1571.
- 53 A. Steiner, J. D. Williams, O. De Frutos, J. A. Rincón, C. Mateos and C. O. Kappe, *Green Chem.*, 2020, 22, 448–454.
- 54 M. B. Plutschack, B. Pieber, K. Gilmore and P. H. Seeberger, *Chem. Rev.*, 2017, 117, 11796–11893.
- 55 H. Ishitani, Y. Saito, B. Laroche, X. Rao and S. Kobayashi, Chapter 1: Recent Perspectives in Catalysis under Continuous Flow, 2020, vol. 2020-January.
- 56 M. Berton, J. M. de Souza, I. Abdiaj, D. T. McQuade and D. R. Snead, *J. Flow Chem.*, 2020, 10, 73–92.
- 57 J. J. Kilbane and K. Jackowski, *J. Chem. Technol. Biotechnol.*, 1996, 65, 370–374.
- 58 F. Lévesque and P. H. Seeberger, *Org. Lett.*, 2011, 13, 5008–5011.
- 59 N. Emmanuel, C. Mendoza, M. Winter, C. R. Horn, A. Vizza, L. Dreesen, B. Heinrichs and J. C. M. Monbaliu, *Org. Process Res. Dev.*, 2017, 21, 1435–1438.
- 60 C. Mendoza, N. Emmanuel, C. A. Páez, L. Dreesen, J. C. M. Monbaliu and B. Heinrichs, *J. Photochem. Photobiol., A*, 2018, 356, 193–200.
- 61 C. Mendoza, N. Emmanuel, C. A. Páez, L. Dreesen, J.-C. M. Monbaliu and B. Heinrichs, *ChemPhotoChem*, 2018, 2, 890–897.
- 62 M. J. Frisch, G. W. Trucks, H. B. Schlegel, G. E. Scuseria, M. A. Robb, J. R. Cheeseman, G. Scalmani, V. Barone, B. Mennucci, G. A. Petersson, H. Nakatsuji, M. Caricato, X. Li, H. P. Hratchian, A. F. Izmaylov, J. Bloino, G. Zheng, J. L. Sonnenberg, M. Hada, M. Ehara, K. Toyota, R. Fukuda, J. Hasegawa, M. Ishida, T. Nakajima, Y. Honda, O. Kitao, H. Nakai, T. Vreven, J. A. Montgomery Jr., J. E. Peralta, F. Ogliaro, M. Bearpark, J. J. Heyd, E. Brothers, K. N. Kudin, V. N. Staroverov, R. Kobayashi, J. Normand, K. Raghavachari, A. Rendell, J. C. Burant, S. S. Iyengar, J. Tomasi, M. Cossi, N. Rega, J. M. Millam, M. Klene, J. E. Knox, J. B. Cross, V. Bakken, C. Adamo,

- J. Jaramillo, R. Gomperts, R. E. Stratmann, O. Yazyev, A. J. Austin, R. Cammi, C. Pomelli, J. W. Ochterski, R. L. Martin, K. Morokuma, V. G. Zakrzewski, G. A. Voth, P. Salvador, J. J. Dannenberg, S. Dapprich, A. D. Daniels, Ö. Farkas, J. B. Foresman, J. V. Ortiz, J. Cioslowski and D. J. Fox, Gaussian 09 (Revision D.01), Gaussian Inc., Wallingford CT, 2009.
- 63 F. Jensen, *J. Org. Chem.*, 1992, 57, 6478–6487.
- 64 A. Greer, F. Jensen and E. L. Clenna, *J. Org. Chem.*, 1996, 61, 4107–4110.
- 65 A. Toutchkine, D. Aebisher and E. L. Clennan, *J. Am. Chem. Soc.*, 2001, 123, 4966–4973.
- 66 E. Baciocchi, T. Del Giacco, F. Elisei, M. F. Gerini, M. Guerra, A. Lapi and P. Liberali, *J. Am. Chem. Soc.*, 2003, 125, 16444–16454.
- 67 S. M. Bonesi, M. Fagnoni and A. Albini, *J. Org. Chem.*, 2004, 69, 928–935.
- 68 E. L. Clennan, S. E. Hightower and A. Greer, *J. Am. Chem. Soc.*, 2005, 127, 11819–11826.
- 69 S. M. Bonesi, S. Crespi, D. Merli, I. Manet and A. Albini, *J. Org. Chem.*, 2017, 82, 9054–9065.
- 70 E. L. Clennan and A. Greer, *J. Org. Chem.*, 1996, 61, 4793–4797.
- 71 K. Ishiguro, M. Hayashi and Y. Sawaki, *J. Am. Chem. Soc.*, 1996, 118, 7265–7271.
- 72 W. S. Jenks, N. Matsunaga and M. Gordon, *J. Org. Chem.*, 1996, 61, 1275–1282.
- 73 F. Jensen, A. Greer and E. L. Clennan, *J. Am. Chem. Soc.*, 1998, 120, 4439–4449.
- 74 S. M. Bonesi, M. Mella, N. D’Alessandro, G. G. Aloisi, M. Vanossi and A. Albini, *J. Org. Chem.*, 1998, 63, 9946–9955.
- 75 W. Zhou and E. L. Clennan, *J. Am. Chem. Soc.*, 1999, 121, 2915–2916.
- 76 A. Toutchkine and E. L. Clennan, *J. Am. Chem. Soc.*, 2000, 122, 1834–1835.
- 77 E. L. Clennan, *Acc. Chem. Res.*, 2001, 34, 875–884.
- 78 S. M. Bonesi, I. Manet, M. Freccero, M. Fagnoni and A. Albini, *Chem. – Eur. J.*, 2006, 12, 4844–4857.
- 79 C. L. Gu and C. S. Foote, *J. Am. Chem. Soc.*, 1982, 104, 6060–6063.
- 80 A. Toutchkine and E. L. Clennan, *Tetrahedron Lett.*, 1999, 40, 6519–6522.

## Supporting information

The section numbering of this supporting information corresponds to the numbering of the supporting information found online.

### 1. Continuous flow setups

#### 1.1 Microfluidic setups and parts

All microfluidic setups were assembled with commercially available parts.

##### 1.1.1 Pumps

ThalesNano microHPLC<sup>®</sup> pumps (wetted parts: SS 316, ruby and sapphire) were utilized to handle the liquid feeds.

##### 1.1.2 Gas module

The gas flow rate was controlled with a Bronkhorst<sup>®</sup> F210CTM mass flow controller (MFC)

##### 1.1.3 Connectors, ferrules and mixers

1/8" PFA tubings (Swagelok<sup>®</sup>) were equipped with Super Flangeless PEEK nuts, ETFE ferrules and SS rings. 1/4" PFA tubings (Swagelok<sup>®</sup>) were equipped with 1/4" PFA Swagelok Tube Fitting unions and elbows. Connectors, ferrules and unions were purchased from IDEX/Upchurch (details in Table S1).

##### 1.1.4 Check-valves

Check-valves (IDEX/Upchurch Scientific) were inserted between the pumps and the reactor.

##### 1.1.5 Back-pressure regulator

A dome-type BPR (Zaiput Flow Technologies, BPR-10) was inserted downstream. The dometype BPR was connected to a compressed gas cylinder (air or nitrogen) to set the working pressure.

##### 1.1.6 Reactor setups

The flow reactor setups were manufactured by Corning SAS. The preliminary experiments relied on a Corning<sup>®</sup> Advanced-Flow™ Lab Photo Reactor (1 fluidic module, 2.6 mL internal volume) and the final optimized setup relied on a Corning<sup>®</sup> Advanced-Flow™ LF/G1 skid Photo Reactor (5 fluidic modules integrated with static mixers and connected in series, 13 mL total internal volume).

##### 1.1.7 Thermoregulatory devices

The reactor was maintained at reaction temperature with a LAUDA Integral XT 280 thermostat. The LED panels were maintained at 10 °C with a LAUDA RP845 (LAUDA Therm 180 silicone oil).

### 1.2 Part numbers & vendors

Standard fluidic elements and connectors were purchased from IDEX/Upchurch Scientific or from Swagelok (Table S1).

Table S1. Connectors, ferrules and unions

Item	Details	Vendor	Reference
Connectors	Super Flangeless™ Nut PEEK, 1/4-28 Flat-Bottom, for 1/8"	IDEX/ Upchurch Scientific	P-331
	Super Flangeless™ Ferrule Tefzel™ (ETFE), 1/4-28 Flat-Bottom, for 1/8" OD	IDEX/ Upchurch Scientific	P-359
	PFA Swagelok Tube Fitting, Union, 1/4 in. Tube Fitting	Swagelok	PFA-420-6
	PFA Swagelok Tube Fitting, Union Elbow, 1/4 in. Tube Fitting	Swagelok	PFA-420-9
Unions	Large Bore Union PEEK for 3/16" OD	IDEX/ Upchurch Scientific	P-134
Check-valve	Check-valve inline cartridge 1.5 psi and cartridge holder, PEEK	IDEX/ Upchurch Scientific	CV-3000
Dome-type BPR	Dome-type BPR, metal-free, with adjustable set point	Zaiput Flow Techn.	BPR-10
Tubing	PFA Tubing, 1/8 in. OD x 0.030 in. wall x 100 feet	Swagelok	PFA-T2-030-100
	PFA Tubing, 1/4 in. OD x 0.047 in. wall x 100 feet	Swagelok	PFA-T4-047-100

### 1.3 Detailed continuous flow setup

Photooxidation of thioethers in a Corning® Advanced-Flow™ LF/G1 skid Photo Reactor. See manuscript for experimental details (Tables 2 and 3).

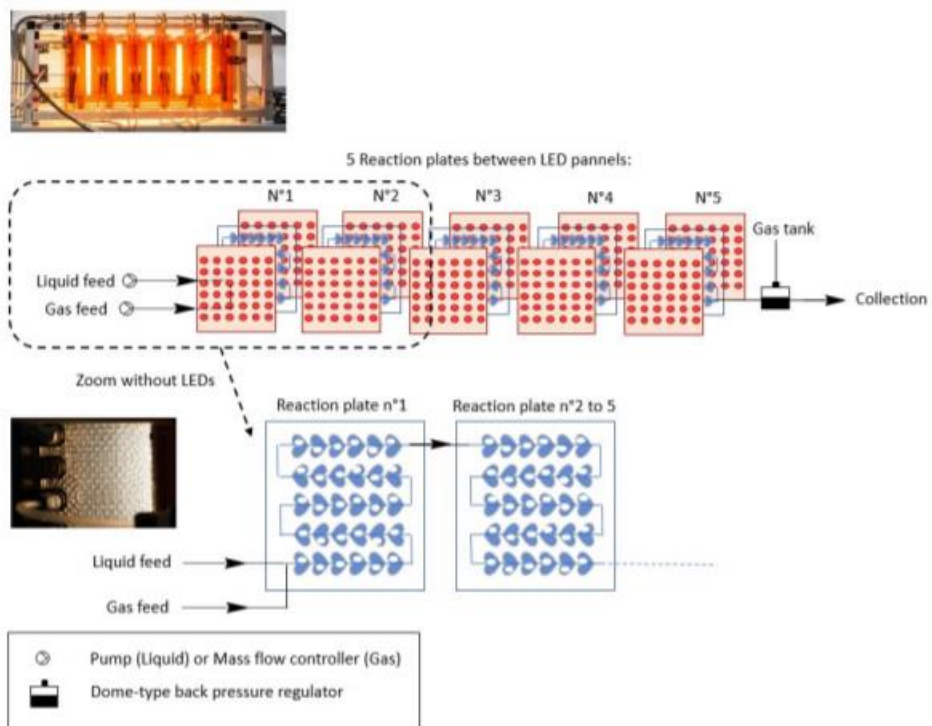


Figure S1. Detailed setup for the continuous flow photooxidation of sulfides.

## 2. Additional experimental details

### 2.1 Chemicals

Chemicals, purities, CAS numbers and suppliers are provided in Table S2.

Table S2. Solvents, chemicals and suppliers

Solvents	Purity (%)	CAS number	Supplier
Ethanol	99	64-17-5	VWR
Acetonitrile	≥99.8	75-05-8	VWR
2-Methyltetrahydrofuran	≥99	96-47-9	Merck
Chemicals	Purity (%)	CAS number	Supplier
Thioanisole (methyl phenyl sulfide)	>99	100-68-5	TCI
Thioanisole sulfoxide (methyl phenyl sulfoxide)	>98	1193-82-4	TCI
Thioanisole sulfone (methyl phenyl sulfone)	>97	3112-85-4	TCI
Dipropyl sulfide	>98	111-47-7	TCI
Dipropyl sulfone	>99	598-03-8	TCI
Thiodipropionic acid	>99	111-17-1	TCI
Benzyl sulfide	>98	538-74-9	TCI
Benzyl sulfoxide	>98	621-08-9	TCI
Benzyl sulfone	>98	620-32-6	Alfa Aesar
Diphenyl sulfide	>98	139-66-2	TCI
Diphenyl sulfoxide	>99	945-51-7	TCI
Diphenyl sulfone	>99	127-63-9	TCI
Tetrahydrothiophene sulfide	>99	110-01-0	TCI
Tetrahydrothiophene sulfoxide	>95	1600-44-8	TCI
Tetrahydrothiophene sulfone	>99	126-33-0	TCI
Benzyl phenyl sulfide	98	831-91-4	Alfa Aesar
Diethyl sulfide	>98	352-93-2	TCI
Benzyl methyl sulfide	>98	766-92-7	TCI
Benzyl methyl sulfone	>98	3112-90-1	Alfa Aesar
Dibenzothiophene sulfide	98	132-65-0	Alfa Aesar
Dibenzothiophene sulfone	>98	1016-05-3	TCI
2-Chloroethylethyl sulfide	>98	693-07-2	TCI
2-Chloroethylethyl sulfone	95	25027-40-1	Sigma Aldrich
Ethyl vinyl sulfide	>93	627-50-9	TCI
Ethyl vinyl sulfone	98	1889-59-4	Sigma Aldrich
Methyl vinyl sulfone	95	3680-02-2	Alfa Aesar
2-Chloroethylphenyl sulfide	>98	5535-49-9	TCI
2-Chloroethylphenyl sulfone	98	938-09-0	abcr
Phenyl vinyl sulfone	99	5535-48-8	Sigma Aldrich
Gas	Purity (%)	Ref	Supplier
Alphagaz 1 Oxygen	O <sub>2</sub> ≥ 99.995	P0361L50S2A 001	Air Liquide
Alphagaz 1 Air	N <sub>2</sub> + O <sub>2</sub> ≥ 99.999	P0291L50S2A 001	Air Liquide

## 2.2 Additional experimental data

### 2.2.1 Analytical methods

Conversions and selectivities were determined by GC-FID or by HPLC-DAD using the following methods:

**GC method:** The GC-FID oven program consisted of the following steps: a 3 min hold at 50 °C, a 20 °C min<sup>-1</sup> ramp to 250 °C, and a 2 min hold at 250 °C. The temperature of the injector was set at 250 °C and the temperature of the FID detector was set at 270 °C. Prior to analysis unless specified otherwise, the sample was homogenized, 50 µL of the sample was mixed with 1 mL of EtOH (denaturated with 5% MeOH) in a 1.5 mL Eppendorf® vial. Conversions and selectivities for compounds **1a** and **CEES** were determined using this method.

#### HPLC method:

Eluent:

A: Water + 0.1% CF<sub>3</sub>COOH (v:v)

B: Acetonitrile

Gradient Table:

Time (min)	A (%)	B (%)
0	100	0
20	20	80
23	20	80
25	100	0
31	100	0

Flow: 1 mL min<sup>-1</sup>

Injection Volume: 10 µL

Column: C18, 100 × 4.6 mm, 3 µm

Oven Temperature: 40 °C

Diode Array Detector: 180-800 nm (processed at 240 nm)

Conversions and selectivities for compounds **1c**, **1d**, **1e** and **1f** were determined using this method.

### 2.2.2 Representative GC results for **CEES** oxidation

GC chromatogram – see manuscript: Table 3, Entry 1

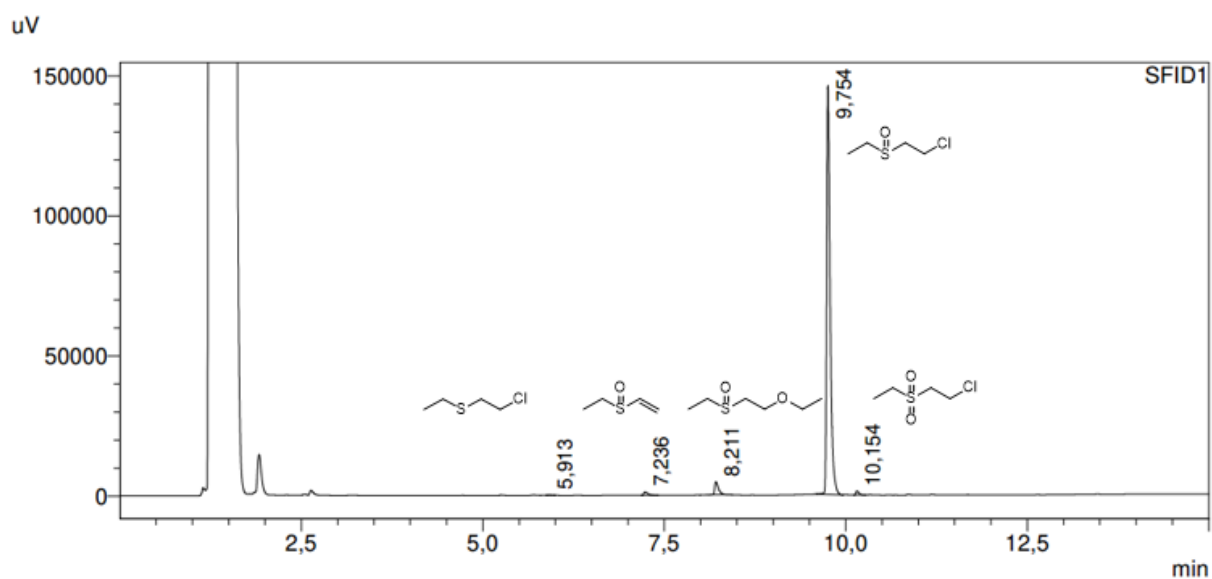


Figure S1. GC chromatogram of the oxidation of **CEES**. See manuscript for experimental details (Table 3, Entry 1).

	Ret. time (min)	Conversion (%)
<b>CEES</b>	5.9	0.10
<b>EVSO (I-2)</b>	7.2	0.94
<b>I-3</b>	8.2	3.39
<b>CEESO</b>	9.75	94.70
<b>CEESO<sub>2</sub></b>	10.15	0.85

Conversion 99.92%

Selectivity for **CEESO** = 94.8%



GC chromatogram – see manuscript: Table 3, Entry 6

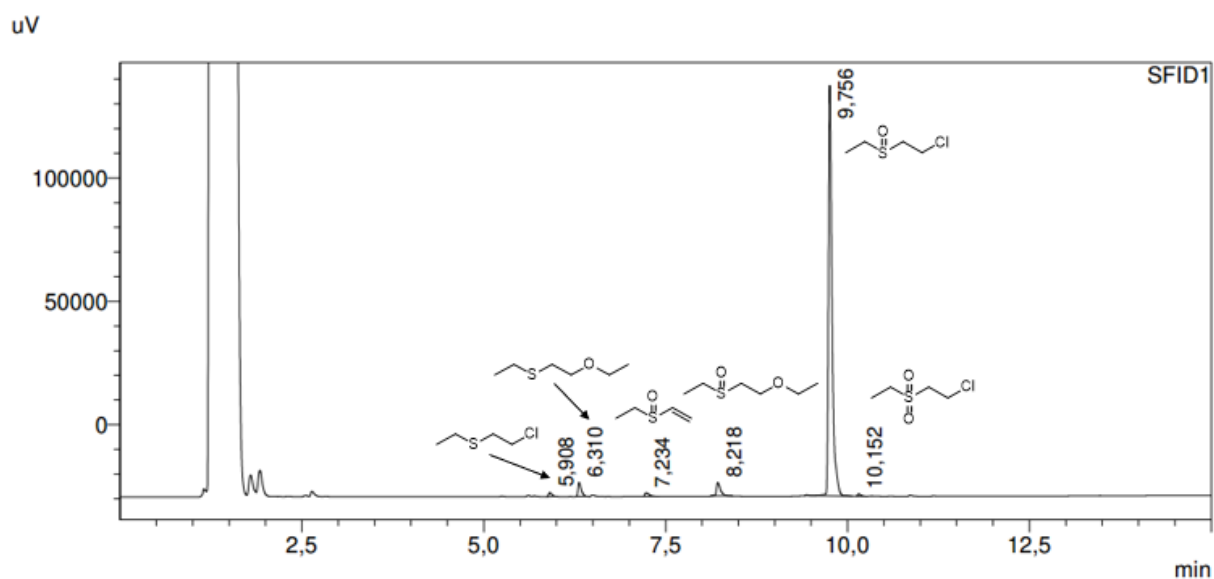


Figure S2. GC chromatogram of the oxidation of **CEES**. See manuscript for experimental details (Table 3, Entry 6).

	Ret. time (min)	Conversion (%)
<b>CEES</b>	5.9	0.79
<b>I-1</b>	6.3	2.79
<b>EVSO (I-2)</b>	7.2	0.95
<b>I-3</b>	8.2	3.36
<b>CEESO</b>	9.75	91.69
<b>CEESO<sub>2</sub></b>	10.15	0.43

Conversion 99.26%

Selectivity for **CEESO** = 92.4%

GC chromatogram – see manuscript: Table 3, Entry 4

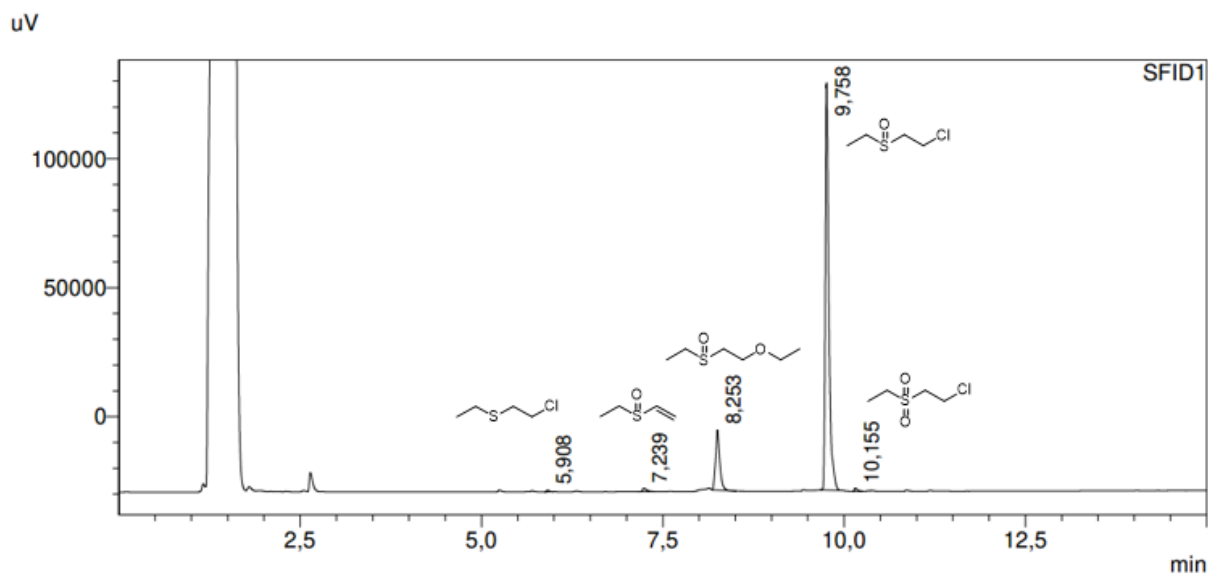


Figure S3. GC chromatogram of the oxidation of **CEES**. See manuscript for experimental details (Table 3, Entry 4).

	Ret. time (min)	Conversion (%)
<b>CEES</b>	5.9	0.27
<b>EVSO (I-2)</b>	7.2	0.79
<b>I-3</b>	8.2	14.56
<b>CEESO</b>	9.75	83.81
<b>CEESO<sub>2</sub></b>	10.15	0.57

Conversion 99.74%

Selectivity for **CEESO** = 84.0%

GC chromatogram – see manuscript: Table 3, Entry 5

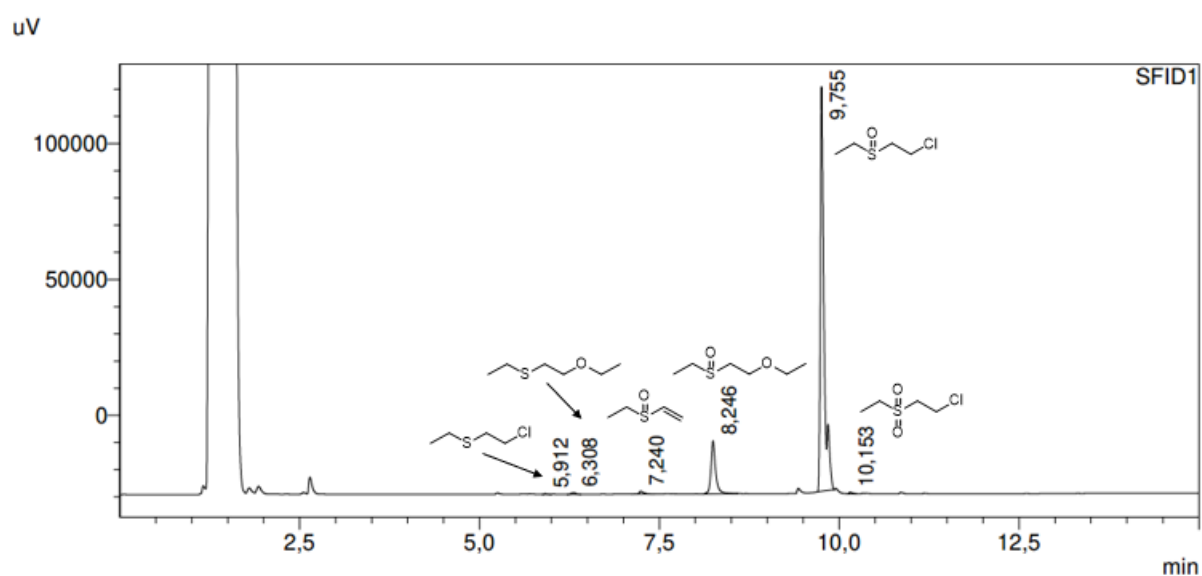


Figure S4. GC chromatogram of the oxidation of **CEES**. See manuscript for experimental details (Table 3, Entry 5).

	Ret. time (min)	Conversion (%)
<b>CEES</b>	5.9	0.13
<b>I-1</b>	6.3	0.43
<b>EVSO (I-2)</b>	7.2	0.76
<b>I-3</b>	8.2	13.71
<b>CEESO</b>	9.75	84.71
<b>CEESO<sub>2</sub></b>	10.15	0.27

Conversion 99.88%

Selectivity for **CEESO** = 84.8%

GC chromatogram – see manuscript: Table 3, Entry 2

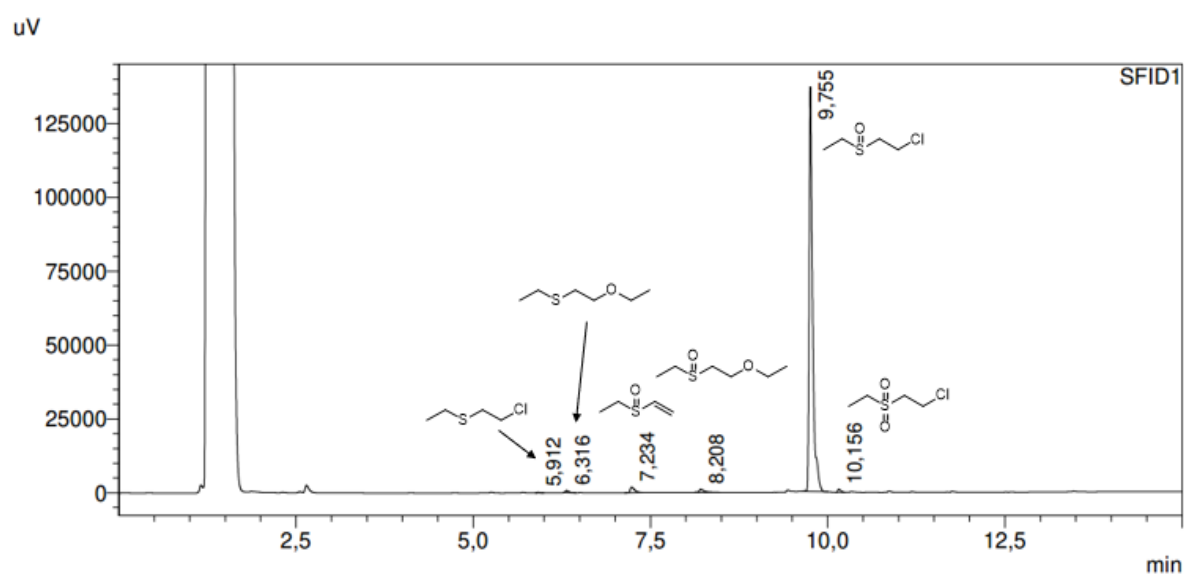


Figure S5. GC chromatogram of the oxidation of **CEES**. See manuscript for experimental details (Table 3, Entry 2).

	Ret. time (min)	Conversion (%)
<b>CEES</b>	5.9	0.12
<b>I-1</b>	6.3	0.49
<b>EVSO (I-2)</b>	7.2	1.58
<b>I-3</b>	8.2	1.26
<b>CEESO</b>	9.75	95.94
<b>CEESO<sub>2</sub></b>	10.15	0.60

Conversion 99.91%

Selectivity for **CEESO** = 96.1%

GC chromatogram – see manuscript: Table 3, Entry 3

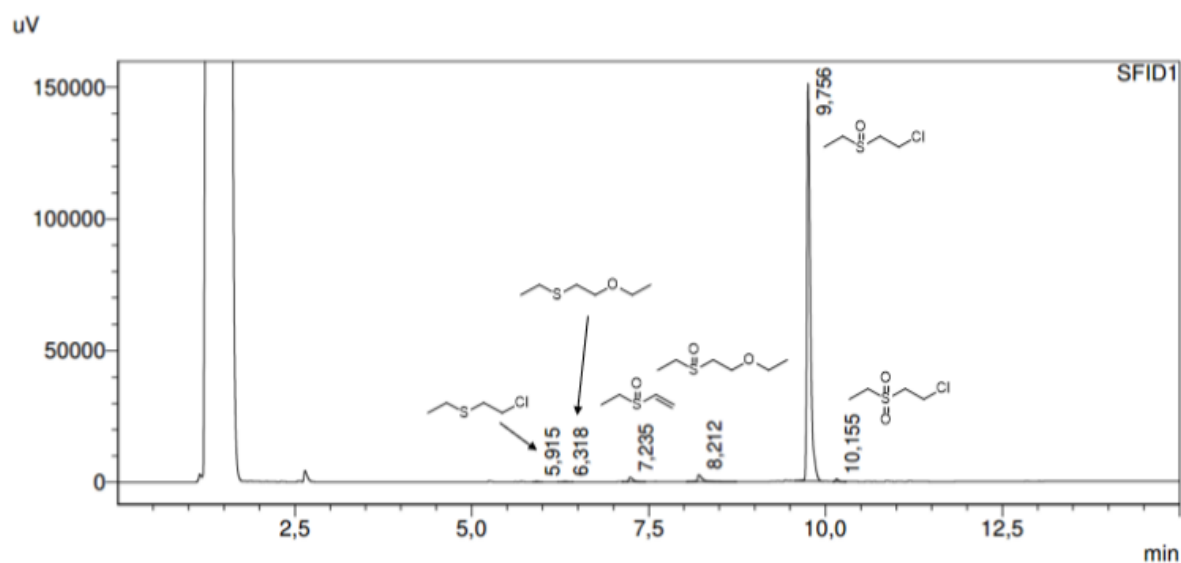


Figure S7. GC chromatogram of the oxidation of **CEES**. See manuscript for experimental details (Table 3, Entry 3).

	Ret. time (min)	Conversion (%)
<b>CEES</b>	5.9	0.10
<b>I-1</b>	6.3	0.12
<b>EVSO (I-2)</b>	7.2	1.41
<b>I-3</b>	8.2	2.51
<b>CEESO</b>	9.75	95.30
<b>CEESO<sub>2</sub></b>	10.15	0.56

Conversion 99.92%

Selectivity for **CEESO** = 95.4%

GC chromatogram – see manuscript: Table 3, Entry 10

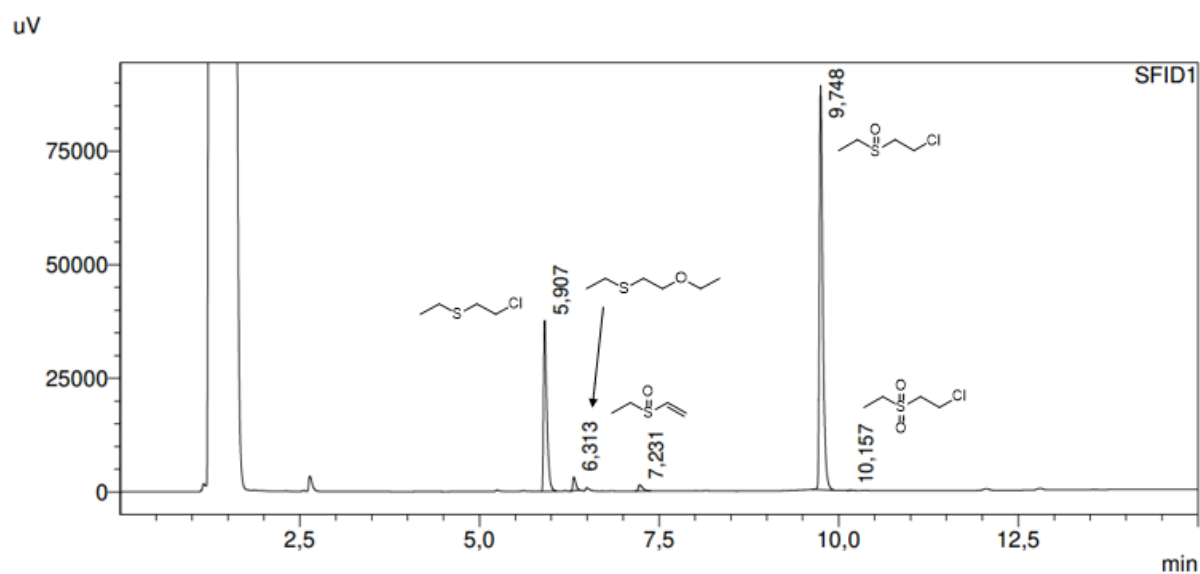


Figure S8. GC chromatogram of the oxidation of **CEES**. See manuscript for experimental details (Table 3, Entry 10).

	Ret. time (min)	Conversion (%)
<b>CEES</b>	5.9	28.15
<b>I-1</b>	6.3	2.02
<b>EVSO (I-2)</b>	7.2	1.28
<b>CEESO</b>	9.75	68.47
<b>CEESO<sub>2</sub></b>	10.15	0.08

Conversion 81.88%

Selectivity for **CEESO** = 95.3%

GC chromatogram – see manuscript: Table 3, Entry 7

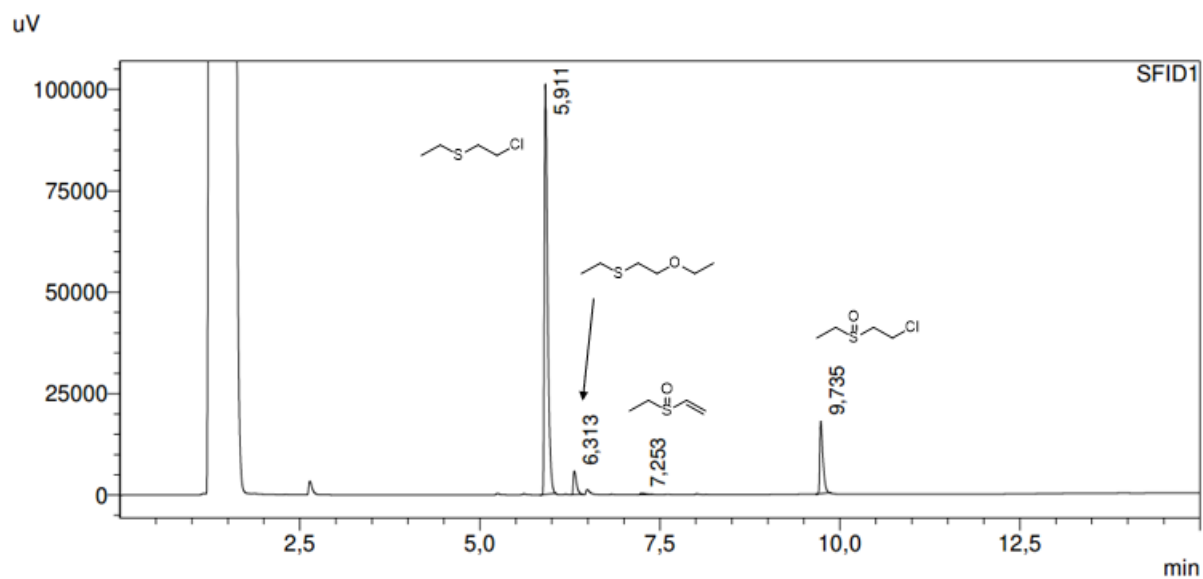


Figure S9. GC chromatogram of the oxidation of **CEES**. See manuscript for experimental details (Table 3, Entry 7).

	Ret. time (min)	Conversion (%)
<b>CEES</b>	5.9	81.06
<b>I-1</b>	6.3	4.48
<b>EVSO (I-2)</b>	7.2	0.44
<b>CEESO</b>	9.75	14.02

Conversion 51.42%

Selectivity for **CEESO** = 74.0%

GC chromatogram – see manuscript: Table 3, Entry 8

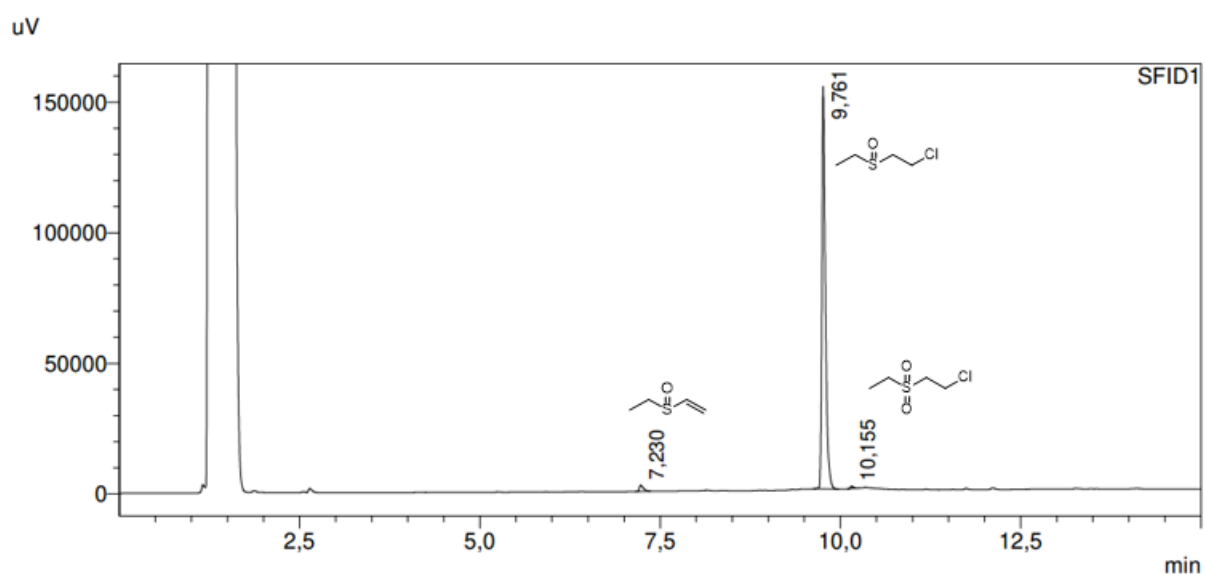


Figure S10. GC chromatogram of the oxidation of **CEES**. See manuscript for experimental details (Table 3, Entry 8).

	Ret. time (min)	Conversion (%)
<b>EVSO (I-2)</b>	7.2	1.68
<b>CEESO</b>	9.75	97.79
<b>CEESO<sub>2</sub></b>	10.15	0.53

Conversion 100%

Selectivity for **CEESO** = 97.8%



GC chromatogram – See manuscript: Table 3, Entry 9

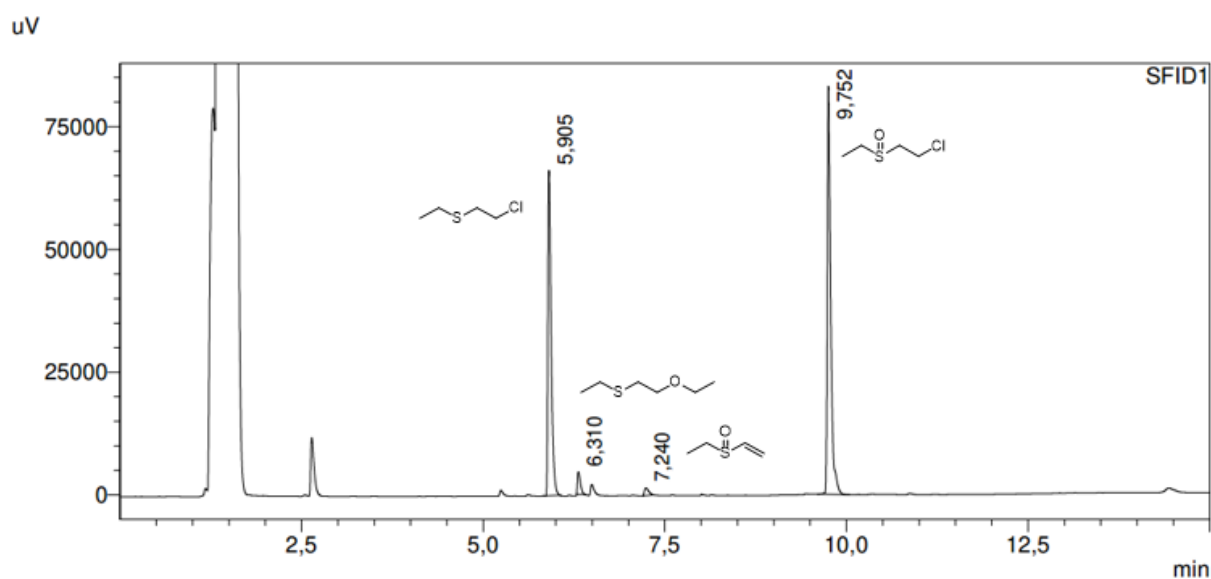


Figure S11. GC chromatogram of the oxidation of **CEES**. See manuscript for experimental details (Table 3, Entry 9).

	Ret. time (min)	Conversion (%)
<b>CEES</b>	5.9	41.43
<b>I-1</b>	6.3	2.56
<b>EVSO (I-2)</b>	7.2	1.27
<b>CEESO</b>	9.75	54.74

Conversion 68.23%

Selectivity for **CEESO** = 93.5%

## 2.2.3 Continuous flow procedure for the photooxidation of sulfides

### 2.2.3.1 Continuous flow procedure for the photooxidation of 2-chloroethylethyl sulfide (**CEES**)

A solution of **CEES** (1 M) and MB (560  $\mu\text{M}$ ) was prepared in EtOH. The pump used to deliver the solution of sulfide/catalyst and the gas flow meter used to deliver oxygen were set to 1 mL  $\text{min}^{-1}$  and 20 mL<sub>N</sub>  $\text{min}^{-1}$ , respectively. Both streams were mixed in the fluidic modules (5 x 2.6 mL internal volume, estimated 4 min residence time) at room temperature under 9 bar of counterpressure. White LEDs (4000K) were selected and used at 100% of their maximum intensity. The reactor effluent was collected at steady state, diluted with ethanol and analyzed by GC-FID (>99% conversion, 97.8% selectivity). Photooxidation of 2-chloroethylethyl sulfide with air was conducted following the same procedure with conditions described in Table 3 (>99% conversion, 84% selectivity).

### 2.2.3.2 Continuous flow procedure for the photooxidation of dipropyl sulfide **1a**

A solution of dipropyl sulfide (**1a**, 1 M) and MB (560  $\mu\text{M}$ ) was prepared in EtOH. The pump used to deliver the solution of sulfide/catalyst and the gas flow meter used to deliver oxygen were set to 0.5 mL  $\text{min}^{-1}$  and 10 mL<sub>N</sub>  $\text{min}^{-1}$ , respectively. Both streams were mixed in the fluidic modules (5 x 2.6 mL internal volume, estimated 10 min residence time) at room temperature under 9 bar of counterpressure. Orange LEDs (610 nm) were selected and used at 70% of their maximum intensity. The reactor effluent was collected at steady state, diluted with ethanol and analyzed by GC-FID (>99% conversion, 97.2% selectivity).

### 2.2.3.3 Continuous flow procedure for the photooxidation of benzyl methyl sulfide **1c**

A solution of benzyl methyl sulfide (**1c**, 1 M) and MB (560  $\mu\text{M}$ ) was prepared in EtOH. The pump used to deliver the solution of sulfide/catalyst and the gas flow meter used to deliver oxygen were set to 0.5 mL  $\text{min}^{-1}$  and 10 mL<sub>N</sub>  $\text{min}^{-1}$ , respectively. Both streams were mixed in the fluidic modules (5 x 2.6 mL internal volume, estimated 10 min residence time) at room temperature under 9 bar of counterpressure. Orange LEDs (610 nm) were selected and used at 70% of their maximum intensity. The reactor effluent was collected at steady state, diluted with ethanol and analyzed by HPLC-DAD (>99% conversion, >99% selectivity).

### 2.2.3.4 Continuous flow procedure for the photooxidation of thioanisole **1d**

A solution of thioanisole (**1d**, 1 M) and MB (560  $\mu\text{M}$ ) was prepared in EtOH. The pump used to deliver the solution of sulfide/catalyst and the gas flow meter used to deliver oxygen were set to 0.5 mL  $\text{min}^{-1}$  and 10 mL<sub>N</sub>  $\text{min}^{-1}$ , respectively. Both streams were mixed in the fluidic modules (5 x 2.6 mL internal volume, estimated 10 min residence time) at room temperature under 9 bar of counterpressure. Orange LEDs (610 nm) were selected and used at 70% of their maximum intensity. The reactor effluent was collected at steady state, diluted with ethanol and analyzed by HPLC-DAD (>99% conversion, >99% selectivity).

### 2.2.3.5 Continuous flow procedure for the photooxidation of diphenyl sulfide **1e**

A solution of diphenyl sulfide (**1e**, 0.1 M) and 9,10-dicyanoanthracene (56  $\mu\text{M}$ ) was prepared in MeCN. The pump used to deliver the solution of sulfide/catalyst and the gas flow meter used to deliver oxygen were set to 0.5 mL  $\text{min}^{-1}$  and 10 mL<sub>N</sub>  $\text{min}^{-1}$ , respectively. Both streams were mixed in the fluidic modules (5 x 2.6 mL internal volume, estimated 10 min residence time) at room temperature under 9 bar of counterpressure. Purple LEDs (395 nm) were selected and used at 70% of their maximum intensity. The reactor effluent was collected at steady state, diluted with MeCN and analyzed by HPLC-DAD (46.6% conversion, >99% selectivity).

#### 2.2.3.6 Continuous flow procedure for the photooxidation of dibenzothiophene **1f**

A solution of dibenzothiophene (**1f**, 0.1 M) and 9,10-dicyanoanthracene (56  $\mu\text{M}$ ) was prepared in MeCN. The pump used to deliver the solution of sulfide/catalyst and the gas flow meter used to deliver oxygen were set to  $0.5 \text{ mL min}^{-1}$  and  $10 \text{ mL}_\text{N} \text{ min}^{-1}$ , respectively. Both streams were mixed in the fluidic modules (5 x 2.6 mL internal volume, estimated 10 min residence time) at room temperature under 9 bar of counterpressure. Orange LEDs (610 nm) were selected and used at 70% of their maximum intensity. The reactor effluent was collected at steady state, diluted with MeCN and analyzed by HPLC-DAD (48.9% conversion, 20.3% selectivity).

#### 2.2.3.7 Continuous flow procedure for the photooxidation of diethyl sulfide

A solution of diethyl sulfide (1 M) and MB (560  $\mu\text{M}$ ) was prepared in EtOH. The pump used to deliver the solution of sulfide/catalyst and the gas flow meter used to deliver oxygen were set to  $0.5 \text{ mL min}^{-1}$  and  $10 \text{ mL}_\text{N} \text{ min}^{-1}$ , respectively. Both streams were mixed in the fluidic modules (5 x 2.6 mL internal volume, estimated 10 min residence time) at room temperature under 9 bar of counterpressure. Orange LEDs (610 nm) were selected and used at 70% of their maximum intensity. The reactor effluent was collected at steady state, diluted with ethanol and analyzed by GC-FID (>99% conversion, 97.3% selectivity).

#### 2.2.3.8 Continuous flow procedure for the photooxidation of thiodipropionic acid

A solution of thiodipropionic acid (1 M) and MB (560  $\mu\text{M}$ ) was prepared in EtOH. The pump used to deliver the solution of sulfide/catalyst and the gas flow meter used to deliver oxygen were set to  $0.5 \text{ mL min}^{-1}$  and  $10 \text{ mL}_\text{N} \text{ min}^{-1}$ , respectively. Both streams were mixed in the fluidic modules (5 x 2.6 mL internal volume, estimated 10 min residence time) at room temperature under 9 bar of counterpressure. Orange LEDs (610 nm) were selected and used at 70% of their maximum intensity. The reactor effluent was collected at steady state, diluted with ethanol and analyzed by NMR (>99% conversion, >99% selectivity).

#### 2.2.3.9 Continuous flow procedure for the photooxidation of tetrahydrothiophene

A solution of tetrahydrothiophene (1 M) and MB (560  $\mu\text{M}$ ) was prepared in EtOH. The pump used to deliver the solution of sulfide/catalyst and the gas flow meter used to deliver oxygen were set to  $0.5 \text{ mL min}^{-1}$  and  $10 \text{ mL}_\text{N} \text{ min}^{-1}$ , respectively. Both streams were mixed in the fluidic modules (5 x 2.6 mL internal volume, estimated 10 min residence time) at room temperature under 9 bar of counterpressure. Orange LEDs (610 nm) were selected and used at 70% of their maximum intensity. The reactor effluent was collected at steady state, diluted with ethanol and analyzed by GC-FID (>99% conversion, >99% selectivity).

#### 2.2.3.10 Continuous flow procedure for the photooxidation of dibenzyl sulfide

A solution of dibenzyl sulfide (0.1 M) and MB (560  $\mu\text{M}$ ) was prepared in EtOH/2-MeTHF. The pumps used to deliver the solution of sulfide/catalyst and the gas flow meter used to deliver oxygen were set to  $0.5 \text{ mL min}^{-1}$  and  $10 \text{ mL}_\text{N} \text{ min}^{-1}$ , respectively. Both streams were mixed in the fluidic modules (5 x 2.6 mL internal volume, estimated 10 min residence time) at  $60 \text{ }^\circ\text{C}$  under 9 bar of counterpressure. Orange LEDs (610 nm) were selected and used at 70% of their maximum intensity. The reactor effluent was collected at steady state, diluted with ethanol and analyzed by HPLC-DAD (>99% conversion, >63.9% selectivity).

#### 2.2.3.11 Continuous flow procedure for the photooxidation of benzyl phenyl sulfide

A solution of benzyl phenyl sulfide (1 M) and MB (560  $\mu\text{M}$ ) was prepared in EtOH. The pump used to deliver the solution of sulfide/catalyst and the gas flow meter used to deliver oxygen were set to 0.1  $\text{mL min}^{-1}$  and 25  $\text{mL}_\text{N} \text{min}^{-1}$ , respectively. Both streams were mixed in the fluidic modules (1 x 2.6 mL internal volume, estimated 1 min residence time) at room temperature under 9 bar of counterpressure. Orange LEDs (610 nm) were selected and used at 70% of their maximum intensity. The reactor effluent was collected at steady state, diluted with ethanol and analyzed by HPLC-DAD (13.1% conversion, 55.7% selectivity).

#### 2.2.3.12 Continuous flow procedure for the photooxidation of 2-chloroethylphenyl sulfide

A solution of 2-chloroethylphenyl sulfide (0.1 M) and MB (56  $\mu\text{M}$ ) was prepared in EtOH. The pump used to deliver the solution of sulfide/catalyst and the gas flow meter used to deliver oxygen were set to 0.5  $\text{mL min}^{-1}$  and 10  $\text{mL}_\text{N} \text{min}^{-1}$ , respectively. Both streams were mixed in the fluidic modules (5 x 2.6 mL internal volume, estimated 10 min residence time) at room temperature under 9 bar of counterpressure. Orange LEDs (610 nm) were selected and used at 70% of their maximum intensity. The reactor effluent was collected at steady state, diluted with ethanol and analyzed by GC-MS (>93.1% conversion, >99% selectivity).

### 2.2.4 Batch procedures for the synthesis of products and by-products resulting from 2-chloroethylethylsulfide oxidation

#### 2.2.4.1 Batch procedure for the synthesis of vinyl ethyl sulfoxide (**EVSO**, **I-2**)

A solution of ethyl vinylsulfide (1 M, 5 mL) was prepared in EtOH and oxidized with an aqueous solution of 30%  $\text{H}_2\text{O}_2$  (1 mL). An aliquot was taken after 5 min, diluted in EtOH, analyzed by GC-FID. Vinyl ethyl sulfoxide (**EVSO**) was detected alongside with vinyl ethyl sulfone (**EVSO<sub>2</sub>**) and identified by MS.

#### 2.2.4.2 Batch procedure for the synthesis of 2-ethoxyethylethyl sulfane (**I-1**)

A solution of 2-chloroethyl ethyl sulfide (1 M, 5 mL) was prepared in EtOH and heated in a microwave oven (CEM Discovery, 150  $^\circ\text{C}$ , 3 x 20 min, 150 W). An aliquot was diluted in EtOH, analyzed by GC-FID and identified by NMR and MS.

The formation of 2-ethoxyethylethyl sulfane (**I-1**) was also studied by leaving a solution of **CEES** (1 M) in EtOH for a week at room temperature without mixing. An aliquot was diluted in EtOH and analyzed by GC-FID over 4 days. From day 1 to day 4, the quantity of 2-ethoxyethylethyl sulfane (**I-1**) increased from 1.19% to 4.03%. Even if **I-1** is detectable in GC when a fresh solution of **CEES** in EtOH is injected, this increase over time demonstrates that the formation of additional **I-1** occurs slowly upon standing in solution at room temperature.

#### 2.2.4.3 Batch procedure for the synthesis of 1-ethoxy-2-(ethylsulfinyl)ethane (**I-3**)

A solution of 2-ethoxyethylethyl sulfane (0.1 M, 2 mL) was prepared in EtOH and oxidized with an aqueous solution of 30%  $\text{H}_2\text{O}_2$  (0.3 mL). An aliquot was taken immediately, diluted in EtOH, analyzed by GC-FID. 1-Ethoxy-2-(ethylsulfinyl)ethane (**I-3**) was identified by MS.

**I-3** was not detected in GC when a solution of **EVSO** (**I-2**) in EtOH was injected; thus rejecting the filiation between **EVSO** and **I-3**.

#### 2.2.4.4 Batch procedure for the synthesis of 1-ethoxy-2-(ethylsulfonyl)ethane

A solution of 2-ethoxyethylethyl sulfane (0.1 M, 2 mL) was prepared in EtOH and oxidized with an aqueous solution of 30% H<sub>2</sub>O<sub>2</sub> (0.3 mL). An aliquot was taken after 5 min, diluted in EtOH, analyzed by GC-FID. 1-Ethoxy-2-(ethylsulfonyl)ethane was identified by MS.

### 2.3 Characterization of compounds

Commercial references for sulfoxides were purchased for **CEES**, **1d** and **1e** (see Table S2). For compounds **1a**, **1c** and **1f**, reference sulfoxides were synthesized by oxidation with H<sub>2</sub>O<sub>2</sub> for peak identification in HPLC or GC. Commercial references for sulfones were purchased for **CEES**, **1a**, **1c**, **1d**, **1e** and **1f** (see Table S2).

#### 2.3.1 In-line NMR

A study of the evolution of **1d** oxidation regarding to an increase of light intensity was conducted. An In-line NMR was equipped downstream (43 MHz Spinsolve™ Carbon NMR spectrometer from Magritek® equipped with the flow-through module). A T-mixer was used to vent the excess gas before entering the NMR flow cell.

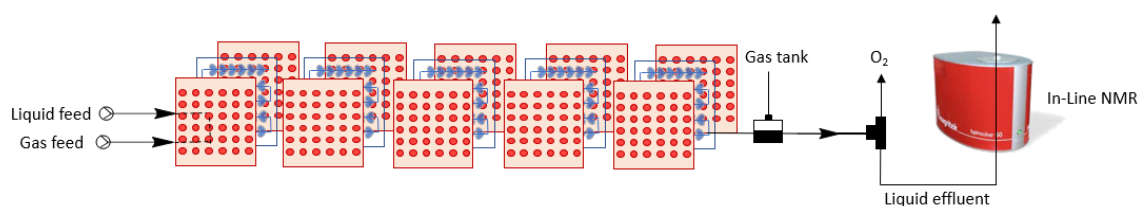


Figure S12. Detailed setup for the continuous flow photooxidation of sulfides.

A solution of **1d** (1 M) and MB (560 μM) was prepared in EtOH. The pumps used to deliver the solution of sulfide/catalyst and the gas flow meter used to deliver oxygen were set to 0.5 mL min<sup>-1</sup> and 10 mL<sub>N</sub> min<sup>-1</sup>, respectively. Both streams were mixed in the fluidic modules (5 x 2.6 mL internal volume, estimated 10 min residence time) at 20 °C under 9 bar of counterpressure. LEDs were set on a 610 nm wavelength with an increasing intensity (from 0% to 100% with a 10% increment). A first <sup>1</sup>H NMR spectrum was recorded for the solvent alone. When the reaction started, a <sup>1</sup>H NMR spectrum was recorded after each increment of light intensity. The evolution of the oxidation can be studied by following the shift of the -CH<sub>3</sub> signal from 2.42 ppm to 2.81 ppm. The reaction reached completion upon irradiation at 70% of light intensity (see Figure S13).

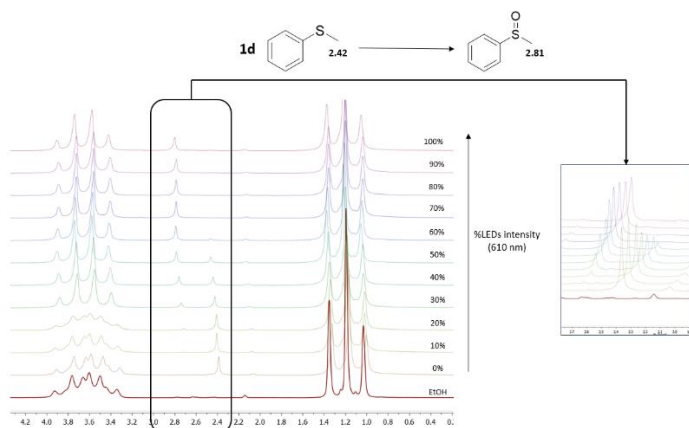


Figure S13. In-line  $^1\text{H}$  NMR (43 MHz) spectra of **1d** photooxidation. Evolution of the sulfoxide appearance with an increase of light intensity.

### 2.3.2 In-line IR

To assess the efficiency of the In-line IR as an analytical tool to follow the oxidation of **CEES**, a first set of experiments was carried out on **1a** as a model thioether (see Figure S14).

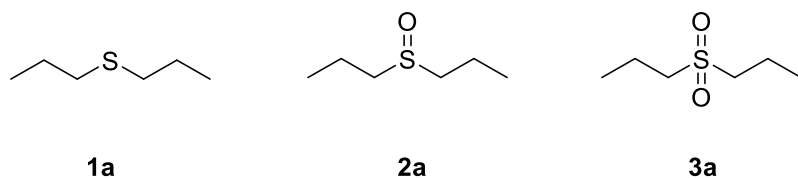


Figure S14. Structures of **1a**, **2a** and **3a**

A solution of dipropyl sulfide (**1a**, 1 M) was prepared in EtOH and injected first. Every 2 min, the amount of **1a** was reduced and the amount of dipropyl sulfoxide (**2a**) was increased to the point where the solution only contained the sulfoxide (1 M). The same procedure was applied with a decrease in sulfoxide and an increase in the corresponding sulfone **3a** until a concentration of 1 M was reached. Compound **1a** does not show any easily distinguishable signals from the solvent backbone and fingerprint. The corresponding sulfoxide **2a** shows a characteristic broad peak between  $980$  and  $1020\text{ cm}^{-1}$  that can be utilized to monitor the appearance of **2a**. The IR spectrum of dipropyl sulfone (**3a**) also displays characteristic vibration bands at  $1130$ ,  $1280$  and  $1315\text{ cm}^{-1}$  (see Figure S15) that can be utilized to monitor variations in its concentration.

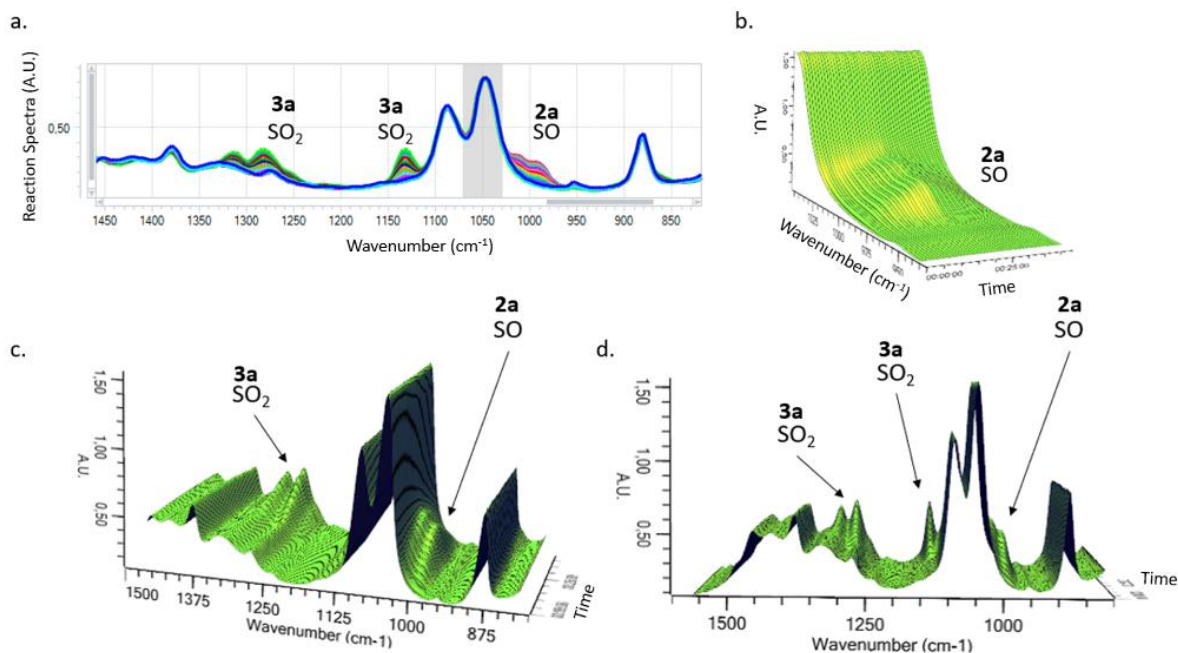


Figure S15. In-line IR spectra following **1a** oxidation to sulfoxide and overoxidation to sulfone.

The same procedure was applied to the oxidation of **CEES** for establishing a usable library of IR spectra. The characteristic vibration bands for the corresponding sulfoxide **CEESO** can be seen at 980 and 1020  $\text{cm}^{-1}$ , while the characteristic vibration bands for the sulfone **CEESO<sub>2</sub>** appear between 1220 and 1360  $\text{cm}^{-1}$  and at about 1730  $\text{cm}^{-1}$  (see Figure S16). These experiments confirm that In-line IR can be used as a suitable monitoring tool for the monitoring of **CEES** oxidation.

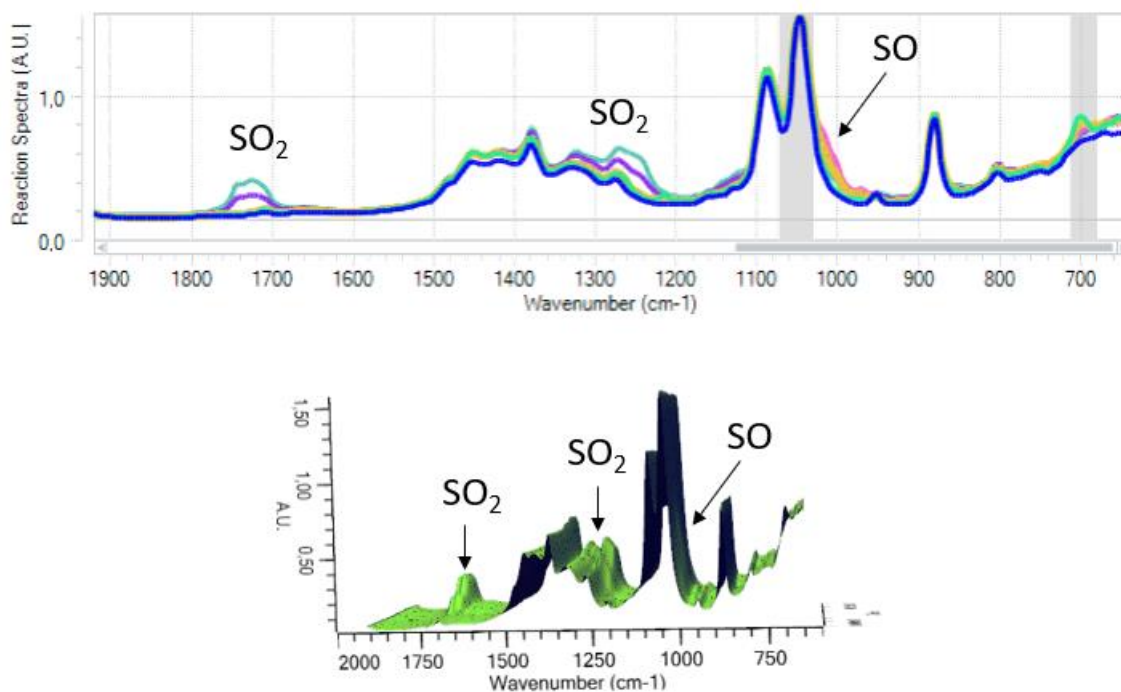
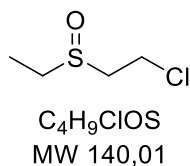
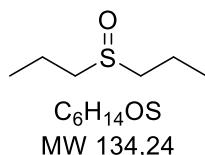


Figure S16. In-line IR spectra following **CEES** oxidation to sulfoxide and overoxidation to sulfone.

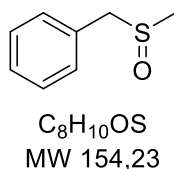
## 2.4 Structural identity of compounds



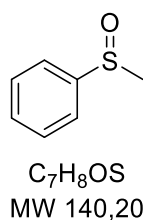
**CEESO.**  $^1H$  NMR ( $CDCl_3$ , 400 MHz):  $\delta$  = 3.96 (m, 2H), 3.21 (m, 2H), 2.91 (m, 2H), 1.37 (t,  $J$  = 7.5 Hz, 3H) ppm. The NMR data match those reported in the literature.<sup>S1</sup> **ESI HRMS**  $m/z$   $C_4H_{10}O^{35}Cl^{32}S^+$  [M+H]<sup>+</sup>: calcd 141.01354; found 141.01366.



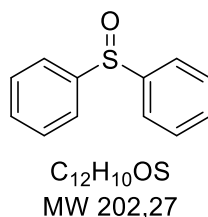
Dipropyl sulfoxide (**2a**).  $^1H$  NMR (MeOD, 400 MHz):  $\delta$  = 2.66 – 8.62 (m, 4H), 1.74 – 1.63 (m, 4H), 1.00 – 0.96 (t,  $J$  = 7.4 Hz, 6H) ppm. The NMR data match those reported in the literature.<sup>S2</sup>



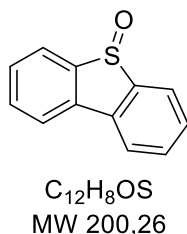
Benzyl methyl sulfoxide (**2c**).  $^1H$  NMR ( $CDCl_3$ , 400 MHz):  $\delta$  = 7.31 – 7.22 (m, 5H), 3.99 (d,  $J$  = 12.9 Hz, 1H), 3.92 (d,  $J$  = 12.9 Hz, 1H), 2.42 (s, 3H) ppm. The NMR data match those reported in the literature.<sup>S3</sup>



Phenyl methyl sulfoxide (**2d**).  $^1H$  NMR ( $CDCl_3$ , 43 MHz):  $\delta$  = 7.69 – 7.62 (m, 5H), 2.79 (s, 3H) ppm. The NMR data match the commercial reference and those reported in the literature.<sup>S4</sup>

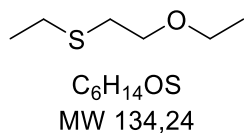


Diphenyl sulfoxide (**2e**).  $^1H$  NMR ( $CDCl_3$ , 400 MHz):  $\delta$  = 7.54 – 7.51 (m, 4H), 7.35 – 7.34 (m, 6H) ppm. The NMR data match the commercial reference and those reported in the literature.<sup>S3</sup>



Dibenzothiophene (**2f**).  $^1H$  NMR ( $CDCl_3$ , 400 MHz):  $\delta$  = 7.98 (d,  $J$  = 7.6 Hz, 2H), 7.81 (d,  $J$  = 7.6 Hz, 1H), 7.70 – 7.63 (m, 3H), 7.57 – 7.52 (m, 2H) ppm. The NMR data match those reported in the literature.<sup>S2</sup>





2-ethoxyethylethyl sulfane (**I-1**). <sup>1</sup>H NMR (CDCl<sub>3</sub>, 400 MHz): δ = 3.52 – 3.32 (m, 4H), 2.63 – 2.53 (m, 2H), 2.48 – 2.38 (m, 2H), 1.15 – 1.03 (m, 6H) ppm. GC-MS: m/z = 134

## 2.5 Copies of NMR spectra

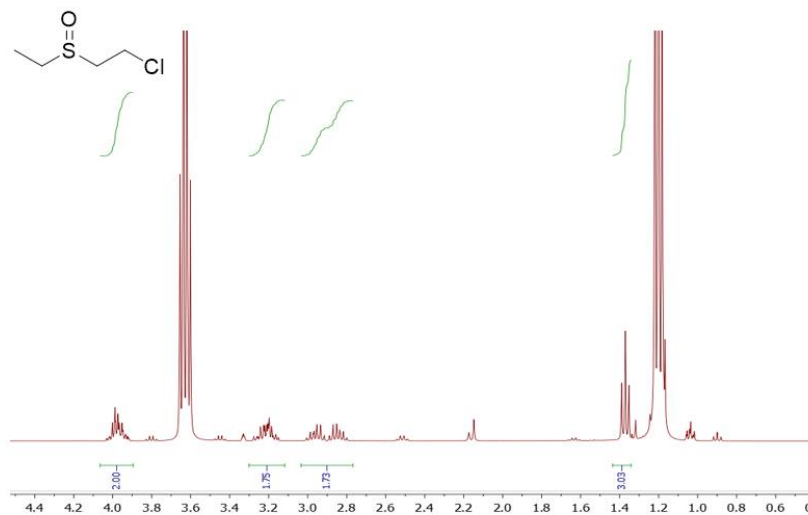


Figure S17. <sup>1</sup>H NMR spectrum (400 MHz) of **CEESO** in CDCl<sub>3</sub>.

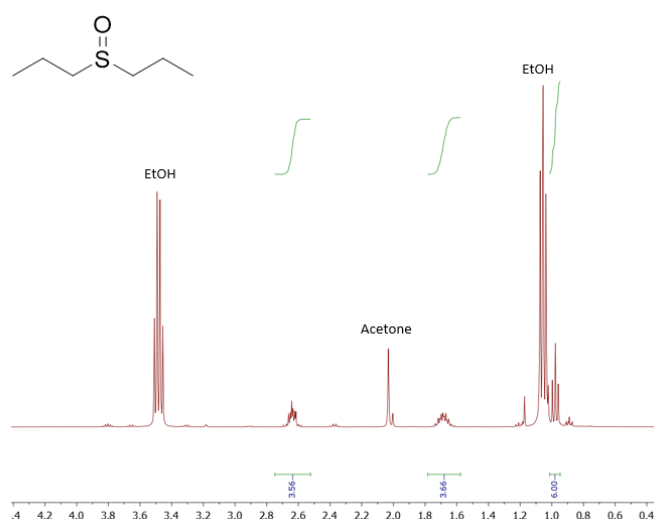


Figure S18. <sup>1</sup>H NMR spectrum (400 MHz) of dipropyl sulfoxide (**2a**) in CDCl<sub>3</sub>.

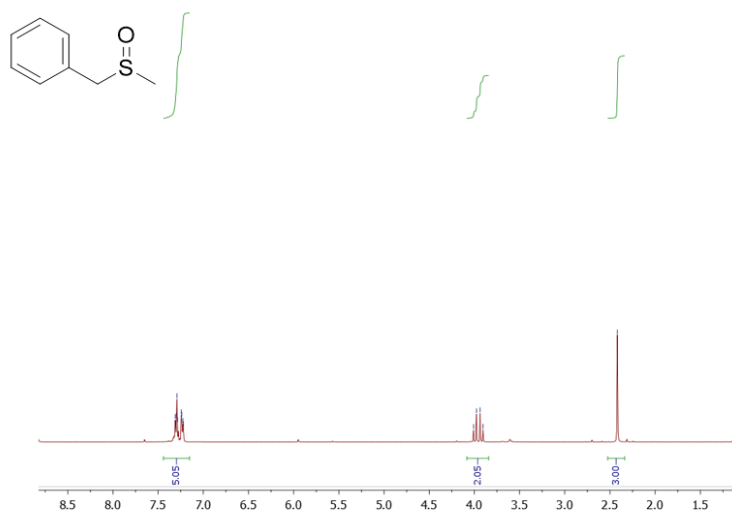


Figure S19. <sup>1</sup>H NMR spectrum (400 MHz) of benzyl methyl sulfoxide (**2c**) in CDCl<sub>3</sub>.

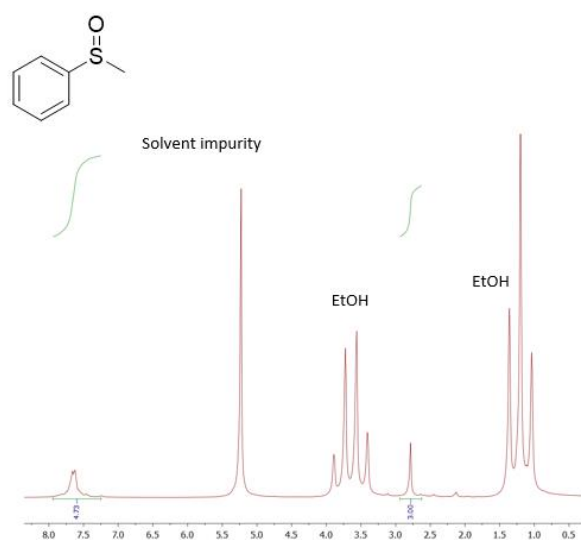


Figure S20. <sup>1</sup>H NMR spectrum (400 MHz) of phenyl methyl sulfoxide (**2d**) in CDCl<sub>3</sub>.

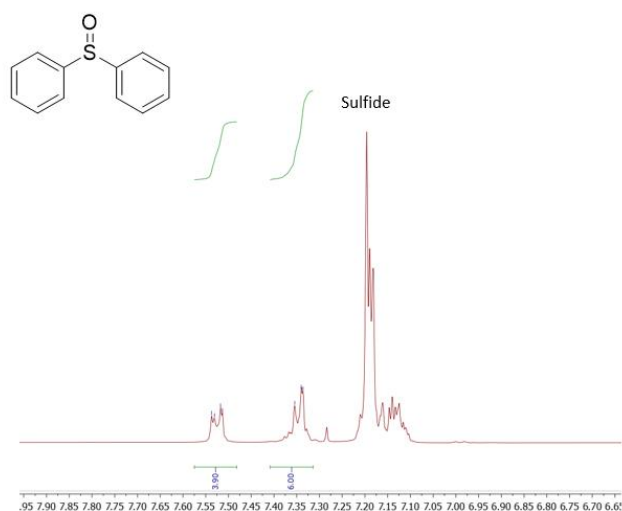


Figure S21.  $^1\text{H}$  NMR spectrum (400 MHz) of diphenyl sulfide (**2e**) in  $\text{CDCl}_3$ .

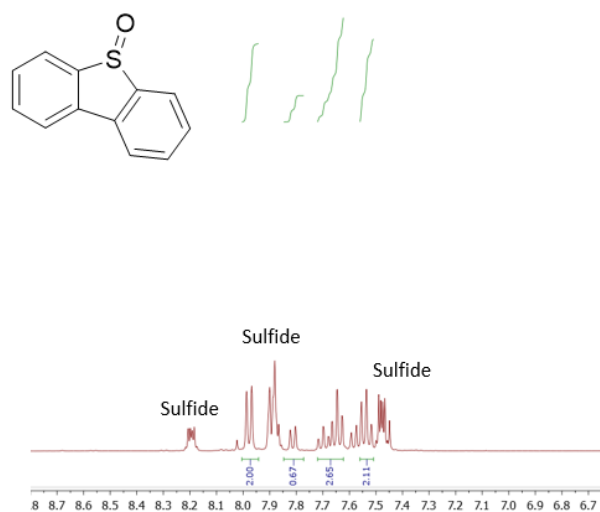


Figure S22.  $^1\text{H}$  NMR spectrum (400 MHz) of dibenzothiophene sulfoxide (**2f**) in  $\text{CDCl}_3$ .

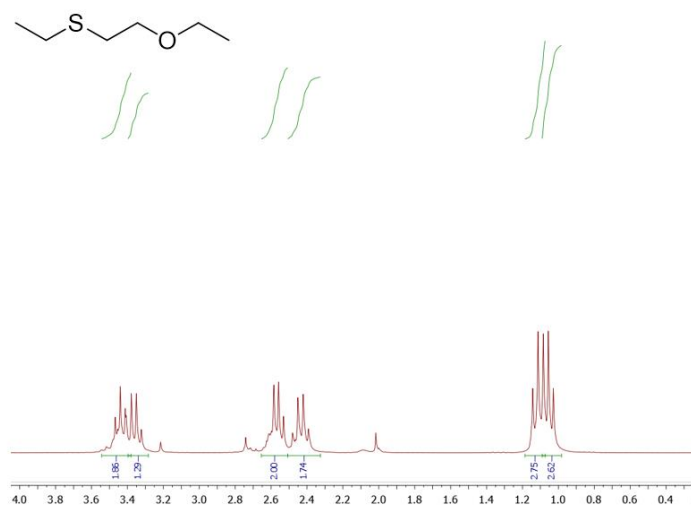


Figure S23.  $^1\text{H}$  NMR spectrum (400 MHz) of 2-ethoxyethyl sulfane (**I-1**) in  $\text{CDCl}_3$ .

### 3. Detailed data on the photooxidation trials

#### 3.1 Photooxidation of model thioethers

Table S3. General table of oxidation tests (part 1). Selectivity is only specified when not total towards the sulfoxide.

n°exp	Substrate	Oxidant	Photosensib.	Solvent	Temp. (°C)	Concentration (M)		Flow rate (mL.min <sup>-1</sup> )		BPR (bar)	Light (nm) (Intensity (%))	Res. Time (min)	Conversion (%)	Selectivity (%)
						Substrate	Photosensib.	Substrate	O <sub>2</sub>					
1	thioanisole	O <sub>2</sub>	MB	EtOH	rt	1	0.00056	1.5	15	8	610 (50)	-4	14.6	
2	thioanisole	O <sub>2</sub>	MB	EtOH	rt	1	0.00056	1.5	15	8	610 (50)	-4	14.4	
3	thioanisole	O <sub>2</sub>	MB	EtOH	rt	1	0.00056	1.5	15	8	610 (50)	-4	14.5	
4	thioanisole	O <sub>2</sub>	MB	EtOH	rt	1	0.00056	2	15	8	610 (50)	-3	10.9	
5	thioanisole	O <sub>2</sub>	MB	EtOH	rt	1	0.00056	2	15	8	610 (50)	-3	11.12	
6	thioanisole	O <sub>2</sub>	MB	EtOH	rt	1	0.00056	2	15	8	610 (50)	-3	10.8	
7	thioanisole	O <sub>2</sub>	MB	EtOH	rt	1	0.00056	20.2	15	8	610 (100)	-3	27.3	
8	thioanisole	O <sub>2</sub>	MB	EtOH	rt	1	0.00056	2.5	15	8	610 (50)	-3	7.8	
9	thioanisole	O <sub>2</sub>	MB	EtOH	rt	1	0.00056	3	15	8	610 (50)	-3	7.1	
10	thioanisole	O <sub>2</sub>	MB	EtOH	rt	1	0.00056	3.5	15	8	610 (50)	-3	6.3	
11	thioanisole	O <sub>2</sub>	MB	EtOH	rt	1	0.00056	1.5	15	8	610 (50)	-4	10.7	
12	thioanisole	O <sub>2</sub>	MB	EtOH	rt	1	0.00056	2	15	8	610 (50)	-3	8.7	
13	thioanisole	O <sub>2</sub>	MB	EtOH	rt	1	0.00056	2.5	15	8	610 (50)	-3	6.7	
14	thioanisole	O <sub>2</sub>	MB	EtOH	rt	1	0.00056	3	15	8	610 (50)	-3	7.2	
15	thioanisole	O <sub>2</sub>	MB	EtOH	rt	1	0.00056	3.5	15	8	610 (50)	-3	7.0	
16	thioanisole	O <sub>2</sub>	MB	EtOH	rt	1	0.00056	1.5	20	8	610 (50)	-3	0.14	
17	thioanisole	O <sub>2</sub>	MB	EtOH	rt	1	0.00056	1.5	25	8	610 (50)	-3	14.2	
18	thioanisole	O <sub>2</sub>	MB	EtOH	rt	1	0.00056	1.5	30	8	610 (50)	-3	10.9	
19	thioanisole	O <sub>2</sub>	MB	EtOH	rt	1	0.00056	1.5	35	8	610 (50)	-2	10.44	
20	thioanisole	O <sub>2</sub>	MB	EtOH	rt	1	0.00056	2	20	8	610 (50)	-3	10.6	
21	thioanisole	O <sub>2</sub>	MB	EtOH	rt	1	0.00056	2	25	8	610 (50)	-3	10.1	
22	thioanisole	O <sub>2</sub>	MB	EtOH	rt	1	0.00056	2	30	8	610 (50)	-3	9.9	
23	thioanisole	O <sub>2</sub>	MB	EtOH	rt	1	0.00056	2	35	8	610 (50)	-2	9.8	
24	thioanisole	O <sub>2</sub>	MB	EtOH	rt	1	0.00056	1.5	10	8	610 (50)	-5	14.6	
25	thioanisole	O <sub>2</sub>	MB	EtOH	rt	1	0.00056	2	10	8	610 (50)	-4	10.9	
26	thioanisole	O <sub>2</sub>	MB	EtOH	rt	1	0.00056	1	15	8	610 (50)	-4	19.8	
27	thioanisole	O <sub>2</sub>	MB	EtOH	rt	1	0.00056	1.5	20	8	610 (60)	-3	16.7	
28	thioanisole	O <sub>2</sub>	MB	EtOH	rt	1	0.00056	1.5	20	8	610 (70)	-3	21.9	
29	thioanisole	O <sub>2</sub>	MB	EtOH	rt	1	0.00056	1.5	20	8	610 (80)	-3	23.9	
30	thioanisole	O <sub>2</sub>	MB	EtOH	rt	1	0.00056	1.5	20	8	610 (90)	-3	32.8	
31	thioanisole	O <sub>2</sub>	MB	EtOH	rt	1	0.00056	1.5	20	8	610 (100)	-3	35.8	
32	thioanisole	O <sub>2</sub>	MB	EtOH	rt	1	0.00056	1	50	8	610 (50)	-2	15.5	
33	thioanisole	O <sub>2</sub>	MB	EtOH	rt	1	0.00056	1	50	8	610 (50)	-2	3.4	
34	thioanisole	O <sub>2</sub>	MB	EtOH	rt	1	0.00056	1	15	8	610 (50)	-4	3.4	
35	thioanisole	O <sub>2</sub>	MB	EtOH	rt	1	0.00056	1.5	15	8	610 (50)	-4	2.6	
36	thioanisole	O <sub>2</sub>	MB	EtOH	rt	1	0.00056	2	15	8	610 (50)	-3	2.2	
37	thioanisole	O <sub>2</sub>	RB	EtOH	rt	1	0.00056	1	50	8	532 (50)	-2	9.2	
38	thioanisole	O <sub>2</sub>	RB	EtOH	rt	1	0.00056	1	15	8	532 (50)	-4	3.7	
39	thioanisole	O <sub>2</sub>	RB	EtOH	rt	1	0.00056	1.5	15	8	532 (50)	-4	10.4	
40	thioanisole	O <sub>2</sub>	RB	EtOH	rt	1	0.00056	2	15	8	532 (50)	-3	10.9	
41	thioanisole	O <sub>2</sub>	MB	EtOH	rt	1	0.00056	1	15	8	610 (100)	-4	43.9	
42	thioanisole	O <sub>2</sub>	MB	EtOH	rt	1	0.00056	0.5	10	8	610 (50)	-7	61.2	
43	thioanisole	O <sub>2</sub>	MB	EtOH	rt	1	0.00056	0.5	15	8	610 (50)	-6	40.8	
44	thioanisole	O <sub>2</sub>	MB	EtOH	rt	1	0.00056	0.5	10	8	610 (100)	-7	88.8	
45	thioanisole	O <sub>2</sub>	MB	EtOH	rt	1	0.00056	0.5	10	8	610 (50)	-7	25.9	
46	thioanisole	O <sub>2</sub>	MB	EtOH	rt	1	0.00056	1	15	8	610 (50)	-4	25.6	
47	thioanisole	O <sub>2</sub>	MB	EtOH	rt	1	0.00056	1.5	15	8	610 (50)	-4	15.05	
48	thioanisole	O <sub>2</sub>	MB	EtOH	rt	1	0.00056	2	15	8	610 (50)	-4	11.6	
49	thioanisole	O <sub>2</sub>	MB	EtOH	rt	1	0.00056	0.5	10	8	610 (50)	-6	6.7	
50	thioanisole	O <sub>2</sub>	MB	EtOH	rt	1	0.00056	0.5	10	9	610 (50)	-10	N.D	
51	thioanisole	O <sub>2</sub>	MB	EtOH	rt	1	0.00056	0.5	10	7	610 (50)	-6	45.4	
52	thioanisole	O <sub>2</sub>	MB	EtOH	rt	1	0.00056	0.5	10	9	610 (50)	-10	94.0	
53	thioanisole	O <sub>2</sub>	MB	EtOH	rt	1	0.00056	0.5	10	9	610 (50)	-10	94.8	
54	thioanisole	O <sub>2</sub>	MB	EtOH	rt	1	0.00056	0.5	10	9	610 (80)	-10	66.2	
55	thioanisole	O <sub>2</sub>	MB	EtOH	rt	1	0.001	0.5	10	9	610 (50)	-10	33.9	
56	thioanisole	O <sub>2</sub>	MB	EtOH	rt	1	0.001	0.5	10	9	610 (50)	-10	39.1	
57	thioanisole	O <sub>2</sub>	MB	EtOH	rt	1	0.001	0.5	10	9	610 (60)	-10	72.8	
58	thioanisole	O <sub>2</sub>	MB	EtOH	rt	1	0.00056	0.5	10	9	610 (70)	-10	99.4	
59	thioanisole	O <sub>2</sub>	MB	EtOH	rt	1	0.00056	0.5	10	9	610 (70)	-10	93.2	
60	thioanisole	O <sub>2</sub>	MB	EtOH	rt	1	0.00056	0.5	10	9	610 (70)	-10	total	
61	thioanisole	O <sub>2</sub>	MB	EtOH	rt	1	0.00056	0.5	10	9	610 (70)	-10	97.6	
62	benzyl methyl sulfide	O <sub>2</sub>	MB	EtOH	rt	1	0.00056	0.5	10	9	610 (50)	-10	total	
63	benzyl methyl sulfide	O <sub>2</sub>	MB	EtOH	t	1	0.00056	0.5	10	9	610 (60)	-10	total	
64	benzyl methyl sulfide	O <sub>2</sub>	MB	EtOH	rt	1	0.00056	0.5	10	9	610 (80)	-10	total	
65	benzyl methyl sulfide	O <sub>2</sub>	MB	EtOH	rt	1	0.00056	0.5	10	9	610 (70)	-10	total	
66	tetrathiophene	O <sub>2</sub>	MB	EtOH	rt	1	0.00056	0.5	10	9	610 (60)	-10	94.8	
67	tetrathiophene	O <sub>2</sub>	MB	EtOH	rt	1	0.00056	0.5	10	9	610 (80)	-10	97.6	97.0
68	tetrathiophene	O <sub>2</sub>	MB	EtOH	rt	1	0.00056	0.5	10	9	610 (70)	-10	total	
69	dipropylsulfide	O <sub>2</sub>	MB	EtOH	rt	1	0.00056	0.5	10	9	610 (80)	-10	total	97.2
70	dipropylsulfide	O <sub>2</sub>	MB	EtOH	rt	1	0.00056	0.5	10	9	610 (70)	-10	total	92.5
71	diphenyl sulfide	O <sub>2</sub>	MB	EtOH	rt	1	0.00056	0.5	10	9	610 (70)	-10	6.2	
72	diphenyl sulfide	O <sub>2</sub>	MB	EtOH	rt	1	0.00056	0.5	10	9	610 (70)	-10	3.8	
73	diphenyl sulfide	O <sub>2</sub>	MB	EtOH	rt	1	0.00056	0.5	10	11	610 (70)	-10	6.0	
74	diethyl sulfide	O <sub>2</sub>	MB	EtOH	rt	1	0.00056	0.5	10	9	610 (70)	-10	total	97.3
75	dibenzothiophene	O <sub>2</sub>	MB	EtOH	rt	1	0.00056	0.5	10	9	610 (70)	-10	0.0	
76	Thiodipropionic acid	O <sub>2</sub>	MB	EtOH	rt	1	0.00056	0.5	10	9	610 (70)	-10	total	
77	dibenzyl sulfide	O <sub>2</sub>	MB	EtOH/2-MeTHF (1:1)	rt	1	0.00056	0.5	10	9	610 (70)	-10	logged reactor	
78	dibenzyl sulfide	O <sub>2</sub>	MB	EtOH/2-MeTHF (1:1)	60	0.1	0.00056	0.5	10	9	610 (70)	-10	total	63.9
79	dibenzyl sulfide	O <sub>2</sub>	MB	EtOH/2-MeTHF (1:1)	70	1	0.00056	0.5	10	9	610 (70)	-10	total	60.5
80	diphenyl sulfide	O <sub>2</sub>	MB	ACN/eau 85:15	rt	1	0.00056	0.5	10	9	610 (70)	-10	0.0	
81	diphenyl sulfide	O <sub>2</sub>	MB	ACN/eau 85:15	rt	1	0.00056	1.5	20	11,6	610 (70)	-4	0.0	
87	thioanisole	air	MB	EtOH	rt	1	0.00056	0.5	10	9	610 (70)	-10	21.5	
88	thioanisole	air	MB	EtOH	rt	1	0.00056	0.5	10	9	610 (70)	-10	19.3	
89	thioanisole	air	MB	EtOH	rt	1	0.00056	1	20	9	610 (70)	-4	15.6	
90	thioanisole	air	MB	EtOH	rt	1	0.00056	1	20	9	610 (70)	-4	15.3	
91	thioanisole	air	MB	EtOH	rt	0.1	0.00056	0.5	10	9	610 (70)	-10	total	
92	thioanisole	air	MB	EtOH	rt	0.1	0.00056	0.5	10	9	610 (70)	-10	total	
93	thioanisole	air	MB	EtOH	rt	0.1	0.00056	1.5	30	5	610 (70)	-2	46.7	
94	thioanisole	air	MB	EtOH	rt	0.1	0.00056	1.5	30	5	610 (70)	-2	46.3	

Table S3. General table of oxidation tests (part 2). Selectivity is only specified when not total toward the sulfoxide.

n°exp	Substrate	Oxidant	Photosensib.	Solvent	Temp. (°C)	Concentration (M)		Flow rate (mL.min <sup>-1</sup> )		BPR (bar)	Light (nm) (Intensity (%))	Res. Time (min)	Conversion (%)	Selectivity (%)
						Substrate	Photosensib.	Substrate	O <sub>2</sub>					
95	propylS	air	MB	EtOH	rt	0.1	0.000056	0.5	10	9	610 (70)	-10	total	
96	propylS	air	MB	EtOH	rt	0.1	0.000056	0.5	10	9	610 (70)	-10	total	
97	diphenyl sulfide	O <sub>2</sub>	MB	ACN	rt	0.1	0.000056	0.5	10	9	610 (70)	-10	0.0	
98	diphenyl sulfide	O <sub>2</sub>	MB	ACN	rt	0.1	0.000056	0.5	10	9	610 (70)	-10	0.0	
99	diphenyl sulfide	O <sub>2</sub>	DCA	ACN	rt	0.1	0.000056	0.5	10	9	395 (100)	-10	N.D	
100	diphenyl sulfide	O <sub>2</sub>	DCA	ACN	rt	0.1	0.000056	0.5	10	9	395 (70)	-10	46.6	
101	dibenzothiophene	O <sub>2</sub>	DCA	MeCN	rt	0.1	0.000056	0.5	10	9	395 (100)	-10	20.1	12.5
102	dibenzothiophene	O <sub>2</sub>	DCA	MeCN	rt	0.1	0.000056	0.5	10	9	395 (70)	-10	22.7	7.9
103	dibenzothiophene	O <sub>2</sub>	DCA	MeCN	rt	0.1	0.000056	0.5	10	9	395 (100)	-10	48.9	20.3
104	dibenzothiophene	O <sub>2</sub>	DCA	MeCN	rt	0.1	0.000056	0.5	10	9	395 (70)	-10	47.8	17.2
105	dibenzyl sulfide	O <sub>2</sub>	DCA	MeCN	rt	0.1	0.000056	0.5	10	9	395 (100)	-10	total	19.0
106	dibenzyl sulfide	O <sub>2</sub>	DCA	MeCN	rt	0.1	0.000056	0.5	10	9	395 (70)	-10	total	21.2
107	CEES	O <sub>2</sub>	MB	EtOH	rt	1	0.000056	0.5	10	9	610 (100)	-10	99.92	94.8
108	CEES	O <sub>2</sub>	MB	EtOH	rt	1	0.000056	0.5	10	9	610 (70)	-10	99.92	95.5
109	CEES	O <sub>2</sub>	MB	EtOH	rt	1	0.000056	1	20	9	610 (100)	-4	99.26	92.4
110	CEES	Air	MB	EtOH	rt	1	0.000056	0.5	10	9	610 (100)	-10	99.74	84.0
111	CEES	Air	MB	EtOH	rt	0.1	0.000056	0.5	10	9	610 (100)	-10	99.88	84.8
112	CEES	Air	MB	EtOH	rt	0.1	0.000056	0.5	10	9	610 (70)	-10	total	83.4
113	CEES	Air	RB	EtOH	rt	0.1	0.000056	0.5	10	9	530 (100)	-10	83.69	83.4
114	CEES	Air	RB	EtOH	rt	0.1	0.000056	0.5	10	9	530 (70)	-10	80.94	79.5
115	CEES	O <sub>2</sub>	RB	EtOH	rt	1	0.000056	0.5	10	9	530 (70)	-10	94.51	97.3
116	CEES	O <sub>2</sub>	MB	EtOH	rt	1	0.000056	0.5	10	9	white light (100)	-10	99.91	96.1
117	CEES	O <sub>2</sub>	RB	EtOH	rt	1	0.000056	0.5	10	9	white light (100)	-10	99.92	95.4
118	CEES	O <sub>2</sub>	MB	EtOH	rt	1	0.000056	2	40	9	610 (100)	-2	81.88	95.3
119	CEES	Air	MB	EtOH	rt	1	0.000056	1	20	9	610 (100)	-4	51.42	74.0
120	CEES	O <sub>2</sub>	MB	EtOH	rt	1	0.000056	1	20	9	white light (100)	-4	total	97.8
121	CEES	Air	MB	EtOH	rt	1	0.000056	1	20	9	white light (100)	-4	68.23	93.5
122	CEPS	O <sub>2</sub>	MB	EtOH	rt	1	0.000056	1	20	9	610 (100)	-4	58.0	97.6
123	CEPS	O <sub>2</sub>	MB	EtOH	rt	1	0.000056	0.5	10	9	610 (100)	-10	57.8	97.6
124	CEPS	O <sub>2</sub>	MB	EtOH	rt	0.1	0.000056	1	20	9	610 (100)	-4	65.4	98.1
125	CEPS	O <sub>2</sub>	MB	EtOH	rt	0.1	0.000056	0.5	10	9	610 (100)	-10	93.11	99.9
126	CEPS	O <sub>2</sub>	MB	EtOH	rt	0.1	0.000056	0.5	10	10	white light (100)	-10	74.7	99.99

### 3.2 CEES photooxidation tests

#### 3.2.1 Impact of the residence time

Table S4. Comparison of residence time for the neutralization of CEES. PS is always MB when not specified, Rose Bengal when (RB) is specified.

In Table 3	[CEES] (M)	[PS] (μM)	Oxidant	Flow rate (mL.min <sup>-1</sup> )		BPR (bar)	Light (nm) (Intensity (%))	Res. time (min)	Conversion (%)	Selectivity (%)
				Liquid	Gas					
Entry 1	1	560	O <sub>2</sub>	0.5	10	9	610 (100)	-10	99.92	94.8
Entry 6	1	560	O <sub>2</sub>	1	20	9	610 (100)	-4	99.26	92.4
Entry 10	1	560	O <sub>2</sub>	2	40	9	610 (100)	-2	81.88	95.3

#### 3.2.2 Comparison of oxygen and air

Table S5. Comparison of oxidant gas for the neutralization of CEES. PS is always MB when not specified, Rose Bengal when (RB) is specified.

In Table 3	[CEES] (M)	[PS] (μM)	Oxidant	Flow rate (mL.min <sup>-1</sup> )		BPR (bar)	Light (nm) (Intensity (%))	Res. time (min)	Conversion (%)	Selectivity (%)
				Liquid	Gas					
Entry 1	1	560	O <sub>2</sub>	0.5	10	9	610 (100)	-10	99.92	94.8
Entry 4	1	560	Air	0.5	10	9	610 (100)	-10	99.74	84
Entry 6	1	560	O <sub>2</sub>	1	20	9	610 (100)	-4	99.26	92.4
Entry 7	1	560	Air	1	20	9	610 (100)	-4	51.42	74
entry 8	1	560	O <sub>2</sub>	1	20	9	white light (100)	-4	total	97.8
Entry 9	1	560	Air	1	20	9	white light (100)	-4	68.23	93.5

### 3.2.3 Comparison of photosensitizers

Table S6. Comparison of photosensitizers for **CEES** oxidation. PS is always MB when not specified, Rose Bengal when (RB) is specified.

In Table 3	[CEES] (M)	[PS] ( $\mu\text{M}$ )	Oxidant	Flow rate ( $\text{mL}\cdot\text{min}^{-1}$ )		BPR (bar)	Light (nm) (Intensity %)	Res. time (min)	Conversion (%)	Selectivity (%)
				Liquid	Gas					
not shown 1	1	560	O <sub>2</sub>	0.5	10	9	610 (70)	-10	99.92	95.5
not shown 2	1	560 (RB)	O <sub>2</sub>	0.5	10	9	530 (70)	-10	94.51	97.3
Entry 5	0.1	56	Air	0.5	10	9	610 (100)	-10	99.88	84.8
not shown 3	0.1	56 (RB)	Air	0.5	10	9	530 (100)	-10	83.69	83.4
Entry 2	1	560	O <sub>2</sub>	0.5	10	9	white light (100)	-10	99.91	96.1
Entry 3	1	560 (RB)	O <sub>2</sub>	0.5	10	9	white light (100)	-10	99.92	95.4

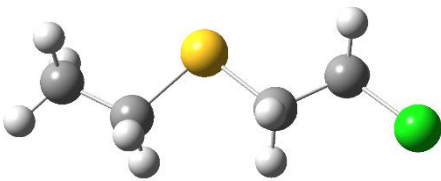
### 3.2.4 Comparison of light (wavelength and intensity)

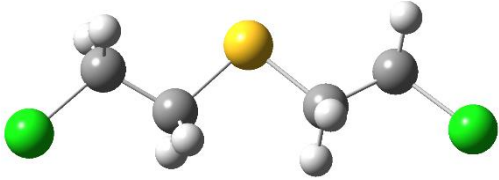
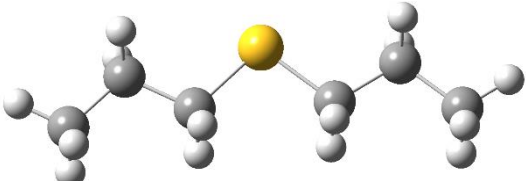
Table S7. Comparison of light for **CEES** oxidation. PS is always MB when not specified, Rose Bengal when (RB) is specified.

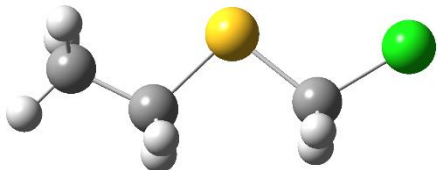
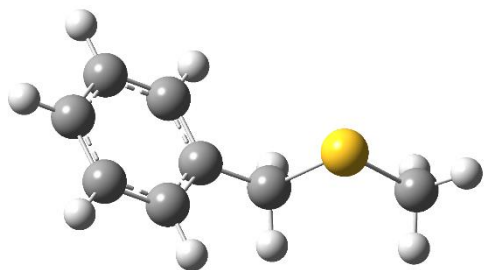
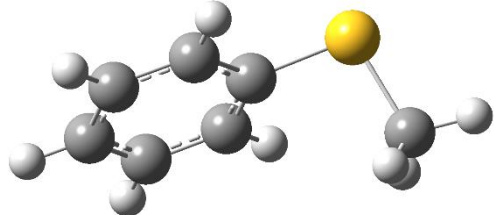
In Table 3	[CEES] (M)	[PS] ( $\mu\text{M}$ )	Oxidant	Flow rate ( $\text{mL}\cdot\text{min}^{-1}$ )		BPR (bar)	Light (nm) (Intensity %)	Res. time (min)	Conversion (%)	Selectivity (%)
				Liquid	Gas					
Entry 1	1	560	O <sub>2</sub>	0.5	10	9	610 (100)	-10	99.92	94.8
not shown 1	1	560	O <sub>2</sub>	0.5	10	9	610 (70)	-10	99.92	95.5
Entry 2	1	560	O <sub>2</sub>	0.5	10	9	white light (100)	-10	99.91	96.1
Entry 6	1	560	O <sub>2</sub>	1	20	9	610 (100)	-4	99.26	92.4
Entry 8	1	560	O <sub>2</sub>	1	20	9	white light (100)	-4	total	97.8
Entry 5	0.1	56	Air	0.5	10	9	610 (100)	-10	99.88	84.8
not shown 4	0.1	56	Air	0.5	10	9	610 (70)	-10	total	83.4
not shown 3	0.1	56 (RB)	Air	0.5	10	9	530 (100)	-10	83.69	83.4
not shown 5	0.1	56 (RB)	Air	0.5	10	9	530 (70)	-10	80.94	79.5
not shown 2	1	560 (RB)	O <sub>2</sub>	0.5	10	9	530 (70)	-10	94.51	97.3
Entry 3	1	560 (RB)	O <sub>2</sub>	0.5	10	9	white light (100)	-10	99.92	95.4
Entry 7	1	560	Air	1	20	9	610 (100)	-4	51.42	74
Entry 9	1	560	Air	1	20	9	white light (100)	-4	68.23	93.5

## 4. Computations

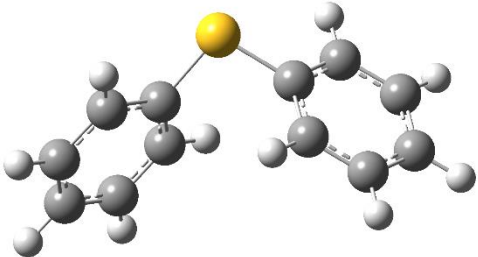
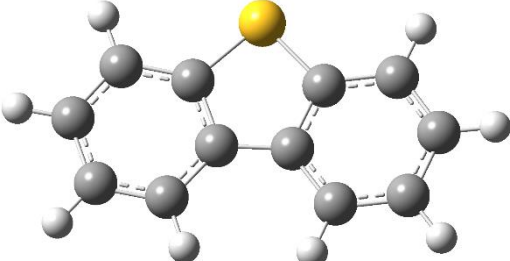
### 4.1 Stationary points for compounds CEES, HD and 1a-f

CEES	MP2/6-31+G** (Hartree)
15	H = -1014.432024
scf done: -1014.569720	G = -1014.476153
S 0.000000 0.000000 0.000000	
C 0.000000 0.000000 1.792323	
C 1.778165 0.000000 -0.253799	
C -1.418766 0.077061 2.322684	
C 2.091289 -0.114762 -1.733662	
Cl 3.863064 -0.185112 -1.939820	
H 0.611517 0.833668 2.134774	
H 0.479444 -0.958472 2.040217	
H -1.897513 1.018484 2.068487	
H -2.018943 -0.753796 1.961510	
H 2.125054 -0.881495 0.298219	
H 2.182014 0.912821 0.181894	
H 1.679041 -1.029718 -2.149896	
H 1.729914 0.743979 -2.292796	
H -1.389099 0.008742 3.390088	
	

<b>HD</b>	<b>MP2/6-31+G** (Hartree)</b>
15 scf done: -1473.592520 S 0.000000 0.000000 0.000000 C 0.000000 0.000000 1.820206 C 1.804791 0.000000 -0.236227 C 2.110725 -0.346458 -1.679465 Cl 3.880480 -0.306183 -1.959382 C -1.388127 0.359382 2.310690 Cl -1.437711 0.315289 4.101684 H 0.717538 0.740596 2.173039 H 0.290074 -0.982675 2.190699 H -1.664799 1.365389 2.008006 H -2.133454 -0.347168 1.954439 H 2.246850 -0.747053 0.422788 H 2.210736 0.980069 0.012172 H 1.771139 -1.348830 -1.924631 H 1.663803 0.368500 -2.365524	H = -1473.462357 G = -1473.509951 
<b>1a</b>	<b>MP2/6-31+G** (Hartree)</b>
21 scf done: -633.914467 S 0.000000 0.000000 0.000000 C 0.000000 0.000000 1.540000 C 1.451926 0.000000 -0.513333 C -1.451926 0.000025 2.053333 C 1.451926 -0.000634 -2.053333 C 2.903849 0.002154 -2.566668 C -1.451926 0.000025 3.593333 H 3.410060 -0.870298 -2.209628 H 3.406441 0.877001 -2.210375 H 2.903849 0.001696 -3.636668 H 0.945720 0.871827 -2.410359 H 0.949329 -0.875471 -2.409640 H 1.956202 0.873871 -0.157026 H 1.956456 -0.873431 -0.156307 H 0.504418 0.873643 1.896667 H 0.504388 -0.873660 1.896667 H -1.956344 -0.873617 1.696667 H -1.956314 0.873685 1.696667 H -0.947508 0.873668 3.950000 H -2.460732 0.000043 3.950000 H -0.947538 -0.873635 3.950000	H = -633.708181 G = -633.756180 
<b>1b</b>	<b>MP2/6-31+G** (Hartree)</b>
12 scf done: -975.379095 S 0.000000 0.000000 0.000000 C 0.000000 0.000000 1.818307	H = -975.272292 G = -975.314752

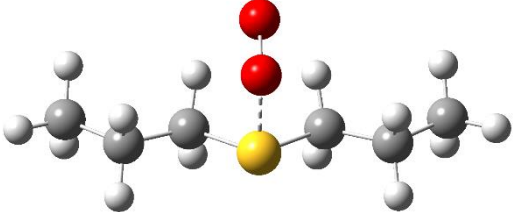
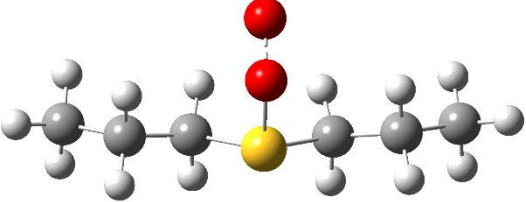
C 1.799460 0.000000 -0.265304 C -1.424972 0.088353 2.345894 H 0.584580 0.852002 2.166642 H 0.479485 -0.914758 2.168073 H -1.906056 1.011875 2.026113 H -2.025321 -0.752543 1.999923 H 2.254083 -0.717680 0.417964 H 2.208892 0.989390 -0.062891 H -1.412332 0.070800 3.435348 Cl 2.135823 -0.470131 -1.927662	
<b>1c</b>	<b>MP2/6-31+G** (Hartree)</b>
19 scf done: -668.343358 S -2.053586 -0.000084 -0.680770 C -3.684737 0.000088 0.102417 C -1.021695 -0.000008 0.821936 C 0.429459 -0.000008 0.436546 C 1.116949 -1.208986 0.251973 C 2.461562 -1.210638 -0.131914 C 3.138224 0.000028 -0.320319 C 2.461522 1.210676 -0.131948 C 1.116910 1.208989 0.251936 H -3.821623 -0.890355 0.713532 H -4.429205 0.000060 -0.691155 H -3.821512 0.890660 0.713367 H -1.257091 0.887812 1.411464 H -1.257086 -0.887764 1.411563 H 0.595190 -2.148260 0.401851 H 2.981818 -2.150839 -0.269979 H 4.180855 0.000040 -0.613839 H 2.981745 2.150892 -0.270040 H 0.595118 2.148249 0.401784	H = -707.359079 G = -707.405066 
<b>1d</b>	<b>MP2/6-31+G** (Hartree)</b>
16 scf done: -668.343357 S 0.000000 0.000000 0.000000 C 0.000000 0.000000 1.782446 C 1.789167 0.000000 -0.300110 C 0.511104 -1.092331 2.501333 C 0.486722 -1.085431 3.898840 C -0.073107 -0.003484 4.588916 C -0.599080 1.077646 3.874408 C -0.558043 1.084222 2.475656 H 0.923556 -1.943237 1.971916 H 0.887379 -1.930398 4.445687 H -0.099439 -0.004497 5.671551 H -1.033777 1.918284 4.401491 H -0.950451 1.928941 1.922456 H 2.252006 0.873983 0.152735	H = -668.204306 G = -668.246695 

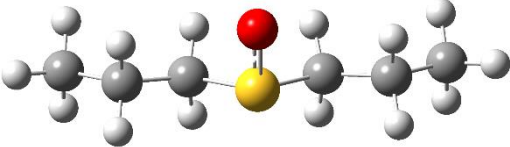
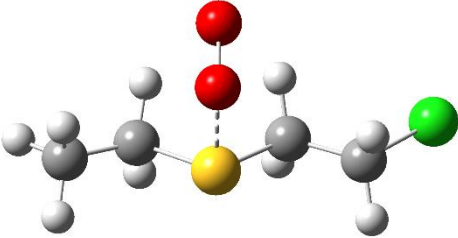


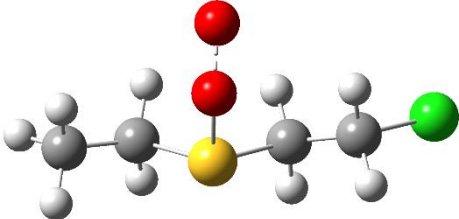
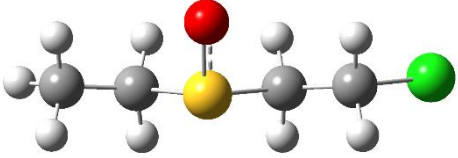
H	1.931386	0.041215	-1.378688		
H	2.251737	-0.907353	0.080207		
<b>1e</b>				<b>MP2/6-31+G** (Hartree)</b>	
23				H = -859.318588	
scf done: -859.512841				G = -859.371122	
S	0.000000	0.000000	0.000000		
C	0.000000	0.000000	1.783633		
C	1.760523	0.000000	-0.284007		
C	2.568803	1.020720	0.241188		
C	3.944685	1.011514	0.000690		
C	4.517217	0.007196	-0.790861		
C	3.707571	-0.996516	-1.331341		
C	2.331385	-1.006744	-1.074285		
C	-0.838860	0.892889	2.464438		
C	-0.894860	0.871065	3.862937		
C	-0.111651	-0.034442	4.585381		
C	0.728501	-0.923675	3.902836		
C	0.770391	-0.924513	2.506508		
H	-1.427658	1.611064	1.906155		
H	-1.543407	1.565895	4.382645		
H	-0.148118	-0.043179	5.667647		
H	1.333639	-1.632348	4.455451		
H	1.411825	-1.622689	1.981196		
H	2.124972	1.804515	0.844196		
H	4.565503	1.796256	0.415988		
H	5.583159	0.007845	-0.982002		
H	4.143571	-1.778185	-1.941561		
H	1.706606	-1.796681	-1.473691		
<b>1f</b>					<b>MP2/6-31+G** (Hartree)</b>
21				H = -858.185869	
sfc done: -858.3527375				G = -858.231417	
S	0.000000	0.000000	0.000000		
C	0.000000	0.000000	1.754929		
C	1.754671	0.000000	-0.030842		
C	2.557844	0.000000	-1.180068		
C	3.943026	0.000000	-1.021781		
C	4.522511	0.000000	0.262174		
C	3.722322	0.000000	1.402038		
C	2.321976	0.000000	1.265399		
C	1.306029	0.000000	2.299326		
C	1.467328	0.000000	3.697018		
C	0.341788	0.000000	4.517234		
C	-0.952155	0.000000	3.960456		
C	-1.134810	0.000000	2.578280		
H	5.600907	0.000000	0.362802		
H	4.578977	0.000000	-1.898668		
H	2.114729	0.000000	-2.168810		
H	4.174636	0.000000	2.387342		

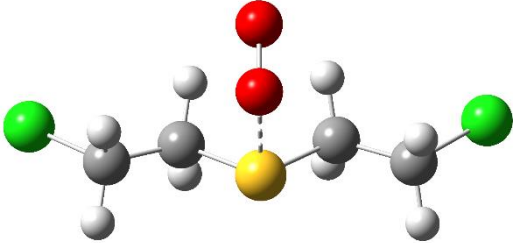
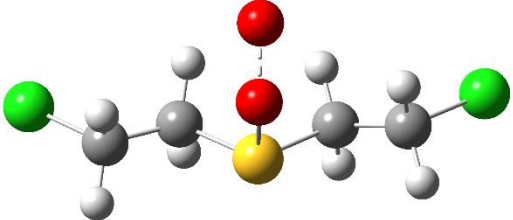
H	-2.131183	0.000000	2.152723
H	-1.817686	0.000000	4.611781
H	0.461410	0.000000	5.593691
H	2.460476	0.000000	4.131761

#### 4.2 Selected transition states, peroxy sulfoxides and sulfoxides

<b>TS<sup>1</sup><sub>1a</sub></b>	<b>MP2/6-31+G** (Hartree)</b>
23 scf done : -783.8306078 S 0.001090 -0.230173 -0.802643 C 1.371445 -0.560524 0.302297 C -1.368535 -0.567589 0.300751 O -0.003749 1.635150 -0.548470 O -0.007288 1.962681 0.769973 H 1.211938 0.151555 1.124357 H 1.256531 -1.580546 0.672130 H -1.253045 -1.590475 0.662164 H -1.209147 0.138421 1.127929 C 2.714263 -0.343585 -0.380861 H 2.815401 -1.024173 -1.228255 H 2.759935 0.675783 -0.768102 C -2.711302 -0.344919 -0.380645 H -2.754759 0.676224 -0.763369 H -2.814224 -1.021559 -1.230966 C 3.854936 -0.570112 0.607725 H 4.817150 -0.413167 0.121601 H 3.781632 0.121402 1.447398 H 3.833986 -1.587507 0.999295 C -3.852298 -0.572873 0.607316 H -4.814169 -0.411296 0.121994 H -3.834290 -1.591904 0.994727 H -3.777135 0.114974 1.449864	H = -783.617775 G = -783.672039 
<b>1Aa</b>	<b>MP2/6-31+G** (Hartree)</b>
23 scf done: -705.4646392 S 0.000000 0.000000 0.000000 O 0.000000 0.000000 1.632804 O 1.372865 0.000000 2.142795 C 1.061157 1.390146 -0.429241 C 1.054479 -1.393613 -0.437150 C 0.467723 -2.699838 0.080800 C 0.420700 2.709889 -0.020802 H 2.007000 1.219826 0.083053 H 1.198791 1.320790 -1.510676 H -0.547928 2.819379 -0.512472 H 0.247740 2.704755 1.056036 H 2.036733 -1.192678 -0.013099	H = -705.310617 G = -705.355168 

H 1.103495 -1.374989 -1.528368 H -0.538012 -2.839294 -0.320754 H 0.388104 -2.646164 1.166718 C 1.355687 -3.874880 -0.319864 H 0.942369 -4.808516 0.059741 H 1.433731 -3.953551 -1.404446 H 2.359631 -3.757324 0.088486 C 1.330023 3.877669 -0.393965 H 1.504217 3.908339 -1.469761 H 0.875846 4.821920 -0.096115 H 2.294371 3.791752 0.107114	
<b>2a</b>	<b>MP2/6-31+G** (Hartree)</b>
23 scf done: -708.9285944 S 0.000000 0.000000 0.000000 O 0.000000 0.000000 1.632804 O 1.372865 0.000000 2.142795 C 1.061157 1.390146 -0.429241 C 1.054479 -1.393613 -0.437150 C 0.467723 -2.699838 0.080800 C 0.420700 2.709889 -0.020802 H 2.007000 1.219826 0.083053 H 1.198791 1.320790 -1.510676 H -0.547928 2.819379 -0.512472 H 0.247740 2.704755 1.056036 H 2.036733 -1.192678 -0.013099 H 1.103495 -1.374989 -1.528368 H -0.538012 -2.839294 -0.320754 H 0.388104 -2.646164 1.166718 C 1.355687 -3.874880 -0.319864 H 0.942369 -4.808516 0.059741 H 1.433731 -3.953551 -1.404446 H 2.359631 -3.757324 0.088486 C 1.330023 3.877669 -0.393965 H 1.504217 3.908339 -1.469761 H 0.875846 4.821920 -0.096115 H 2.294371 3.791752 0.107114	H = -708.717905 G = -708.766896 
<b>TS<sup>1</sup><sub>CEES</sub></b>	<b>MP2/6-31+G** (Hartree)</b>
17 scf done: -1164.482060 S 0.000000 0.000000 0.000000 C 0.000000 0.000000 1.789866 C 1.774045 0.000000 -0.283965 O -0.258618 1.826513 -0.186958 O 0.566664 2.535674 0.633915 C 2.085775 0.116971 -1.766937 C -1.415598 -0.099510 2.324229 Cl -1.369695 0.020003 4.105785 H 2.166592 -0.916977 0.155039	H = -1164.337868 G = -1164.386512 

H 2.131050 0.866780 0.281900		
H 1.688229 -0.726025 -2.329350		
H 1.683864 1.041752 -2.176465		
H 0.462901 0.967797 2.035413		
H 0.627229 -0.821659 2.132371		
H -2.029965 0.720006 1.960869		
H -1.880032 -1.048909 2.073243		
H 3.167516 0.132391 -1.890482		
<b>CEESOO</b>	<b>MP2/6-31+G** (Hartree)</b>	
17 scf done: -1164.4888327	H = -1164.342699 G = -1164.391685	
S 0.888064 -0.272016 -0.659449		
O 0.999348 1.351888 -0.559551		
O 0.774977 1.788057 0.819654		
C -0.682107 -0.630748 0.156663		
C 2.042211 -0.870504 0.588597		
C 3.474415 -0.583499 0.166704		
C -1.794041 0.138153 -0.531620		
Cl -3.343617 -0.250641 0.265914		
H 1.839625 -1.939456 0.671268		
H 1.770784 -0.362256 1.511530		
H 3.721778 -1.070824 -0.774761		
H 3.643386 0.487130 0.071114		
H -0.582742 -0.336324 1.198192		
H -0.818441 -1.709080 0.067109		
H -1.632012 1.207033 -0.435266		
H -1.888347 -0.136564 -1.578951		
H 4.140964 -0.966479 0.937524		
<b>CEESO</b>		<b>MP2/6-31+G** (Hartree)</b>
16 scf done: -1089.5818305		H = -1089.439828 G = -1089.485407
S 0.000000 0.000000 0.000000		
O 0.000000 0.000000 1.630775		
C 1.757404 0.000000 -0.414364		
C -0.433364 1.692868 -0.440747		
C -1.883155 1.978776 -0.083066		
C 2.426993 -1.197316 0.233266		
Cl 4.156509 -1.201202 -0.210771		
H -0.248817 1.761431 -1.513955		
H 0.262301 2.328306 0.103370		
H -2.565928 1.313874 -0.609142		
H -2.044355 1.882773 0.988724		
H 2.177967 0.933885 -0.050597		
H 1.801083 -0.049989 -1.502941		
H 2.363749 -1.128356 1.314601		
H 1.999820 -2.135586 -0.110879		
H -2.110621 3.003502 -0.371716		

<b>TS<sup>1</sup><sub>HD</sub></b>	<b>MP2/6-31+G** (Hartree)</b>
17 scf done: -1623.501380 S 0.000000 0.000000 0.000000 C 0.000000 0.000000 1.792322 C 1.778165 0.000000 -0.253799 O -0.221301 1.830609 -0.194652 O 0.635652 2.526376 0.604954 C 2.091289 0.114762 -1.733662 C -1.418767 -0.077036 2.322683 Cl -1.369262 0.036962 4.103784 H 2.182014 -0.912821 0.181894 H 2.125075 0.881481 0.298229 H 1.729914 -0.743979 -2.292796 H 1.679041 1.029718 -2.149896 H 0.479444 0.958472 2.040216 H 0.611517 -0.833669 2.134774 H -2.018930 0.753831 1.961509 H -1.897531 -1.018450 2.068487 Cl 3.863063 0.185112 -1.939820	H = -1623.364778 G = -1623.416916 
<b>HDOO</b>	<b>MP2/6-31+G** (Hartree)</b>
17 scf done: -1623.5013185 S 0.000000 0.000000 0.000000 C 0.000000 0.000000 1.792323 C 1.778164 0.000000 -0.253799 O -0.221301 -1.830611 -0.194652 O 0.635666 -2.526379 0.604936 C -1.418767 0.077036 2.322684 Cl -1.369262 -0.036962 4.103785 C 2.091287 -0.114737 -1.733664 Cl 3.863062 -0.185088 -1.939823 H 0.611503 0.833679 2.134775 H 0.479444 -0.958472 2.040217 H -1.897531 1.018450 2.068488 H -2.018930 -0.753831 1.961510 H 2.125053 -0.881495 0.298219 H 2.182016 0.912813 0.181910 H 1.679038 -1.029685 -2.149914 H 1.729915 0.744015 -2.292783	H = -1623.364796 G = -1623.417406 
<b>HDO</b>	<b>MP2/6-31+G** (Hartree)</b>
16 scf done: -1548.6024474 S 0.000000 0.000000 0.000000 C 0.000000 0.000000 1.818220 C 1.808010 0.000000 -0.187222 O -0.478699 -1.395541 -0.430838 C -1.427710 -0.105771 2.316231	H = -1548.468056 G = -1548.517443

Cl	-1.443668	-0.130669	4.104558	
C	2.155318	-0.116456	-1.658278	
Cl	3.932253	-0.134343	-1.860394	
H	0.464737	0.931059	2.145582	
H	0.594233	-0.853590	2.147648	
H	-2.024582	0.746006	1.999767	
H	-1.892606	-1.026858	1.977126	
H	2.198552	-0.848668	0.376037	
H	2.179326	0.935341	0.233369	
H	1.773842	-1.042852	-2.077579	
H	1.774077	0.728807	-2.225859	

## References

- S1 Yangyang Liu, Ashlee J. Howarth, Joseph T. Hupp, and Omar K. Farha, *Angew.Chem. Int. Ed.*, **2015**, 54, 9001–9005
- S2 Bing Yu, An-Hua Liu, Liang-Nian He, Bin Li, Zhen-Feng Diao and Yu-Nong L, *Green Chem.*, **2012**, 14, 957 - 962.
- S3 Tomáš Nevesely, Eva Svobodová, Josef Chudoba, Marek Sikorski, and Radek Cibulka, *Adv. Synth. Catal.*, **2016**, 358, 1654–1663.
- S4 Jitka Dad'ová, Eva Svobodová, Marek Sikorski, Burkhard König, and Radek Cibulka, *ChemCatChem.*, **2012**, 4, 620–623.

## Chapter 4. Photooxidation of sulfides into APIs – synthesis of smart drug modafinil

### 4.1. Introduction

Narcolepsy is a neurological disorder affecting 1:2000 person.<sup>1</sup> Patients suffering from narcolepsy present symptoms such as excessive daytime sleepiness often accompanied by abnormal muscle weakness (cataplexy). During their sleep time, patients can also experience sleep paralysis, hypnagogic hallucinations or unusual rapid eye movement.<sup>2</sup> In 1998, The U.S Food and Drug Administration (FDA) approved modafinil (2-[(diphenylmethyl)sulfinyl] acetamide) (Figure 57) as a treatment of narcolepsy and expanded this approbation in 2003 to shift work sleep disorders and obstructive sleep apnea/hypopnea syndrome.<sup>3</sup>

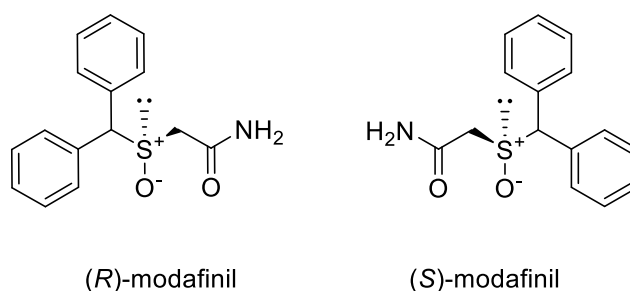


Figure 57 – Structure of modafinil enantiomers.

Modafinil is a well-tolerated wake-promoting agent that represents an interesting alternative to standard psychostimulant, such as amphetamines or methylphenidate, as it rarely induces dependence behavior, lowering the potential for abuse.<sup>4</sup> Such a molecular structure makes modafinil poorly soluble in water and not stable above 180 °C which diminishes the chances of abuse by smoking or intravenous injection. The U.S Congress wrote, in 1970, a classification of controlled drugs based on (A) their potential of abuse, (B) their medical usefulness, (C) their potential of generating dependence (Table 2).<sup>5</sup> While Amphetamines, methamphetamines and methylphenidate have been classified as Schedule II category, modafinil belongs to the safer Schedule IV drug category.<sup>6</sup>

Table 2 – Schedules of controlled substances from Comprehensive Drug Abuse Prevention and Control Act of 1970. Public Law 91-513, HR 18583, October 27, 1970.

Schedule	Findings required
I	(A) The drug or other substance has a high potential for abuse. (B) The drug or other substance has no currently accepted medical use in treatment in the United States. (C) There is a lack of accepted safety for use of the drug or other substance under medical supervision.
II	(A) The drug or other substance has a high potential for abuse. (B) The drug or other substance has a currently accepted medical use in treatment in the United States or a currently accepted medical use with severe restrictions. (C) Abuse of the drug or other substances may lead to severe psychological or physical dependence.
III	(A) The drug or other substance has a potential for abuse less than the drugs or other substances in schedules I and II. (B) The drug or other substance has a currently accepted medical use in treatment in the United States. (C) Abuse of the drug or other substance may lead to moderate or low physical dependence or high psychological dependence.
IV	(A) The drug or other substance has a low potential for abuse relative to the drugs or other substances in schedule III. (B) The drug or other substance has a currently accepted medical use in treatment in the United States. (C) Abuse of the drug or other substance may lead to limited physical dependence or psychological dependence relative to the drugs or other substances in schedule III.
V	(A) The drug or other substance has a low potential for abuse relative to the drugs or other substances in schedule IV. (B) The drug or other substance has a currently accepted medical use in treatment in the United States. (C) Abuse of the drug or other substance may lead to limited physical dependence or psychological dependence relative to the drugs or other substances in schedule IV.

Modafinil is the first validated pharmaceutical nootropic agent that can enhance cognitive performances and alertness and is therefore qualified as “smart drug” or “dose of intelligence”.<sup>7</sup> Accordingly, modafinil not only is under investigation to treat cocaine addiction<sup>8</sup> but also drew the attention of the army and NASA. Soldiers on field regularly face sleep deprivation and particularly need to stay focus and alert for extended period of time. Several surveys were notably performed by the U.S. Air Force and Army<sup>9</sup>, the French Air Force<sup>10</sup> and the Republic of Singapore Air Force<sup>3</sup> in which aviators were given modafinil to help with fatigue during service. The experiment that was reported by the Singapore Air Force lasted 7 years and was conducted on 243 aircrew members. The study highlighted the low occurrence of side effects (2.47%) including headache, diarrhea, anxiety and insomnia. Similar experiments were conducted by NASA. Astronauts were provided with modafinil and sent to the International Space Station for long-term missions.<sup>11</sup> In the U.S, modafinil is sold under the name Provigil® but can be found in other countries as Modiodal®, Alertec®, Nuvigil® (armodafinil) or Modasomil®. This white crystalline powder can be sold as a racemic mixture but the *S*-(+)-enantiomer is eliminated 3 times faster than the *R*-(-)-enantiomer.<sup>12</sup> The metabolization happens in the liver for the major part of the drug while the rest is excreted renally.

The three-step synthesis of modafinil was first reported by Lafon laboratories in 1979 (Figure 58). They started the synthesis from Benzhydrylthioacetic acid (**1**) reacted with SOCl<sub>2</sub> to obtain an acid chloride (**2**) in the first step. **2** was then reacted with ammonia to result in the formation of the corresponding acetamide (**3**). In the final step, modafinil (**4**) is obtained after an oxidation of the sulfide with hydroperoxide in acetic acid.<sup>13</sup>



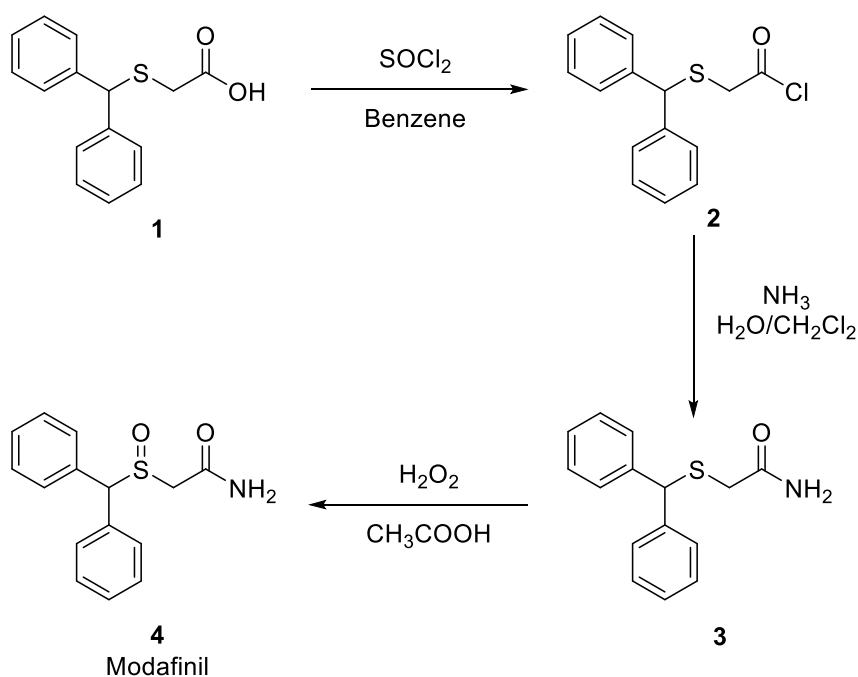
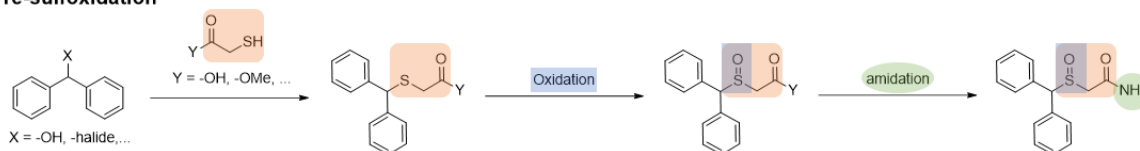


Figure 58 – Modafinil synthesis by Lafon laboratory (1979, U.S. Pat. No. 4,177,290).

Since then, diverse methods have been developed to synthesize modafinil. The majority of them also involve three steps and the order of these steps defines the category of synthesis the method belongs to. When the sulfoxidation is performed before the amidation, the synthesis is designated as a “pre-sulfoxidation approach”. If the sulfoxidation occurs after the amidation, the method will be known as a “post-sulfoxidation approach” (Figure 59).<sup>14</sup>

#### Pre-sulfoxidation



#### Post-sulfoxidation

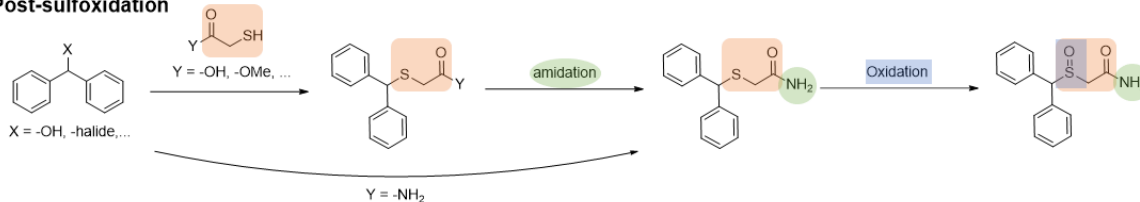


Figure 59 – comparison between pre- and post-sulfoxidation approach.

Alexander *et al.* described their post-sulfoxidation method starting from benzhydryl bromide (**5**) (Figure 60).<sup>15</sup> The acid **1** that was the starting material in Lafon synthesis was obtained here by the reaction of **5** and sodium mercaptoacetate (**6**). Next steps followed Lafon method and modafinil **4** was obtained in 43% yield.

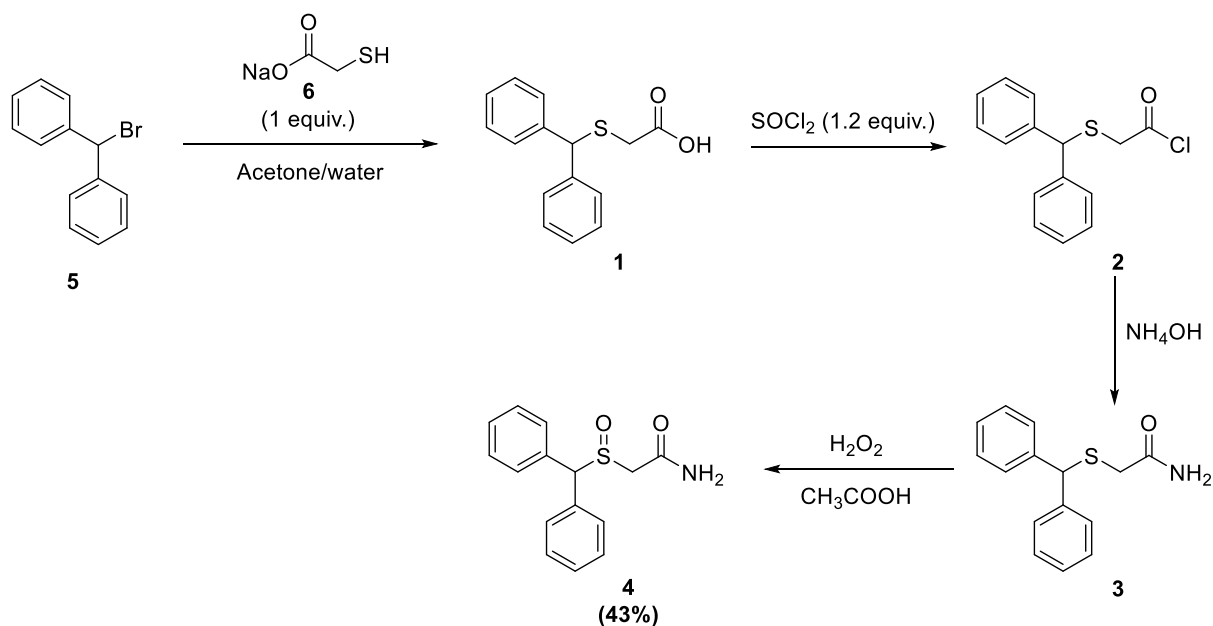


Figure 60 – Modafinil synthesis starting from benzhydryl bromide by Alexander *et al.*<sup>15</sup>

Similarly to Alexander's method, the syntheses found in literature almost always start from a reaction between benzhydryl halide or benzhydryl alcohol with a mercaptoacetic acid derivative to create the structural backbone of modafinil that only needs to be modified with an amidation and an oxidation with peroxides.

Kumar *et al.* performed both pre- and a post-sulfoxidation approaches in step economic procedures.<sup>14</sup> In the pre-sulfoxidation approach (Figure 61A), benzhydryl alcohol (**7**) is activated under the action of an acidic catalyst (Nafion-H) and reacts with methylthioglycolate (**8**) in 2-methyltetrahydrofuran (2-MeTHF) to obtain the corresponding ester (**9**). **9** is then oxidized with peroxides in acetic acid. The sulfoxide (**10**) obtained is then mixed with ammonia in MeOH at 50 °C for 5 h to afford Modafinil in 79% yield. However, the post-sulfoxide approach (Figure 61B) leads directly to the amide and does not involve the ester **9**, which shortens the reaction. The first reaction on **7** is essentially the same as in the pre-sulfoxidation approach, except that methylthioglycolate is replaced by **11**, which directly affords amide **3**. Amide **3** is subsequently oxidized with peroxides. This faster method allowed to reach a higher yield of 91%.

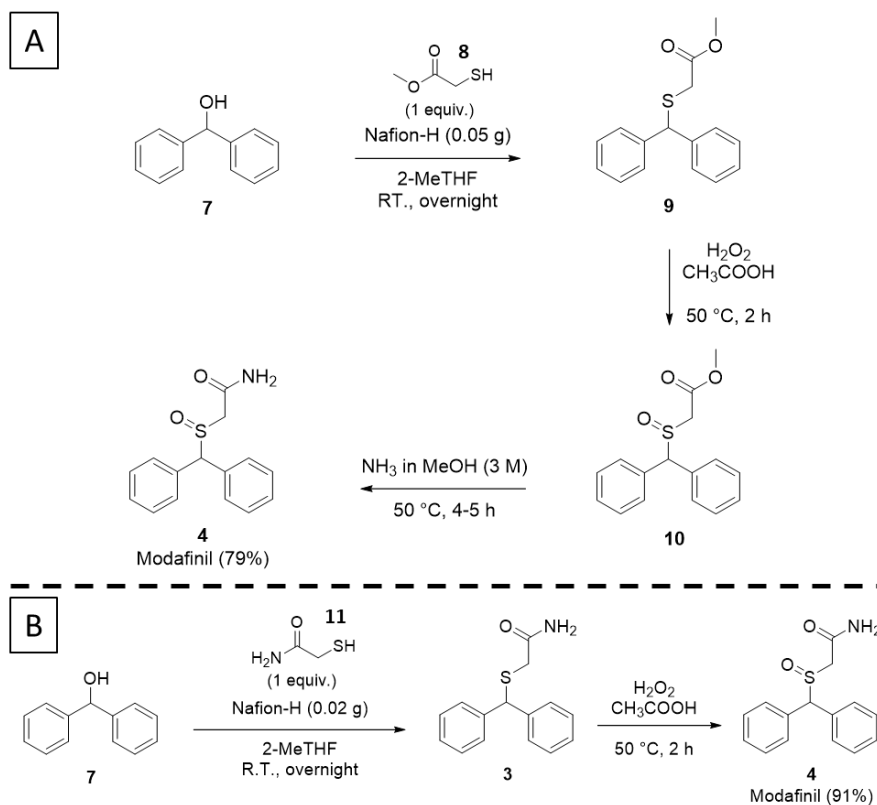


Figure 61 – A – Pre-sulfoxidation approach for the synthesis of modafinil. B – Post-sulfoxidation approach for the synthesis of modafinil.

A few publications can be found in the literature in which the authors brought modifications to the classical methods. Mykhailiuk et al. proposed a post-sulfoxidation approach starting from benzhydryl chloride (Figure 62).<sup>16</sup> However, instead of a mercaptoacetic acid derivative, thiourea served as a sulfur source while the rest of modafinil structure was brought in the molecule by chloroacetamide. In this synthesis, thiourea and benzhydryl chloride (**12**) were mixed in 2-propanol and heated at 100 °C. The reaction was allowed to cool down to room temperature before the addition of KOH and chloroacetamide (**13**). The mixture was heated at 60 °C for 2 hours while remaining constantly in an ultrasonic bath for solubility. The mixture was then cooled down to trigger the sulfide precipitation. After purification by flash chromatography, the sulfide was finally oxidized with peroxides in a mixture of MeOH and acetic acid, leading to modafinil in 45% yield.

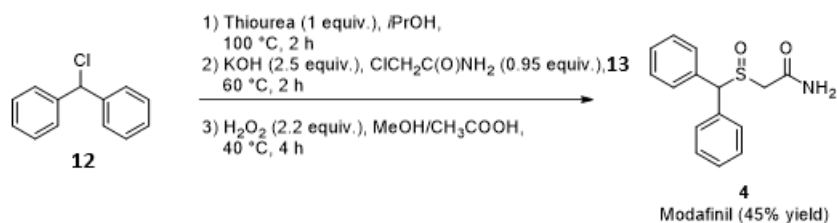


Figure 62 – Modafinil synthesis with thiourea as a sulfur source.

Similarly, Morkovniv *et al.* worked on a novel synthetic route for the synthesis of modafinil in which the sulfide source is a Bunte salt ( $\text{RSSO}_3^- \text{Na}^+$ , **SCS**) that already contains the structure of the mercaptoacetamide (Figure 63).<sup>17</sup> **SCS** was prepared by mixing aqueous solutions of chloroacetamide (**13**) and  $\text{Na}_2\text{S}_2\text{O}_3$  at 70 °C. The Bunte salt was then reacted with **7** and formic acid to form modafinil sulfide. The sulfide was then oxidized with peroxides and modafinil was obtained in 93% yield.

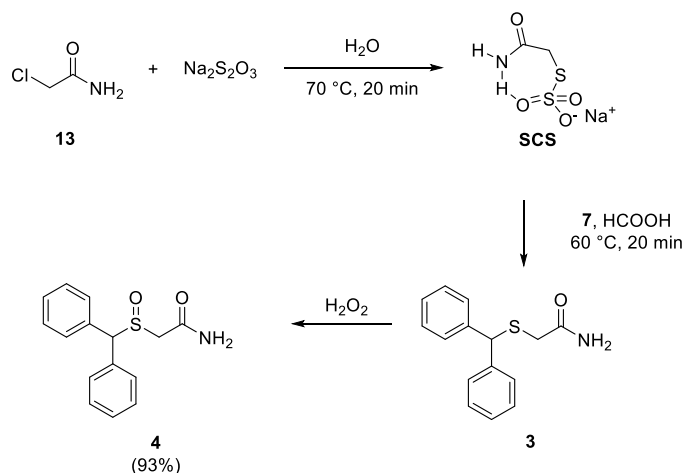


Figure 63 – Preparation modafinil with a Bunte salt as sulfide source.

Galatti *et al.* chose to change the oxidant from the classic method to control the selectivity of the oxidation (Figure 64).<sup>12</sup> As peroxides tend to yield to both sulfoxide and sulfone depending on the oxidation time, the authors opted for a molybdenum complex known to be more selective.<sup>18</sup> In this post-sulfoxidation synthesis, both modafinil and its sulfone were prepared using different molybdenum catalyst to perform a single or a double oxidation. The aquo (N-oxo of pyridine) molybdenum (VI) oxodiperoxo complex led to a single oxidation affording modafinil **4** in 92% yield while the aquo (pyrazol) molybdenum (VI) oxodiperoxo complex resulted in the formation of the sulfone **15** in 80% yield.

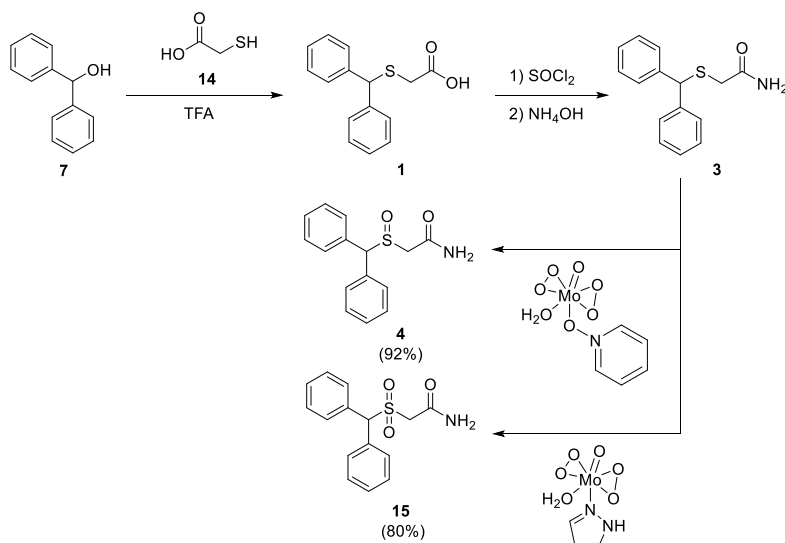


Figure 64 – Modafinil sulfoxide and sulfone synthesis with a molybdenum catalyst for a mild and selective oxidation.

Nuvigil® (Armodafinil), is the enantiopure version of modafinil. The *R*-(-)-modafinil is indeed known to have a longer lifetime as well as a better affinity to the dopamine transporter.<sup>19</sup> Therefore, Prisinzano *et al.* developed a synthesis affording modafinil enantiomers in their absolute configuration (Figure 65).<sup>20</sup> The first steps (from **7** to **17** on Figure 65) follow the classical pre-sulfoxidation pathway with an esterification to ester **16** that is only useful here because the authors also prepared Adrafinil, a modafinil derivative but can be ignored for modafinil preparation. Acid **1** could be oxidized to **17** directly. **17** underwent a fractional crystallization with  $\alpha$ -methylbenzylamine, a chiral amine, to separate both enantiomers before the formation of the amide to afford modafinil **4** in an absolute configuration.

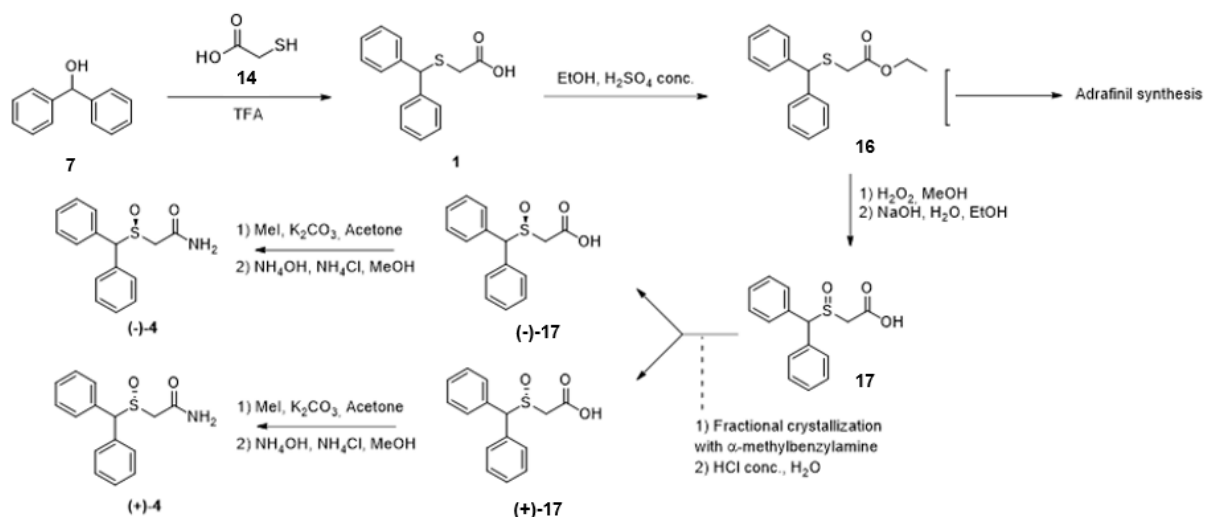
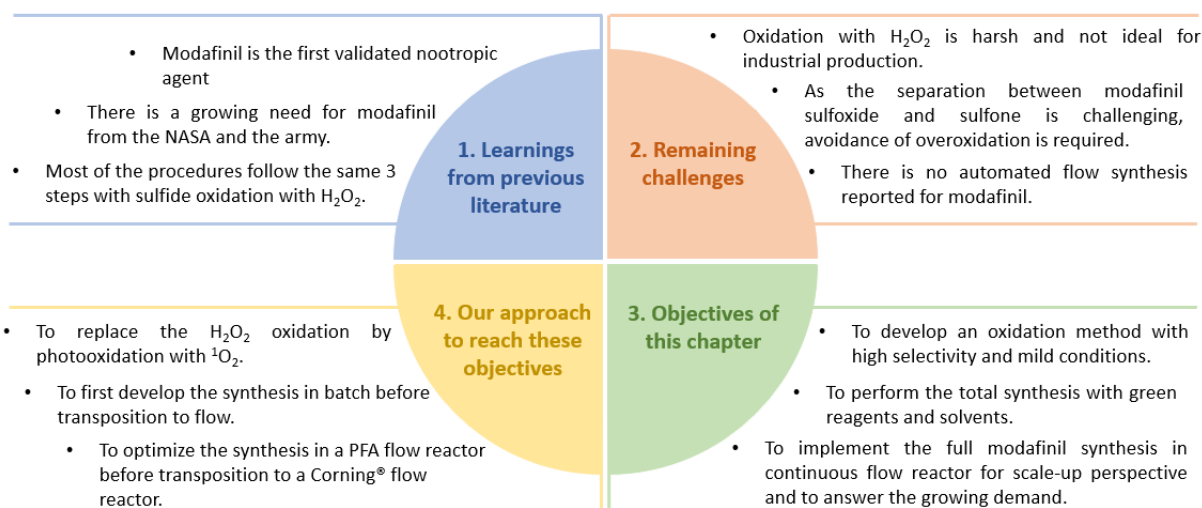


Figure 65 – Enantiopure synthesis of R-(-)-modafinil and S-(+)-modafinil.

The context and objectives of this chapter are summarized in the diagram below:



The presence of modafinil as a target for selective sulfoxidation in this PhD dissertation is stimulated by the growing demand of modafinil promoted among others by the NASA and the army. The challenging separation of modafinil sulfoxide from its sulfone is a problem discussed in the patent written by Cephalon in 2009<sup>13</sup> on modafinil synthesis process. The replacement of the sulfide oxidation with H<sub>2</sub>O<sub>2</sub> by a photooxidation with <sup>1</sup>O<sub>2</sub> can help avoiding overoxidation. However, in opposition to all our previous targets, our work here was not limited to the oxidation step alone but proposes a continuous flow implementation of the total synthesis of the drug.

## 4.2. Modafinil synthesis

### 4.2.1. Batch synthesis

In the first phase of this work, the synthesis was designed to follow a classical post-sulfoxidation approach. For the first step, **7** and methylthioglycolate (**8**) were selected as starting reagents (Figure 66). 2-MeTHF and EtOH were tested as solvents but as they both gave similar results, EtOH was conserved for the experiments. Several homogeneous and heterogeneous acidic catalysts were investigated such as Nafion™ NR50, Amberlite IR-120, *p*-toluenesulfonic acid, formic acid and trifluoroacetic acid (TFA). The best conversion (96.5%) was obtained when **7** and 1 equivalent of **8** reacted with TFA as a catalyst in EtOH at 90 °C. The product was purified by silica gel chromatography but did not correspond to the expected ester **9** (see supporting information in section 4.5). The NMR spectra of the product obtained correspond to a dimer of **7**.

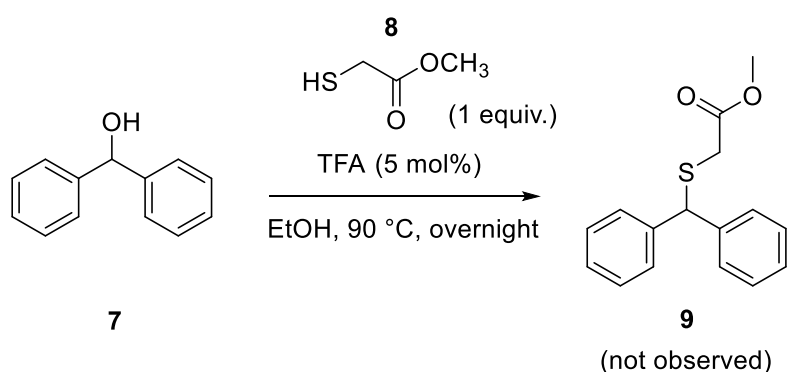


Figure 66 – First step of batch post-sulfoxidation procedure.

The synthesis procedure was thus adapted from Morkovniv.<sup>17</sup> Morkovniv's protocol was first performed in batch and begins with the preparation of the Bunte salt, sodium carbamoylmethyl sulfate (**SCS**) (Figure 67).  $\text{Na}_2\text{S}_2\text{O}_3$  (201.1 mmol, 31.8 g) and **13** (214.5 mmol, 20.06 g) were mixed in 50 mL of water at 70 °C until complete dissolution of the amide (approx. 30 min). When both salts were completely dissolved, the heating and mixing were stopped and the solution was allowed to slowly cool down. The product was filtered off on a Buchner, washed with cold water and dried, **SCS** was obtained as a pure white crystal (33.35 g, 88.8% yield) and was analyzed by NMR (see supporting information in section 4.5).

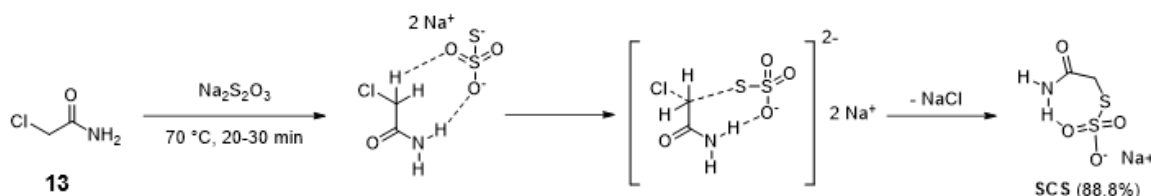


Figure 67 – Preparation of a sodium carbamoylmethyl sulfate for modafinil synthesis.

Replacing liquid methylthioglycolate by a solid in the protocol considerably reduces the strong odor due to the sulfur presence. **SCS** (75 mmol, 14.1 g) was then dissolved in a mixture of formic acid (80%, 50 mL) and water (12.5 mL) along with **7** (50 mmol, 9.2 g) and the solution was heated to 80 °C until complete homogenization (20 – 30 min). The solution was then allowed to cool down at RT and 25 mL

of cold water were added in the solution, triggering **3** precipitation. **3** precipitated as a white solid and was dried in a vacuum oven at 80 °C for 4 h and in an oven at 60 °C overnight (12.6 g, 98%) (Figure 68). **3** was analyzed in HPLC and NMR (see supporting information in section 4.5).

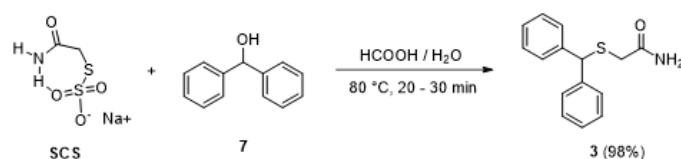


Figure 68 – Synthesis of **3** by benzhydrylation of **SCS** by **7**.

The oxidation step is performed with peroxides in the publication of reference. To check the adaptability of the synthesis to our photooxidation protocol, both peroxide and singlet oxygen oxidations were attempted. **3** was dissolved in the same solvent mixture then in the previous step. In one vial, 5 mL of H<sub>2</sub>O<sub>2</sub> 30% was added dropwise to the 40 mL solution followed after 1 min by 25 mL of cold water. A mixture of **3** and **4** was obtained and **4** was identified by HPLC and NMR.

In the other vial, 1 mol% of RB were added in the 40 mL of solution of **3** (0.625 M) under intense mixing. After dissolution of RB, the solution was irradiated for 2 h with green LEDs (540 nm) and oxygen was bubbled through the solution the whole time (Figure 69). As bulk product gave untractable results on both HPLC and NMR, 25 mL of cold water was poured into the solution. The solid was identified as **4** by HPLC and NMR (see supporting information in section 4.5) but still contained traces of HCOOH and **SCS** from previous step as well as a lot of RB even after crystallization in MeOH/water and extraction in ethyl acetate. RB was finally removed by filtration on charcoal. Usually, such a high quantity of RB is not necessary for photooxidations but as RB is not stable under acidic condition, a larger amount was employed. However, no traces of modafinil sulfone could be detected.

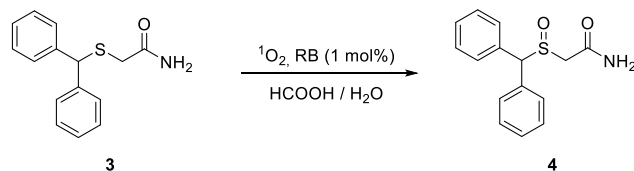


Figure 69 – Photooxidation of **3** with singlet oxygen into modafinil.

#### 4.2.2. Continuous flow synthesis

Each of the 3 steps of the reaction: A – **SCS** synthesis, B – Benzhydrylation of **SCS**, C – Photooxidation, were performed separately. The two first steps were conducted in a PFA coil heated in an oil bath while the photooxidation was conducted in a Corning® Advance-Flow™ Lab Photo Reactor.

##### A – **SCS** synthesis

A PFA coil reactor ( $V_{\text{int}} = 1 \text{ mL}$ , I.D. 1/16") was heated in an oil bath at 70 °C. As **13** is sensitive to hydrolysis, its stability in water was assessed by heating a solution of this amide in D<sub>2</sub>O to 90 °C. As no traces of 2-hydroxylamide were detected at 90 °C, **13** was declared stable at the reaction temperature (70 °C). Feed solutions of Na<sub>2</sub>S<sub>2</sub>O<sub>3</sub> (1 M) and **13** (1 M) in water were injected at equal flow rates. A solution of **13** required to be priorly sonicated until complete dissolution to be pumped in the reactor without clogging. The system was let to stabilize for 2 residence times before collection of samples at the outlet. Samples were collected for residence times between 2 (flow rates of 0.25 mL min<sup>-1</sup>) and 5 min (flow rates of 0.1 mL min<sup>-1</sup>) and quickly analyzed in NMR before the crystallization of **SCS**. The conversion increased from 80% to 99.9% for these residence times (Figure 70).

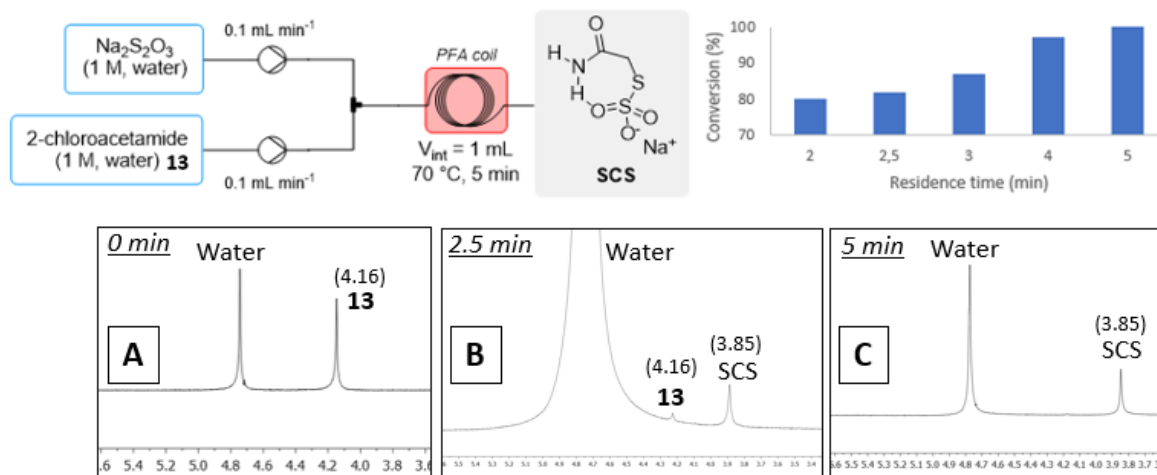


Figure 70 – Continuous flow setup for the preparation of SCS with NMR spectra obtained for residence times of A – 0 min, B – 2.5 min, C – 5 min.

### B – Benzhydrylation of SCS

The same PFA coil reactor ( $V_{\text{int}} = 1$  mL, I.D. 1/16") was heated in an oil bath. In respect of Morkovniv's protocol, a **7**/SCS 2:3 ratio was maintained for the reaction. However, in experiments B-1 to B-6, the HCOOH concentration was increased to 98% instead of 80% for solubility reasons (Figure 71). These experiments were carried for residence times of 3 and 5 min at 80, 100 and 120 °C each. A back-pressure regulator of 40 psi was added at the outlet of the reactor to maintain the liquid phase. HPLC analysis gave results that are shown in Table 3.

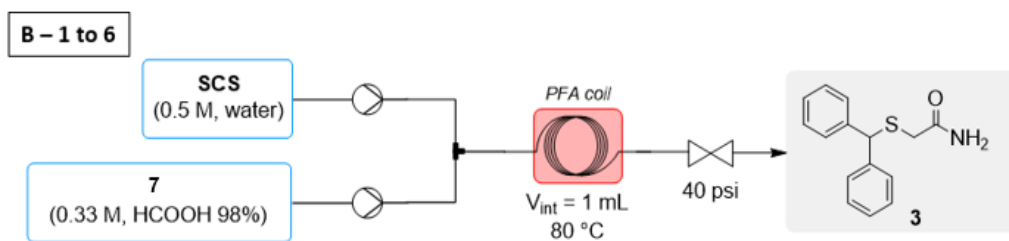


Figure 71 – Continuous flow setup for the synthesis of **3**, with HCOOH as the acid.

Table 3 – Results of the experiments B-1 to B-6.

Exp	Flow rates (mL min <sup>-1</sup> )*1	Residence time (min)	Temperature (°C)	Conv.(%) (Selectivity (%))
B-1	0.166	3	80	75 (84)
B-2	0.1	5	80	72 (84)
B-3	0.166	3	100	76 (86)
B-4	0.1	5	100	75 (86)
B-5	0.166	3	120	71 (78)
B-6	0.1	5	120	65 (57)

\*1Flow rates of both feeds were kept equal.



As the conversion did not exceed 75%, formic acid (pKa 3.8) was replaced with TFA (pKa 0.3), a stronger acid. However, TFA is not a good solvent for **7**, which resulted in clogging the reactor. To address this problem, the concentration of **7** was decreased from 0.33 M to 0.165 M (Figure 72). In order to conserve the 2:3 ratio inside the reactor, feeds flow rates were, this time, set at different values. Residence times from 1 to 4 min were covered as longer residence time resulted again in a crystallization inside the PFA coils. Results are shown in Table 4 and were obtained from HPLC analysis. In all experiments, the conversion was total. However, the best selectivity was found for a residence time of 4 min (Exp B-10 in Table 4).

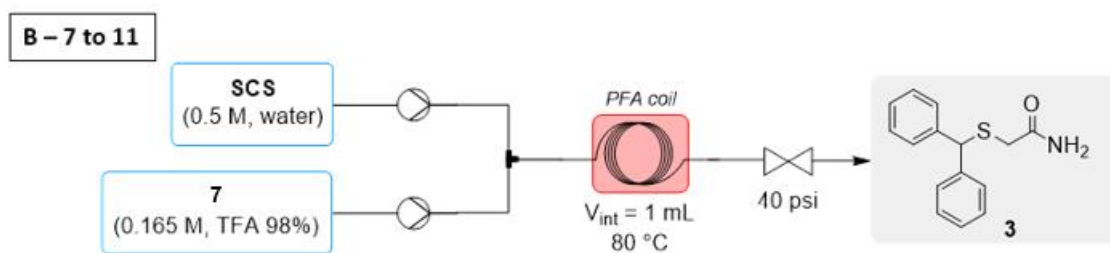


Figure 72 – Continuous flow setup for the synthesis of **3**, with TFA as the acid.

Table 4 – Results of the experiments B-7 to B-11.

Exp	Flow rate SCS (mL min <sup>-1</sup> )	Flow rate <b>7</b> (mL min <sup>-1</sup> )	Residence time (min)	Temperature (°C)	Conv.(%) (select.(%))
B-7	0.333	0.666	1	80	Tot. (85.2)
B-8	0.166	0.333	2	80	Tot. (90.2)
B-9	0.111	0.222	3	80	Tot. (93.2)
B-10	0.083	0.166	4	80	Tot. (97)
B-11	0.033	0.066	10	80	Clogging

### C – Photooxidation with singlet oxygen

Photooxidation of **3** was first performed in conditions that would already be suitable for a concatenated process. **3** was thus dissolved in the same solvents and at the same concentration than at the outlet of the previous step. The concentration of RB was increased to 2 mol% as RB is even less stable in TFA than it was in HCOOH due to TFA high acidity. Unfortunately, with this setup no conversion was observed (Figure 73). This can be explained by the presence of the strong acid in solution which increases the solubility of **7** but reduces the solubility of the PS that forms aggregates.

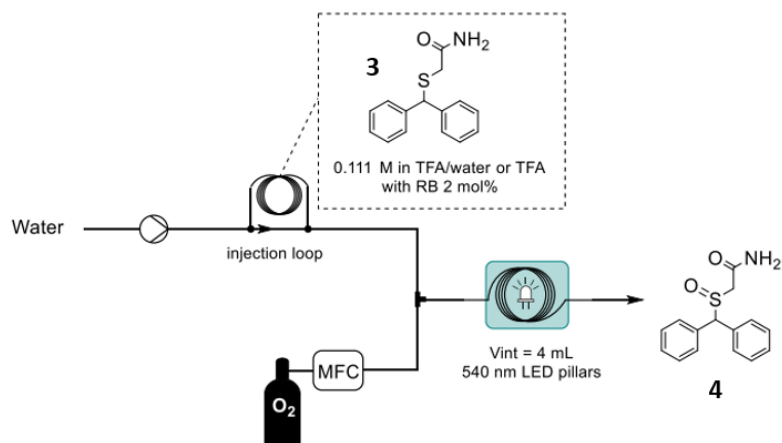


Figure 73 – Photooxidation of **3** with singlet oxygen in a PFA coil.

The solvent was thus changed to EtOH and allowed to obtain a slight conversion of 17% for a residence time of 2 min. To increase the quality of internal mixing, a few experiments in EtOH were conducted in the Corning® Advance-Flow™ Lab Photo Reactor. For each experiment, **3** (0.1 M) was oxidized in EtOH with oxygen or air and with methylene blue as a photosensitizer (560  $\mu$ M). Several conditions lead to total conversions but experiment B-14 gives the highest selectivity (85%) with a 5 min residence time (Table 5). The comparison between results obtained in PFA tubing and in the Corning® Advance-Flow™ Lab Photo Reactor demonstrates the impact of the internal mixing quality on the reaction outcome. Oxidation with air resulted in lower conversion than with oxygen for equivalent residence times but still afforded to reach 86% conversion. No modafinil sulfone was detected in these experiments.

Table 5 – Results of **3** photooxidation with singlet oxygen and **MB** (560  $\mu$ M) as a PS in a Corning® Advance-Flow™ Lab Photo Reactor.

Exp.	Oxidant	Liq. Flow rate (mL min <sup>-1</sup> )	Gas Flow rate (mL min <sup>-1</sup> )	BPR (bar)	Irradiation		Residence Time	Conv.(%)	Select.(%)
					(nm)	Intensity (%)			
B-12	O <sub>2</sub>	0.5	10	10	610	(70)	8 min 15 s	Total	70
B-13	O <sub>2</sub>	1	10	10	610	(70)	6 min 23 s	99	87
B-14	O <sub>2</sub>	1.5	10	10	610	(70)	4 min 57 s	Total	85
B-15	air	0.5	10	8.5	610	(70)	7 min	36	36
B-16	air	1.5	30	5	610	(70)	1 min 53	25	88
B-17	air	0.5	10	10	610	(100)	8 min 15 s	86	65
B-18	air	0.5	10	10	610	(70)	8 min 15 s	84	75
B-19	O <sub>2</sub>	0.5	10	10	610	(100)	8 min 15 s	Total	64
B-20	O <sub>2</sub>	0.5	10	10	610	(70)	8 min 15 s	Total	65

To improve the productivity, a solution of higher concentration of **3** was photooxidized. As 0.1 M is already the solubility limit in EtOH, the solvent was replaced with a mixture of EtOH/2-MeTHF (1:1). 2-MeTHF for **3** solubilization and EtOH for MB. In this new solvent mixture, a concentration of 1 M could be reached with sonication. To reduce the quantity of **3** required for the test, the experiment was carried in the smaller Corning® Lab Photo™ Reactor (Table 6) that offers the same internal mixing quality than the Corning® Advance-Flow™ Lab Photo Reactor but with only one plate of 2.6 mL instead of 5. With such a small internal volume, only a short residence time was tested.

Table 6 – Results of **3** (1 M) photooxidation with singlet oxygen and **MB** (560  $\mu$ M) as a PS in a Corning® Lab Photo™ Reactor.

Exp.	Oxidant	Liq. Flow rate (mL min <sup>-1</sup> )	Gas Flow rate (mL min <sup>-1</sup> )	BPR (bar)	Irradiation (nm)	Residence Time	Conv.(%)	Select.(%)
					Intensity (%)			
B-21	O <sub>2</sub>	0.1	25	8	610 (100)	49 s	64	87.5

The oxidation of the 1 M solution, although not complete, demonstrates the possibility of synthesizing modafinil in flow for production scale.

### 4.3. Conclusion

Modafinil, a wake-promoting agent approved by the FDA, was successfully synthesized in batch with a greener process than what is usually found in the literature. Our synthesis was inspired by the more environmentally friendly Morkovnik's protocol<sup>17</sup> but the peroxide oxidation was replaced by a <sup>1</sup>O<sub>2</sub> photooxidation that never resulted in the formation of the undesired sulfone. The complete process could be transposed in flow, step by step. These flow steps are not yet fully optimized and not concatenated. Our synthesis still needs improvements. Precipitation and clogging were the real challenges in each steps of this flow synthesis and forces us to work at very low concentrations which is not compatible with our intention to produce modafinil at industrial scale. Another solvent or acid could ameliorate the benzhydrylation step to increase feeds' concentrations without clogging the reactor. Solvent change is partially responsible for the difficulty to concatenate different steps, especially when reactants tend to precipitate. However, this work is a good starting point for further improvements and demonstrates the feasibility of implementing a total synthesis involving a photooxidation with singlet oxygen in flow for the production of commercialized APIs.

## 4.4. References

- 1 S. Nishino and T. Kanbayashi, *Sleep Med. Rev.*, 2005, **9**, 269–310.
- 2 J. S. Ballon and D. Feifel, *J. Clin. Psychiatry*, 2006, **67**, 554–566.
- 3 T. Ooi, S. H. Wong and B. See, *Aerosp. Med. Hum. Perform.*, 2019, **90**, 480–483.
- 4 D. R. Jasinski, *J. Psychopharmacol.*, 2000, **14**, 53–60.
- 5 *Comprehensive Drug Abuse Prevention and Control Act - Schedules of controlled substances*, U.S Congress, 1970.
- 6 D. R. Jasinski and R. Kovačević-Ristanović, *Clin. Neuropharmacol.*, 2000, **23**, 149–156.
- 7 R. M. Battleday and A. K. Brem, *Eur. Neuropsychopharmacol.*, 2015, **25**, 1865–1881.
- 8 C. A. Dackis, K. M. Kampman, K. G. Lynch, H. M. Pettinati and C. P. O'Brien, *Neuropsychopharmacology*, 2005, **30**, 205–211.
- 9 J. A. Caldwell, M. M. Mallis, J. L. Caldwell, M. A. Paul, J. C. Miller and D. F. Neri, *Aviat. Sp. Environ. Med.*, 2009, **80**, 29–59.
- 10 D. Lagarde, *Ann. Pharm. Fr.*, 2007, **65**, 258–264.
- 11 R. Thirsk, A. Kuipers, C. Mukai and D. Williams, *Can. Med. Assoc. J.*, 2009, **180**, 1216–1220.
- 12 Q. B. Cass and T. Ferreira Galatti, *J. Pharm. Biomed. Anal.*, 2008, **46**, 937–944.
- 13 US 7,541,493 B2, 2009.
- 14 S. Maurya, D. Yadav, K. Pratap and A. Kumar, *Green Chem.*, 2017, **19**, 629–633.
- 15 N. Chatterjie, J. P. Stables, H. Wang and G. J. Alexander, *Neurochem. Res.*, 2004, **29**, 1481–1486.
- 16 A. V. Bogolubsky, Y. S. Moroz, P. K. Mykhailiuk, E. N. Ostapchuk, A. V. Rudnichenko, Y. V. Dmytriv, A. N. Bondar, O. A. Zaporozhets, S. E. Pipko, R. A. Doroschuk, L. N. Babichenko, A. I. Konovets and A. Tolmachev, *ACS Comb. Sci.*, 2015, **17**, 348–354.
- 17 A. V. Bicherov, A. R. Akopova, V. I. Spiglazov and A. S. Morkovnik, *Russ. Chem. Bull.*, 2010, **59**, 91–101.
- 18 F. Batigalia, M. Zaldini-Hernandes, A. G. Ferreira, I. Malvestiti and Q. B. Cass, *Tetrahedron*, 2001, **57**, 9669–9676.
- 19 C. J. Loland, M. Mereu, O. M. Okunola, J. Cao, T. E. Prisinzano, S. Mazier, T. Kopajtic, L. Shi, J. L. Katz, G. Tanda and A. Hauck Newman, *Biol. Psychiatry*, 2012, **72**, 405–413.
- 20 T. Prisinzano, J. Podobinski, K. Tidgewell, M. Luo and D. Swenson, *Tetrahedron Asymmetry*, 2004, **15**, 1053–1058.

## 4.5. Supporting information

### 4.5.1. Flow experiments

Outside of photooxidations, all flow experiments were conducted in a continuous flow setup constructed from high purity PFA capillaries (800  $\mu\text{m}$  internal diameter). ThalesNano microHPLC<sup>®</sup> pumps (wetted parts: SS 316, ruby and sapphire) were utilized to handle the liquid feeds that were injected through static mixers (T-Mixer, IDEXUpchurch, natural PEEK 1/4-28 thread for 1/16" o.d. tubing, 0.02" through hole). A PFA injection loop was added after the pump for acidic solutions.

Photooxidations were performed in flow reactors manufactured by Corning SAS: B-12 to B-20 experiments on a Corning<sup>®</sup> Advanced-Flow<sup>™</sup> LF skid Photo Reactor (5 fluidic modules integrated with static mixers and connected in series, 13 mL total internal volume) and B-21 on a Corning<sup>®</sup> Advanced-Flow<sup>™</sup> Lab Photo Reactor (1 fluidic module, 2.6 mL internal volume).

### 4.5.2. HPLC method:

Eluent:

A: Water + 0.1% CF<sub>3</sub>COOH (v:v)

B: Acetonitrile

Gradient Table:

Time (min)	A (%)	B (%)
0	100	0
20	20	80
23	20	80
25	100	0
31	100	0

Flow: 1 mL min<sup>-1</sup>

Injection Volume: 10  $\mu\text{L}$

Column: C18, 100  $\times$  4.6 mm, 3  $\mu\text{m}$

Oven Temperature: 40 °C

Diode Array Detector: 180-800 nm (processed at 225 nm)

### 4.5.3. NMR spectra

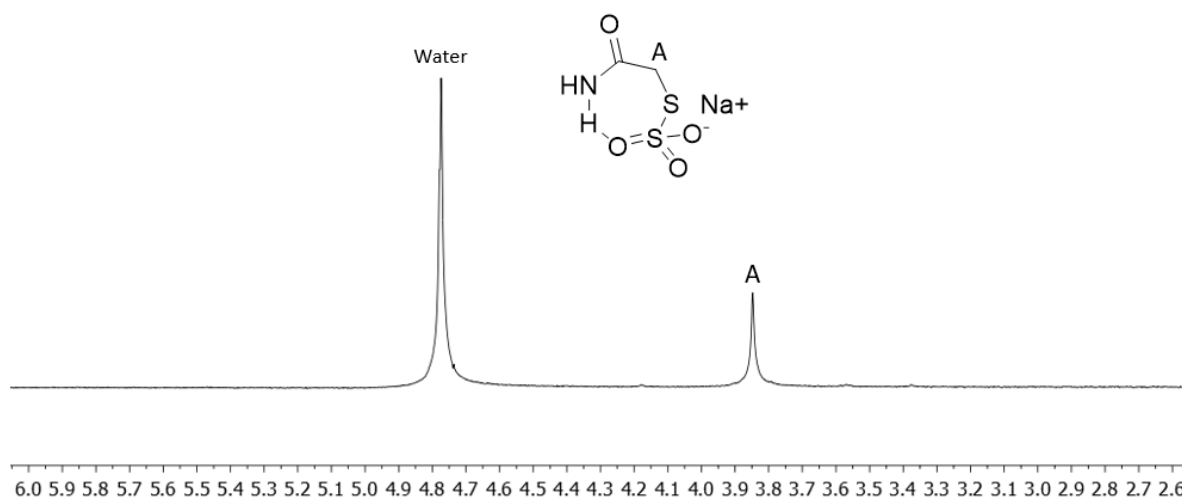


Figure S1 -  $^1\text{H}$  NMR spectrum (43 MHz) of SCS in water.

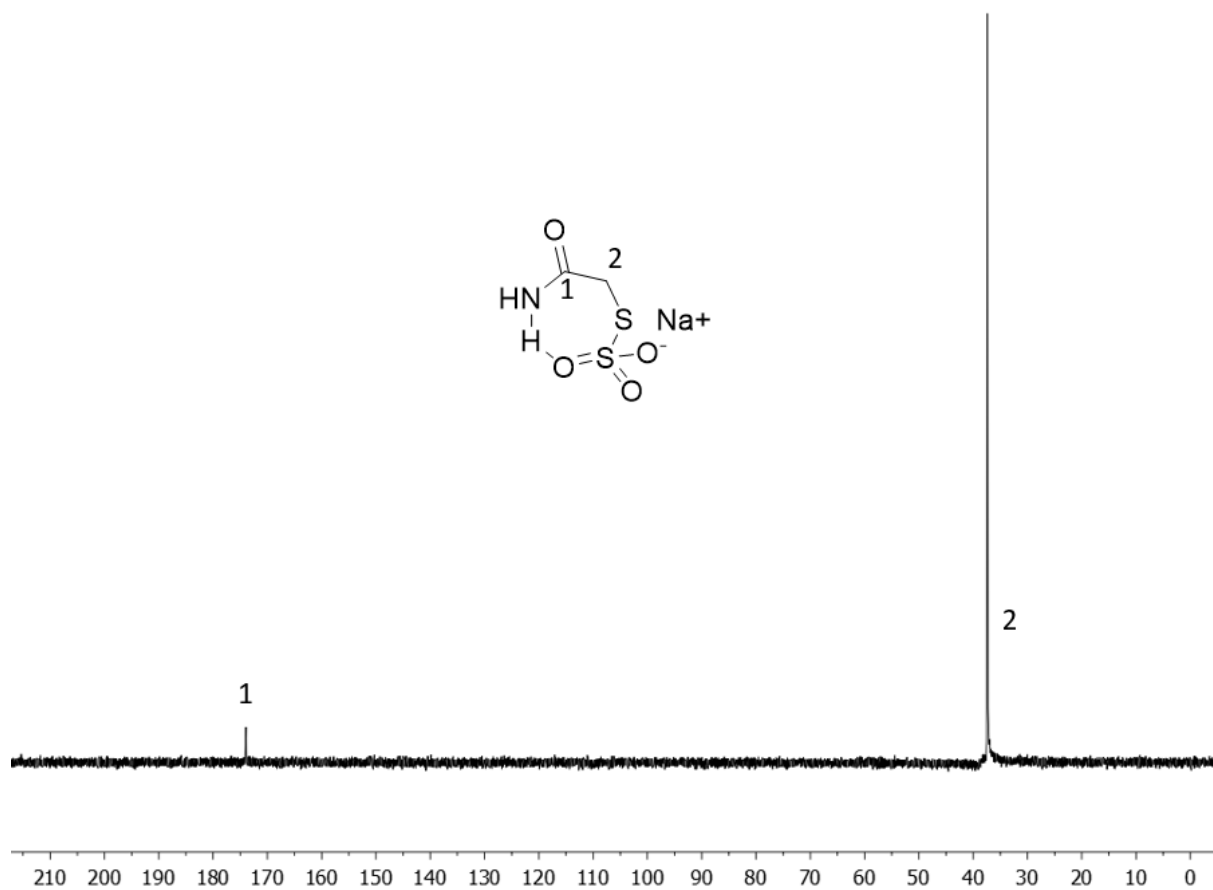


Figure S2 -  $^{13}\text{C}$  NMR spectrum (400 MHz) of SCS in  $\text{D}_2\text{O}$ .

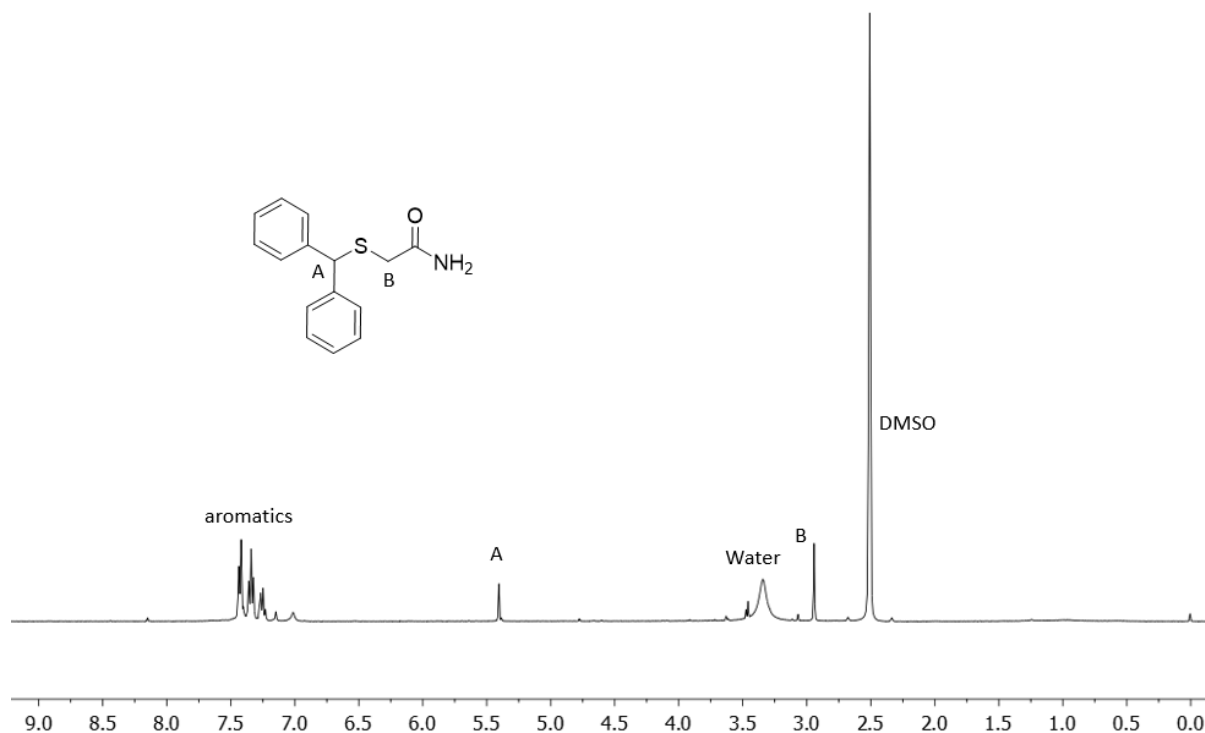


Figure S3 -  $^1\text{H}$  NMR spectrum (400 MHz) of modafinil sulfide in DMSO.

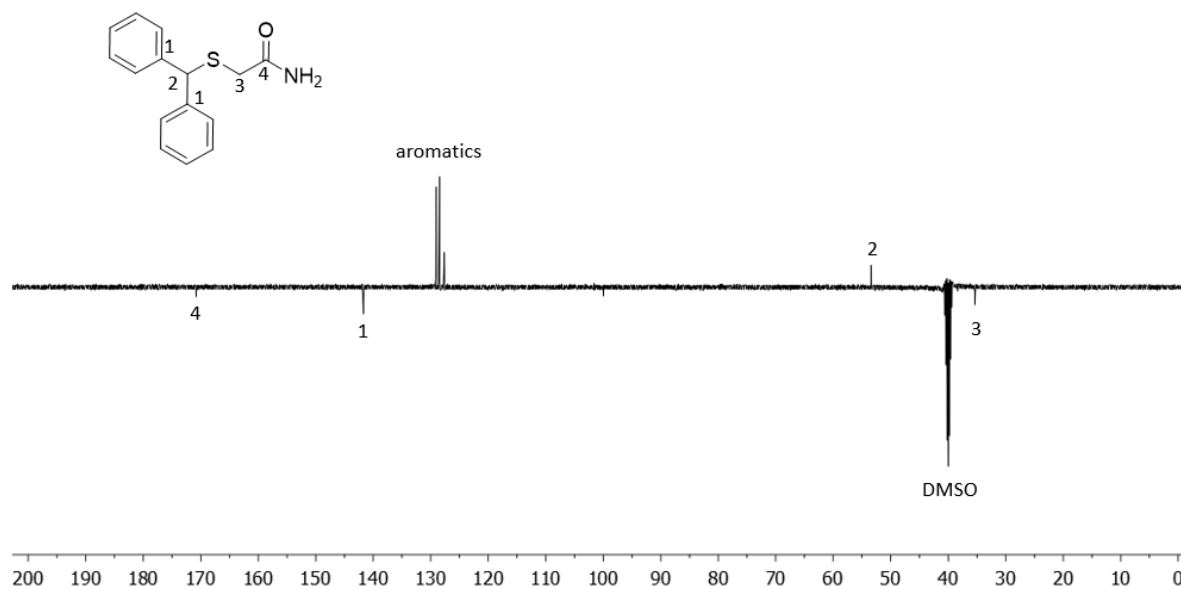


Figure S4 -  $^{13}\text{C}$  NMR spectrum (400 MHz) of modafinil sulfide in DMSO.

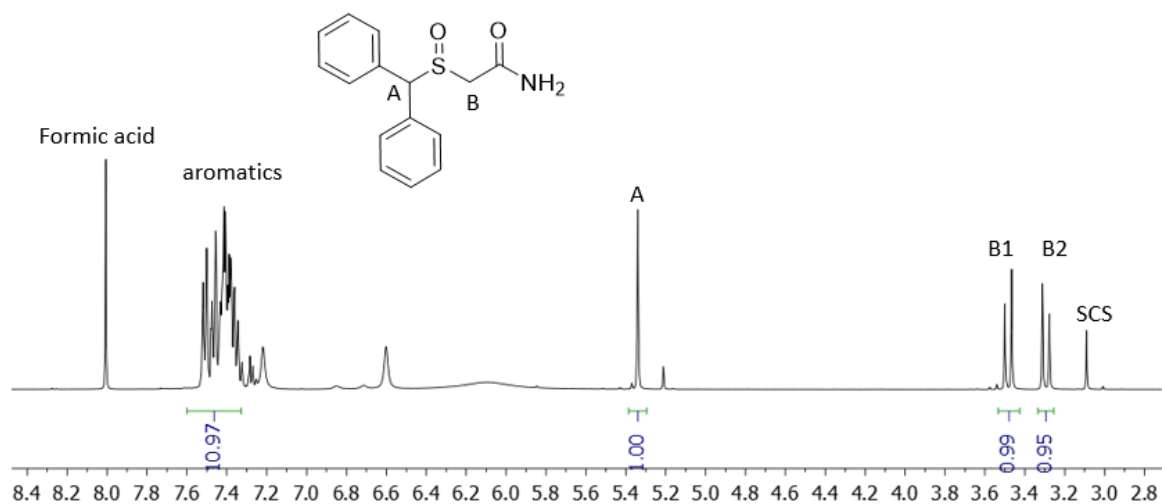


Figure S5 –  $^1\text{H}$  NMR spectrum (400 MHz) of modafinil sulfoxide in  $\text{CDCl}_3$ .

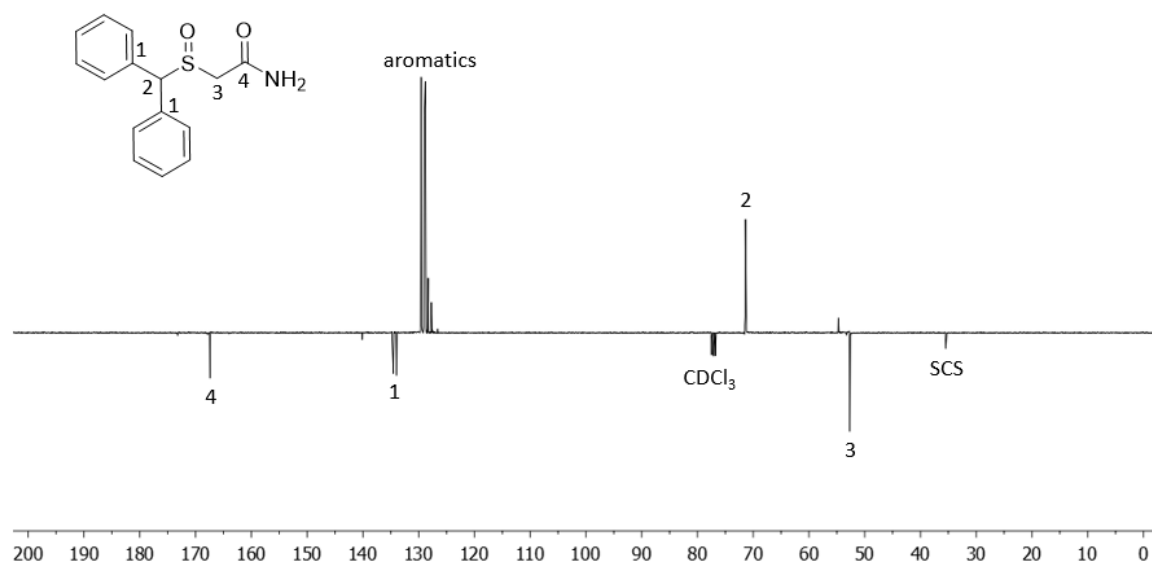


Figure S6 –  $^{13}\text{C}$  NMR spectrum (400 MHz) of modafinil sulfoxide in  $\text{CDCl}_3$ .



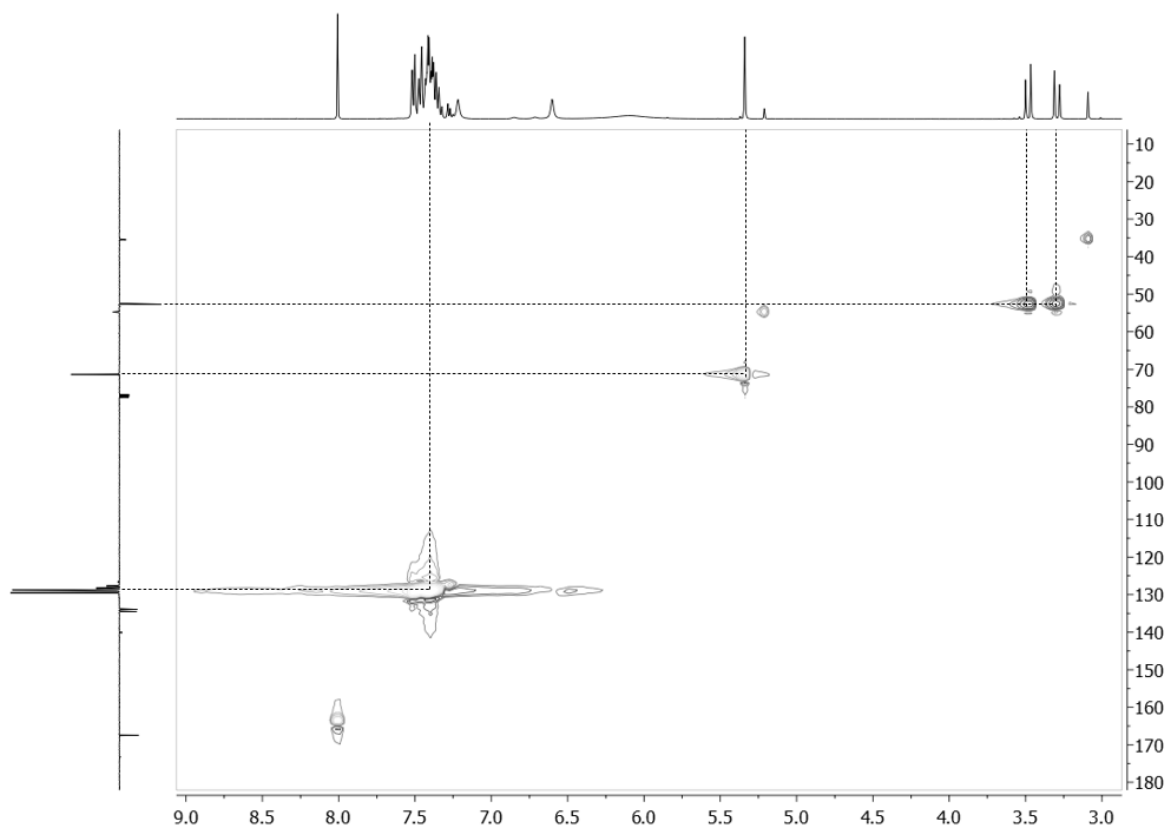


Figure S7 – HSQC NMR spectrum (400 MHz) of modafinil sulfoxide in  $CDCl_3$ .

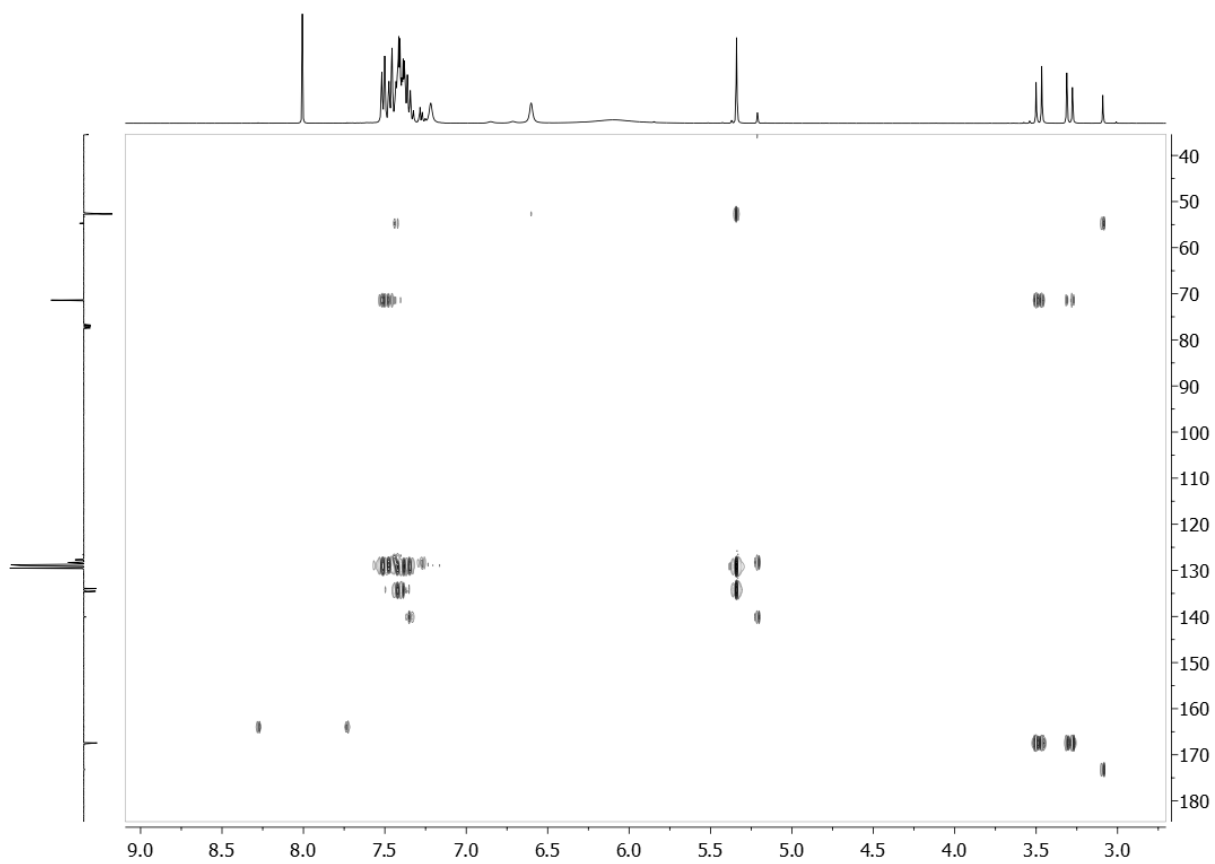


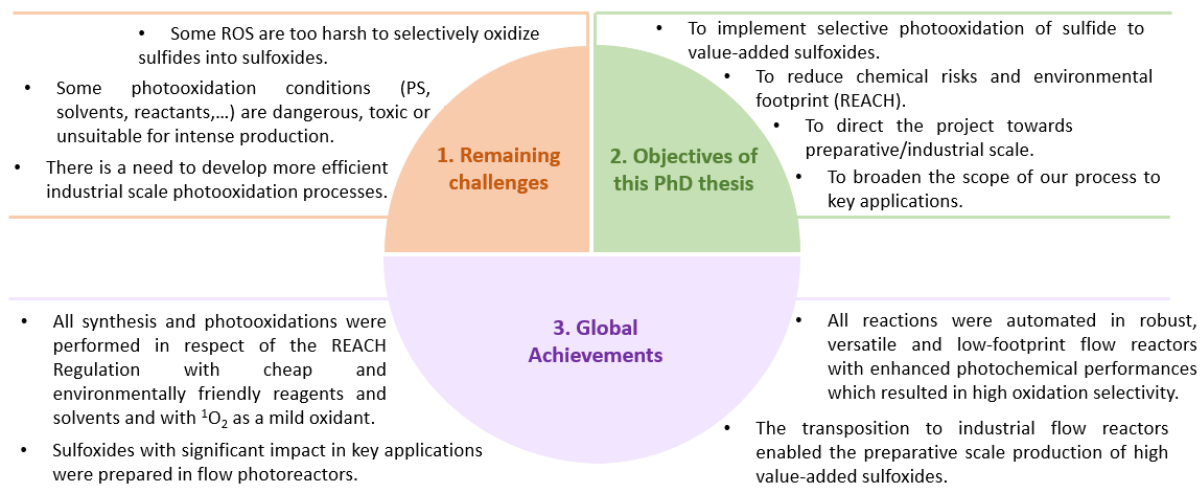
Figure S8 – HMBC NMR spectrum (400 MHz) of modafinil sulfoxide in  $CDCl_3$ .

## Chapter 5. Conclusion and perspectives

### 5.1. Summary and conclusion of the PhD results

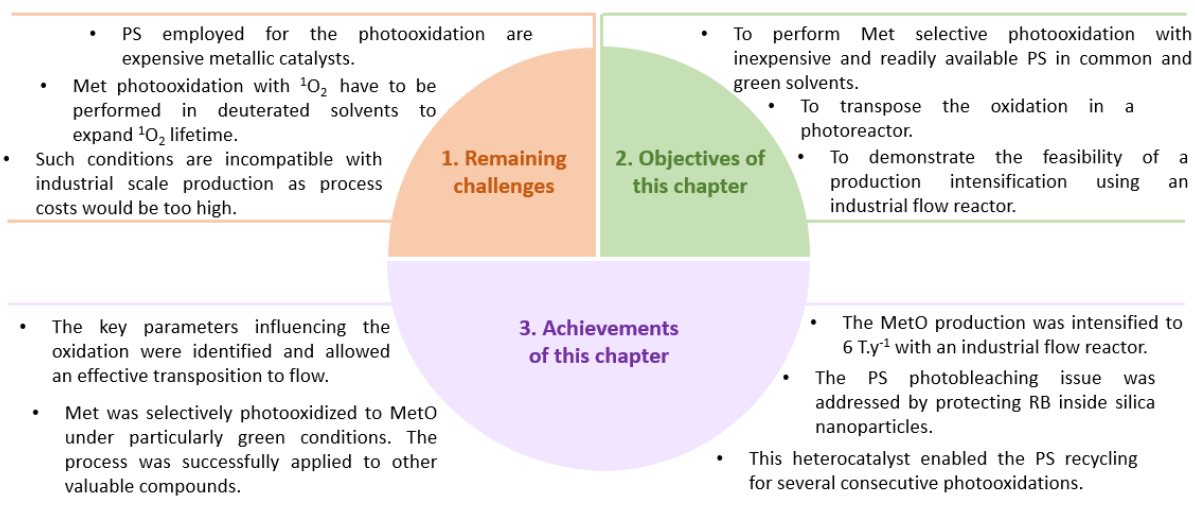
The REACH Regulation established by the European Commission in 2007, aims for a transition of chemical production practices. This PhD dissertation describes the implementation in continuous flow reactors for photooxidation of sulfides with singlet oxygen into high-added value compounds and fits into the scheme of REACH's priority guidelines. All photooxidations were performed in robust, versatile and low footprint continuous flow devices, PFA tubings or Corning® reactors, that enable automation and that contribute to mitigating the risks related to operator exposure or to process operation. The inherent assets of flow photochemistry favored a reduction of waste production thanks to a more efficient use of chemicals which was reflected by high selectivities. Furthermore, the choice of oxygen as a cheap, widely available and environmentally friendly mild oxidant combined to harmless PS and light adhere to the "safe and sustainable-by-design approach to chemicals". All oxidation protocols were performed in innocuous or biobased solvents.

The diagram below summarizes the global achievements of this PhD thesis in regard to the objectives described in section 1.5:



Model sulfides oxidized served for a rationalization based on computational studies, all other target molecules were selected based on their post-oxidation potential and commercial demand. Hence, our work proposed safe and scalable photooxidation procedures leading to significant achievements.

### 5.1.1. Conclusion and achievements of Chapter 2



The project was conducted in close collaboration with the engineering department. This collaboration enabled a kinetic study of the photooxidation of methionine in batch reactor and the identification of limiting parameters which were key information for the transposition to flow. Our process offers an alternative to previously reported photooxidations in deuterated solvents with metallic catalysts as it has been conceived under strictly environmentally friendly conditions ( $^1\text{O}_2$ , RB, water) and could be adapted to other valuable molecules such as ascaridole and rose oxide: a precursor of antibacterial vinylglycine, an anthelmintic drug and a fragrance respectively. The implementation of our flow process to an industrial reactor (Corning® flow reactor) could lead to an intensive and unprecedented production of methionine sulfoxide ( $6 \text{ T y}^{-1}$ ). The incorporation of RB inside mesoporous silica nanoparticles provided a practical solution to photobleaching and allowed the recycling of the PS for several oxidation cycles.

#### **Perspectives**

Moreover, optimizing the incorporation of RB or any PS more resistant to photobleaching in mesoporous silica nanoparticles could lead to fully integrated photoreactors where the reactor's walls would be coated with heterogeneous PS (Figure 74). RB is suitable for functionalization thanks to its carboxylic group but is sensitive to photobleaching and a balance between PS protection and PS efficiency needs to be found. Immobilizing a PS on a reactor wall is only advantageous if the PS can be recycled and remain efficient for a high number of oxidation cycles. Our results on the reusability of heterogeneous RB are encouraging for such applications. A coated microreactor would allow to perform several photooxidation of different substrates in a row. In this configuration, all solvents would be suitable as it does not require to solubilize the PS anymore.

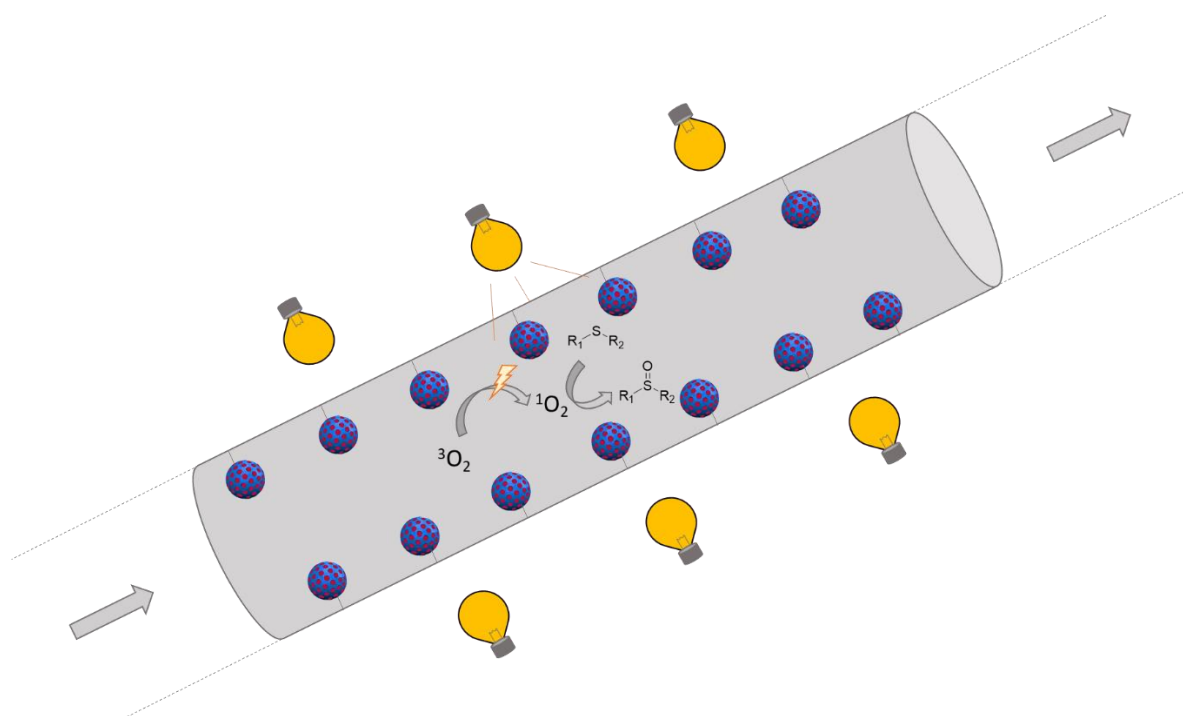
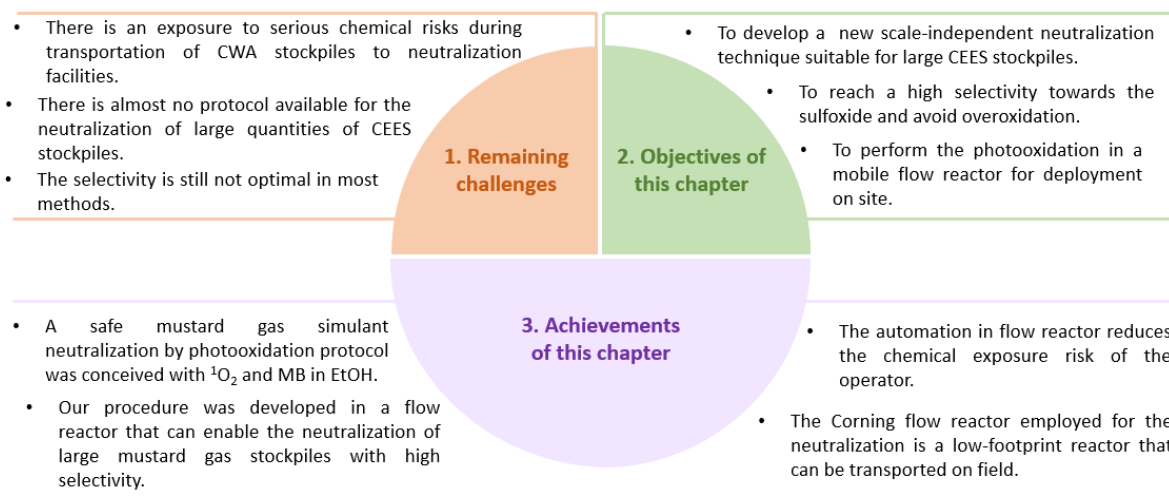


Figure 74 – Photoreactor with walls coated with heterogeneous PS.

### 5.1.2. Conclusion and achievements of Chapter 3



A new method was developed to proceed to the rapid and secure neutralization of a mustard gas simulant. The simulant, CEES, was fully oxidized with high selectivity under mild conditions ( $^1\text{O}_2$  with MB in EtOH). These conditions were applied to other sulfides with distinctive structures which helped for a rationalization of the oxidation mechanism. The compact flow reactor is suitable for large scale oxidations and transportation on field where the operator can then proceed to the CWA neutralization without being exposed to the chemical risks usually encountered during CWA handling. The automation of the neutralization reinforces this exposure reduction.

## Perspectives

In the field of chemical warfare agents, our neutralization protocol could be extended to other hazardous substances. For example, VX is an organophosphorous nerve agent that can be destroyed by the cleavage of its S-P bond. VX is currently neutralized by addition of highly concentrated NaOH aqueous solution but this can result in the P-O bond cleavage that leaves a product with similar toxicity (Figure 75). A neutralization with a mild oxidant could help in increasing the selectivity of the reaction and avoid the formation of toxic products.

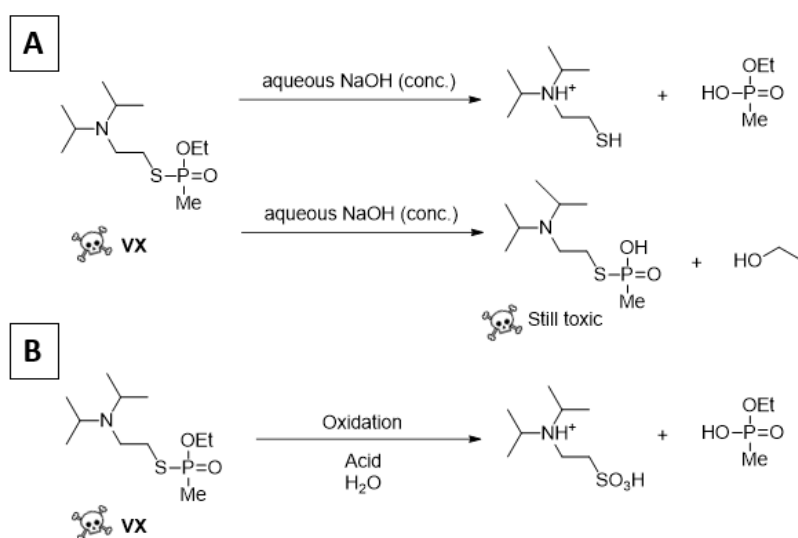
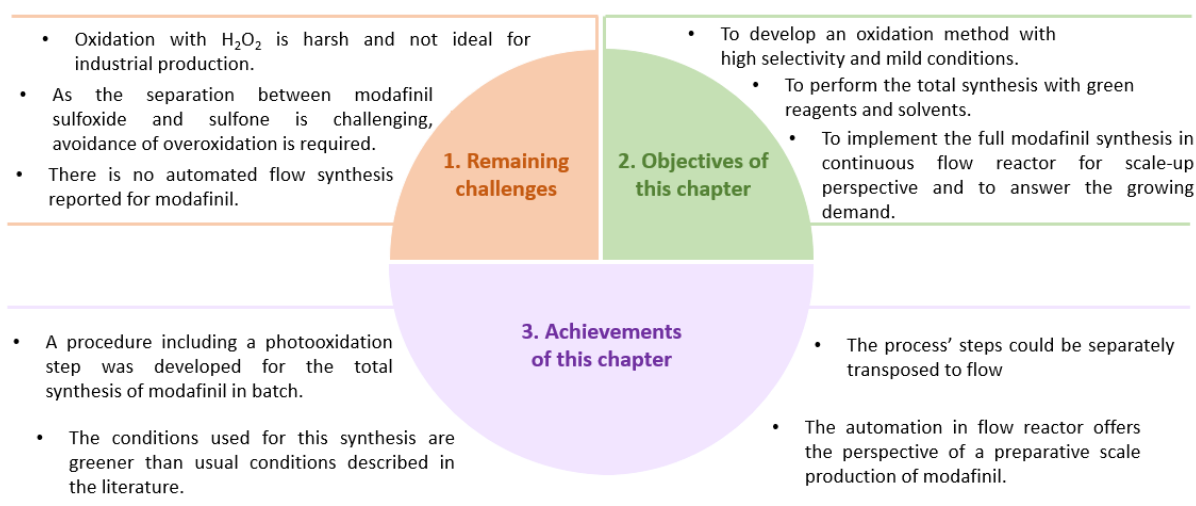


Figure 75 – Current (A) and Potential (B) neutralization pathway for nerve agent VX.

### 5.1.3. Conclusion and achievements of Chapter 4



The synthesis of smart-drug modafinil, a wake-promoting agent, was successfully developed in batch under greener conditions than what is usually described in the literature. The peroxide oxidation was replaced by <sup>1</sup>O<sub>2</sub> photooxidation. All steps could be implemented in flow, although optimization is still required. This chapter lays the foundation for further researches to propose a robust and concatenated flow process that can produce modafinil in sufficient quantity to answer its commercial demand.

## Perspectives

The priority in pursuing this work would be to optimize Modafinil synthesis as it still requires some work before being robust enough for industrial production. Although current results prove the feasibility of the concept, conversions, yields and selectivities are not yet satisfying and the reaction concentrations are still too low. Reactant concentrations in the second step, the benzhydrylation of SCS, were lowered because of clogging occurrence. This problem requires to find other conditions to perform the reaction at higher concentrations. Another acid and another solvent that solubilizes the reactants without altering the conversion need to be found. The concatenation of the three steps (Figure 76) will be challenging as the reactants and products of the three steps are not all soluble in the same solvents and as our photooxidation protocol has never been performed in such acidic conditions. However, with in-line liquid-liquid extraction, solvent changes are feasible in flow and could solve solubility issues.

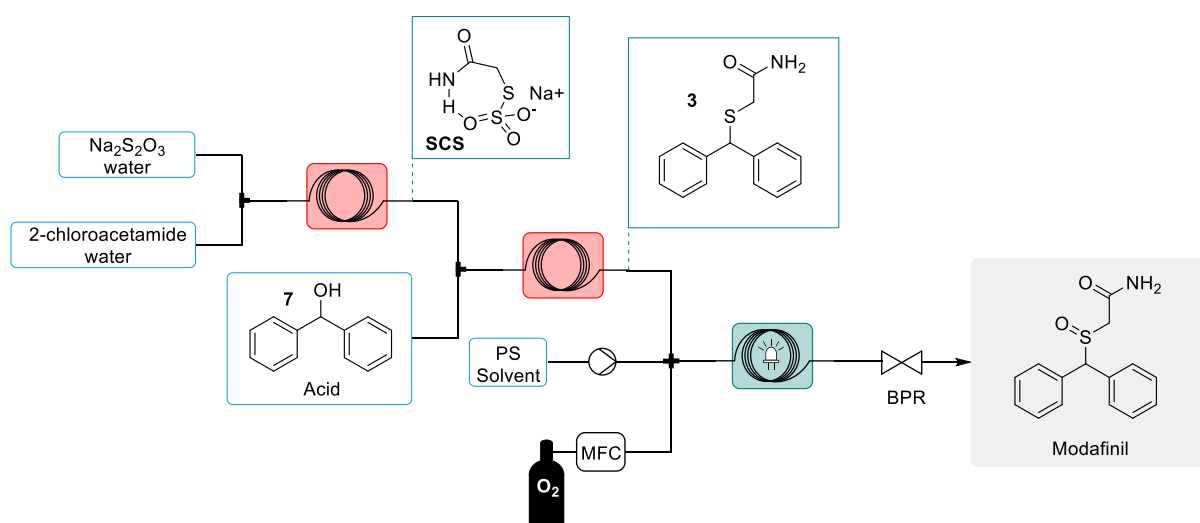
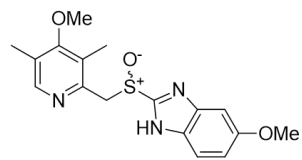


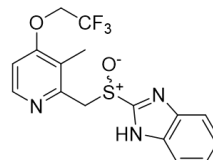
Figure 76 – Modafinil synthesis in flow with concatenation of all steps (not achieved yet).

Also, our results have the potential to be adapted to other valuable compounds and other relevant applications. The prazole is a drug family that is prescribed to treat stomach excessive acidity (Figure 77). Those proton pump inhibitors contain a sulfoxide moiety and could be relevant target for photooxidations. A few preliminary experiments photooxidation with singlet oxygen on Pantoprazole and Rabeprazole were attempted in our reactors without success. This could be due to the bulkiness of the molecule that makes it difficult for the oxygen to access the sulfur atom or to the availability of sulfur's lone pair that could be involve in the surrounding aromaticity. However, longer reaction times, solvents favoring singlet oxygen lifetime or other PS could help in achieving the oxidation.

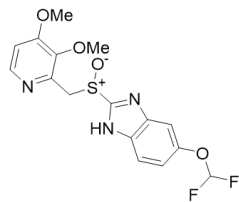
The efficiency of these APIs highly depends on their configuration. Both enantiomers do not have the same biological properties.  $^1\text{O}_2$  could be employed for stereoselective photooxidation of sulfides that would selectively generate the most active enantiomer.



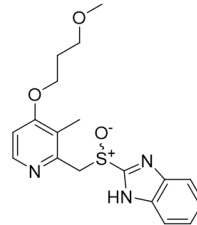
Omeprazole



Lansoprazole



Pantoprazole



Rabeprazole

Figure 77 – Examples of some prazole drugs' structure containing a sulfoxide moiety.

